Aston University

Some pages of this thesis may have been removed for copyright restrictions.

If you have discovered material in Aston Research Explorer which is unlawful e.g. breaches copyright, (either yours or that of a third party) or any other law, including but not limited to those relating to patent, trademark, confidentiality, data protection, obscenity, defamation, libel, then please read our Takedown policy and contact the service immediately (openaccess@aston.ac.uk)

THE CREEP BEHAVIOUR OF PRESSURE DIECAST ZINC - ALUMINIUM BASED ALLOYS

MEHMET DURMAN

Doctor of Philosophy

THE UNIVERSITY OF ASTON IN BIRMINGHAM

June 1989

This copy of the thesis has been supplied on condition that anyone who consults it is understood to recognise that its copyright rests with its author and that no quotation from the thesis and no information derived from it may be published without the author's prior, written consent.

THE UNIVERSITY OF ASTON IN BIRMINGHAM

THE CREEP BEHAVIOUR OF PRESSURE DIECAST ZINC - ALUMINIUM BASED ALLOYS

MEHMET DURMAN Ph.D. 1989

THESIS SUMMARY

The creep behaviour of three pressure diecast commercial zinc-aluminium based alloys: Mazak 3, corresponding to BS 1004A, and the new alloys ZA.8 and ZA.27 with a series of alloys with compositions ranging from 0% to 30% aluminium was investigated. The total creep elongation of commercial alloys was shown to be well correlated using an empirical equation. Based on this a parametrical relationship was derived which allowed the total creep extension to be related to the applied stress, the temperature and the time of test, so that a quantitative assessment of creep of the alloys could be made under different conditions. Deviation from the normal creep kinetics occurred in alloys ZA.8 and ZA.27 at very low stresses, 150°C, due to structural coarsening combined with partial transformation of ε-phase into T' phase. The extent of primary creep was found to increase with aluminium content, but secondary creep rates decreased in the order Mazak 3, ZA.8 and ZA.27. Thus, based on the above equation, ZA.8 was found to have a substantially better total creep resistance than ZA.27, which in turn was marginally better than Mazak 3 for strains higher than 0.5%, but inferior for smaller strains, due to its higher primary creep extension. The superior creep resistance of ZA.8 was found to be due to the presence of strictly-orientated, thin plate-like precipitates of ε ($CuZn_4$) phase in the zinc matrix of the eutectic and the lamellarly decomposed β phase, in which the precipitation morphology and orientation of ε in the zinc matrix was determined. Over broad ranges of temperature and stresses, the stress exponents and activation energies for creep were found to be consistent with some proposed creep rate mechanisms; i.e. viscous glide for Mazak 3, dislocation climb over second phase particles for ZA.8 and dislocation climb for ZA.27, controlled by diffusion in the zinc-rich phase. The morphology of aluminium and copper-rich precipitates formed from the solid solution of zinc was clearly revealed. The former were found to further increase the creep rate of inherently low creep resistant zinc, but the latter contributed significantly to the creep resistance. Excess copper in the composition, however, was not beneficial in improving the creep resistance. Decomposition of β in copper-containing alloys was found to be through a metastable Zn-Al phase which is strongly stabilised by copper, and the final products of the decomposition had a profound effect on the creep strength of the alloys. The poor creep resistance of alloy ZA.27 was due to the presence of particulate products derived from decomposed β-phase and a large volume of fine, equiaxed products of continuously decomposed α-dendrites.

Key words: **Creep Kinetics, Metallography, Pressure Die-castings, Zinc-Aluminium Alloys,**

DEDICATION

To my parents : for their tolerance and support over the years.

ACKNOWLEDGEMENTS.

I would like to take this opportunity to express my sincerest gratitude to my supervisor Dr. S. Murphy for his ceaseless help, guidance and encouragement throughout the duration of this work, without whom this project would not have been possible.

I would also express my gratitude to the staff of the Mechanical and Production Engineering Department of Aston University, particularly R. Howell, J. Foden, D. Farmer, J.Jeff, M.J. Scattergood, P.A. Pizer, A.G. Evitts and ex-staff E.T. Watson for their valuable assistance.

I am also grateful for the financial support of the Republic of Turkey and AM&S Europe Ltd. for funding the work.

Particular thanks are due to T. Burbery in the Department of Physical Metallurgy in Birmingham University for his assistance on TEM work, and K.Sawalha for his help during the preparation of this thesis.

LIST OF CONTENTS

		Page
	TITLE PAGE	1
	SUMMARY	2
	ACKNOWLEDGEMENTS	3
	LIST OF CONTENTS	4
	LIST OF TABLES	7
	LIST OF FIGURES	8
1.0	INTRODUCTION	21
2.0	LITERATURE SURVEY	23
2.1	**Definition of creep and creep curve**	23
2.2	**The Main Creep Types**	24
2.3	**High Temperature Creep Mechanisms**	26
	2.3.1 Climb-Controlled Glide Model	26
	2.3.2 Viscous Glide Model	28
	2.3.3 Dislocation-Jog Model	29
	2.3.4 Recovery-Creep Model	30
	2.3.5 Nabarro-Herring-Coble Creep	31
2.4	**Correlation of Creep Data**	33
	2.4.1 Time-Dependence of the Creep Strain	33
	2.4.2 Stress-Dependence of Secondary Creep Rate	35
	2.4.3 Temperature Dependence of Secondary Creep Rate	36
2.5	**The Equilibrium Phase Diagrams**	37
	2.5.1 The Binary Zn-Al System	37
	2.5.2 The Binary Zn-Cu System	41
	2.5.3 The Ternary Zn-Al-Cu System	43
2.6	**Phase transformations**	53
	2.6.1 Binary Zn-Al Alloys	53
	2.6.2 Ternary Zn-Al-Cu Alloys	60
2.7	**Creep and superplasticity in binary zinc-aluminium alloys**	61
	2.7.1 Grain Boundary Sliding and Rate Controlling Mechanisms in Superplasticity	66
2.8	**Creep in the Ternary and Higher Alloys.**	71

2.9 **Pressure Die-Cast Commercial Zn-Al Alloys** 73

2.9.1 The background and general characteristics of commercial pressure die-cast Zn-Al alloys 73

2.9.1.1 The Effect of Alloying Elements on general properties 78

2.9.2 Creep Behaviour of Commercial Pressure Die-Cast Zinc-Aluminium Based Alloys 78

2.10 **Concluding Summary** 87

3.0 **EXPERIMENTAL WORK** 90

3.1 **Experimental Alloys** 90

3.1.1 Commercial Pressure Die Cast Alloys 90

3.1.2 The Other Pressure Die-Cast Experimental Alloys 90

3.1.2.1 Preparation of Ingots 91

3.1.2.2 Die Casting of the Alloys 91

3.1.3 Gravity Casting 98

3.2 **Creep Testing** 98

3.2.1 Creep Machines and Strain Recording Equipment 99

3.2.2 Test Procedure 101

3.3 **Metallography** 104

3.3.1 Optical and Scanning Electron Microscopy 104

3.3.2 Transmission Electron Microscopy 105

3.3.2.1 Preparation of Thin Foils 105

3.3.2.2 Transmission Electron Microscopy 107

4.0 **EXPERIMENTAL RESULTS** 110

4.1 **Chemical Composition of the Experimental Alloys** 110

4.2. **Creep Results of Commercial Alloys** 111

4.2.1. Primary Creep Extension 112

4.2.2 Secondary Creep Rate 113

4.2.3 Total Creep Extension 114

4.3 **Metallography of the commercial alloys Mazak.3, ZA.8 and ZA.27** 131

4.3.1 Alloy Mazak 3 131

4.3.2 Alloy ZA.8 141

4.3.3 Alloy ZA.27 165

4.4 **Creep Results of Die-Cast the Alloys** 178

4.5	Metallography of the Die-Cast. Alloys	180
4.6	Gravity Cast Alloys	195
5.0	DISCUSSION OF EXPERIMENTAL RESULTS	199
5.1	Correlation of Creep Data of the Commercial Alloys Mazak 3, ZA.8 and ZA.27	199
5.2	Theoretical and Metallographic Consideration	227
5.2.1	Alloy Mazak.3	229
5.2.2	Alloy ZA.8	232
5.2.3	Alloy ZA.27	237
6.0	CONCLUSIONS	241
7.0	SUGGESTIONS FOR FURTHER WORK	245
	REFERENCES	247
	APPENDICES	262
	APPENDIX A	262
	APPENDIX B	275

LIST OF TABLES

Table 1. The Solid Solubility of Zinc in Aluminium. **39**

Table 2. The Solid Solubility of Copper in Zinc. **43**

Table 3. The Binary and Ternary Phases of Zn-Al-Cu Ternary System. and their Approximate Formulas. **49**

Table 4. Contribution of GBS to total elongation in regions I, II and III. **66**

Table 5. Chemical composition of commercial pressure diecast alloys. **76**

Table 6. Typical mechanical properties of the commercial zinc-aluminium alloys and other engineering materials. **79**

Table 7. Operating Conditions of Electropolishing for Commercial Alloys. **107**

Table 8. Composition of the experimental alloys (wt.%). **110**

Table 9. Secondary creep rates (s^{-1}) of M.3, ZA.8 and ZA.27 at 40 MPa. **114**

Table 10. STEM microanalysis of the phases of alloy M.3. **133**

Table 11. Mean STEM microanalysis of the phases in the alloy ZA.8. **147**

Table 12. Mean STEM microanalysis of the phases in the alloy ZA.27 **167**

Table 13. Creep data of the alloys 1 to 10 die-cast. **183**

Table 14. Creep data of gravity-cast alloys tested at 40 MPa and 120°C. **196**

Table 15. Results of the Regression analyses for parametric plots and values of the creep constant C' for the alloys Mazak.3, ZA.8 and ZA.27. **222**

Table 16. Maximum continuous design stresses (MPa) to produce % strain in 100,000 hours (11.4 years). **222**

LIST OF FIGURES

Figure 1.	Typical creep curve, showing the primary, secondary and tertiary regions (curve (a)) and logarithmic creep (curve (b).	**23**
Figure 2.	The creep diagram: the condition of temperature and stress. which produce the four principal types of creep.	**24**
Figure 3.	Nabarro-Herring creep. (a) Mass motion of atoms and vacancies across a small grain of dimension d under an applied stress. (b) Change in shape of a grain under the mass motion shown in (a).	**32**
Figure 4.	Zinc-Aluminium phase diagram compiled by Anderson & Anderko.	**39**
Figure 5.	Accepted phase diagram of binary Zinc-Aluminium system.	**40**
Figure 6.	The equilibrium phase diagram of the binary Zn-Cu system.	**42**
Figure 7.	Isothermal section of Zn-Al-Cu system at 700°C.	**45**
Figure 8.	Isothermal section of Zn-Al-Cu system at 550°C.	**45**
Figure 9.	Isothermal section of Zn-Al-Cu system at 350°C.	**46**
Figure 10.	Isothermal section of Zn-Al-Cu system at 200°C.	**46**
Figure 11.	Isothermal section of Zn-Al-Cu system at 350°C after Murphy.	**50**
Figure 12.	Isothermal section of Zn-Al-Cu system at 290°C after Murphy.	**50**
Figure 13.	Isothermal section of Zn-Al-Cu system at 280°C after Murphy.	**51**
Figure 14.	Isothermal section of Zn-Al-Cu system at 270°C after Murphy.	**51**

Figure 15. Isothermal section of Zn-Al-Cu system at 250°C after Murphy. 52

Figure 16. Solid-state reactions in the low-copper part of the Zn-Al-Cu system according to Murphy. 52

Figure 17. Al-Zn phase diagram(38)with the chemical and coherent spinodal curves. 57

Figure 18. A scheme of transformation in Al-Zn alloys according to Toldin et al. 59

Figure 19. Phase diagram of Zn-Al system with metastability boundaries. 59

Figure 20. Plasticity (a) and flow stress (b) of Zn-Al alloys at different temperatures. 63

Figure 21. Tensile fracture strain as a percentage vs initial strain rate and the corresponding plots of maximum flow stress vs initial strain rate (lower), showing three stages of deformation characteristic of the superplastic eutectoid alloy. 65

Figure 22. Grain switching process; the grains moves from the initial, through the intermediate state to final state while remaining approximately equiaxed. 68

Figure 23. Combined GBS and grain strain in the first quadrant of a superplastic specimen. Displaced left: grain motion without accommodation, the grains initially overlap and finally spread apart. Right: dark grains from adjacent Z planes fill the gaps. 69

Figure 24. Variation of the Ultimate Tensile Stress of the alloys Mazak.3, ZA.8 and ZA.27. with temperature. 80

Figure 25. Variation of the 0.2% Proof Stress of the alloys Mazak.3, ZA.8 and ZA.27. with temperature. 81

Figure 26.	Variation of the % Elongation of the alloys Mazak.3, ZA.8 and ZA.27. with temperature.	**82**
Figure 27.	Tensile Creep Properties of Pressure Die Casting Alloy M.3 at 25°C.(% allowable strain in indicated time vs. allowable stress.).	**85**
Figure 28.	Tensile Creep Properties of Pressure Die Casting Alloy M.3 at various temperatures.	**85**
Figure 29.	Tensile Creep Properties of Pressure Die Casting Alloy M.5 at various temperatures.	**86**
Figure 30.	Inverse secondary creep rate of ZA alloys as a function of stress at 20°C and 100°C.	**86**
Figure 31.	Commercial diecast plate from which samples were taken.	**90**
Figure 32.	E.M.B 10B Cold-Chamber Pressure Diecast Machine.	**92**
Figure 33.	Die cavity design for thin section plates.	**96**
Figure 34.	Decrease of the sections along the flow path of the feed system of the die.	**97**
Figure 35.	Actual diecast rectangular plates with runner system.	**97**
Figure 36.	B.S. Rectangular section test piece.	**98**
Figure 37.	Standard creep machine and strain recording equipment.	**102**
Figure 38.	Designed creep equipment with air circulation furnace and strain recording equipment.	**102**
Figure 39.	Appearance of creep specimen and calibration scale on the film.	**103**
Figure 40.	Measurescope (Optical microscope with LVDT attachment and digital indication unit.	**103**

Figure 41.	The Tenupol jet electropolisher with DC voltage supply unit.	**106**
Figure 42.	Creep curve of alloy M.3 at 30 MPa and 60°C.	**116**
Figure 43.	Creep curve of alloy M.3 at 80 MPa and 60°C.	**116**
Figure 44.	Creep curve of alloy M.3 at 10 MPa and 150°C.	**117**
Figure 45.	Creep curve of alloy M.3 at 30 MPa and 150°C.	**117**
Figure 46.	Creep curve of alloy ZA.8 at 40 MPa and 60°C.	**118**
Figure 47.	Creep curve of alloy ZA.8 at 80 MPa and 60°C.	**118**
Figure 48.	Creep curve of alloy ZA.8 at 10 MPa and 150°C.	**119**
Figure 49.	Creep curve of alloy ZA.8 at 40 MPa and 150°C.	**119**
Figure 50.	Creep curve of alloy ZA.27 at 40 MPa and 60°C.	**120**
Figure 51.	Creep curve of alloy ZA.27 at 100 MPa and 60°C.	**120**
Figure 52.	Creep curve of alloy ZA.27 at 10 MPa and 150°C.	**121**
Figure 53.	Creep curve of alloy ZA.27 at 15 MPa and 150°C.	**121**
Figure 54.	Variation of average primary creep extension of the alloys M.3, ZA.8 and ZA.27 with temperature.	**122**
Figure 55.	Variation of primary creep with aluminium content of the experimental alloys.	**123**
Figure 56.	Variation of secondary creep rates of the alloy M.3 with applied stress at different temperatures.	**124**
Figure 57.	Variation of secondary creep rates of the alloy ZA.8 with applied stress at different temperatures.	**125**

Figure 58. Variation of secondary creep rates of the alloy ZA.27 with applied stress at different temperatures. **126**

Figure 59. Variation of secondary creep rates of the alloys with the reciprocal test temperatures at 40 MPa. **127**

Figure 60. Variation of time to 1% creep strain with applied stress at different temperatures for alloy M.3. **128**

Figure 61. Variation of time to 1% creep strain with applied stress at different temperatures for alloy ZA.8. **129**

Figure 62. Variation of time to 1% creep strain with applied stress at different temperatures for alloy ZA.27. **130**

Figure 63. SEM. As-Cast structure of Alloy M.3 at low magnification, showing primary η particles and eutectic.(365x) **135**

Figure 64. SEM. As-Cast structure of Alloy M.3 at medium magnification, showing eutectic β formed on primary η particles.(730x) **135**

Figure 65. SEM. As-Cast structure of Alloy M.3 at high magnification.(1460x) **135**

Figure 66. TEM micrograph of small primary η particles set in the eutectic matrix.(11250x) **136**

Figure 67. TEM. Precipitation of Al-rich phase a in a primary η particle surrounded by a thin aluminium rich eutectic "halo"(27250x) **136**

Figure 68. (a) TEM micrograph of Al-rich precipitates in a primary η particle in detail.(51750x)
(b) SADP taken from area (a), consisting of the reflections $[1\bar{2}10]$ zone of hcp zinc matrix. **137**

Figure 69. TEM micrograph of irregular ribbon -like eutectic morphology in the alloy M.3.(31500x) **138**

Figure 70. TEM. Branching of eutectic in a complex three-dimensional morphology.(51750x) **138**

Figure 71. SEM micrograph of alloy M.3 tested at 40 MPa and 120°C, showing cavities formed randomly within the primary η particles.(400x) **139**

Figure 72. SEM. Alloy M.3 tested at 40MPa and 120°C, exhibiting deformation of η particles without cavitation.(825x) **139**

Figure 73. SEM. Creep fracture of alloy M.3 at 40 MPa and 120°C.(410x) **139**

Figure 74. TEM micrograph of alloy M.3 tested at 40 MPa and 120°C, showing growth of aluminium-rich precipitates in high length-to-width shape in the primary η dendrite.(14625x) **140**

Figure 75. TEM. Alloy M.3 tested at 40 MPa and 120°C, showing dislocations in the zinc matrix attached to the phase boundaries in the primary η particle.(19125x) **140**

Figure 76. SEM. As-Cast structure of Alloy ZA.8 at low magnification, showing primary β particles in the eutectic matrix.(365x) **151**

Figure 77. SEM. As-Cast structure of Alloy ZA.8 at medium magnification, showing decomposed β particles surrounded by lamellar eutectic.(1460x) **151**

Figure 78. SEM. As-Cast structure of Alloy ZA.8 at high magnification, showing decomposition of β dendrites into fine lamellar and coarse granular mixture of the phases.(3650x) **151**

Figure 79. TEM micrograph of general structure of alloy ZA.8 (4050x) **152**

Figure 80. TEM. Eutectic in the alloy ZA.8 with irregular ribbon-like α - lamellae, enclosing a metastable phase.(24750x) **152**

Figure 81. CBDP from eutectic Al-rich lamellar of alloy ZA.8. Beam direction is [110]. **153**

Figure 82. Same CBDP as above at high camera length, showing perfect fcc symmetry of α - phase **153**

***Figure* 83.** CBDP from the metastable phase, exhibiting a rhombohedral distortion of the fcc lattice, corresponding to the rhombohedral α_m'' phase with beam direction [110]. **153**

Figure 84. TEM micrograph of eutectic in the alloy ZA.8, showing heterogenously nucleated precipitation of ε phase in large densities covering the entire zinc matrix.(24750x) **154**

Figure 85. TEM. Precipitation of ε phase in the eutectic at high magnification.(112500x) **154**

Figure 86. SADP from the eutectic in alloy ZA.8, consisting of [0001] zone. **155**

Figure 87. SADP from the eutectic in alloy ZA.8, consisting of $[01\bar{1}2]$ zone of hcp zinc matrix. **155**

Figure 88. SADP from the eutectic in alloy ZA.8, consisting of $[\bar{2}4\bar{2}3]$ zone of hcp zinc matrix. **155**

Figure 89. SADP from the eutectic in alloy ZA.8, consisting of $[01\bar{1}1]$ zone of hcp zinc matrix. **155**

Figure 90. (a) SADP from the eutectic in alloy ZA.8, consisting of $[0\bar{1}10]$ zone of hcp zinc matrix, showing streaked reflections of ε precipitates
b) Indexing of the above pattern. **156**

Figure 91. (a) SADP from the eutectic in alloy ZA.8, consisting of $[1\bar{2}10]$ zone of hcp zinc matrix, showing streaked reflections of ε precipitates
b) Indexing of the above pattern. **157**

Figure 92. (a) Bright field image of the eutectic with ε-precipitates.(40500x)
(b) SADP of the area from the beam direction closely parallel to $[0\bar{1}10]$.

(c) Dark field image of the above area obtained from (0002) streaks (circled) 158

Figure 93. Stereographic projection of Zn and ε phases representing the orientation relationship between the two phases. 159

Figure 94. TEM A small β - particle decomposed into irregular ribbon-like lamellae.(51750x). 160

Figure 95. TEM. Decomposition of β - into regular lamellae.(67500x) 160

Figure 96. TEM micrograph of decomposed β phase into lamellae with metastable phases accommodated within the Al-rich lamellae. (191250x) 161

Figure 97. TEM. Decomposition of β into a coarse mixture of phases.(51750x) 161

Figure 98. SEM micrograph of alloy ZA.8 tested at 40 MPa and 120°C.(760x) 162

Figure 99. SEM. Alloy ZA.8 tested at 40MPa and 120°C, exhibiting nil deformation of β particles, and very little cavitation.(1520x) 162

Figure 100. SEM. Alloy ZA.8 tested at 40MPa and 120°C, showing coarsening of coarsening of fine (a+η) particulates at the edge of the former β primaries into continous rims of α and η. (3500x) 162

Figure 101. TEM micrograph of shoulder part of the alloy ZA.8 tested at 10 MPa and 150°C, exhibiting a considerable amount of coarsening of primary particle and eutectic, and decomposition of metastable phases into the equilibrium phases.(11250x) 163

Figure 102. TEM. Eutectic area from shoulder part of the sample tested at 10 MPa and 150°C.(51750x) 163

Figure 103. (a) SADP from the eutectic area in Figure 102, consisting of $[0\bar{1}10]$ zones of hcp zinc matrix and ε - precipitates, shows transformation of ε - precipitates into T' phase with an orientation relationship; $[0\bar{1}10]_{Zn}$ // $[0\bar{1}10]_{\varepsilon}$ // $[011]_{T'}$, (using cubic indexing for T').
(b) Indexing of the above pattern. **164**

Figure 104. SEM. As-Cast structure of Alloy ZA.27 at low magnification, showing α - cored dendrites in β and η - matrix.(165x) **169**

Figure 105. SEM. As-Cast structure of Alloy ZA.27 at medium magnification, showing decomposition morphology of α-dendrites, surrounded by decomposed β and eutectic.(1650x) **169**

Figure 106. SEM. As-Cast structure of Alloy ZA.27 at high magnification, showing fine equiaxed structure of α - dendrites surrounded by decomposed β and eutectic.(4150x) **169**

Figure 107. TEM micrograph of alloy ZA.27 illustrating precipitation of ε -phase in both zinc lamellae and eutectic in high densities, together with discrete ε - particles.(40500x) **170**

Figure 108. TEM. Interdendritic area with ε precipitates and particles and eutectic containing an appreciable amount of metastable phases.(31500x) **170**

Figure 109. CBDP from the ε -particle seen in Figure 108, showing the hcp symmetry of $[0\bar{1}11]$ zone. **171**

Figure 110. TEM micrograph of alloy ZA.27, illustrating the complex decomposition of an α' - dendrite and coexistence of the cellular colonies, the continuously decomposed matrix and the metastable phases decorating the dendrite.(14600x) **171**

Figure 111. TEM. Spinodally decomposed α - matrix with a very fine mixture of the phases, surrounded by coarse lamellare.(14600) **172**

Figure 112. TEM. Spinodally decomposed α matrix at high magnification, showing fine, irregular mixture of the phases.(90000x) **172**

Figure 113. TEM. Decomposition of β in the alloy ZA.27, showing the regular structure and branching of the lamellae.(31500x) **173**

Figure 114. TEM. Occurrence of different modes of decomposition of β in particulate and lamellar products with a considerable amount of metastable phases.(24800x) **173**

Figure 115. TEM. Same area shown in figure 114 in detail, illustrating the evidence for the lamellar growth suppressed by particulate phases and also for two stage decomposition.(40500x) **174**

Figure 116. SEM. As-Cast structure of Alloy ZA.27, showing microshrinkage porosity in the interdendritic area.(415x) **175**

Figure 117. Alloy ZA.27 tested at 40MPa and 120°C, showing the coalescence of the cavities.(340x) **175**

Figure 118. Alloy ZA.27 tested at 40MPa and 120°C, showing zinc-rich stringers crossing the α - dendrites, normal to the stress direction.(1340x) **175**

Figure 119. SEM. Alloy ZA.27, tested at 40MPa and 120°C, showing zinc-rich stringers crossing a dendrite, terminated by a coarsened Al-rich rim around the dendrite.(3350x) **176**

Figure 120. Alloy ZA.27 tested at 30MPa and 150°C, showing extensive break-up of the α - particles.(375x) **176**

Figure 121. Above area in detail, showing the curved interphase boundaries with cusps.(1500x) **176**

Figure 122. SEM. Alloy ZA.27, tested at 10MPa and 150°C, showing coarsening of fine decomposed β particles.(1400x) **177**

Figure 123. Alloy ZA.27 tested at 10MPa and 150°C at high magnification, showing coarsening of α-lamellae.(3650x) **177**

Figure 124. Creep curves of the alloys (1 to 10) die-cast, tested at 120°C under the stress of 40 MPa. **182**

Figure 125. Variation of the average primary creep elongations of the alloys (1 to 10) with increasing Al content. **184**

Figure 126. Variation of the average secondary creep rates of the alloys (1 to 10) with increasing Al content. **185**

Figure 127. Variation of the average times to produce 1% creep strain of the alloys (1 to 10) with increasing Al content. **186**

Figure 128. SEM. As-cast structure of die-cast alloy.2(M.3) **187**

Figure 129. SEM. As-cast structure of die-cast alloy.3. **187**

Figure 130. SEM. As-cast structure of die-cast alloy.4. **188**

Figure 131. SEM. As-cast structure of die-cast alloy.5(ZA.8) **188**

Figure 132. SEM. As-cast structure of die-cast alloy.5(ZA.8), showing the cores of the dendrites still undecomposed. **189**

Figure 133. The structure of alloy.5(ZA.8) at high magnification, showing the absence of lamellar structure. **189**

Figure 134. SEM. As-cast structure of die-cast alloy.6(ZA.12). **190**

Figure 135. SEM. General as-cast structure of die-cast alloy.7. **190**

Figure 136. SEM. As-cast structure of die-cast alloy.7 at higher magnification, showing undecomposed β phase around α cores. **191**

Figure 137. SEM. As-cast structure of die-cast alloy.8. **191**

Figure 138. SEM. As-cast structure of die-cast alloy.8 at higher magnification. **192**

Figure 139. SEM. As-cast structure of die-cast alloy.9(ZA.27). **192**

Figure 140. SEM. As-cast structure of die-cast alloy.9(ZA.27). **193**

Figure 141. SEM. General as-cast structure of die-cast alloy.10. **193**

Figure 142. SEM. Cored structure of die-cast alloy.10 at higher magnification, with less β - phase around the cores. **194**

Figure 143. SEM. As-Cast structure of gravity-cast Alloy 4.(400x) **197**

Figure 144. SEM. As-Cast structure of gravity-cast Alloy 5(ZA.8).(160x) **197**

Figure 145. SEM. As-Cast structure of gravity-cast Alloy 5(ZA.8).(1560x) **197**

Figure 146. Creep curves of the gravity cast alloys 3, 4, and 5(ZA.8), tested at 40 MPa and 120°C. **198**

Figure 147. Variation of ln(times(s) to 1% creep strain) with stress for alloy Mazak.3 at different temperatures. **208**

Figure 148. Variation of ln(times(s) to 1% creep strain) with stress for alloy ZA.8 at different temperatures. **209**

Figure 149. Variation of ln(times(s) to 1% creep strain) with stress for alloy ZA.27 at different temperatures. **210**

Figure 150. Variation of ln(times(s) to 1% creep strain) with ln[Sinh(ασ)] for alloy Mazak.3 at different temperatures. **211**

Figure 151. Variation of ln(times(s) to 1% creep strain) with ln[Sinh(ασ)] for alloy ZA.8 at different temperatures. **212**

Figure 152. Variation of ln(times(s) to 1% creep strain) with ln[Sinh(ασ)] for alloy ZA.27 at different temperatures. **213**

Figure 153. Ln(times(s) to 1% creep strain) versus reciprocal of test temperature for all 3 alloys at 20MPa. **214**

Figure 154. Ln(times(s) to 1% to various creep strains) versus creep parameter for alloy Mazak.3. **215**

Figure 155. Ln(times(s) to 1% to various creep strains) versus creep parameter for alloy ZA.8. **216**

Figure 156. Ln(times(s) to 1% to various creep strains) versus creep parameter for alloy ZA.27. **217**

Figure 157. Ln(times(s) to 1% creep strain) versus creep parameter for alloys Mazak.3, ZA.8 and ZA.27. **218**

Figure 158. Ln(times(s) to 0.7% creep strain) versus creep parameter for alloys Mazak.3, ZA.8 and ZA.27. **219**

Figure 159. Ln(times(s) to 0.5% creep strain) versus creep parameter for alloys Mazak.3, ZA.8 and ZA.27. **220**

Figure 160. Ln(times(s) to 0.2% creep strain) versus creep parameter for alloys Mazak.3, ZA.8 and ZA.27. **221**

Figure 161. Variation of constant C' with creep elongations for alloys Mazak.3, ZA.8 and ZA.27. **223**

Figure 162. Maximum continous design stresses for various allowable creep strains in 100000 hours (11.4 years) design life for alloy Mazak.3. **224**

Figure 163. Maximum continous design stresses for various allowable creep strains in 100000 hours (11.4 years) design life for alloy ZA.8. **225**

Figure 164. Maximum continous design stresses for various allowable creep strains in 100000 hours (11.4 years) design life for alloy ZA.27. **226**

CHAPTER 1

1.0 INTRODUCTION

The first major alloys developed for the zinc industry were the pressure die-casting alloys Mazak 3 and 5 (BS 1004A and B, respectively) which are traditionally associated with economic production of intricate decorative, functional or structural castings in large quantities at low cost.

They have for many applications, a very desirable combination of mechanical and physical properties over other types of pressure die-casting alloys; particularly their ability to be cast by the hot chamber pressure die-cast process in which production rates are typically high, making them a cornerstone of the die-casting industry since their introduction.

However, one property which sets a main limitation on their use, is their comparatively low resistance to deformation under a constant applied load, particularly in applications subjected to moderately elevated temperatures. In other words they have a low creep strength.

A need for a creep-resistant alloy to meet the requirements of structural applications in the zinc industry later led to the development of improved creep-resistant alloys ILZRO 14 and 16. However, due to their low aluminium content, the other mechanical properties of these alloys are inferior to those of the conventional alloys, and they cannot be cast by the traditional hot chamber die-casting process, which severely limits their use on the market.

Finally, during the last decade, the zinc industry developed a new range of higher aluminium zinc alloys (ZA foundry alloys designated as ZA.8, ZA.12 and ZA.27) to

supplement the above alloys. The evolution of this new family of zinc-aluminium alloys in the market place has been rapid. Their excellent mechanical and casting properties and significant market development efforts have led to ZA alloys being specified for an increasing range of industrial applications. This applies particularly to the die-casting sector where ZA alloys are being selected over traditional zinc and aluminium alloys to meet more stringent property requirements. Although originally developed as sand and gravity die-casting alloys, they can all be readily die-cast in cold chamber machines, and the alloy ZA.8, with its lower melting point and lower aluminium content, is also being routinely pressure die-cast by the traditional hot chamber die casting process, which makes this alloy, commercially, the most popular of all. It is highly probable that ZA alloys may be used more extensively for the production of pressure die-cast components for service at elevated temperatures, where applications of conventional alloys are usually limited because of their poor resistance to creep. At these temperatures the creep properties are more important than the short-term tensile properties and have become a major concern as a limiting factor in design.

One important aspect of this investigation was to determine the relative creep resistances of the newer alloys ZA.8 and ZA.27, in comparison with the established alloy Mazak 3, and also to provide a complete characterisation of their creep behaviour.

The overall object of this research on the other hand, was to establish a better understanding of the behaviour of zinc-aluminium pressure die-casting alloys in general, in terms of their creep kinetics and metallographic structure. Such understanding is essential for designers and specifiers and will increase the scope for their application and further development.

CHAPTER 2

2.0 LITERATURE SURVEY

2.1 Definition of creep and creep curve

When a stress is applied to a metal or an alloy, after an instantaneous strain which occurs on loading, the material continues to deform in a time-dependent manner and may eventually fail. This time dependent deformation is known as creep and can occur at all temperatures above absolute zero.

Creep behaviour of metals or alloys is usually determined by a test in which a constant load or stress is applied to a specimen and the creep strain is recorded graphically as a function of time.

Figure 1, curve (a) schematically shows a typical creep curve which exhibits various stages.

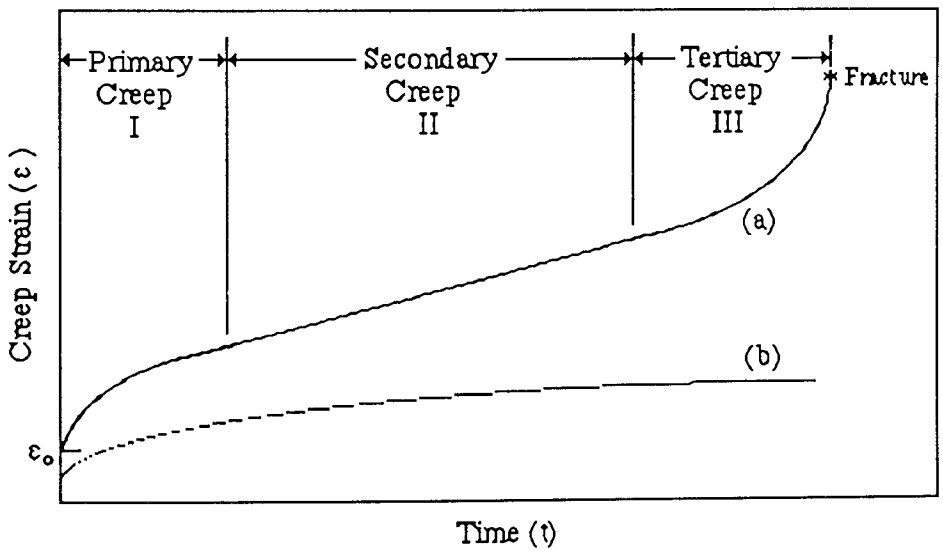

Figure 1. Typical creep curve, showing the primary, secondary and tertiary regions (curve (a)) and logarithmic creep (curve (b).

Immediately on application of the load, there is an instantaneous strain which exhibits characteristics of plastic deformation but, of course, includes elastic deformation. This

is followed by a period of primary creep in which the strain rate decreases with time until it reaches a constant rate, a period of secondary or steady-state creep in which the strain rate remains essentially constant, and then a period of tertiary creep in which the strain rate increases rapidly to final fracture.

2.2 The Main Creep Types

The creep which is observed in a given test can be classified as belonging to one of three well-defined types, depending on the test temperature and applied stress.

Figure 2 shows a temperature-stress diagram, indicating the regions in which each of these types is to be found[1].[1]

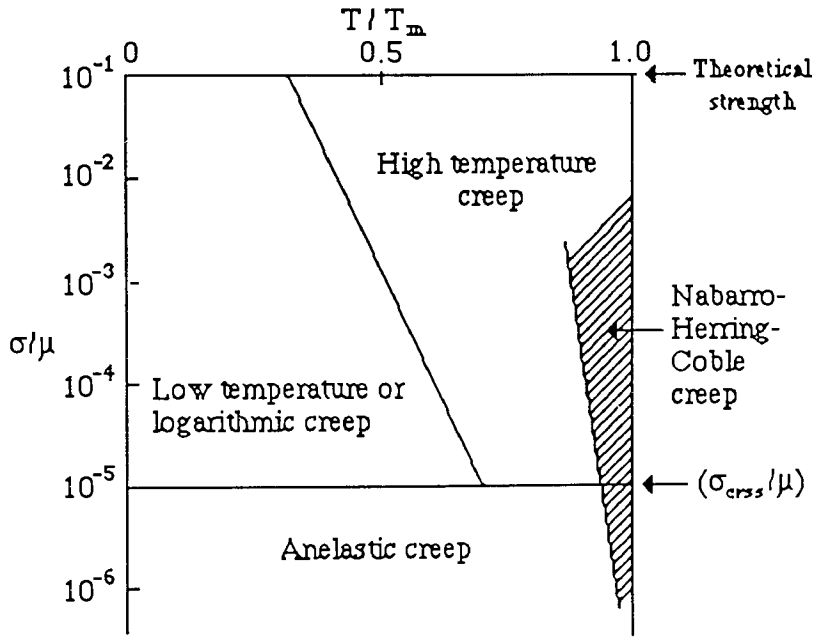

Figure 2. The creep diagram: the condition of temperature and stress which produce the four principal types of creep[1].

The upper limit of the diagram is set by the theoretical shear stress which represents

[1] *In order to treat different materials, with different elastic modulus and melting temperatures, on equal scale, stress and temperature are normalized by shear modulus and melting temperature of the material, so that the different types of creep fall roughly in the same regions on the diagram even though materials tested differ widely in their melting points and elastic constants.*

the stress required to cause shear of one plane atom over an adjacent plane. The bottom limit of the diagram is set by critical resolved shear stress which is the theoretical stress below which the amount of dislocation motion and multiplication is slight, and thus little plastic deformation takes place. Creep deformation which occurs at smaller than σ_{crss} arises through mechanisms other than the large scale of motion of dislocations. Thus, its contribution to the total strain is negligible compared to the dislocation contribution of other mechanisms.

At relatively high stresses and temperatures, the latter usually below 0.3 of the absolute melting temperature, an applied stress can produce dislocation multiplication and move dislocations over long distances, causing deformation. But this also causes strain-hardening, because of increasing dislocation density, which makes dislocation motion on slip planes increasingly difficult and eventually causes them to stop. Motion of dislocations in other directions, in order to escape from the obstacles at which they are held, and rearrange themselves on other planes is difficult, and can only be achieved by thermally activated processes such as cross-slip and climb. So, since diffusion is slow at low temperatures, the motion of dislocations in directions other than parallel to their slip planes is also slow. As a result, the more the sample is deformed, the more difficult does further deformation become. Therefore, the rate of creep deformation decreases with increasing time (*Figure 1 - curve (b)*) and contribution of low-temperature creep to total creep strain is also comparatively low. This type of creep is known as logarithmic creep, or low temperature creep, and the time-dependent strain which accumulates in a logarithmic manner is given by[1]:

$$\varepsilon = \varepsilon_e + \varepsilon_i + \varepsilon_o \log (1 + vt) \qquad (1)$$

where ε_e is the elastic strain; ε_i the instantaneous strain and ε_o and v constants dependent on stress and temperature.

However, creep at high temperatures, usually above 0.3 of the absolute melting

temperature, becomes a more thermally activated process. Thermal agitation stimulates difficult dislocation processes. Dislocations are thereby no longer constrained to move in their slip planes. By the process of climb, dislocations acquire a new degree of freedom in their motion and are free to move in any plane. As a result extensive strains can be produced in some tests without specimen failure, under stresses which produce only a small amount of strain at low stresses. That is why creep in high temperature ranges becomes a major concern as a limiting factor and it is considered as a unique deformation mechanism at elevated temperatures.

2.3 High Temperature Creep Mechanisms

The secondary creep stage is normally chosen as the parameter most representative of the material behaviour and the theories of high temperature creep are concerned primarily with explaining the steady-state part of the creep curve.

2.3.1 Climb-Controlled Glide Model

A mechanism for steady state creep based on the climb of edge dislocations was first proposed by Weertman[2,3]. He proposed two slightly different models. According to both, the relation between creep rate and stress can be expressed by power laws. For polycrystals the first model gives a power of 3, and a second model a power of 4.5. But, later on, it was reported that only the second model was in good agreement with experimental observations[3]. In this model, Weertman considered a case where dislocations were emitted from a source, but being confined to their glide planes, were eventually arrested and piled up at obstacles and, after a sufficient number of dislocation loops had been emitted, the elastic back stress then prevented further source operation.

For a material subjected to a constant stress, this situation would rapidly lead to a discontinuation of dislocation motion and therefore of deformation. The leading dislocation of the pile-ups would, however, climb out of its slip plane by vacancy emission. After climbing a distance, the dislocation may either be annihilated by a

dislocation of opposite sign or may be free to glide in a new slip plane. In either case, a new dislocation loop would be emitted from the source and creep would continue. For such a process the creep ($\dot{\varepsilon}$) rate may be expressed by the following equation[4]:

$$\dot{\varepsilon} = \frac{3\pi^2\sigma^2 D}{2\sqrt{2}\,\mu^2 b^2} \operatorname{Sinh}\left(\frac{\sqrt{3}\,\sigma^{2.5} b^{1.5}}{8 b^{1.5}\sqrt{M}\,kT}\right) \qquad (2)$$

where σ is the measured stress, D the coefficient of self-diffusion (D is equal to $D_A D_B / (D_A C_B + D_B C_A)$ in an alloy where C_A and C_B are the fractional concentrations of the alloy species and D_A and D_B are their diffusion constants), b the length of the burgers vector, μ the shear modulus, k is Boltzmann's constant, T is the absolute temperature, and M is the density of Frank-Read sources on one slip system. At low stresses this equation reduces to the power law equation[4]:

$$\dot{\varepsilon} = \frac{3\sqrt{6}\,\pi^2\sigma^{4.5} D}{2^5\sqrt{b}\,\sqrt{M}\,\mu^{3.5} kT} \qquad (3)$$

which predicts a stress exponent of 4.5, as was said earlier. This model has been proved experimentally to be valid for various alloy systems[4] and is considered as one of the main mechanisms which operates at high temperatures. However, it has been reported[4] that the stress exponent over the stress levels where the power law is valid, was dependent on the content of alloys, in that the exponent value decreases from values around 4.5 towards values close to 3 by increasing the alloy content. The same tendency has also been observed for many solid solution alloys due to increasing stress[5]. This behaviour has been attributed to a change in the rate controlling process upon alloying from climb to any one of a number of microcreep mechanisms, proposed by Weertman[4], based on viscous glide of the dislocations.

2.3.2 Viscous Glide Model

In the dislocation climb theory, it is considered that dislocations alternately glide and climb. These are sequential processes (i.e. climb is always preceded by glide) and therefore, the rate-controlling process will be associated with the slowest of the two . This has led to development of a viscous glide model, which applies only to solid solution alloys, where one of the microcreep mechanisms formulated by Weertman[4] governs the deformation. According to this mechanism, dislocation motion under stress is controlled by the velocity of solute drag along the dislocation line, the rate of which is given by[4]:

$$\dot{\varepsilon} = \frac{0.35\,\sigma^3}{\mu^2 A^2} \qquad (4)$$

where A is a constant which can be evaluated from the particular microcreep mechanism. This model predicts that the creep rate of solid solutions should be proportional to the third power of stress, indicating a slower process than dislocation-climb mechanism.

Several different viscous drag processes have been proposed, including the segregation of solute atoms to moving dislocations, the chemical interaction of solute atoms with extended dislocations, the destruction of short-range order and stress induced local ordering of solute atoms[4,5]. Among these, however, the major force retarding the glide of dislocations was found to be the presence of impurity atmospheres[6,7]. In this case the value of A in *equation (4)* is given by [6]:

$$A = \frac{e^2 c\, b^5 \mu^2}{k\,T\,D'} \qquad (5)$$

where e is the solute-solvent size difference, c is the concentration of solute atom and D' is the diffusion coefficient for the solute atom.

2.3.3 Dislocation-Jog Model

The point where a dislocation jumps from one plane to another is known as jog, and jogs on a screw dislocation are always edge jogs in character since they are perpendicular to their Burgers vector which lies along the screw axis. If the screw dislocation is forced to move, there are two ways in which the jog can move. Since the jog is merely a small piece of edge dislocation it may move sideways conservatively along the screw dislocation and attach itself to an edge component of the dislocation line[8]. In this case, jogs on the edge dislocations do not materially restrain the motion of an edge dislocation because the orientation of the slip planes of the jogs is such that they can move along the dislocation by slip[9].

At high temperatures, when a screw dislocation is forced to move, on the other hand, it has been proposed that jogs may be dragged non-conservatively along with the screw dislocation as it glides and maintains its position in the screw dislocation, with the aid of thermal activation. This is possible only by emission or absorption of point defects (vacancies or interstitials), depending on which way the jog is forced to climb[10]. In view of the high energy of formation of interstitials (i.e. the equilibrium concentration of interstitials is negligible), it is generally accepted that the vacancy mechanism is the much more probable mechanism[9-11]. In that case, the jogs accompany the dislocations only by emission of vacancies, the local vacancy concentration near the jog increases and this gives rise to a chemical force (dragging force) that retards the motion of dislocation. When the chemical (dragging force) is equal to the driving force (applied stress) a steady-state velocity is attained.

Conversely, in the case of the vacancy-absorbing jogs, the rate of the process is controlled by the vacancies which diffuse to jogs, causing a decrease in vacancy concentration near the jog which gives rise to dragging force on the jog.

The secondary creep rate for this mechanism is given by[10].

$$\dot{\varepsilon}_s = 2\pi\rho_s D\,\alpha \left(\frac{b}{a_o}\right)^3 \mathrm{Sinh}\left(\frac{\sigma b^2 \lambda}{2\,kT}\right) \qquad (6)$$

where ρ_s is the mobile screw dislocation density, D the self-diffusion coefficient, α the number of atoms per unit cell, b the Burgers vector, a_o the lattice parameter, and λ is the average spacing between jogs.

2.3.4 Recovery-Creep Model

The most recent formulation of this mechanism is given by McLean[12] and Lagneborg[13]. In agreement with direct observation, these authors assumed the dislocations to be arranged in a three dimensional network, and the creep process consisting of consecutive events of recovery and strain-hardening. It was assumed that the strength was provided by the attractive and repulsive junctions of the network. Some of these junctions would break as a result of fluctuations, and released dislocations would move a certain distance until they are held up by the network, and thereby give rise to strain movement and also to an increase in the internal stress (i.e. strain-hardening), since, at the same time, the dislocation density increases. Simultaneously, the recovery process would tend to increase the average mesh-size of the network (i.e. to decrease the dislocation density). Eventually, some link would be long enough for the junctions to be sufficiently weak to break with the aid of the thermal fluctuations and the applied stress, and the consecutive events of recovery and strain hardening would repeat themselves.

This model also gives an explanation of the primary creep behaviour, in a way that, for the low dislocation densities at short creep times, the recovery rate cannot catch up with the rate of strain-hardening and therefore, the creep rate in primary region will be high and decreasing. As the dislocation density increases the recovery accelerates and

eventually a stage will be attained where strain-hardening and recovery balance each other.

McLean formulated this process quantitatively by means of an Arrhenius type expression ;

$$\dot{\varepsilon} = \dot{\varepsilon}_o \exp\left[-\frac{V(h\varepsilon - rt)}{kT}\right] \qquad (7)$$

where $\dot{\varepsilon}_o$ is the initial creep rate, V the activation volume, h the strain-hardening coefficient, r the recovery rate and t is the time.

2.3.5 Nabarro-Herring-Coble Creep

Figure 2 also shows a special kind of creep (Nabarro-Herring-Coble creep) which occurs at very high temperatures near to the melting point and at stress levels which are too low for dislocation processes to be significant.

Under these circumstances, creep can occur by diffusional flow of atoms from parts on grain boundaries where they are under compression, to parts which are under tension. To transport atoms in this way involves creating vacancies on the faces under tension and destroying them on the other faces (*Figure 3a*). This stress directed flow of atoms renders the specimen longer in the tensile direction (*Figure 3b*). This type of creep was first suggested by Nabarro[14] and subsequently by Herring[15]. Grain boundaries play a control role for diffusion creep since they can accommodate or release atoms or, in other words, generate or annihilate atomic vacancies. That is why this type of creep can usually dominate as a deformation mechanism when the grain size is small.

The rate-controlling step of the diffusion creep is the diffusion over distances of the order of the grain size, d, while the applied stress σ presents the driving force, then,

the creep rate is proportional to stress and inversely proportional to the square of the grain size, as given by Nabarro and Herring[14,15]:

$$\dot{\varepsilon} = \frac{\alpha_v \sigma \Omega D_v}{kT\, d^2} \qquad (8)$$

where D_v is the diffusion coefficient in the grains, Ω atomic volume, and α_v is a dimensionless numerical factor the magnitude of which depends on the shape of the grain.

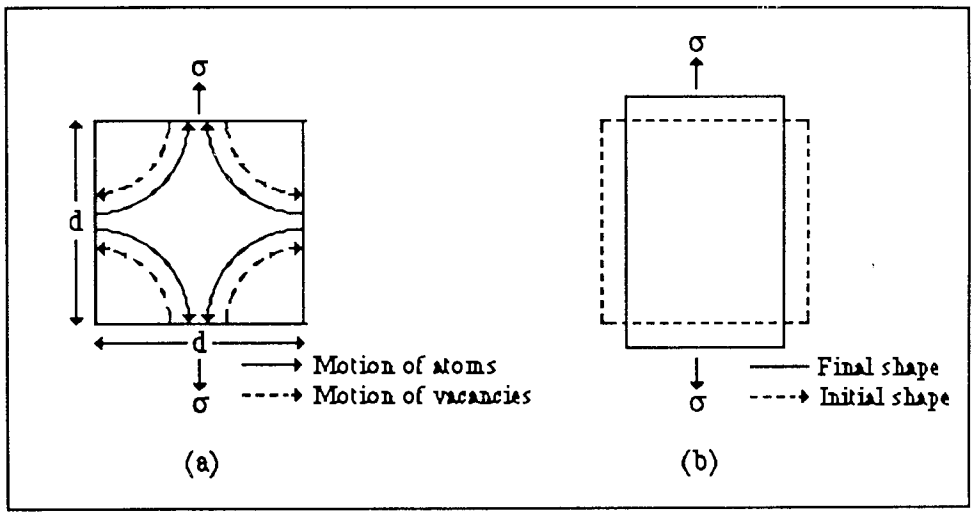

Figure 3. Nabarro-Herring creep. (a) Mass motion of atoms and vacancies across a small grain of dimension d under an applied stress. (b) Change in shape of a grain under the mass motion shown in (a).

In this theory, developed by Nabarro and Herring, diffusion was considered to occur only through the crystal lattice. However, Coble[16] showed that the diffusion path was not necessarily confined to the interior of a grain and could occur along grain boundaries. The creep rate, in that case, was found to be also proportional to stress, but inversely proportional to the cube of the grain size as given by:

$$\dot{\varepsilon} = \frac{\alpha_{gb} \sigma \Omega \delta D_{gb}}{kT\, d^3} \qquad (9)$$

where α_{gb} has a value of around 50 and δD_{gb} is the grain boundary diffusion coefficient.

2.4 Correlation of Creep Data

Simple graphical representation of creep curve is adequate when tests are performed to establish how certain parameters, such as the time to produce a certain creep strain, vary with stress and temperature for any material. However, for many practical and theoretical purposes, it is often desirable to develop equations which define the rate of strain accumulation with time, so that graphical representation can be replaced by analytical procedures which would allow the creep curves to be specified in terms of a set of parameters. Other equations can then be evolved which would describe how these parameters vary with stress, temperature or material parameters. In this way, the creep characteristics of a material can be expressed in terms of one or more constitutive equations which relate stress-strain-time-temperature.

2.4.1 Time-Dependence of the Creep Strain

The relation between time and creep strain (ε) in primary and secondary stages has often been described by[17]:

$$\varepsilon = \varepsilon_o + \beta t^m + \dot{\varepsilon}_s t \qquad (10)$$

Where ε_o is the instantaneous strain, β and m are constants independent of time, and ($\dot{\varepsilon}_s$) is the secondary creep rate.

The value of m has been found to range from 0.03 to nearly 1.0 for many metal and solid solution alloys, and depends on both temperature and stress[17].

This equation, however, has been shown to predict an infinite initial creep rate and an untrue transient creep[18].

These deficiencies were eliminated by using the following exponential expression[18]:

$$\varepsilon = \varepsilon_o + \varepsilon_t\left(1-e^{-r\,t}\right) + \dot{\varepsilon}_s\,t \qquad (11)$$

where ε_t is the transient strain during the primary stage, and r is the ratio of transient creep rate to the transient creep strain.

Although this equation yields an adequate description for most of the creep life for many metals and alloys, a general deviation overestimating the creep life has also been reported[19,20].

An important finding of these studies was that the creep rate in primary stage was proportional to the secondary creep rate over considerable ranges of stress and temperature, suggesting that the mechanism controlling the creep deformation was the same throughout the primary and secondary stages.

The idea that the mechanism of creep is the same throughout the primary and secondary stages provides a justification for the fact that most fundamental studies have concentrated exclusively on the experimental determination and the theoretical interpretation of the ways in which secondary creep rates vary with temperature, stress and material parameters, since this approach offers numerous advantages.

Very recently, a new creep life prediction method (θ - projection concept) has been claimed, by Evans et al[21-24], to quantify the shape of the creep curve with stress and temperature. This project envisages normal creep curves as the sum of a decreasing primary and accelerating tertiary regions (a steady-state does not exist), with the increase in creep strain with time.

The strain-time behaviour has been described using the expression:

$$\varepsilon_c = \theta_1\,(1 - e^{-\theta_2 t}) + \theta_3\,(e^{\theta_4 t} - 1) \qquad (12)$$

where θ_i (i = 1 - 4) is a parameter depending on stress and temperature.

Once θ_i is determined at any set of testing conditions, the shape of the creep curves of other conditions can be predicted. Although this concept has been claimed to offer numerous theoretical and practical advantages, it can only be applied to describe the creep curves under a constant stress, and only a few reports are available at present to confirm the applicability of the method.

2.4.2 Stress-Dependence of Secondary Creep Rate

It is frequently observed that secondary creep rate ($\dot{\varepsilon}_s$) of a polycrystalline material may vary over a wide range of stress. At very low stress levels the relation between ($\dot{\varepsilon}_s$) and stress is usually observed to be linear and this relation is given[25]:

$$\dot{\varepsilon}_s = K\,\sigma \qquad (13)$$

It is believed that creep in this range is not due to dislocation motion, but rather is due to a stress-directed atom migration process (Nabarro-Herring-Coble Creep).

At intermediate stress levels, the stress dependence of creep rate is usually described using the power law equation:

$$\dot{\varepsilon}_s = A\,\sigma^n \qquad (14)$$

where A and n are independent of stress.

In general, the stress exponent, n, ranges between 4 and 6 for pure metals, and between 2 and 4 for alloys, depending on the material and test conditions[17].

At high stress levels, the secondary creep rate increases much more rapidly than predicted by this equation. This phenomenon is described as the power-law break-

down, and, at these higher stress levels, the secondary creep rate is better expressed by an exponential expression[17,25]:

$$\dot{\varepsilon}_s = A' \exp(\beta\sigma) \qquad (15)$$

where A' and β are constant at constant temperature.

Alternately, a single relation proposed by Garofalo[26] has been found to satisfy conditions for both low and high stresses. This relation is given by:

$$\dot{\varepsilon}_s = A'' (\text{Sinh } \alpha\sigma)^n \qquad (16)$$

where A'' and α are constant at constant temperature. For values of $\alpha\sigma < 0.8$ *equation (16)* reduces to power law *equation (14)* where $A = A'' \alpha^n$ and for values $\alpha\sigma > 1.2$ *equation (16)* reduces to the exponential *expression (15)* where $A' = A'' / 2^n$ and $\beta = n\alpha$.

2.4.3 Temperature Dependence of Secondary Creep Rate

Since creep is a thermally activated process, the temperature dependence of the creep rate is normally well presented in terms of an Arrhenius-type expression with a characteristic activation energy for the rate controlling mechanism:

$$\dot{\varepsilon}_s = B \exp\left(-Q_c / RT\right) \qquad (17)$$

where A is a constant for a given creep stress, and exponential term expresses the rate at which a controlling process with activation energy, Q_c, allows the process to proceed. T is the absolute temperature and R is the universal gas constant.

The variation in Q_c at temperatures above ~0.5 is slight with increasing temperature and the value of Q_c usually approaches the activation energy for self diffusion.

Therefore, it is believed that the deformation mechanism in that region is due to non-conservative motion of dislocation[25]. Between 0.3 and 0.4 Tm, the activation energy for creep is usually less than that for self-diffusion, and the rate controlling process is believed to be associated with cross-slip of dislocations[25].

If it is considered that stress has a major influence as well as the temperature, especially at low temperature levels, both temperature and stress dependence terms can be incorporated in one equation to produce:

$$\dot{\varepsilon}_s = C\,\sigma^n \exp\left(-Q_c/RT\right) \qquad (18)$$

or in a more unified form:

$$\dot{\varepsilon}_s = C'(\mathrm{Sinh}\,\alpha\,\sigma)^n \exp\left(-Q_c/RT\right) \qquad (19)$$

2.5 The Equilibrium Phase Diagrams

2.5.1 The Binary Zn-Al System

The binary equilibrium diagram of the Zn-Al system has been one of the most investigated phase diagrams over a period of more than 80 years.[27,28] Numerous phase diagrams that have been published over this period are now obsolete, with the exception of the liquidus curves and temperatures of the three phase equilibria. For many years, the major conflict among the investigators was the possibility of a peritectic reaction. The earliest workers[29-31] proposed an equilibrium phase diagram which was similar in that it showed, (a) an intermediate phase of variable composition around 78% Zn, generally denoted as β, and formed by a peritectic reaction (at about 443°C) of the melt with the aluminium base solid solution containing about 70% Zn; (b) a eutectic of β and the zinc-based solid solution at 95% Zn, 380°C, and (c) an eutectoid decomposition of β, with the eutectoid point at about 78% Zn, 270-280°C. Later, however, Owen and Pickup[32] and Elwood[33,34], studying the system by

high temperature X-ray camera methods, were unable to confirm the existence of a peritectic reaction. Fink and Willey[35], using resistivity and microscopic techniques at temperature, concluded that the peritectic reaction was non-existent. Gayler and Sutherland[36] also reached this conclusion, on the basis of thermal, microscopic and dilometric evidence. The thermal arrest which they found at 443°C was attributed to a rapid change in composition of the α' solution along the solidus.

Figure 4 shows the Zn-Al phase diagram compiled by Anderson and Anderko[37], from the results of Elwood and earlier workers, eliminating the peritectically formed intermediate phase of variable composition that was suggested for the Zn-Al binary system.

The most important recent, and probably the most accurate, representation of the binary diagram, which accounts for all the experimental fact, was produced by the consecutive work of Presnyakov et al[38] and Goldak and Parr[39].

Presnyakov et al studied a small portion of the diagram in great detail and discovered a very narrow two-phase field, which led them to conclude that (a) the peritectic reaction did, in fact, exist at about 443°C; (b) a β phase, distinct from the α phase, existed and involved a discontinuity in the solubility; (c) there was a second eutectoid decomposition of the α' phase into $\alpha+\beta$ at about 340°C, with the eutectoid point at about 70% Zn.

Later, this work was confirmed explicitly by Goldak and Parr in their high temperature X-ray diffractometer study of the Zn-Al system in the region 40-75 wt % Zn.

It is now considered that the phase diagram of Presnyakov et al, confirmed by Goldak and Parr, is probably the most accurate representation of the binary diagram to date, as reproduced in *Figure 5*.

Aston University

Content has been removed for copyright reasons

Aston University

Content has been removed for copyright reasons

In the range of 351°C and 340°C, the Al-rich solid solutions break down into two phases α and α', which are both a solid solution of zinc in aluminium with different percentages of zinc. This gap of miscibility extends from 49 to 69.5% Zn at 340°C and shrinks regularly to reach the singular point at 351°C. From here, the solubility increases with decreasing temperature to a value of 69.5% Zn at 340°C, then rises to 70% at peritectic temperature. The $\alpha'+\beta$ field is very narrow, ~ 1 wt % wide[39], extending from an eutectoid point at 69.5% Zn to the peritectic point at 443°C.

At the zinc end the solidus and liquidus slopes down sharply to the eutectic. The solubility of aluminium in zinc is small, approximately 1.1% Al at eutectic temperature (383°C), decreasing to 0.65% Al at eutectoid temperature (275°C) and 0.42% Al at 227°C[28]

β phase is f.c.c. with its lattice parameter at 340°C decreasing from 4.04Å at 70% Zn to 4.03Å at 76% Zn[38]. At 275°C, it decomposes by an eutectoid reaction into $\alpha+\eta$ with the eutectoid point at 78% Zn. The lattice parameter of pure aluminium at 25°C is 4.0414Å[40] and this decreases almost linearly to 4.0Å at 65% Zn in the α region[34]. Zinc is a hexagonal close packed crystal structure with lattice parameters[40]; a=2.6595Å, c= 4.9368Å when pure and a = 2.665Å, c = 4.987Å when saturated with aluminium[41].

2.5.2 The Binary Zn-Cu System

The equilibrium diagram of the binary Zn-Cu system presented in *Figure 6*[42] can be regarded as very well established. It shows five peritectic reactions. Four intermediate phases exist, β, γ, δ and ε, which, with the exception of the δ phase, have broad ranges of solid solubility. Because of the nature of this work, which involves the alloys containing up to 2% copper, only the lower copper part of the Zn-Cu equilibrium system will be considered here.

Aston University

Content has been removed for copyright reasons

As it can be seen from *Figure 6*, solubility of copper in Zinc decreases with decreasing temperature as given in *Table 2*[37].

Table 2 : The Solid Solubility of Copper in Zinc.

Temperature (°C)	Solubility (wt %)
100	0.3
200	0.9
300	1.65
400	2.5
424	2.7

Therefore, a supersaturated solid solution of η-phase yields upon ageing precipitates of the ε-phase. Both phases have essentially the same crystal structure with lattice spacings as given below:

ε : a = 2.735Å c = 4.285Å at 21% at.% Cu[40]

η : a = 2.668Å c = 4.870Å at 1.55% at.% Cu[41]

In the ε phase, the axial ratio decreases from about 1.58 to 1.55 with increasing concentration of zinc in the region of 68 - 88 %. Conversely, in the η phase, the initial ratio is considerably above the ideal value and increases from about 1.78 near the (ε + η)/η boundary to 1.856 at pure zinc[410,43].

2.5.3 The Ternary Zn-Al-Cu System

The Zn-Al-Cu ternary system has become known as a result of intensive studies of Koster and Moeller[44-46] in 1941 and 1942 and of Gebhard[47-49] in 1941, 1942 and 1943. Cu-rich areas of the system were also thoroughly studied by Bauer and Hansen[50,51] and Fletcher and Thomas[52].

The isothermal sections of the Zn-Al-Cu system at 700, 550, 350 and 200°C are given in *Figures 7, 8 ,9 and 10*, respectively, as compiled by Willey[54].
Diagrams were compiled from the evaluation by Arndt and Moeller[55,56] from diagrams by Koster and Moeller[44-46] in the areas bounded by approximately 60 Al - 40 Cu, 15 Al - 81 Cu, 40 Cu - 60 Zn and 20 Cu - 80 Zn. The Cu-rich parts were from Bauer and Hansen[50,51] and from Fletcher and Thomas[52]. The Zn-rich sites at 20 to 55% Cu were principally from Gebhardt[47-49].

The arrangement of the phase fields within the ternary system conforms well with the binary faces, except in the range from about 15 to 26% Al of the Al-Cu binary system. At temperatures of 700 to 550°C (*Figures 7 and 8*), Arndt and Moeller showed a single phase, γ, from about 16 to 22% Al. At 350 and 200°C (*Figures 9 and 10*), they divided this region into three parts, the Cu-rich γ' (16 - 19% Al), the intermediate γ_1 (19 - 20.5% Al), and the Al-rich γ_2 (20.5 - 22% Al). Within the approximate limit of 700 to 200°C and 16 to 22% Al, the phase fields in the Al-Cu binary system were identified as γ_2 (16 to 20% Al), $\gamma_2 + \delta$ (20 - 21% Al), and δ (21 - 22% Al). Furthermore, within the composition range of approximately 22 to 26% Al, Arndt and Moeller showed a single phase, ζ_1 at 700°C, and ζ_2 at 550°C.

Within the ternary system, the β phase of the Al-Cu binary system forms a complete solid solution with β phase of the Cu-Zn binary system above the decomposition temperature for Al-Cu β phase at 565°C. The various forms of the γ phase of the Al-Cu binary system were shown to be completely soluble within the γ phase of the Cu-Zn binary system, within the full temperature range of stability, the ζ_1 phase of the Al-Cu binary system was shown to be completely soluble with the Cu-Zn δ phase in a narrow range of temperature between the temperature of formation of the δ phase at ~ 699°C and ~ 680°C.

Aston University

Content has been removed for copyright reasons

Aston University

Content has been removed for copyright reasons

In addition to the binary phases present in the binary system, one ternary phase (T) formed by a peritectic reaction was found stable within a narrow strip. At 700°C, the T phase has a narrow range of composition about 70% Cu, 9% Zn and 21% Al. With decreasing temperature, the composition range of T widens towards higher Al and Zn contents and lower Cu contents. Between 600 and 550°C, a related ternary intermediate phase T' appears in the Al-rich end of the T homogeneity range. At 550°C, the T phase has a wide range of composition surrounding 62% Cu, 18% Zn, 20% Al, and the T' phase has a wide range of composition surrounding 62% Cu, 11% Zn and 27% Al. At 250°C however, immiscibility occurs and the homogeneity range is separated into the Zn-rich T phase and Al-rich T' phase. At 200°C, the T phase has a narrow range of composition surrounding 55% Cu, 32% Zn, 13% Al, and the T' phase has a relatively narrow range of composition surrounding 56% Cu, 12% Zn, 33% Al.

The η_1 and η_2 phases of the Al-Cu binary system and the ε phase of the Cu-Zn system form a pseudobinary system below 626 and 597°C, the respective temperature of formation. The T-T' ternary phase range is intersected by this system above ~ 250°C.

The solid solubility of copper in aluminium was shown by Gebhardt[47,48] and Strawbridge et al[57] to increase with increasing zinc. The latter reported an increase in the solubility from 2.8% Cu with 0% Zn to about 3.4% Cu with 8% Zn at 460°C. Solubilities of aluminium and copper in the Zn-phase have been determined by Gebhardt[47,48] and Burkhardt[58]. The mutual solubilities are at a maximum along the locus of the Zn corners of the Al + ε + Zn phase field, with about 1.3% Al and 2.8% Cu soluble at 377°C, and with 0.8% Al and 1.7% Cu soluble at 275°C.

Recently, the low copper part of the Zn-Al-Cu ternary system was also investigated by Murphy[59]. In general, results of this investigation were in good agreement with

Gebhardt's works[47-49]. *Figure 11* from this work, shows the isothermal section of the system at 350°C. It shows considerable solid solubility of copper in the α and β phases, which is different than those reported earlier by Koster and Moeller[44] and Gebhardt[47,48], in that both of the previous workers found only 1.5% Cu in α in equilibrium with the θ and T', but in the recent work 3.3% Cu was found in the α. Besides previous workers had reported 1.5% Cu and 5% Cu, respectively, in the β phase in equilibrium with T' and ε. In the work of Murphy it was found that solid solubility of copper increased with zinc content to a maximum of 4.5% copper at a zinc content of 70.9%, which is in close agreement with Gebhardt's figure.

The isothermal section at 290°C, which is shown in *Figure 12*, is very similar to 300°C isotherm of Gebhardt, and broadly similar to that of the same work at 350°C. However, the development of a wide α + β field in the Zn-Al system has introduced a broad α + β + T' field in the ternary diagram. The copper content of the α and β solid solutions has decreased to 2.5%, and the two-phase fields have all narrowed. Particularly, the β + T' two phase field was found to be extremely narrow, indicating an imminent Class II four-phase reaction.

$$\beta + T' \Leftrightarrow \alpha + \varepsilon$$

On the other hand, the α phase in equilibrium with θ and T' has increased considerably with the amount of copper in the solid solution as found at 350°C.

Figure 13 shows the 280°C isothermal section at which four-phase reaction has been completed, and a narrow phase field separates two three-phase fields; α + T' + ε and α + β + ε.

In *Figure 14*, at 270°C, two important changes were reported to take place; β-phase has disappeared and (α + ε + η) phase field has taken its place,furthermore,the (α+ ε) phase field has narrowed, indicating another four-phase reaction just below 270°C.

$$\alpha + \varepsilon \Leftrightarrow T' + \eta$$

At 250°C, *Figure 15*, the large ($\alpha + T' + \eta$) three-phase field resulting from the above reaction was observed to cover a large part of the diagram.

Murphy also observed that β had already decomposed at 275°C. Since, according to the binary diagram of the Zn-Al system (*Figure 2*), this decomposition takes place at 275°C, he concluded that β-phase decomposes at a higher temperature in the ternary system and the Class II four-phase reaction, hypothesized by Gebhardt[47], actually has taken place:

$$\beta + \varepsilon \Leftrightarrow \alpha + \eta$$

with the $\alpha + \beta + \eta$ phase field contracting to the binary edge. The reaction sequences in binary and ternary systems were summarized in this work and are given in *Figure16.*

The designations for the binary and ternary phases that appear in this survey and their approximate formulas are given in *Table 3*[54].

Table 3 : The Binary and Ternary Phases of Zn-Al-Cu Ternary System and their Approximate Formulas.

Phase	Cu-Al	Cu-Zn	Phase	Cu-Al	Cu-Zn
Binary Phases					
β	Cu_3Al	CuZn	δ	.....	$CuZn_3$
β'	.....	CuZn	ζ_1	Cu_4Al_3	.....
γ	Cu_9Al_4	Cu_5Al_8	ζ_2	Cu_4Al_3	.....
γ'	Cu_9Al_4	.....	ε	.....	$CuZn_4$
γ_1	$Cu_{32}Al_{19}$	.....	η_1, η_2	CuAl	.....
γ_2	Cu_3Al_2	.....	γ	$CuAl_2$	.....
Ternary Phases					
T .....Cu-Zn rich; composition range varies with temperature.					
T' .....Cu-Al rich; composition range varies with temperature.					

Aston University

Content has been removed for copyright reasons

Aston University

Content has been removed for copyright reasons

Aston University

Content has been removed for copyright reasons

The structure of the T phase has been investigated by a number of workers. Koster and Moeller[44,45] found the T phase isomorphous with Al_6Cu_3Ni in the Zn-Al-Cu ternary system, having an ordered CsCl-type bcc structure at high temperature. At temperatures below 450°C, the Al-rich end of the single phase field (at approximately Al_5Cu_4Zn) was found to have a structure of lower symmetry, while the other end of the phase field, corresponding to approximately $Al_{3.5}Cu_{4.5}Zn_2$, was retaining the CsCl structure. It was suggested that at low temperatures, the large difference in radius of copper and aluminium atoms renders the CsCl structure unstable, but that zinc atoms of intermediate size help to stabilize the CsCl structure. Koster and Moeller denoted the CsCl structure as T-phase, and called the lower symmetry structure T'.

The structure of the T' phase was established by the work of Murphy[60]. It was found that T' had a rhombohedral super lattice structure with a= 8.676Å and α = 27.41°, based on an assembly of five small CsCl-type cells, joined corner to corner along [111] direction. The presence of a vacant lattice site in the middle of the central CsCl cell was responsible for the rhombohedral symmetry.

2.6 Phase transformations

2.6.1 Binary Zn-Al Alloys

Based on the phase diagram of the binary Zn-Al system (*Figure 5*), supersaturated solid solutions of the system that could be subjected to any possible phase transformation can be classified as:

(a) Al-rich phase

(b) Monotectoid phase α / α'

(c) Eutectoid β phase and

(d) Zn-rich phase η

In the literature, considerable attention has been given to the transformation sequence of dilute Al-rich solid solutions and of more concentrated Al-Zn alloys. However, the Zn-rich side of the system has not been investigated at all.

It has been established by a large number of workers[61-67], and now it is generally accepted, that dilute (up to 30 wt % Zn) f.c.c. Al-rich alloys, on ageing, decompose to give the Al-rich solid solution (α) and the following series of precipitation sequence:

Spherical G.P. zones $\rightarrow$ Rhombohedral transition phase α''_m $\rightarrow$ f.c.c transition phase α'_m $\rightarrow$ Zn - rich stable precipitates

The rhombohedral α''_m phase differs only slightly in lattice parameters (a = 3.992, $\alpha' = 91.36$) from the cubic α'_m phase (a = 3.995)[65].

The first stage of the transformation is characterized by a rapid segregation of Zn atoms into spherical regions, to form G.P. zones, fully coherent with cubic α-matrix. On prolonged ageing, when they reach a critical diameter (30-35 Å)[63], the anisotrophy of coherency strain leads to the growing of zones and the contraction of spacings along one of the (111) directions[62,65,66,67] inside the zones and, thus, to the rhombohedral deformation of their lattice together with the change of the spherical shape of the zones into the ellipsoidal one. In the next stage of the decomposition, the partial loss of coherency of the zones with α-matrix, except in the {111} habit planes, leads to development of the transition rhombohedral phase, and then, the loss of coherency of the rhombohedral phase in the {111} - habit planes leads to non-coherent f.c.c. α'_m phase.

Finally, stable Zn-rich precipitates are formed preferentially on dislocations and at grain boundaries[65,66], by continued precipitation from α'_m phase by epitaxial growth of hexagonal Zn-platelets with an orientation relationship[65-67];

$$(111)_{Al} \;//\; (0001)_{Zn} \;;\; [1\bar{1}0]_{Al} \;//\; [10\bar{1}0]_{Zn}$$

More concentrated Zn-Al alloys have been investigated less thoroughly. The decomposition products of the solid solutions in high Zn alloys entirely depend on the cooling rate and the heat treatment temperature, and may result from mainly one of two, (or both), distinct decomposition mechanisms given below:

(a) A conventional cellular (or discontinuous) reaction, mainly resulting in grain boundary nucleated lamellar segregates of $\alpha + \beta$

(b) Spinodal decomposition of η-phase in Al-rich matrix.

Of the two types of reactions observed in the Zn-Al system, conventional cellular decomposition occurs most frequently. This type of reaction has been investigated in detail by Ramaswamy et al[68] in Al-50% Zn, and more recently by Vijayalakshmi et al[69,70] in alloys with 60 and 75% Zn. After solution treatment, on aging the alloys, it was observed in both works that cellular reaction started at grain boundaries. The evidence for the nucleation stage at grain boundaries was explained by the aid of mechanisms proposed by Fournelle and Clark[71]. According to this mechanism, the migration of a curved grain boundary of the α' matrix leads to a net reduction in the grain boundary areas. The higher diffusivities of the solute atoms across a mobile boundary facilitate the nucleation of stable η precipitates, resulting in the pinning of the boundary. Thus, a narrow region behind the migration boundary becomes depleted of solute atoms by diffusion to newly formed allotriomorphs on η, resulting in the formation of a narrow precipitate free-zone. In the late stage of the decomposition, the lamellar structures were found to develop from these grain boundary allotriomorphs and to grow into the parent grain. During the growth of the lamellae, the establishment of a unique lamellar spacing was found to be achieved by two mechanisms; namely:

(a) By branching of the existing lamellae[68-70] and less frequently;

(b) By the nucleation of fresh lamellae at an advancing interface[69,70].

The interlamellar spacings and the rate of growth was found[72,73] to vary as a function of applied undercooling and ageing temperature, in that the interlamellar spacings decrease with decreasing temperature. The relationship between the spacings, S and the undercooling, ΔT in a eutectoid alloy under isothermal condition was found[73] to be:

$$S \propto \Delta T^{-0.9}$$

It was reported[72] that during the growth of the cells, the lamellae maintain the following orientation relation across their interface:

$$\{111\}_\alpha \;//\; \{0001\}_\eta \quad \text{with} \quad \langle 1\bar{1}0\rangle_\alpha \;//\; \langle 1\bar{2}10\rangle_\eta$$

However, in some cases, it was observed that within a single colony the Zn lamellae may change their direction quite frequently, without constraining themselves to a single habit plane. For example, another orientation relationship $\{111\}_\alpha // \{10\bar{1}1\}_\eta$ was also reported[69,70].

The quenched samples of the concentrated Zn-Al alloys, on the other hand, may also exhibit an entirely different, fine-grained equiaxed granular structure depending on the ageing temperature. For example, it was shown[74,75] that decomposition of the eutectoid alloy during slow cooling, or isothermally transforming at high temperatures, produced a typical lamellar structure. However, decomposition at room temperatures after a rapid quench produced a fine (~ 1μm) mixture of equiaxed Zn-rich and Al-rich grains.

A possible interpretation of the responsible mechanism for this type of decomposition can be made in terms of the process of spinodal decomposition.

Rundman and Hilliard[76] have calculated a spinodal curve for Zn-Al system, as

given in *Figure 17*.[2] It can be seen from this diagram that the supersaturated solid solutions of α, α' and β may decompose into the equilibrium phases along two different reaction paths. At small undercoolings or low supersaturations, the precipitation of equilibrium phases occurs mainly by a cellular decomposition process, as mentioned earlier.

However, at large supersaturations or high undercoolings, solutions become unstable and the two equilibrium phases could emerge continuously, resulting in a granular equiaxed structure.

Aston University

Illustration has been removed for copyright restrictions

The morphological change from a lamellar to a granular equiaxed structure depends strongly on the applied undercooling, ΔT. It has been observed in an eutectoid alloy that as ΔT was increased beyond 100K, 30% of the discontinuous product changed to a granular morphology[72].

[2] *Authors referred to Al-Zn phase diagram compiled by Anderson and Anderko, given in Figure 1, but in the text here, the terminology of the accepted phase diagram (Figure 2) will be used.*

Toldin et al[77] studied in detail the process of decomposition of supersaturated solid solutions in Al-Zn alloys with 40, 50 and 60% Zn (AlZn II) and in an alloy containing 73% Zn (AlZn III). They generalized the possible sequences of transformations that could occur depending on composition, cooling rate and heat treatment temperature, as shown in *Figure 18*. As can be seen from the figure, there are 11 sequences of phase transformations that could occur through metastable phases (R, α'_m) or from G.P. zones. α'_m is formed in AlZn II alloys by both isothermal transformation and quench-aging process. A number of sequences (6-9) which begin with the formation of G.P. zones is formed on quench-aging. R-phase is formed preferably by the mechanism of spinodal decomposition and metastable α'_m phase by nucleation. [3]

Metastable state of the phases which might exist in the binary system was investigated further by the same authors in their extended works[78,79] and Krupkowski et al[80] They indicated that two types of metastable state might exist in the low temperature ($\alpha + \eta$) region, one being defined by solubility limits of the ($\alpha + \beta$) region, which continue to the low temperature ($\alpha + \eta$) region, and the other bounded in the same way by the boundaries of the ($\alpha + \alpha'$) region which continue to the low temperature ($\alpha + \eta$) region, shown in *Figure 19*.

---

[3] *In the original publication(Fig.18), authors referred to the phases as follows:*

$$\alpha'_m \rightarrow \alpha'$$
$$\alpha \rightarrow \alpha_1$$
$$\beta \rightarrow \alpha_2$$
$$\eta \rightarrow \beta$$

For convenience, the terminology of accepted binary phase diagram (Fig.5) has been used in the text.

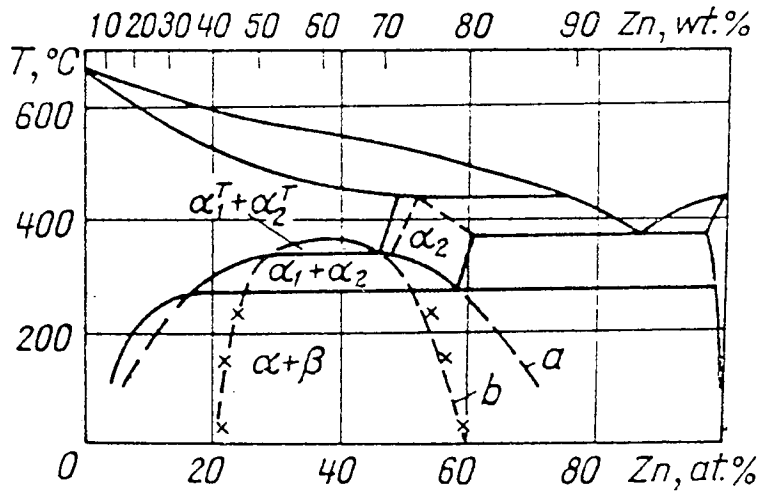

Figure 19. Phase diagram of Zn-Al system with metastability boundaries(a,b).

2.6.2 Ternary Zn-Al-Cu Alloys

The phase transformations in Zn-Al-Cu system have been investigated by a large number of investigators, and as a result, the phase diagram of this system has been partly established, as discussed in (2.5.3).

The effects of Cu additions on the kinetics of the phase transformation in the binary system have also been studied by a number of workers. These effects can be classified mainly as:

(a) Retarding the exceptionally high transformation rate of binary Zn-Al alloys[81-83]

(b) Causing dimensional change that can occur on ageing of the alloys [48, 84,85,86].

Phase transformations that are suggested to be responsible for these effects:

(a) $\alpha\ (\alpha')$ or $\beta \rightarrow \alpha + \eta + \varepsilon$ and a four phase reaction:

(b) $\alpha + \varepsilon \rightarrow T' + \eta$

Reaction (a) is a relatively short term reaction but slower than those which may occur in the binary Zn-Al system. The new phase, ε, that forms when copper is present in a relatively short term after quenching of a supersaturated alloy, is not a stable phase at room temperature and undergoes a four phase reaction (b) that occurs below 273°C[59] to form a new stable Cu-rich phase (T')[48,49,59,83,84]. This reaction involves diffusion of Cu over a relatively long distance, and a period of months or years is required to complete the reaction at room temperatures. The average density of the products of this reaction was found to be less than those of the reactants, resulting in an increase in volume[84-86].

2.7 Creep and superplasticity in binary zinc-aluminium alloys

Current theories tend to regard creep and superplasticity as distinct kinds of deformation which may sometimes overlap and in which grain-boundary sliding (GBS) may sometimes emerge as important. Superplasticity of a material is characterized by its ability to deform at low applied stresses to exceptionally large strains, and it is now recognized that[87-90] there are two major requirements for superplastic behaviour:

(a) a temperature above approximately 0.4 of the melting point of the matrix in absolute degrees and

(b) a fine stable and equiaxed grain size, typically (but not necessarily) less than about 10 μm in size.

Since the first requirement is generally incompatible with the retention of small grain size, because grain growth occurs at elevated temperatures, optimal superplastic materials tend to be either two-phase eutectic or eutectoid alloys,where grain growth is limited by the presence of two phases[88] or alloys containing a fine stable dispersion of a second phase which acts as a grain refiner[89-90]. From the view of these two requirements, the binary Zn-Al system suggests an excellent choice for producing superplastic alloys. The Zn-Al eutectoid (Zn-22% Al) is preferred due to the peculiarities of spinodal decomposition which produce an equiaxed fine-grained structure. It was, therefore, investigated in great detail, in terms of stress, temperature, grain size and deformation rate[91-94]. It was established that the maximum attainable ductility of this alloy increased with increasing temperature and/or decreasing initial grain size, and occurred at intermediate strain rates.

The influence of the structure and the phase composition on the appearance of the superplasticity in a composition range from 0.4% Zn to 50% Zn was investigated in detail, by Kaybyshev et al[95]. This work was quite interesting as it showed that the appearance of superplasticity was not only a characteristic of the eutectoid

composition, but was strongly dependent on the original grain size, the stability of the structure and the quantitative ratio of the zinc and aluminium rich phases. In this work, to produce a fine grained structure, all alloys, except those with 0.4 and 2% Al, were quenched and hot-extruded and then cold-rolled. Tests were carried out at various temperatures from 20°C to 250°C at a constant deformation rate of 10^{-2} 1/s. *Figure 20* summarizes the results for alloys in the quenched and rolled conditions. At 250°C, only the quenched sample of eutectoid composition showed superplasticity, which diminished rapidly on deviation to either side of the eutectoid concentration *(Figure 20.a)*. The variation of the flow stresses of the quenched samples as a function of composition was in complete agreement with the plasticity. The eutectoid alloy had the minimum flow stress *(Figure 20.b)*

Cold-rolling increased the plasticity of the alloys considerably, especially for alloys with 10% Al where its effect was greatest. At 250°C, after rolling, the plasticity of alloys with Al contents from 10 to 22 was very similar with a difference of 100-150% in a total elongation of 1000%. When the Al content went above the eutectoid composition, the plasticity fell off rapidly.

Figure 20 a and b also show the temperature dependence of deformation. For alloys with Al contents above 10%, plasticity decreased with decreasing temperature. Flow stress passed through a minimum at 18 and 2% Al at temperatures of 150 and 20°C, respectively.

The behaviour of the alloy with 0.4% Al is very interesting. The plasticity of this alloy increased with decreasing temperature. At 20°C, this composition had the highest plasticity. As the temperature was increased to 150°C, the plasticity decreased and the flow stress reached a minimum value. At 250°C, the plasticity decreased to a minimum value as flow stress reached a maximum. This rather interesting behaviour at 250°C was attributed to different characteristics of the present phases (α and η) at

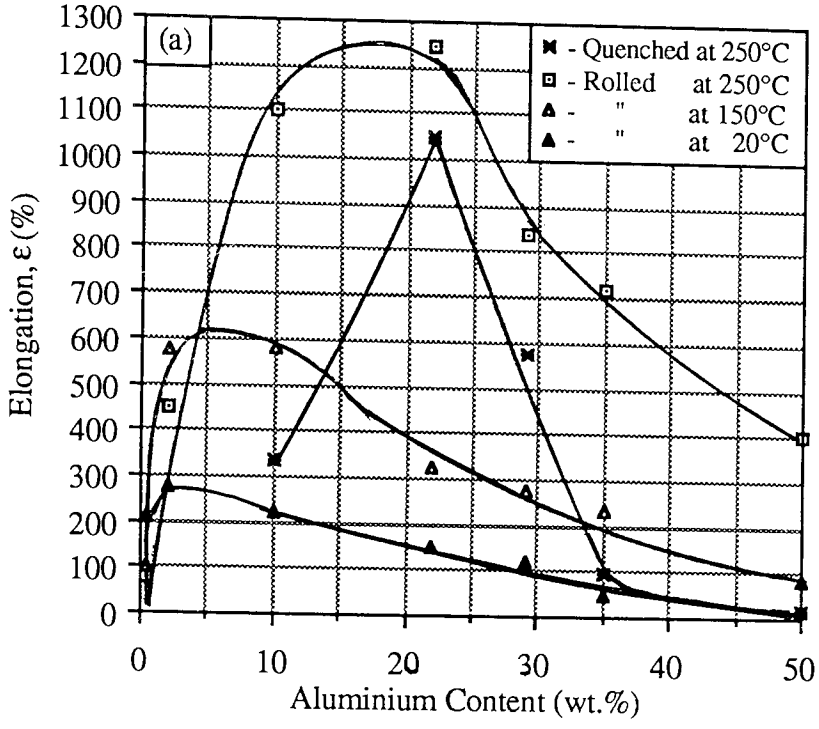

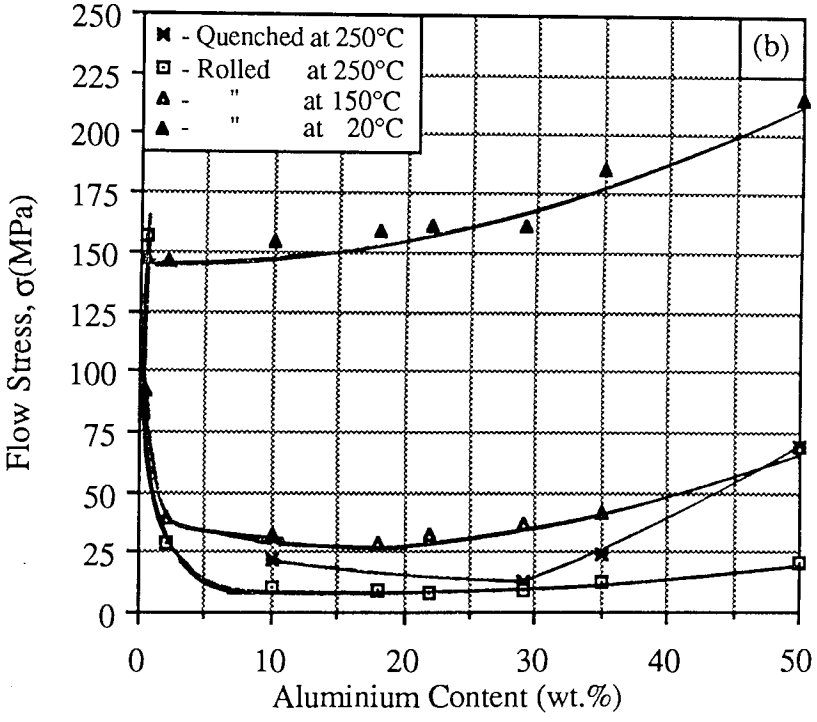

Figure 20. Plasticity (a) and flow stress (b) of Zn-Al alloys at different temperatures.

different temperatures. But obviously, this cannot be the reason since at this temperature all Al dissolves in the Zn solid solution and the alloy is a single phase (Solubility of Al in Zn is 0.6% at 275°C and 0.4% at 225°C).

A similar result was also reported by Cook and Risebrough[96] on an alloy with 0.2% Al. The most interesting feature of this work was that superplasticity was associated with a very high strain rate sensitivity (m) of 0.72, obtained at quite a low temperature (23°C). The eutectoid at this temperature was not superplastic, and m values were less than 0.1. It was therefore, concluded that in the absence of the higher melting point phase, the Zn-rich phase itself was superplastic at much lower temperatures compared with the eutectoid alloy.

It has been experimentally established[92-94] that superplastic deformation of the eutectoid alloy had two principle facts:

(a) The relation between stress and strain rate had three distinct regions.

(b) The fine grained microstructure remained equiaxed throughout the deformation.

Figure 21[92] shows the experimental example of the three stage behaviour in the eutectoid alloy, with values of m of 0.22 and 0.50 in regions I and II, respectively; the value of m in region III was not determined but is probably close to 0.2. As can be seen from *Figure 21* maximum deformation occurs over an intermediate range of stress and strain rate and there is a decrease in the strain at both high and low values of stress and strain rate. Region II is therefore, considered to be responsible for superplastic behaviour.

There is a general agreement on the deformation mechanism in region III, but some controversy on that in regions I and II. It has been well established that the rate controlling mechanism in region III is due to climb of edge dislocations in addition to slight grain boundary sliding[87,97]. In the low stress region (Region I), the precise

details of the rate controlling mechanism are uncertain at present. Mechanisms which have been proposed for this region are Nabarro Herring diffusion creep[93], Coble creep[97,98] or diffusion accommodated flow of grain boundaries[99].

Region II is usually considered a transition phase where two mechanisms contribute to the deformation.

Figure 21. Tensile fracture strain as a percentage vs initial strain rate and the corresponding plots of maximum flow stress vs initial strain rate (lower), showing three stages of deformation characteristic of the superplastic eutectoid alloy[92].

All models proposed for deformation mechanism agree that grain boundary sliding (GBS) plays the dominant role in the superplastic deformation process, and they differ only in the accommodation process which accompanies the GBS and allows sliding to occur continuously on all boundaries.

The contribution of GBS to total strain in Zn-Al alloy was investigated by a number of workers[95,100,101]. *Table 4* summarizes the results of these works.

Table 4.Contribution of GBS to total elongation in regions I, II and III.

Alloy	Test Temp. (°C)	Elongation (%)	ε_{gbs} (%)			Ref.
			I	II	III	
Zn-0.4% Al	20	20	~40	~50	~30	95
Zn-22% Al	200	100	10±5	11±5	6±3	101
Zn-22% Al	250	20	~30	~60	~20	100

It can be seen from the *table* that the contribution of GBS to total strain is significant, with the exception of the results of Sheriat et al[101] who reported lower values. However, it was reported that this was not due to a true decrease in the importance of sliding at high elongations, but it arose due to constraints in the experimental procedures. In this work it was also shown that maximum sliding tended to occur at Zn-Zn intercrystalline boundaries, there was slightly less sliding at the Zn-Al interphase boundaries and sliding was found to be at a minimum at Al-Al crystalline boundaries.

2.7.1 Grain Boundary Sliding and Rate Controlling Mechanisms in Superplasticity

Theoretical models of GBS fall into two general categories, those involving dislocation mechanisms and those involving diffusion mechanisms. In the dislocation theory[102] dislocations generated in the bulk of the grain travel along their slip planes until they are stopped by a high-angle boundary. Further movement of dislocations takes place by climb and then glide, which continually keeps the dislocations in the boundary region, causing GBS.

In diffusional models[103] it is assumed that sliding on the regular smooth portions of the grain boundary is easy. A small shear stress therefore, would cause sliding on such a boundary. However, initial sliding in a real boundary, containing steps, ledges

and other irregularities, after a stress is applied, is limited to the displacement which results in an elastic strain in the irregularities and is stopped when an opposing elastic strain develops. The rate of sliding is then controlled by the rate of removal of the irregularities by a stress-directed diffusional process.

No matter which process is controlling the mechanisms, both processes have the same effect of grains rearranging themselves in such a way that one pair of grains moves between two others that separate longitudinally, thus lengthening the specimen. However, as the grains slide during deformation, they must change their shape to fit their new neighbours in order to maintain structural continuity. The specific process by which the shape change process takes place, therefore accommodates the GBS and determines the rate of deformation.

The accommodation mechanism for GBS proposed in the literature can be divided into two main groups, namely:

(a) Diffusional accommodation

(b) Accommodation due to dislocation motion.

The diffusion accommodation mechanism is based on a model proposed by Ashby and Verrall[99]. In this model, the superplasticity region (region II) is considered as a transition region between the diffusion accommodated flow, operative at low strain rates, and diffusion controlled dislocation climb at high strain rates. Diffusion accommodated flow was claimed to take place in such a way that a small cluster of grains undergoes a rearrangement by diffusional transport, as illustrated in *Figure 22*. These grain switching events are envisaged as occurring randomly throughout the specimen, with various clusters of grains in different stages of the switching process. Characteristic of this model is the fact that units of four grains must deform co-operatively in order to achieve a unit strain of 0.55 and, at the same time, maintain compatibility across grain boundaries. This model predicts an activation energy for superplastic flow varying between the value of the activation energy for grain

boundary diffusion and that for lattice self diffusion.

This grain switching model has been observed in an in-situ experiment of the eutectoid alloy in a 1 MV microscope[104].

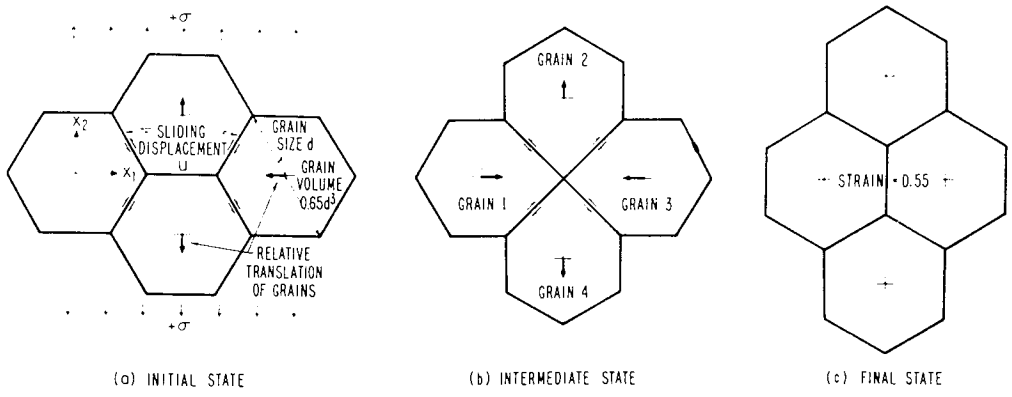

Figure 22. Grain switching process; the grains moves from the initial, through the intermediate state to final state while remaining approximately equiaxed[99].

The model, however, does not explain that there is no obvious way in which the switching can proceed further after the strain of 0.55. A continuous model has therefore, been proposed by Hazzledine and Newbury[105] and illustrated in *Figure 23*. In this model, grains are strained continuously in order to accommodate the GBS. As the material deforms, the area of the plane increases and thus gaps appear between the initially compact grains (left). At the same time, the thickness of the material decreases and grains from both adjacent layers fill the gaps (dark grains). This process may continue indefinitely and grains may remain at all times approximately equiaxed. An important feature of this model is that the surface voids may be explained on this process by the fact that on the surface only half of the gaps between the grains would be expected to be filled. On the other hand, there are relatively detailed models that utilize GBS with accommodation by dislocation motion, which is rate controlling.

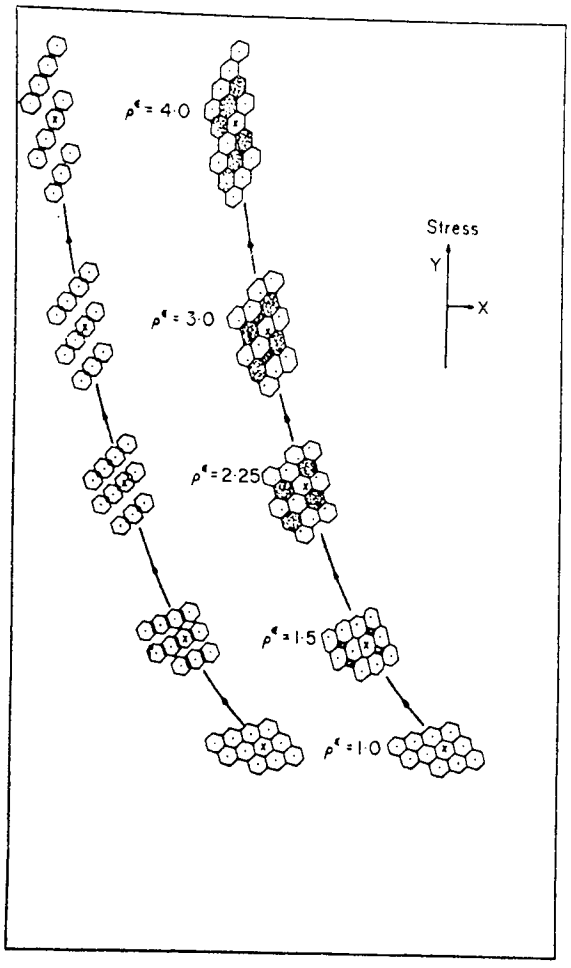

Figure 23. Combined GBS and grain strain in the first quadrant of a superplastic specimen. Displaced left: grain motion without accommodation, the grains initially overlap and finally spread apart. Right: dark grains from adjacent Z planes fill the gaps[105].

Regarding the accommodation due to dislocation motion, Ball and Hutchinson[106] proposed a model in which groups of grains slide as a unit, until unfavourably oriented grains obstruct the process. The local stresses could generate dislocations in the blocking grains. These dislocations pile-up against the opposite grain boundary until the back up stress prevents further activation of source, and sliding stops. The leading dislocation in the pile-up can then climb into and along the grain boundaries. The continual replacement of these dislocations would permit GBS at a rate governed by the kinetics of dislocation climb along grain boundaries to annihilation sides.

A similar model was proposed by Mukherjee[107] with an exception that grains slide individually, while pile-ups of dislocation are produced by ledges and protrusions in the grain boundaries.

In another model, proposed by Gifkins[108,109], sliding is considered to take place by the motion of grain boundary dislocations that pile-up at triple points, which generate stress concentration. Under the stress concentration, dislocations dissociate into partial dislocations in the sliding grains which then glide and climb in the mantle (peripheral of the grain) along the adjacent grain boundaries until they meet each other. Then they may annihilate or re-combine with them to form different grain boundary dislocations. This complete sequence of events will produce grain rotation and rearrangement in agreement with microstructural studies. An important feature of this model is that it does not require that the compatibility between adjacent grains be maintained at all stages of deformation. Instead, as proposed by Hazzledine and Newbury[105], gaps (voids) are opened at interfaces to be filled up by grain sliding from adjacent planes in the specimen.

Gittus[110], in his model, considered that G.B. dislocations piled up in interphase boundaries (IPB), then climb away into adjacent disordered segments of IPB. Sources in the dislocation boundary operate and introduce new dislocations to replace those that have climbed away from the head of the pile-up. Sliding occurs at the IPBs as the dislocations in the pile-up glide toward the head of the pile-up. The flow of the matter to the dislocations, as they climb the disordered regions of grain boundary, permits the changes in shape that are needed to preserve continuity of the boundaries during deformation.

A most recent model proposed by Spingarn and Nix[111], considers a stress concentration mechanism through slip bands which are blocked by grain boundaries. The strain at the boundary is accommodated by diffusional flow in the boundaries.

This model predicts relatively large stress exponents, varying from 1 to 5, as the stress increases.

2.8 Creep in the Ternary and Higher Alloys.

In spite of possessing advantageous forming properties, Zn-Al binary alloys have poor mechanical properties, especially a very low resistance to creep due to their superplastic characteristics.

Many workers have studied the effect of alloying additions on Zn-Al alloys, mainly with the intention of improving their creep resistance. Naziri and Pearce[112] investigated the effect of copper additions, of up to 1%, on creep behaviour of slightly hyper-eutectoid alloys (20% Al). It was found that copper additions did not have a significant effect above about 150°C. At room temperature, however, the addition of up to 1% copper was found to continuously improve the creep resistance and, at 1%, the improvement was by a factor of 140.

Nuttall[113], later, investigated the room temperature creep properties of two eutectoid-based ternary alloys, one with 4% Cu and the other with 0.2% Mn, after various heat treatments, by measuring the steady-state creep resistance at a stress of 35 MPa. In conjunction with the results of Naziri and Pearce[112] it was indicated that the copper addition up to 1% significantly increased the room temperature creep resistance of the alloys. There was however, no benefit in increasing the copper content from 1 to 4%. On the other hand, the creep resistance of a manganese containing alloy was found to be substantially better that that of any of the alloys containing copper.

Mulvania et al[114] has made an attempt to modify the composition of eutectoid alloys to improve the creep resistance, with the addition of single elements; titanium, chromium, manganese, copper and magnesium. In generally, it was found that, at

room temperature, creep resistance was improved by alloying. Titanium, manganese and chromium were found to have little effect on improving creep resistance. The most significant improvement was, however, observed with magnesium and copper additions. It was found that copper additions up to 0.5% improved creep resistance, but that additional copper was not beneficial. Results indicated that 0.018% Mg, which produced the highest creep strength overall, produced a much greater improvement than 0.06% Mg. The optimum combination of high creep strength and low superplastic flow stress was obtained in an alloy with 0.42% Cu and 0.002 Mg, the creep resistance of which was found to be equivalent to that of a commercial zinc die casting.

Recently, the creep behaviour of one eutectoid and two near-eutectoid alloys, containing 3 and 4% Cu in both as-cast and heat-treated conditions, was investigated by Savaskan and Murphy[115-117] over a range of stress and temperature. Heat treatment of the alloys was carried out by homogenizing the alloys for 3 hours at 350°C, and then quenching and aging at 200°C for 2 hours.

It was shown that the alloys containing 3 and 4% Cu, in both as-cast and heat-treated conditions, had much lower secondary creep rates than the binary alloys; and as-cast alloys, in turn, had substantially lower secondary creep rates than heat-treated alloys of the same composition. Among the ternary alloys, it was observed that the alloy with 4% Cu showed a lower creep rate than that with 3% Cu in the as-cast condition. In heat-treated condition, however, it was reversed. This was attributed to the overall copper content which increased the creep resistance of as-cast alloys, and to the matrix copper content in the case of heat-treated alloys.

In the first two works[115,116], it was also shown that the secondary creep rates of the alloys in both conditions could be correlated using an equation of the form:

$$\dot{\varepsilon}_s = A\,\sigma^n \exp\left(-Q_c / RT\right) \qquad (20)$$

where n = 3, and a mean value of Q_c = 87 kJ/mole.

Later, Murphy et al [117] showed that the creep data of the above work could be correlated more satisfactorily by an empirical equation of the form:

$$f(e) = C\,t\,\sigma^n \exp\left(-Q_c / RT\right) \qquad (21)$$

where f(e) denotes some function of creep elongation, C is a constant, σ the stress, n the stress exponent, Q the activation energy for creep, T the absolute temperature, and R the universal gas constant. The stress exponent was found to be 3.33 for alloys tested in the stress range 10 to 60 MPa. The activation energies for the as-cast alloys were found to be similar, with a mean value of 122 kJ/mole and varying in the range 60-107 kJ/mol. for heat treated alloys.

2.9 Pressure Die-Cast Commercial Zn-Al Alloys

2.9.1 The background and general characteristics of commercial pressure die-cast Zn-Al alloys:

Alloying of zinc with aluminium, copper and other metals, in order to improve zinc properties began early in this century[118]. Until 1929 attempts had been made to die-cast zinc alloys, but although the castings seemed satisfactory, in many cases rapid deterioration set in after a few months of service and results were disastrous. The problems were found to result from intercrystalline corrosion and overageing; the former caused by the presence of impurities, such as lead and tin which have almost negligible solubility in solid zinc[119], the latter by high copper content[120].

Availability of high purity zinc (99.99%) and advances in alloying technology provided the basis for the introduction, by the New Jersey Zinc Company of Zamak 3

and 5 (known as Mazak 3 and 5 in the United Kingdom)[4], for pressure die casting alloys in the 1930's[119,120]. Both alloys when properly alloyed, cast and applied, provide widely-used useful engineering materials with reliable properties. They show a unique combination of properties which permits the rapid, economic casting of strong, durable, accurate parts and, hence, these alloys have dominated the market since their introduction.

They have many advantages over other die-casting materials such as aluminium and magnesium alloys as zinc alloys are more easily cast, are stronger and more ductile, require less finishing, can be held to lower tolerances and can be cast in thinner sections. Because of the low casting temperatures, die life for zinc die castings far exceeds that for other die casting materials. The production rate (shots/hour) is also much higher[121]. They are used in a vast number of applications, ranging from the simplest drawer handle to the most complex precision automotive part[122]. Nominal compositions of the alloys are shown in *Table 5*[123,124].

Mazak 3 is a 4% Al alloy with an excellent retention of impact strength and long term dimensional stability. Mazak 5, which has virtually the same composition but with a higher copper content, has similar mechanical and casting properties, with a higher ultimate tensile and creep strength. Both alloys, however, have poor resistance to creep in applications involving sustained loads at temperatures above 100°C[122]. Hence ILZRO[5] research was conducted towards developing a die-casting alloy that would have high creep resistance without sacrificing the other excellent properties of Mazak 3 and 5 alloys. This work in the mid-1960's led initially to the development of an alloy ILZRO.14, which, as a result of further research, was superceded by ILZRO.16. The composition of which is given in *Table 5*[121]. Both of these alloys have creep resistance markedly superior to that of alloys Mazak 3 and 5 at all

[4] *Mazak 3 and 5 corresponds to the specification of BS1004A and of BS1004B respectively, in British Standards (1972).*

[5] *ILZRO: International Lead Zinc Research Organisation*

temperatures and under all conditions. It has been shown, for example, that when tested at room temperature, that an aged sample of Mazak 3 had about the same creep resistance as an aged sample of ILZRO.16 tested at 177°C[125]. High creep resistance of these alloys has been shown to be due to their alloying constituents of Ti and Cr. These elements with high melting points form a fine eutectic intergrowth of intermetallic compounds with zinc, e.g. $TiZn_{15}$ in Ti alloys.[126-128] It was shown that the presence of such particles created an effective barrier to grain growth, but most importantly increased the structural stability and creep resistance by eliminating substantial numbers of high energy, mobile grain boundaries[127,128].

However, the other room temperature mechanical properties of these alloys are inferior to those of Mazak 3 and 5[121,125] and they, unlike Mazak 3 and 5, cannot be die-cast in a hot chamber die casting machine; that is one in which the injection plunger sleeve and gooseneck are continuously immersed in molten zinc in the machine pot or furnace. Because ILZRO.14 and 16 have a low aluminium content, it would slowly dissolve iron if left in contact with the steel plunger sleeve and cast iron gooseneck. Hence, they must be cast in cold-chamber die casting machines[129]. These disadvantages of both these alloys have limit severely their use on the market.

In view of these limitations, a new family of high strength zinc-aluminium (ZA) alloys were developed, beginning with ILZRO.12, a 12% Al alloy which was first proposed by ILZRO in 1962[130]. Subsequent work on the alloy led to a reduction in the Al content to 11%, which together with other changes gave improved properties. This improved alloy is now called ZA.12[131]. In the late 1970's, two additional alloys, ZA.8 and ZA.27, were developed by further work of Noranda Corporation, at their research centre[131]. Compositional ranges of these three alloys according to ASTM B 669-82 ingot specification are also shown in *Table 5*[138].

The evolution of this new family of ZA alloys in the market place has been rapid. Each alloy was designated specifically to meet market needs, and the family collectively provides alternatives to other well-developed alloy systems, such as the brasses, bronzes, aluminium-based alloys and cast irons. Advantages often associated with the use of the ZA alloys include high mechanical properties, excellent bearing characteristics, non-sparking properties, ease of finishing and low energy, as well as pollution-free melting[120,132-137].

Table 5. Chemical composition of commercial pressure diecast alloys.

Alloy	Zn (%)	Al (%)	Cu (%)	Mg (%)	Ti (%)	Cr (%)
Mazak.3	balance	3.9-4.3	—	0.04-0.06	—	—
Mazak.5	"	3.9-4.3	0.75-1.25	0.04-0.06	—	—
Ilzro.16	"	0.01-0.04	1.0-1.5	0.02	0.15-0.25	0.1-0.2
ZA.8	"	8.0-8.8	0.8-1.3	0.015-0.03	—	—
ZA.12	"	10.5-11.5	0.5-1.25	0.015-0.03	—	—
ZA.27	"	25.0-28.0	2.0-2.5	0.01-0.02	—	—

Although these alloys were originally developed as sand and gravity die-casting alloys, experience has shown that they may be used in a very wide range of casting processes, including pressure die-casting. They can all be die-cast in cold chamber machines; ZA.8 alloy, because of its lower melting point and low Al content, could even be used in conventional hot chamber machines[138-140]. *Table 6* shows some principal mechanical properties of ZA alloys in different casting conditions compared with those of conventional Zn die-casting alloys and those of some other engineering materials[131,133,138]. The *table* highlights their strength relative to conventional die-casting alloys, cast iron and other non-ferrous alloys. Although harder than other non-ferrous alloys, they cannot, however, match cast iron in this respect. Within the family, ZA.27 has the highest strength and hardness followed by ZA.12 and ZA.8. The tensile strength of ZA.27 is not significantly affected by casting techniques, whereas the tensile properties and hardness of ZA.8 and ZA.12 are significantly

higher in die cast condition. Thus, the tensile and yield strengths of ZA.8 in the gravity cast condition, are raised by close to 50% by die-casting; for ZA.12, these properties are increased by approximately 30% and 45% respectively. It is believed that these improvements are brought about principally by microstructural refinement, resulting from the fast cooling rate characteristic of the die casting process[138].

The effect of elevated temperatures in the range of 20°C to 260°C on the tensile properties of the die-cast alloys Mazak 3, ZA.8 and ZA.27 was investigated by a collaborated work of the present author[141]. The variations with temperature of the ultimate tensile strength, proof stress and elongation are shown in *Figures 24, 25 and 26*, respectively. The ambient temperature tensile properties were found to be in good agreement with those reported in *Table 6*. ZA.27 had the highest strength, some 60% greater than that of Mazak 3, followed by ZA.8 which was 30% higher than Mazak 3. As seen from *Figures 24 and 25* that the ultimate tensile strength and proof stress of the alloys decreased with increasing temperature. The rate of decrease was found to be proportional to the aluminium content. In the case of ZA.27, the decrease was quite sharp. These properties of the alloys were virtually equal at 160°C and 165°C, respectively. Elongation results *(Figure 26)* showed a very pronounced temperature dependence. The ductility of ZA.27 increased very slowly below 100°C, then at an increasing rate with rise in temperature up to the maximum temperature tested, exhibiting an expected characteristic of the superplasticity of the alloy. Mazak 3 behaved in a different manner to ZA.27 in that there was a rapid initial rise in elongation, but this increase peaked between 150-200°C and decreased thereafter. ZA.8 showed an intermediate behaviour in elongation between ZA.27 and Mazak 3. It elongated in a very similar manner to that of ZA.27 in temperature range of 20 to 150°C, and then peaked at about 200°C and decreased in a similar manner to that of Mazak 3.

A similar work, in a more limited temperature range up to 150°C, was later carried out

by Loong[142], including alloys ZA.12 and Mazak 5. His results for the alloys Mazak 3, ZA.8 and ZA.27 were in complete agreement with our own. The tensile strength of alloys Mazak 5 and ZA.12 were found to be between those of Mazak 3 and ZA.8, and of ZA.8 and ZA.27, respectively, as expected. The elongations of ZA.12 and Mazak 5 were very similar to that of ZA.27 and ZA.8, respectively.

2.9.1.1 The Effect of Alloying Elements on general properties

The principal alloying elements of ZA alloys are copper and magnesium. Copper additions up to 2 or 2.5% significantly increase the tensile strength and hardness of the alloys. It was reported that the increase between 0 and 1% Cu was most rapid[131]. This is very similar to the effect of Cu on creep properties of a eutectoid alloy, mentioned earlier. However, excess copper reduces ductility and, if above 1%, can cause dimensional growth on ageing due to four-phase reaction (*Section 2.6.2*). Magnesium additions in small amounts of up to 0.01% are also very effective in increasing the tensile strength and hardness, but at the expense of ductility. The effect of 0.01% Mg on tensile strength, for example, was found to be similar to that of a 2% Cu addition[131]. Mg also prevents intergranular corrosion, which may take place when low levels of impurities such as lead, tin and cadmium are present[131].

2.9.2 Creep Behaviour of Commercial Pressure Die-Cast Zinc-Aluminium Based Alloys

Although a considerable amount of creep work has been done to characterize the creep behaviour of alloys Mazak 3 and 5 over the years, a systematic correlation of the creep data of the alloys, based on theoretical equations, had not been suggested. Most of the published creep data of these alloys are based on the actual creep tests and/or simple limited extrapolation of the creep data of the tests.

Table.6. Typical mechanical properties of the commercial zinc-aluminium alloys and other engineering materials

Properties at 20°C	ZA.8			ZA.12			ZA.27			Zinc (BS 1004)		Brass	Aluminium	Cast Iron	
	Sand Cast	Gravity Cast	Pressure Diecast	Sand Cast	Gravity Cast	Pressure Diecast	Sand Cast	Gravity Cast	Pressure Diecast	M.3	M.5	BS1004 SCB3	LM6M	Blackheart Malleable	Grey
Tensile Strength (MPa)	248-276	221-255	365-386	275-317	310-345	392-414	400-440	424	407-441	283	324	185-240	160-185	290-345	160-345
Yield Strength 0.2% offset (MPa)	—	207	286-294	207	214	312-328	365	—	363-378	195*	—	—	—	—	—
Elongation (%)	1-2	1-2	6-10	1-2	1-2	4-7	3-6	1	1	15	9	15-30	5-7	6-12	<0.5
Hardness (BHN)	82-89	85-90	99-107	90-110	85-95	95-105	110-120	110-120	116-122	83	92	45-65	55-60	110-149	200-250
Modulus of Elasticity (GPa)	—	85	90*	83	—	—	75	—	76*	83*	—	83	71	169	75-145

* Author's unpublished work

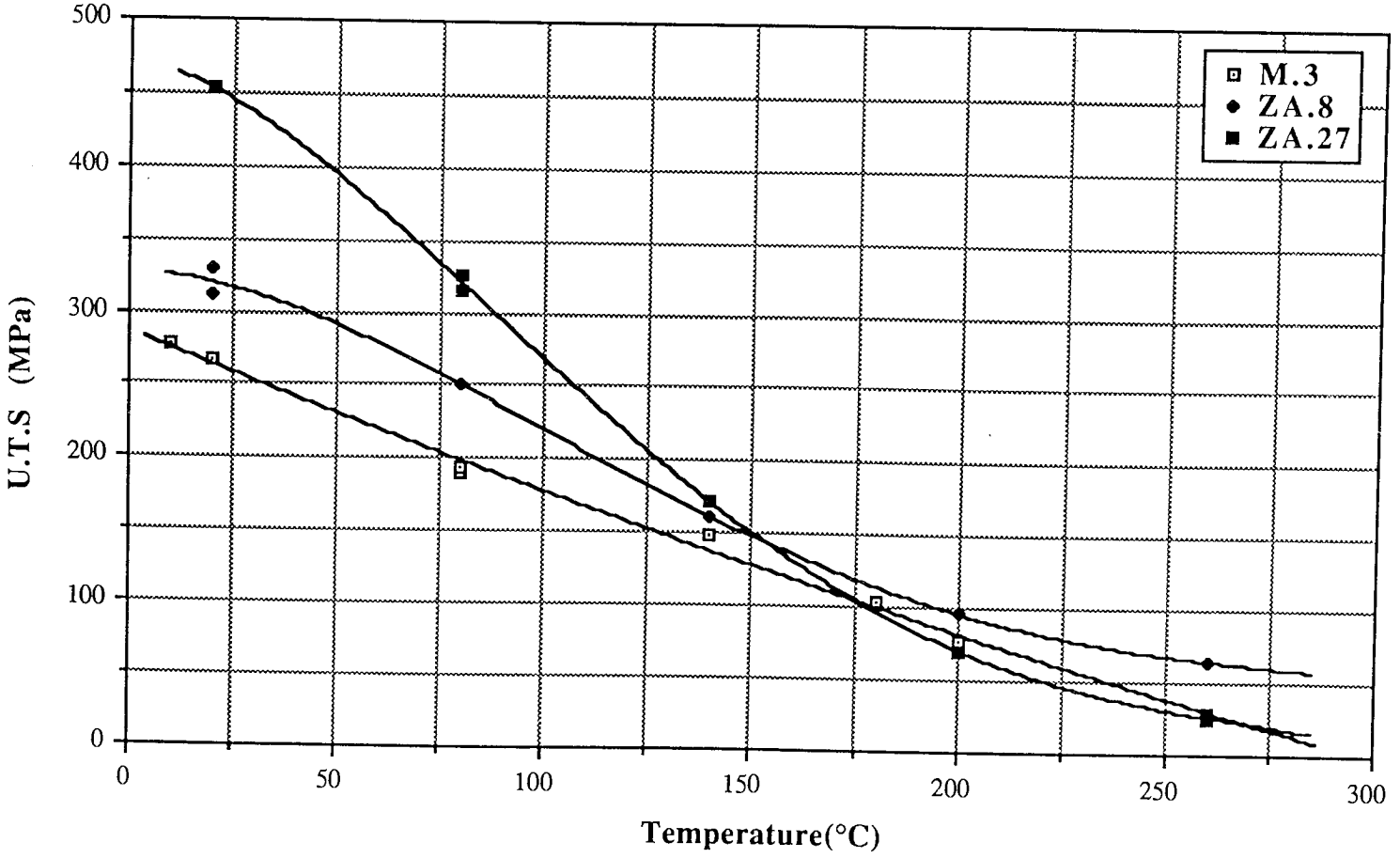

Figure 24. Variation of the Ultimate Tensile Stress of the alloys Mazak.3, ZA.8 and ZA.27 with temperature.

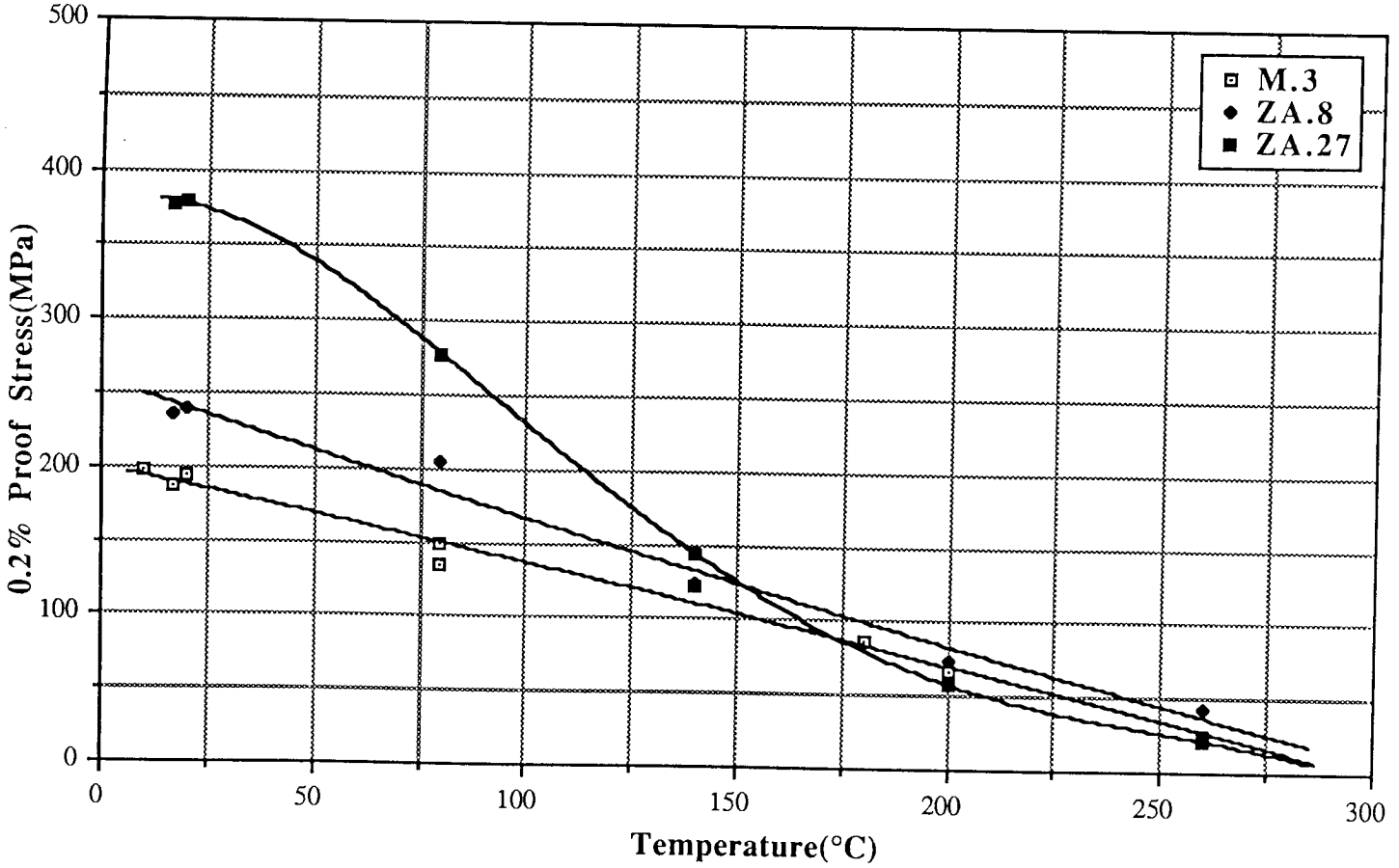

Figure 25. Variation of the 0.2% Proof Stress of the alloys Mazak.3, ZA.8 and ZA.27 with temperature.

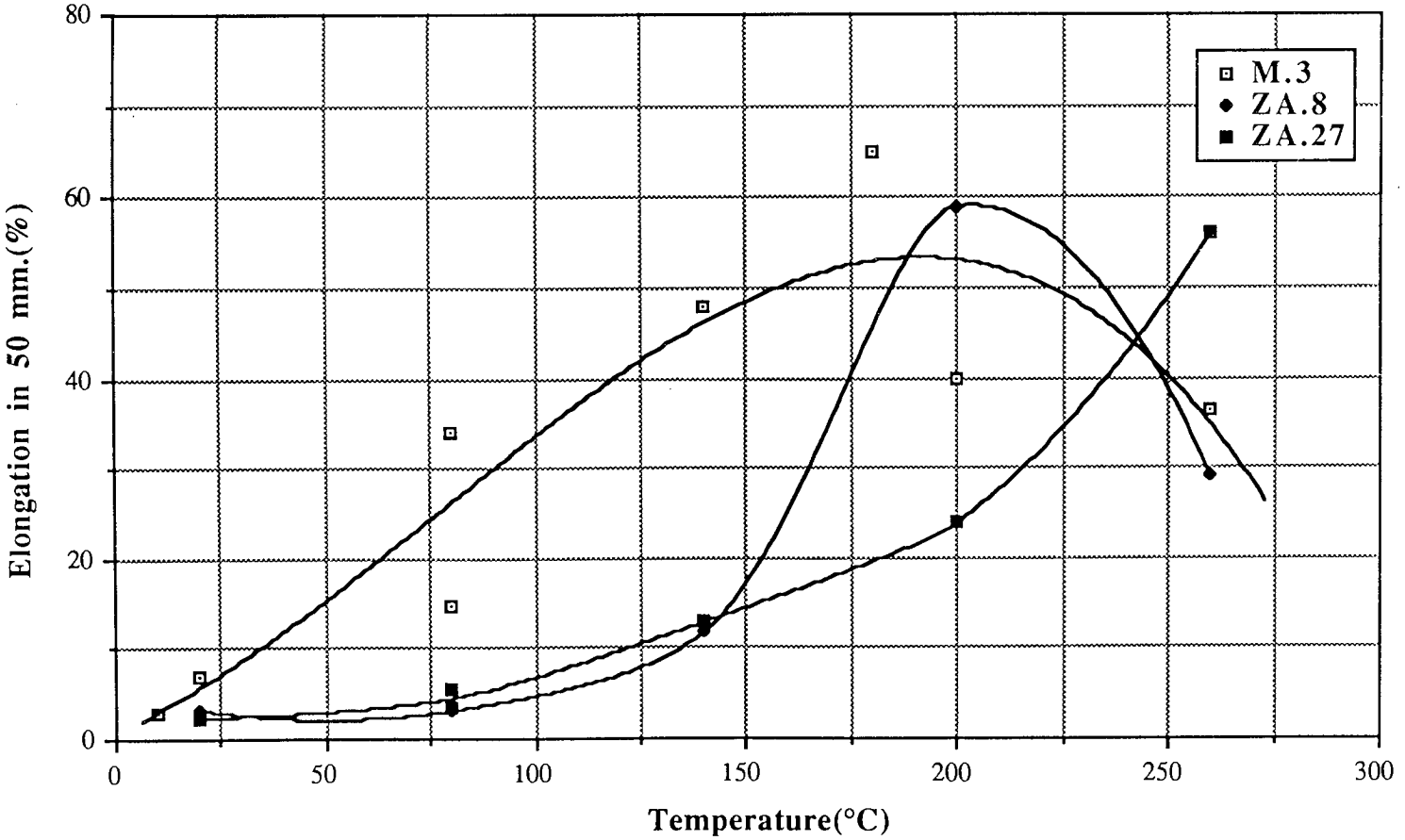

Figure 26. Variation of the % Elongation of the alloys Mazak.3, ZA.8 and ZA.27 with temperature.

Figure 27[121] shows tensile creep data for Mazak 3 at 25°C in such a form for various times ranging from instantaneous to 10 years. The creep test for this data was conducted up to 5 years, and data for 10 years was obtained from the extrapolation of the five year test. *Figure 27* enables us to compute the permissible design stress at 25°C for allowable design strain up to approximately 0.8% in desired service life up to 10 years.

Data on the effect of temperature up to 100°C on the allowable design stress for both Mazak 3 and 5 are also available [121] and are shown in *Figure 28 and Figure 29*, respectively. Data in these *figures* are based on secondary creep rates expressed as % creep strain in 10,000 hours. The *figures* clearly show that Mazak 5 is more creep resistant than Mazak 3 under all conditions. It can also be noticed that the difference in the secondary creep rates increases with increasing stress, indicating a different stress-dependence behaviour of the alloys.

The data obtained from these temperature studies have led to a development of a rough empirical equation giving the permissible stress at any temperature[121]

$$S_T = \frac{S_{25°C} \times 28}{T} \qquad (22)$$

Where S_T is permissible stress at any temperature from 25°C to 100°C, $S_{25°C}$ the permissible stress at 25°C and T the given temperature in °C.

Regarding the creep behaviour of the new family of ZA alloys in die-cast condition, since they are relatively new, there was very little information available before the present study started.

As a part of an overall programme in determining the properties of ZA alloys, creep tests to determine the creep resistance of the alloys in the die-cast condition were initiated by the Noranda Corporation[138]. The program was designed to establish the

design stress of the alloys as defined by the ASME pressure vessel code, in which the design stress is specified the stress to produce a secondary creep rate of 1% at a given temperature over 100,000 hours. (11.4 years). So far, results have become available at 20°C for three alloys (ZA.8, ZA.12 and ZA.27) and at 100°C for ZA.27[138,142]. *Figure 30* shows the results for secondary creep rates in a form of inverse creep rates (days/% elongation) versus stress.

Based on these results, it was indicated that ZA.8, ZA.12 and ZA.27 displayed approximately the same room temperature creep resistance and, according to that, the design stress of the three alloys according to the ASME Boiler Code, would be three times greater than that of Mazak 3[138]. The creep resistance of ZA.27 at 100°C was found to be significantly lower than that at 20°C. The projected design stress of ZA.27 was reduced from approximately 69 MPa at room temperature to 5.6 MPa at 100°C, and it was expected that ZA.8 and ZA.12 alloys would also behave similarly.

However, this was proved to be wrong by an investigation of Murphy et al[117] on alloys Mazak 3, ZA.8, ZA.12 and ZA.27 at 120°C. Using the time to a total creep elongation of 1% as a measure, ZA.8 was found to have the best creep resistance, closely followed by ZA.12. ZA.27 was slightly better than Mazak 3, but both of these alloys elongated ten times more quickly than ZA.8.

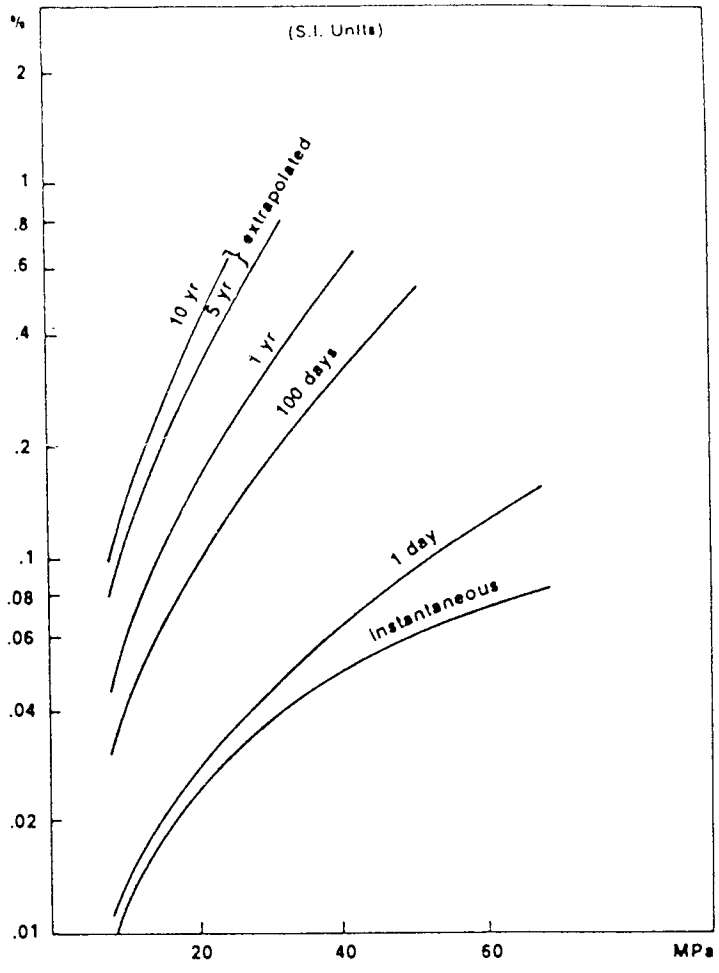

Figure 27. Tensile Creep Properties of Pressure Die Casting Alloy M.3 at 25 °.(% allowable strain in indicated time vs. allowable stress.)

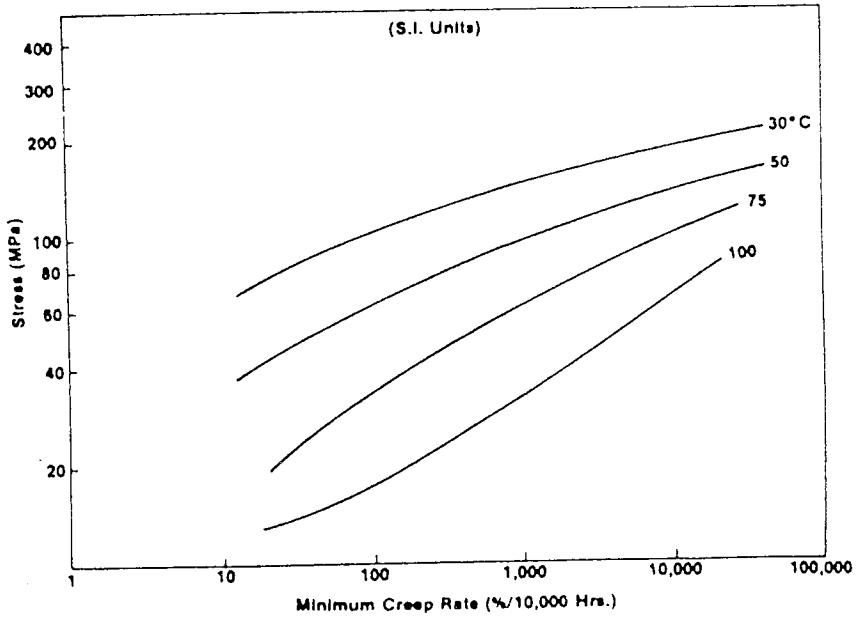

Figure 28. Tensile Creep Properties of Pressure Die Casting Alloy M.3 at various temperatures.

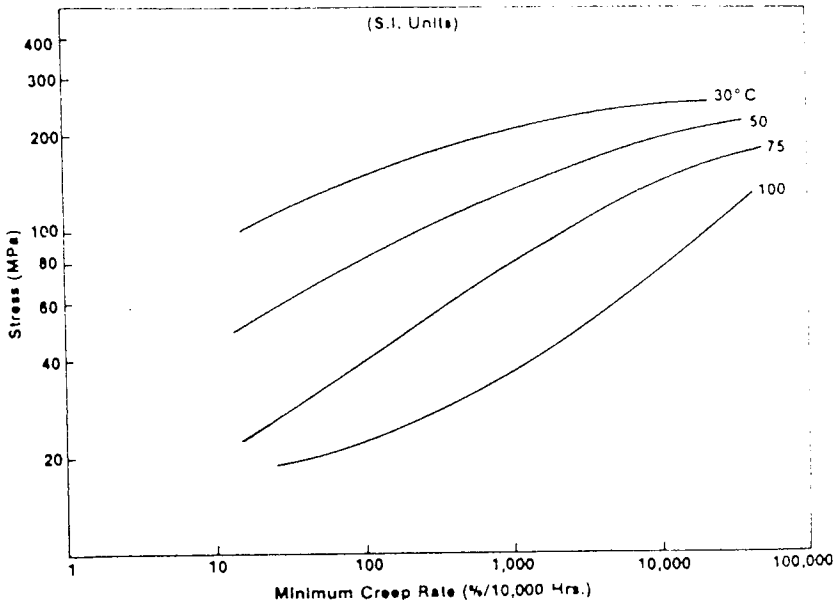

Figure 29. Tensile Creep Properties of Pressure Die Casting Alloy M.5 at various temperatures.

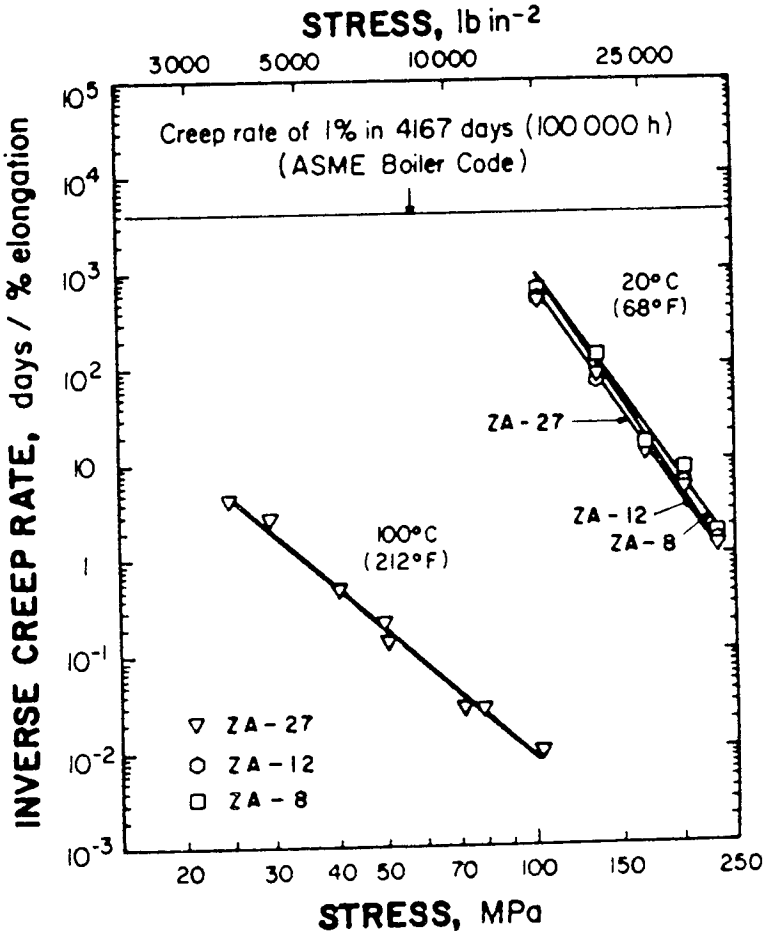

Figure 30. Inverse secondary creep rate of ZA alloys as a function of stress at 20°C and 100°C[142].

2.10 Concluding Summary

Zinc-aluminium alloys have been of commercial significance and use in technological applications for many decades. As a result of extensive work carried out over this period, the equilibrium phase diagram of the binary zinc-aluminium system has now been well established, and a considerable amount of information made available on the ternary zinc-aluminium system.

Two features of the binary system: a eutectic reaction at about 5% Al, 382°C and a eutectoid reaction at about 22% Al, 275°C, are of great importance from a technological point of view, in that conventional zinc-aluminium die casting alloys (Mazak 3 and 5) take advantage of the low freezing range of near eutectic compositions for their excellent castability, whereas the well known superplastic zinc-aluminium alloys take advantage of the eutectoid decomposition to produce the required fine-grained structure.

In the literature, considerable attention has been focused on eutectoid and hypo-eutectoid alloys, with the intention of developing a superplastic alloy with adequate mechanical properties. As a result the transformation kinetics of aluminium-rich solid solutions α, α' and β were exploited with respect to the structural changes arising from the phase transformation, depending upon composition, heat treatment temperature and cooling rate.

On the other hand, experiments with additions of other alloying elements has revealed that such additions, particularly copper and magnesium, had a profound effect on the transformation kinetics and improved the mechanical properties of the resultant alloys.

The experience gained over the years has eventually led to the development of a new family of ZA alloys. Although these alloys were originally intended for gravity or

sand castings, they are all being increasingly used in cold-chamber die-casting processes, and the alloy ZA.8, because of its low aluminium content and lower melting point, is being routinely produced by the conventional hot-chamber process which is normally recognised as one of the most economical and productive methods of producing moderate to high quantity castings of conventional die-casting alloys Mazak 3 and 5.

ZA alloys now offer exceptional versatility and superior properties, including high strength, hardness, excellent bearing and wear characteristics over conventional die-casting alloys and some other structural materials.

It is highly probable that ZA alloys may be used more extensively for production of pressure die-cast components for service at elevated temperatures, where creep is more important than the short-term tensile properties, and becomes of major concern as a limiting factor in design.

This review of the literature has clearly shown that the creep behaviour of these alloys has not been well established. Limited creep data is available for ZA alloys and Mazak 3, which is based on simple creep tests which have not been quantitatively analysed for the full characterisation of their creep behaviour. It is therefore the primary objective of the present study to extend the creep experiments to determine the full creep characteristics of the alloys Mazak 3, ZA.8 and ZA.27, over a broad stress and temperature range, and attempt a quantitative assessment of their behaviour.

On the other hand, the creep characteristics of these alloys must be directly related to their metallographic microstructures. At present, there is no information available with respect to microstructure and the effect of the alloying elements which they contain. For example, the alloy ZA.8 is now being claimed to have superior creep performance over the alloys Mazak 3 and ZA.27. The additional elements copper and magnesium

have always been reported to be beneficial in improving the creep resistance of zinc-aluminium based alloys, but firm structural reasons for these claims are not known. The present study therefore, also aims to make an effort to reveal the structural characteristics of the alloys in detail, by the most advanced metallographic techniques, which I believe will take us one more step closer to full theoretical understanding of creep in these alloys.

CHAPTER 3

3.0 EXPERIMENTAL WORK

3.1 Experimental Alloys

3.1.1 Commercial Pressure Die Cast Alloys

The main creep work has been carried out using the commercial alloys Mazak 3, ZA.8 and ZA.27, which were all cold-chamber pressure die cast at an industrial unit, and were provided by Mazak Ltd. as diecast plates with guaranteed composition.

They were pressure die cast into 2.18mm thin section plates 250mm long by 50mm wide with shallow ribs and bosses. A picture of the actual plates is shown in *Figure 31*. The chemical composition of the alloys is given in *Table 8 (Chapter 4)*.

Figure 31. Commercial diecast plate from which samples were taken.

3.1.2 The Other Pressure Die-Cast Experimental Alloys

To investigate the detailed effects of the different phases present in various compositions, ten alloys (including the commercial alloys Mazak 3, ZA.8, ZA.12 and ZA.27) with compositions in the range from 0% Al to 30% Al were also prepared and pressure diecast in our own foundry in a cold chamber machine. The commercial alloys Mazak 3, ZA.8, and ZA.27 were included in this series for the sake of comparability of the results of the same casting condition with those of the rest of the alloys.

3.1.2.1 Preparation of Ingots

For die casting of commercial alloys, standard ingots for each alloy, provided by Mazak Ltd., were used. For the others, ingots weighing 20kg were prepared from high purity (99.99%) zinc and (99.985%) aluminium.

To prepare each ingot, the calculated amount of zinc and aluminium was melted in a silicon-carbide crucible, in an induction furnace at temperatures between 550 and 700°C, depending on the alloy composition. For those requiring ternary addition of copper, a calculated amount of a master alloy containing 50% Cu and 50% Al was added to the melt, accompanied by vigorous stirring. Magnesium addition to the melts was done at as low a temperature as possible, to avoid losses of magnesium, again with vigorous stirring. The resultant alloy was poured into a flat steel ingot mould. The chemical compositions of all alloys are shown in *Table 8 (Chapter 4)*.

3.1.2.2 Die Casting of the Alloys

Die casting of the alloys was performed by using an industrial pneumatic cold-chamber pressure die casting machine, shown in *Figure 32*. The machine was an E.M.B. 10B with a maximum locking force of 76tonf., and operated in two stages:

Stage 1: a fixed low speed movement of the injection plunger

Stage 2: a high speed acceleration of the injection plunger, the speed of which could be adjusted.

The first injection stage was designed to start the movement of metal in the shot sleeve in such a way as to avoid the formation of waves and to expel as much air as possible from the sleeve and die cavity. This stage continued at a relatively slow constant speed until the metal reached the gate of the die cavity. At this point the fast phase (second stage) was actuated, which forced metal

into the die cavity at the appropriate speed.

Usually, a third stage, known as the intensification phase, exists in advanced die casting machines, whose purpose is to apply a high pressure to the casting during final stages of solidification to compensate for shrinkage and gas porosity and minimize the occurrence of defects due to this phenomenon [143,144]. However, the machine which was used for casting the experimental alloys did not have this feature and maximum pressure was reached by bringing in a high pressure pump at the end of the injection stroke of the stage 2, with no further sophistication.

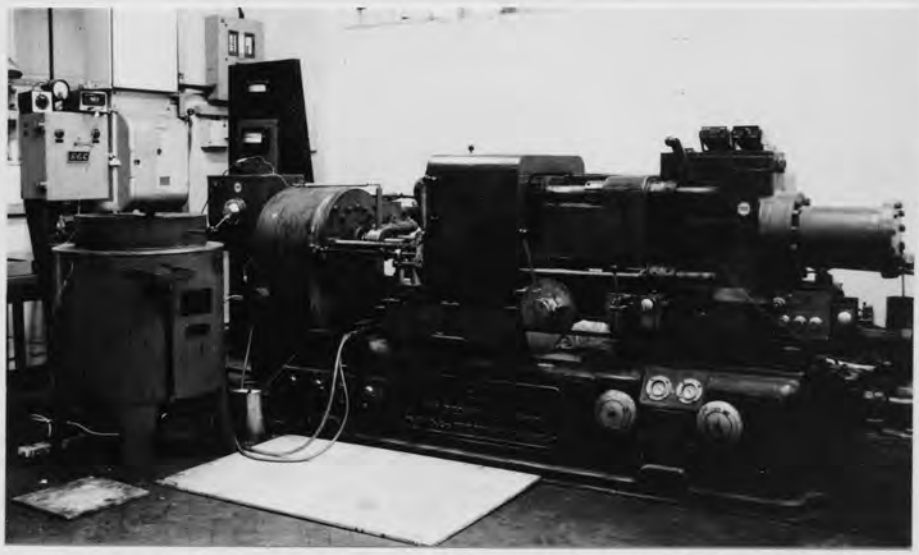

Figure 32. E.M.B 10B Cold-Chamber Pressure Diecast Machine.

The die used in the die casting machine was designed by the present author. The die was designed to produce two identical impressions of thin section rectangular plates. Correct design of the feed system of the die was crucial to produce a good quality casting. The primary purpose of the feed system is to transport the molten metal from the shot sleeve of the cold chamber machine to the cavity. Cavity fill time, gate velocity and fill pattern all affect casting quality, and these factors are in turn directly influenced by the design of the feed system[145]. Correct design therefore, requires a knowledge of the basic laws of hydrodynamic behaviour of the metal. These basic laws individually

are very simple in nature but more difficult to apply in practice. A considerable amount of time was spent in understanding the requirements for the feed system. An excellent review of the design of the feed systems is given by Allsop and Kennedy[145].

Designing a die involves the calculation of many factors associated with the feed system of the casting. The calculations are very complex, time consuming and tedious to carry out, with the associated problem of possible numerical errors. Computer programs are available that carry out these calculations, where all the designer has to do is to input basic data concerning the casting. For that reason, a computer program. which was originally developed by Mazak Limited. was adapted to run on Macintosh computers. The program runs in a way that the machine characteristics (the maximum available pressure of the machine, the maximum dry shot speed of the plunger, plunger diameter and line pressure) and volume of the casting are entered into the computer. For the selected conditions, the possible fill conditions which the machine can achieve are displayed with recommended gate areas, gate velocities and cavity fill times. If these cannot be achieved then a different plunger size, line pressure and/or gate length can be selected.

Figure 33 shows a drawing of the die cavity designed by following the above procedures, and it is characterized by the following design parameters:

Machine calibration parameters:	
Plunger diameter :	44.4 mm
Line pressure :	1.03 MPa
Maximum pressure on metal :	33.73 MPa
Dry shot speed :	7.6 m/sec
Working parameters:	
Plunger diameter :	44.4 mm
Line pressure :	0.93 MPa
Casting data:	
Number of components in shot :	2
Total component weight :	2 x 37.8 = 75.6 g

Total component volume :	2(2 x 25 x 120) = 12000 mm^3
Selected casting conditions:	
Gate area:	60 mm^2
Gate velocity :	58.1 m/s
Fill time :	3.4 ms
Gate dimensions:	
Gate length :	100 mm
Gate thickness :	0.30 mm

Figure 34 shows good hydrodynamic behaviour obtained from the design by smoothly decreasing sections from the feed system to the gate of the cavity. However, first trials produced castings with high porosity at the bottom corners of the samples. This was found to be due to the turbulent flow of the metal, because of the sharp changes in the flow, caused by the closed end of the gate area at the bottom of each impression. This was later corrected by machining the gate lengths down to the levels of the impressions, to give a gate length of 110mm for each gate. Good quality castings were thereafter achieved. *Figure 35* shows an example of the actual castings with runner system.

Die casting of the alloys was carried out by following the general recommendations of the guidelines[138,146] which had been proposed for commercial alloys as follows:

The type of furnace used to melt the ingots and to hold the molten metal at a constant temperature was a small resistance furnace which consisted of a steel case lined with refractory bricks into which a crucible was placed. The temperature of the molten metal was controlled by monitoring the temperature by means of a chromel-alumel thermocouple which was in direct contact with the melt.

Crucible and melting tools: a clay-graphite crucible with a charge capacity of 20-30kg was used. The melting tools and ladle were of steel. They were coated by a water-based graphite paste in order to prevent any

contamination from the molten metal, which might occur as a result of reaction of molten metal with iron.

Bath conditioning: Upon melting of the ingot and prior to any metal transfer operation, the bath was vigorously stirred to prevent aluminium segregation from the zinc, and the surface of the homogeneous melt was skimmed to remove any oxides and other solids.

Bath temperatures of the alloys were maintained at 40-50°C above the liquidus temperature of the alloys.

Die temperature range was between 175°C and 210°C, depending on the alloy being cast. For alloys with 12% Al or lower, the temperature was kept between 200 and 210°C, and for those with higher Al it was between 175 and 200°C. The uniform heating of the die was ensured by monitoring the temperature by means of two chromel-alumel thermocouples which were located in the die block at a distance of 20mm away from the middle of each impression.

The die lubricant used to lubricate the die faces was an oil based lubricant, Dycote-2021 provided by Foseco Ltd., which was applied to the die faces by a spray gun.

Castings of each alloy were made by using variable machine parameters of injection speed and pressure, until the best casting combination was obtained. The best casting combination was obtained, especially for alloys with low freezing range, at highest injection pressure and the plunger speed near to the highest setting at a gate velocity of about 53 m/s which was calculated by measuring the ram speed, using a displacement transducer.

Porosity of each cast sample was checked by X-ray examination, and those free of macro-porosity were selected for experimental uses.

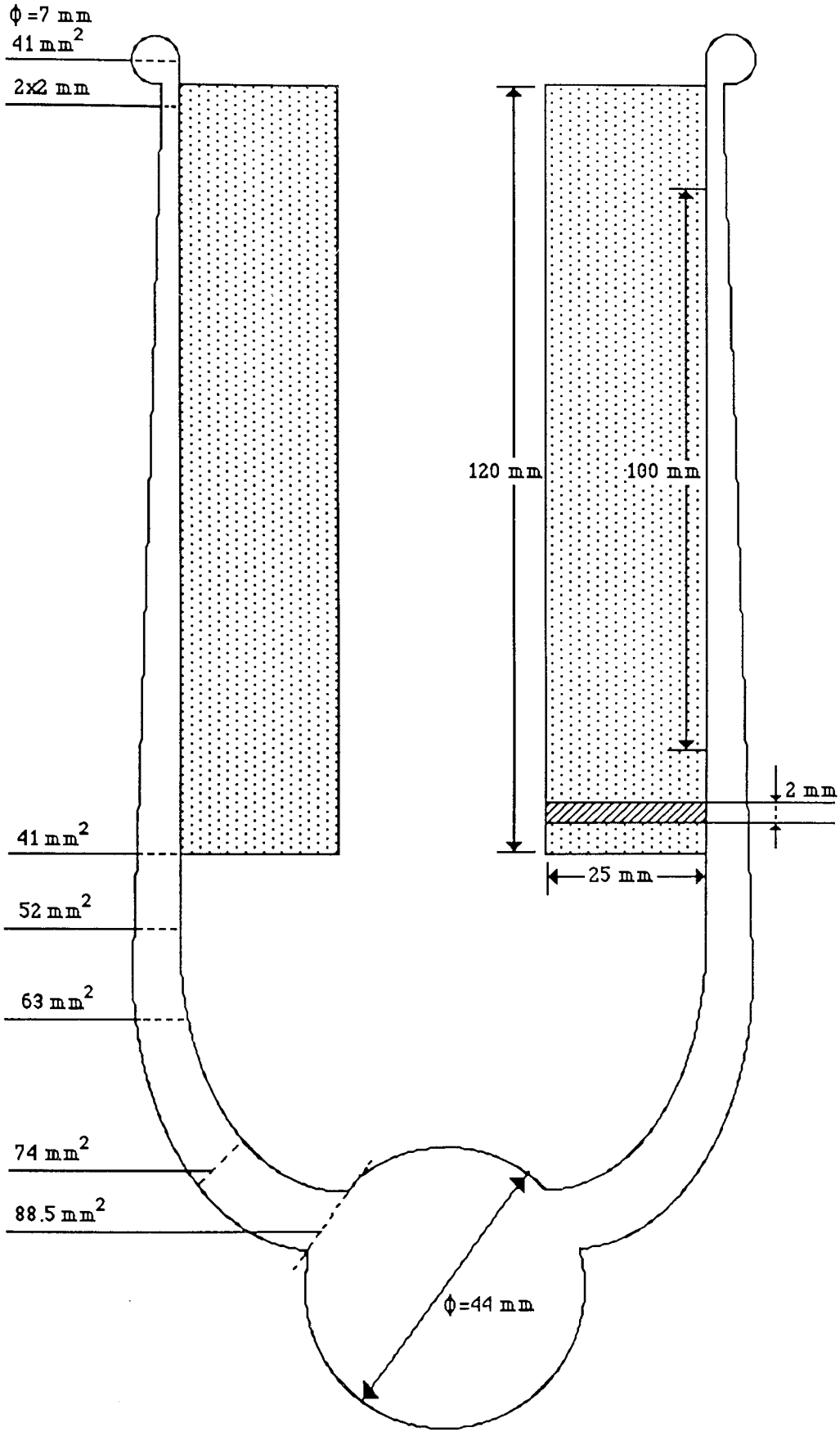

Figure 33. Die cavity design for thin section plates.

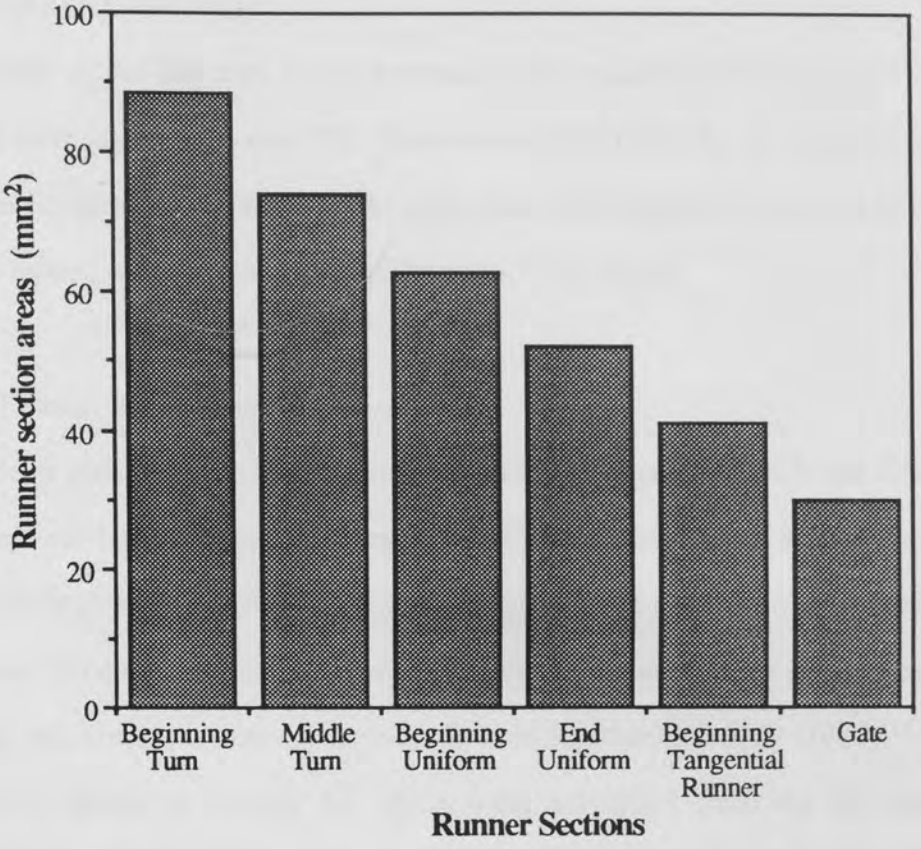

Figure 34. Decrease of the sections along the flow path of the feed system of the die.

Figure 35. Actual diecast rectangular plates with runner system.

3.1.3 Gravity Casting

In addition to the die cast alloys prepared, two eutectic alloys 3 and 4 and also 5(ZA.8) were also gravity cast. The alloys were melted in a clay-graphite crucible in a gas-fired furnace at about 600°C. The melts were then vigorously stirred and chill-cast into pre-heated mild steel moulds as 10mm thick flat ingots.

3.2 Creep Testing

Main creep tests were performed with the alloys of Mazak 3, ZA.8 and ZA.27. The tests were carried out at temperatures of 60°C, 90°C and 150°C, and at stress levels from 10MPa to 100MPa. At critical stress levels, a large number of experiments were duplicated to better establish the creep behaviour of the alloys. For these experiments, flat strip test pieces, in accordance with British Standard's, BS 18 (1970)[147] tensile test pieces shown in *Figure 36*, which were machined from the die cast plates *(Figure 31)* were used. Gauge lengths of 30mm were marked by fine parallel lines inscribed on the central portions of the parallel lengths of the samples which had been painted by ink to increase contrast between sample surfaces and gauge lines.

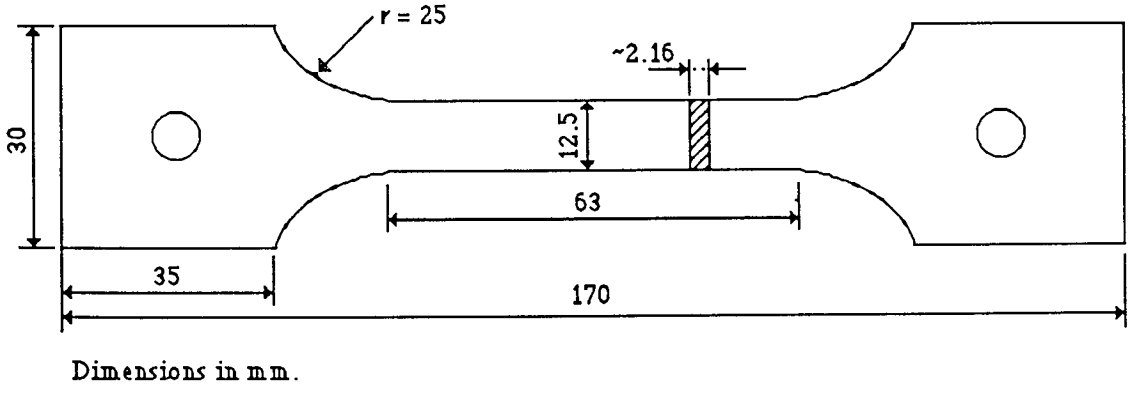

Figure 36. B.S. Rectangular section test piece.

The creep tests of the other experimental alloys (alloys 1 to 10) were performed at only one condition of 40MPa and 120°C. Test samples for these alloys, which were machined from the cast plates *(Figure 35)* according to British Standard[147], were similar to those used for the main creep work *(Figure 36)* with smaller dimensions,

6mm wide, 2mm thick and 120mm long in size. Gauge lengths marked on these samples were 25mm.

3.2.1 Creep Machines and Strain Recording Equipment

Creep tests were performed by using a standard weighted lever arm creep machine, complying with the loading accuracy requirements of British Standards 1610 Grade A, with a lever arm ratio of 10:1, and by using other creep equipment designed by the present author. Creep extensions were measured indirectly by a photographic method, in that the creep elongations were monitored by periodically photographing the gauge marks on the samples through a window on the furnaces.

The furnace part of the standard machine and strain recording equipment were set up as shown in *Figure 37*. This consists of:

(1) A cylindrical copper tube of the furnace, having a diameter of 50mm and a length of 100mm with a 25 by 50mm rectangular port, through which the specimens were illuminated and photographs were taken.

(2) A heating jacket had been wrapped around the copper tube, the temperature of which was controlled by a standard temperature controller.

(3) An Olympus OM10 quartz camera fitted with an autowinder, 135mm lens and extension tubes for recording the specimen gauge dimensions. This was attached directly onto the frame of the creep machine to prevent any accidental movement.

(4) A twin boom fibre optic light unit used to illuminate the specimen and provide contrast.

(5) An electronic interval timer which could be set to take one photograph at different rates, from one every 15 seconds to one photograph every 30 hours. The time at which each exposure was made was automatically recorded on the film by a data-back fitted to the camera. A second timer on this equipment also switched the light source on as the shutter was fired for a period of 3 seconds. This equipment also provided power for the light unit and the camera's autowinder.

An improved type of creep equipment was designed by the author, and is shown in *Figure 38* with its strain recording equipment. The pieces of equipment were designed to operate on the basis that the creep specimens could be loaded by a direct loading system, since the load range which was required for tests of the alloys at the selected temperatures were sufficiently low to enable the specimens to be loaded directly without using a lever arm mechanism. The equipment consisted of mainly:

(1) A hydraulic jack which raised the weights to load the specimen and sustain the load during the experiment.

(2) A universal joint which allowed the upper rod to align itself freely.

(3) A Canon T70 programmable camera fitted with a flash unit, 80-200mm lens and extension tubes. This could be programmed to take photographs at rates from one frame every second to one frame every 24 hours. The time at which each exposure was made was automatically recorded on the film.

(4) A D.C. voltage supplier which supplied continuous power to the flash unit.

(5) A hand pump connected to the hydraulic jack.

(6) A load scale and loading weights

(7) A standard temperature controller

(8) A base plate resting on a base frame

(9) Spacers and rubber bungs on which the loaded bottom rod rested and which provided gradual loading of the specimen.

(10) A fan connected to the furnace, which circulated hot air through the furnace during the heating and experiment

(11) A furnace consisting of two cylindrical steel tubes, in one of which a heating element was placed, which provided constant temperature to the second cylinder in which the samples were suspended.

(12) Two support columns

(13) A top plate.

3.2.2 Test Procedure

In order to obtain the selected stress level on the gauge-area of each test sample, a suitable weight was calculated by taking into account the lever arm ratio and weights of the bottom rods of the machines.

The test temperatures of the specimens inside the furnaces of both types of equipment were measured by a digital potentiometer, using chromel / alumel thermocouples which were attached to two different points on the specimens, in order to check for and thus avoid any temperature gradients along the gauge length.

Before each experiment was started, a reasonably long time was allowed for the temperature to stabilize, and temperature changes were limited to a maximum of $\pm 1°C$ for the whole period of the tests.

The procedure for the recording of creep extensions was as follows: Before each experiment was started, the camera was focused on the specimen and two photographs were taken to record the initial gauge length on film. As soon as the specimen was loaded, two more photographs were taken to give a measurement of initial creep strain. The interval timer was then reset at reasonable intervals in the course of the experiment. The experiments were conducted to a minimum creep extension of 1%. After the test, the films were processed and dried. Appearance of a test sample on a negative film is shown in *Figure 39*, which also shows a calibration scale attached to the specimen parallel to the gauge length, but it was not subjected to any loading. The purpose of this was to eliminate any shrinkage error which was likely to occur unevenly from one frame of the film to another when the films were developed, and any accidental movement of focal distance of the camera. The extensions and the scale lengths were measured on each frame of the films in succession, by using an optical microscope with a linear voltage displacement transducer attachment, which was connected to a digital indication unit as shown in

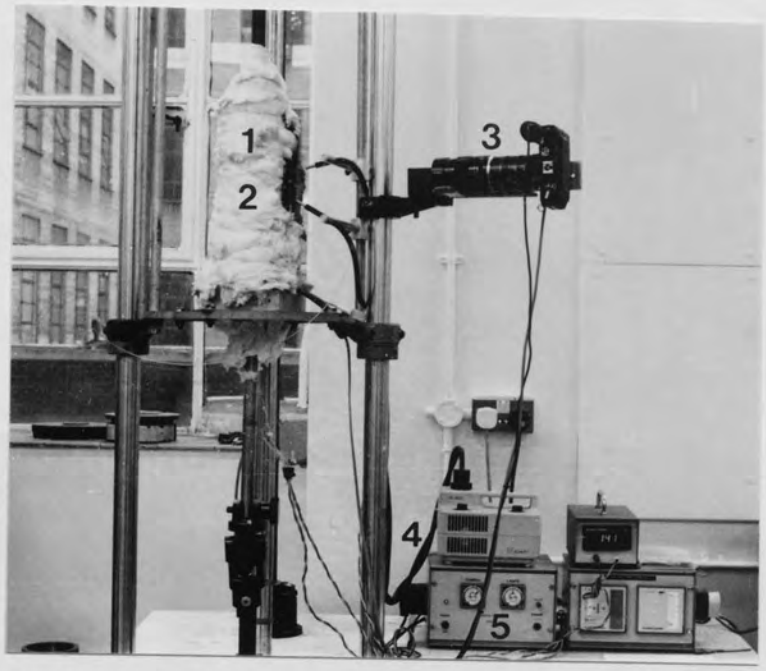

Figure 37. Standard creep machine and strain recording equipment.

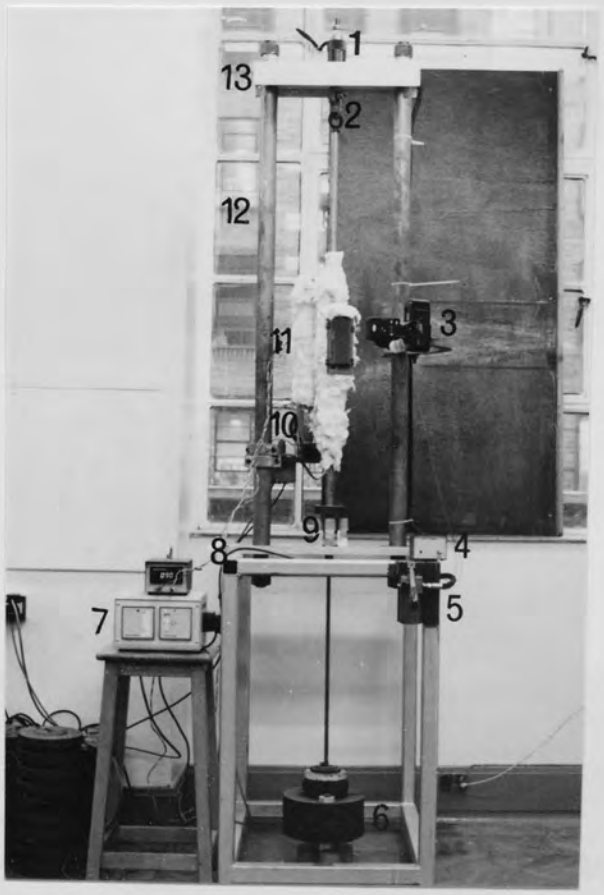

Figure 38. Designed creep equipment with air circulation furnace and strain recording equipment.

Figure 40. Linear accuracy of the unit was ± 1μm. Creep strain was then obtained by calculating the extension and by compensating the shrinkage and/or any focal error for each frame of the films, on which the corresponding line to creep strain had been automatically recorded by the camera.

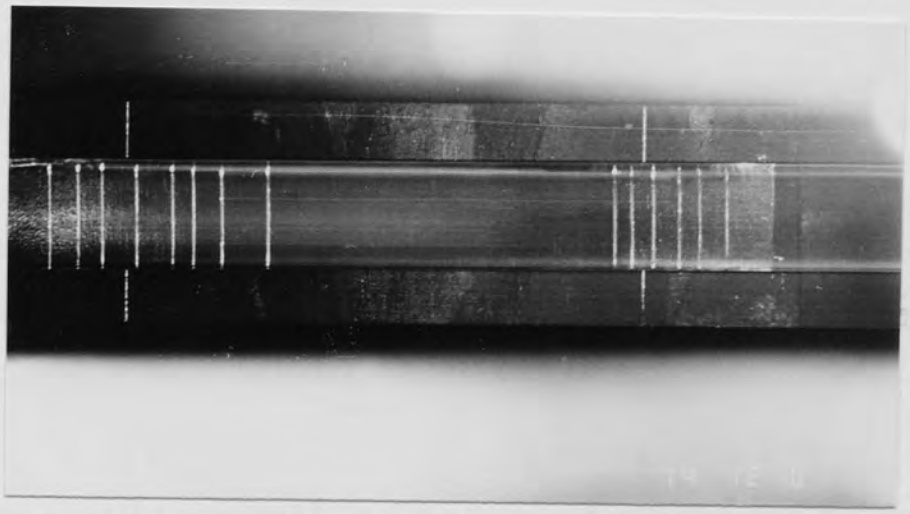

Figure 39. Appearance of creep specimen and calibration scale on the film.

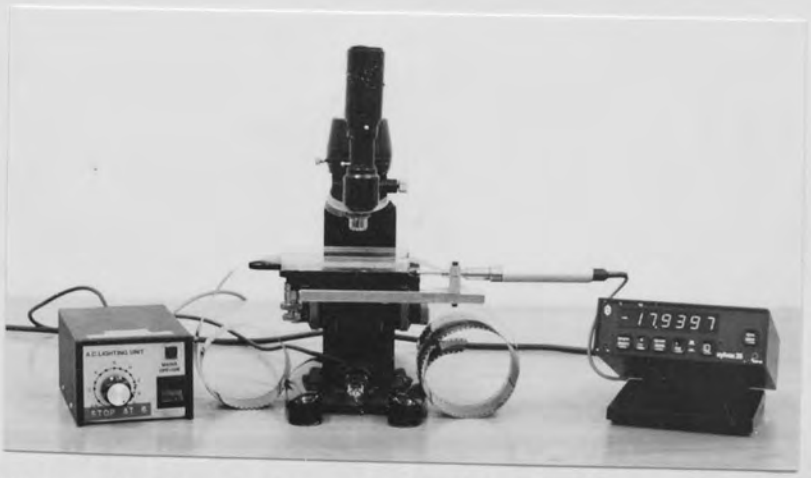

Figure 40. Measurescope (Optical microscope with LVDT attachment and digital indication unit).

3.3 Metallography

3.3.1 Optical and Scanning Electron Microscopy

Samples from each alloy in the as-cast condition and after the creep tests, were examined by optical and electron microscopy to study the structures and the effects of creep deformation. Samples were cut from the flat components to provide sections through the thickness of the plates. These were mounted in bakelite and were ground on silicon carbide papers, followed by polishing using diamond abrasive to a final finish of 1/4 μm to obtain a scratch-free mirror surface.

For optical metallography, the structures were revealed by etching the polished samples in either 2% Nital or Finkeldey etchants, for a varying length of time depending on the alloy.

However, since the structure of the alloys tested was extremely fine, as a result of fast cooling rate due to the pressure die casting process, the resolution of optical microscopy was found to be inadequate, in the majority of cases, to examine the fine details of the structures.

To obtain better resolution and to take advantage of the big difference between atomic numbers of the two main constituent elements (Zn and Al) of the alloys, backscattered electron scanning electron microscopy was adopted as the general investigation method, since by using backscattered electrons, contrast could be achieved from the difference in average atomic number Z of various phases in the sample. Higher Z regions have more nuclear charge and hence give rise to a great number of backscattered and smaller number of absorbed electrons than low-Z regions. For this work, two scanning microscopes, Cambridge Instruments SEM 2A and SEM 150 fitted with a special large area, back-scattered electron detector were used.

3.3.2 Transmission Electron Microscopy

Detailed examination of the as-cast structure of the commercial diecast alloys Mazak 3, ZA.27 and particularly of ZA.8 was made on the transmission electron microscope using thin foil samples.

3.3.2.1 Preparation of Thin Foils

The thin foil samples were prepared in three stages:

(1) Initial thinning of flat samples was carried out by wet-grinding on silicon carbide papers with grit size of 120 or 160, down to about 150μm thickness.

(2) Discs of 3mm diameter were produced from the thinned samples by spark-erosion in a Servomet spark-erosion machine, and discs were further wet-ground on 1200 grit abrasive paper, by using a small jig, down to about 100μm to obtain flat and parallel-sided faces.

(3) Final thinning of the disc samples was carried out by electropolishing in a commercial double jet electropolisher, the Tenupol (Struers Ltd.) shown in *Figure 41*, which consisted of a polishing cell and a pump which circulated electrolyte through the dual jets which were directed at the centre of the 3mm disc sample. This was mounted in a removable sample holder and the anode potential was applied via a platinum strip which runs through the centre of the holder, where the sample was placed. Twin jets thinning both sides of the specimen together, eroded a concave hollow on each side. As soon as a hole formed, usually in the middle of the specimen, the polishing action was stopped automatically by detecting the moment of penetration of light through the sample from the light source on one side of the cell to a sensitive photodiode on the other.

A number of electrolytes suggested for electropolishing of Zn, Zn-alloys and Al-Zn alloys, which were usually based on mixtures of perchloric acid (10-20%) and ethanol were tested; but none of these produced satisfactory polishing. The main problem with these solutions was found to be due to the chemical attack of the strong oxidizing agent (perchloric acid), on the sample surface at even a very low temperatures (-30 to -40°C), as soon as the polishing process was stopped.

Figure 41. The Tenupol jet electropolisher with DC voltage supply unit.

A new electrolyte was developed by taking into account the drawbacks of the recommended solutions; the amount of perchloric acid was kept to a minimum to avoid the formation of oxide layer on the surface of the disc during transference of the disc from the cell to the cleaning agents. Resistance of solution was increased by the addition of 2-butoxyethanol. This also increased the resistance of the anodic film and provided a uniform thinning of the samples at relatively slow speeds.

Several mixtures of these two agents in ethanol were tested to obtain an optimum solution, and a mixture, the content of which is given below, produced the most satisfactory results under the operating conditions listed in *Table 7*.

Electrolyte: 30cc Perchloric acid (d = 1.54 g/ml)

250cc 2-Butoxyethanol

700cc Ethanol

Table 7. Operating Conditions of Electropolishing for Commercial Alloys.

Alloy	Voltage (V)	Current density (Amp./cm^2)	Flow Rate	Temperature (°C)
M.3	25-35	0.3-0.37	6.5	-15-(-25)
ZA.8	25-35	0.28-0.34	6.5	-15-(-25)
ZA.27	25-35	0.25-0.28	6.5	-20-(-30)

The electrolyte was kept cooled to below-zero temperatures with liquid nitrogen poured on top of the container.

Extra care was taken to clean the samples as soon as the polishing process was stopped. This was done by washing the sample under running water, followed by passing it through at least four sets of cooled ethanol and then drying it in between two filter papers.

The whole process produced excellent results for the alloys examined.

3.3.2.2 Transmission Electron Microscopy

Thin foils of samples were examined in three different transmission electron microscopes; a Jeol JEM 100B, a Philips EM 300 and a Philips EM 400T, which were all operated at an accelerating voltage of 100 kV. The majority of the work was particularly carried out on the Philips EM 400T, equipped with a scanning transmission electron microscope (STEM) and a quantitative energy dispersive x-ray analysis (EDX) system. The excellent features of this equipment enabled the author to study the structure of the experimental alloys in great detail. Three main operation

modes of this equipment were exploited as follows:

In conventional TEM mode, bright and dark field images of the structures were studied with corresponding selected area diffraction patterns (SADP). The tilting technique, using a double-tilt stage, was used in order to obtain three dimensional information and allowed the selection of particular crystallographic directions to reveal structure and to differentiate the diffraction patterns of small particles with similar lattice parameters to the matrix phase. To obtain selected crystallographic directions, tilting about the direction indicated by the Kikuchi lines was followed by using schematic Kikuchi maps as an aid in selecting tilt axes. This was done by tilting first to the nearest obtainable and recognizable pole and then calculating the angle between the beam direction of this pole and that of the pole of interest, and finally tilting this known angle about a defined tilt axis, indicated by the Kikuchi map. This process usually required tilting through large angles and was a rather difficult task in CTEMs since the areas of interest, which were usually small, moved, and as a result corresponding SADPs of these areas disappeared during tilting. This difficulty was overcome to a significant extent by using a small convergent probe (convergent beam), the angle of which was controlled by the size of the second condenser lens aperture and the size by the strength of the first condenser. This mode of operation focused the size of the second condenser lens aperture onto the specimen, producing diffraction patterns consisting of various sizes of discs, depending on the size of the second condenser lens aperture being used. In this mode, convergent beam diffraction patterns (CBDP) of very small areas were also obtained.

The STEM mode of the microscope was also utilized to analyse the chemical composition of the present phases. To be able to analyse some extremely small phases, the smallest probe was obtained by switching off the second condenser lens and increasing the strength of the first lens and using the smallest second condenser lens aperture, and then focusing the probe onto the area to be analysed, using the objective lens.

X-ray microanalysis of the phases were carried out as an integral part of the STEM by using the EDX system. For this purpose, a special carbon specimen holder was used to avoid any X-ray contamination generated from standard specimen holders, and analyses were carried out at the thinnest areas of the samples. X-ray intensities from the elements being analysed were obtained after various times between 200 and 500 live-seconds. Background fitting to characteristic peaks of the elements was carried out by use of a computer program which also allowed modification of a fitted background in some regions which were clear of characteristic peaks of the elements. When a satisfactory fit was obtained, it was subtracted from the characteristic peaks to give real intensities of the elements. The intensities of the elements were also computed to obtain the true concentrations with atomic number correction only.

CHAPTER 4

4.0 EXPERIMENTAL RESULTS

4.1 Chemical Composition of the Experimental Alloys

The Composition of the alloys was determined by atomic-absorption spectroscopy and the results are given in *Table 8*.

Table 8. Composition of the experimental alloys (wt.%).

Alloy	Zn (%)	Al (%)	Cu (%)	Mg (%)	Fe (%)
Mazak.3	Remainder	4.2	<0.003	0.049	<0.01
ZA.8	"	8.1	1.060	0.024	"
ZA.27	"	28.5	2.180	0.016	0.10
1	"	0	<0.003	0.048	<0.01
2(M.3)	"	4.1	"	0.049	"
3	"	5.3	0.030	0.050	"
4	"	5.1	1.020	0.030	"
5(ZA.8)	"	8.2	1.200	0.024	0.01
6(ZA.12)	"	11.5	0.880	0.023	0.02
7	"	18.0	1.100	0.026	"
8	"	28.1	1.160	0.019	0.01
9(ZA.27)	"	25.9	2.340	0.015	0.02
10	"	30.4	1.080	0.020	"

4.2. Creep Results of Commercial Alloys

For each creep experiment, the variation of creep strain with time was plotted as creep strain (ε) versus time (ks). In all cases, curves exhibited the same general form of the creep curve, that is to say a primary creep stage of steadily decreasing strain rate, followed by a linear steady-state region. Since the experiments were usually conducted to produce a minimum creep strain of 1%, which was usually reached in the secondary creep region, the tests were not generally allowed to proceed into tertiary region. However, when they were allowed for comparatively short term experiments, they showed a well defined tertiary creep region as well. In some experiments, 1% creep strain was reached in the rather early stages of creep, either in primary or in early secondary creep regions. In these cases, to obtain a reliable secondary creep-rate data, the experiments were extended until well defined secondary creep regions were obtained.

Because of the rather large number of creep curves to present here, some examples were selected to show characteristic time-creep strain behaviour of the alloys, as seen in *Figures 42 to 53*. In general, the alloy, Mazak 3, had least primary creep and ZA.27 the greatest. The secondary creep regions of the creep curves of the alloy Mazak 3, were comparatively short and tertiary creep was reached in the early stage of the creep extension. On the other hand, for alloys ZA.8 and ZA.27 prolonged secondary creep regions were observed, and in the case of ZA.27 that was the greatest.

Secondary creep rates ($\dot{\varepsilon}_s$) were calculated from the steady-state regions of the curves, using linear regression analysis. The slope of the regressions was taken to be the value of the secondary creep rate and the intercept of the slope on strain ordinate at zero time, the primary creep strain including instantaneous creep strain. Besides, to obtain the relative creep performances of the alloys to a selected total creep elongation,

the times to produce a creep strain of 1%, 0.7%, 0.5% and 0.2% were calculated from the curves. All data for each test condition was tabulated in tables for alloys Mazak 3, ZA.8 and ZA.27, respectively in Appendice A.

Creep data of Murphy et al [117] at 120°C, which had been obtained using the same die-cast plates as used in this work and using the same testing facilities, was also included in these tables, to reveal the temperature-dependent behaviour of the alloys over a complete temperature range from 60°C to 150°C.

4.2.1. Primary Creep Extension

As seen from the results, no clear stress-dependence of primary creep extension at any temperature for any alloy was found.

Temperature-dependence of the primary creep extensions for the alloys Mazak.3, ZA.8 and ZA.27 were plotted in *Figures 54* as average primary creep strain obtained at one temperature versus temperature range in which the alloys were tested. As seen from the figure, temperature did not have any clear effect on primary creep for the alloys Mazak 3 and ZA.8, both of which showed rather consistent primary creep elongation over all temperature ranges. In the case of ZA.27, however, it was found that primary creep extension of this alloy was strongly dependent on temperature, and increased with increasing temperature At 60°C, the average primary creep extension of this alloy was similar to that of the alloy ZA.8, but increased rapidly above this temperature. At 90°C, it was approximately twice as high as the value of that at 60°C and stayed steady within the scatter limit of the data between 90°C and 120°C, and increased rapidly again to reach a maximum value at 150°C.

The primary creep results of the alloys, on the other hand, yielded another important fact that the primary creep of the alloys increased with increasing aluminium content. The mean value of the contribution of primary creep to

total creep strain for each alloy was calculated and found to be 0.16, 0.23 and 0.50% for the alloys Mazak 3, ZA.8 and ZA.27, respectively, and plotted against the aluminium content of the alloys as seen in *Figure 55*, which clearly yielded a linear relationship between primary creep and the aluminium content within the composition range of the alloys.

4.2.2 Secondary Creep Rate

Secondary creep rates ($\dot{\varepsilon}_s$) of the alloys Mazak 3, ZA.8 and ZA.27 are plotted in the form of ln $\dot{\varepsilon}_s$ versus ln stress (σ) as shown in *Figures 56, 57 and 58*, respectively. According to the power law equation *(Equation 14)*, this type of plot should yield straight lines with a constant slope at a constant temperature. As seen from the figures, reasonably good correlation with constant slopes were obtained for all alloys over much of the stress and temperature range, although increased slopes were observed at high stresses for Mazak 3, at high and low stresses for ZA.8 and at low stresses for ZA.27. The slopes over much of the stress and temperature range for alloys Mazak 3, ZA.8 and ZA.27 were found to be 3.5, 4.0 and 4.5, respectively. For the alloys Mazak 3 and ZA.8, these slopes increased above 60 MPa and appeared to yield a stress exponent value of around 6 and 7, respectively. However, there was not sufficient data above this stress to define the exact value of the slopes. Although the alloy Mazak 3 did not show an increased slope above 60 MPa at 120°C and 150°C, and for alloy ZA.8 at 150°C, this may have been due to the fact that these alloys were not tested at higher stresses above 60 MPa at these temperatures and any increase in the slope may not have been detected.

Deviations from the constant slopes also appeared at low stress levels in ZA.8 and ZA.27 at 150°C only *(Figures 57 and 58)*.

From these graphs, the secondary creep rates for a fixed stress of 40 MPa

were obtained and are listed in *Table 9* for the temperatures 60 to 150°C.

Table 9. Secondary creep rates (s^{-1}) of M.3, ZA.8 and ZA.27 at 40 MPa.

Temp. (°C)	60	90	120	150
M.3	5.60×10^{-9}	1.07×10^{-7}	1.51×10^{-6}	1.18×10^{-5}
ZA.8	7.58×10^{-10}	1.07×10^{-8}	1.37×10^{-7}	1.52×10^{-6}
ZA.27	2.65×10^{-9}	4.57×10^{-8}	9.19×10^{-7}	1.01×10^{-5}

Based on these data, a graph shown in *Figure 59* was plotted as ln $\dot{\varepsilon}_s$ versus the reciprocal of the testing temperature (K). According to *Equation 17*, such a plot should yield straight lines of slope Q_c/R and therefore the activation energy for creep at a constant stress.

For each alloy, good straight lines were obtained. Activation energy obtained from the slopes of the lines were 99.5 ± 0.5 kJ/mole for the alloys Mazak 3 and ZA.8, and 108 kJ/mole for the alloy ZA.27.

At high stresses, where increased slopes were observed for the alloys Mazak 3 and ZA.8, the data was not sufficient to obtain an accurate nature of the activation energies. However, they were calculated from the available data at 60 and 90°C for the alloy Mazak 3, and 60, 90 and 120°C for the alloy ZA.8 and found to be 103 and 90 kJ/mole, respectively.

4.2.3 Total Creep Extension

From the creep curves, the times to produce 1% creep strain were obtained and plotted as a function of ln stress (σ) for each temperature. These are shown for the alloys Mazak 3, ZA.8 and ZA.27 in *Figures 60, 61 and 62*, respectively. In all cases, such graphs were linear with a constant slope over much of the stress range, yielding a similar stress exponent of 3.5 for all three alloys. Deviations from this slope appeared at very high stress levels (above ~50 MPa) in all alloys, and at very low stress levels at 150°C in ZA.8 and

ZA.27. Deviations at high stress levels were not found at 120°C and 150°C for the alloy Mazak 3, and at 150°C for the alloys ZA.8 and ZA.27, possibly because the alloys were not tested at high enough stresses at these temperatures.

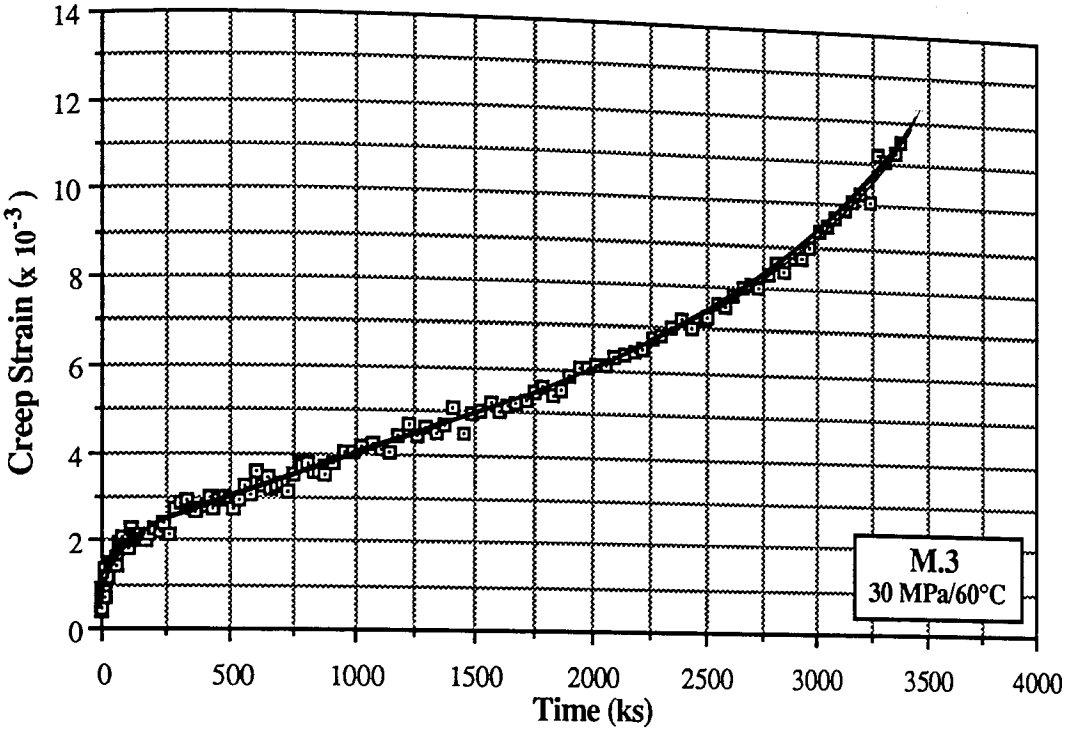

Figure 42. Creep curve of alloy M.3 at 30 MPa and 60°C.

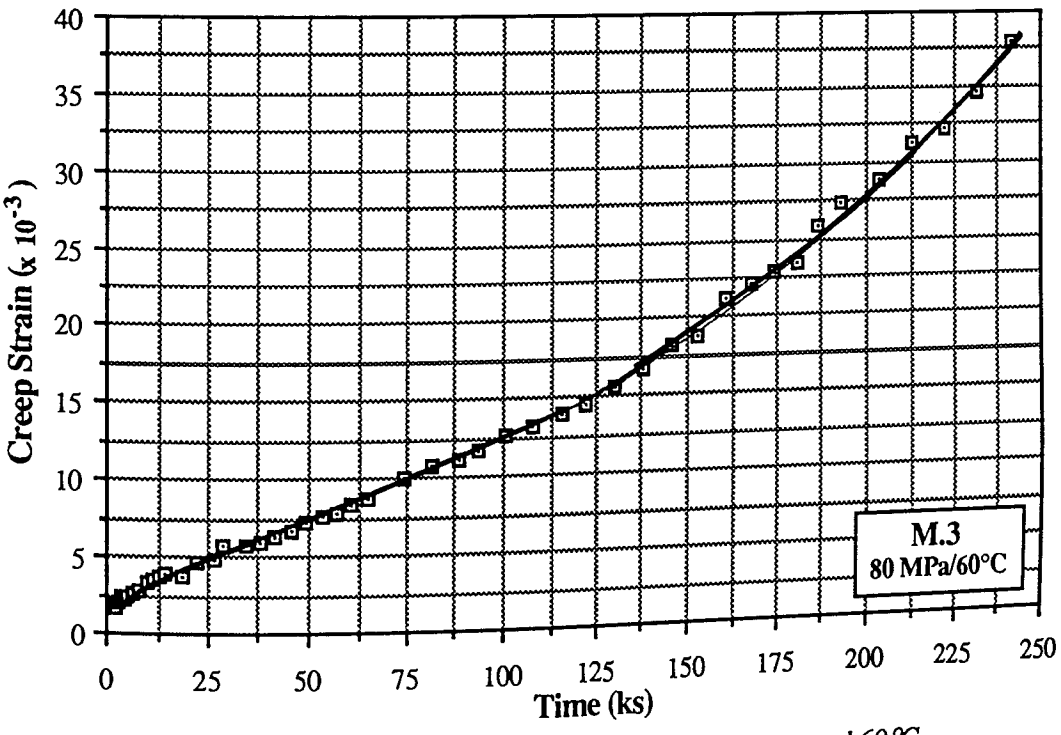

Figure 43. Creep curve of alloy M.3 at 80 MPa and 60°C.

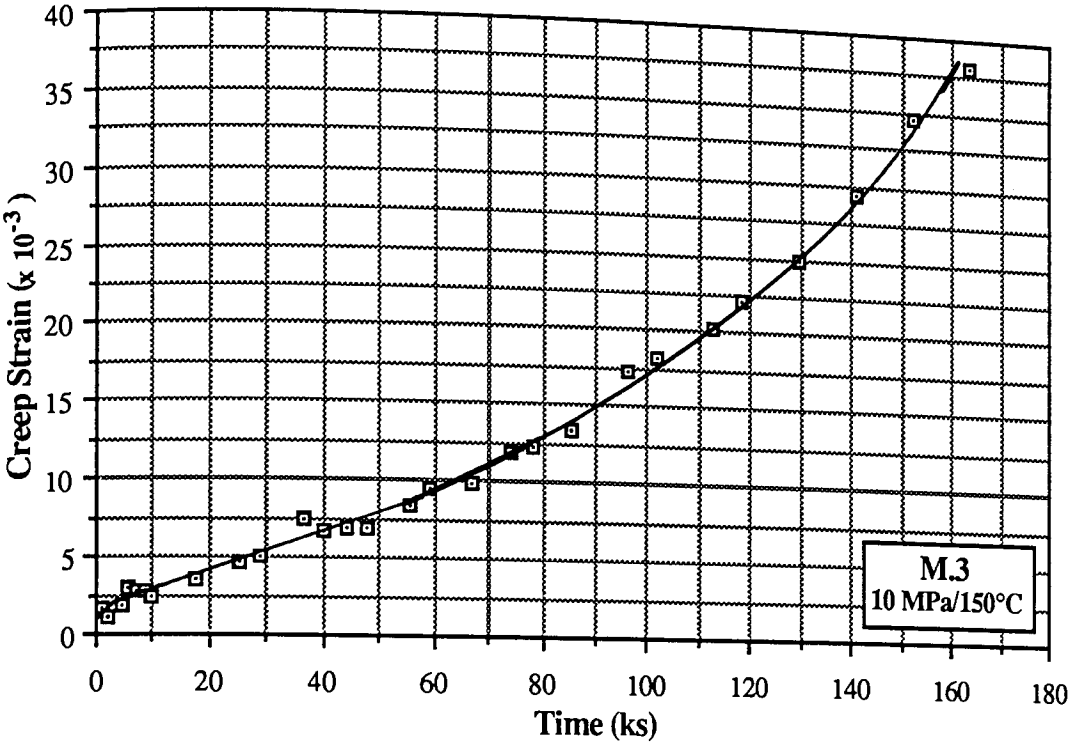

Figure 44. Creep curve of alloy M.3 at 10 MPa and 150℃.

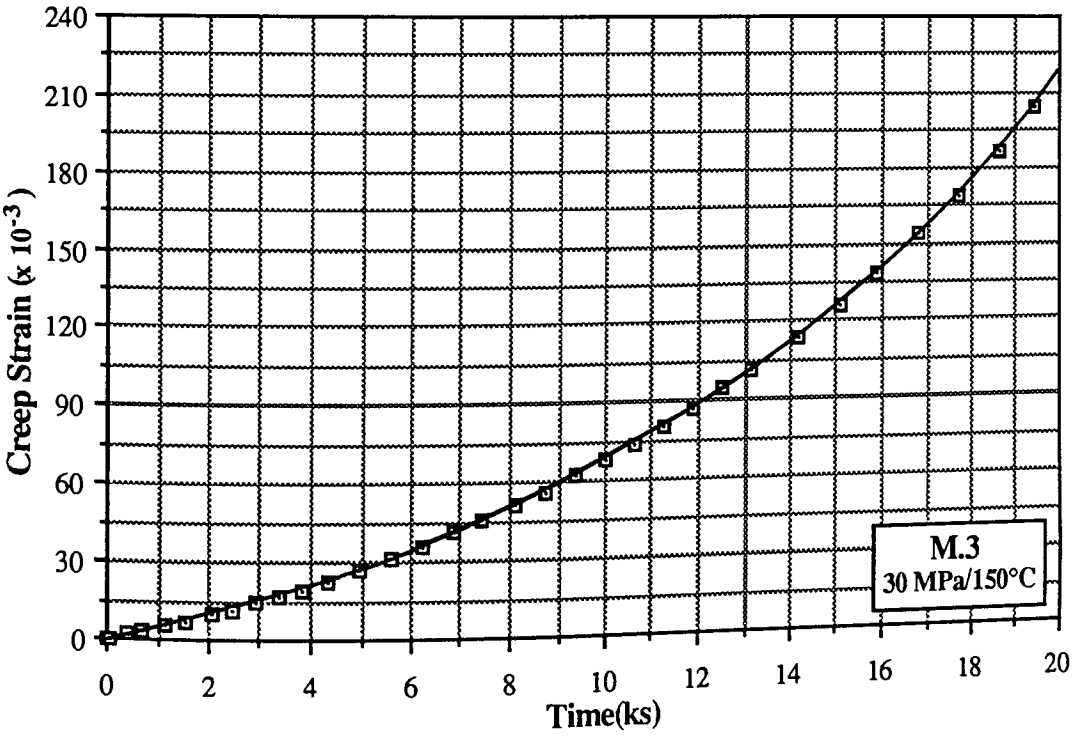

Figure 45. Creep curve of alloy M.3 at 30 MPa and 150℃.

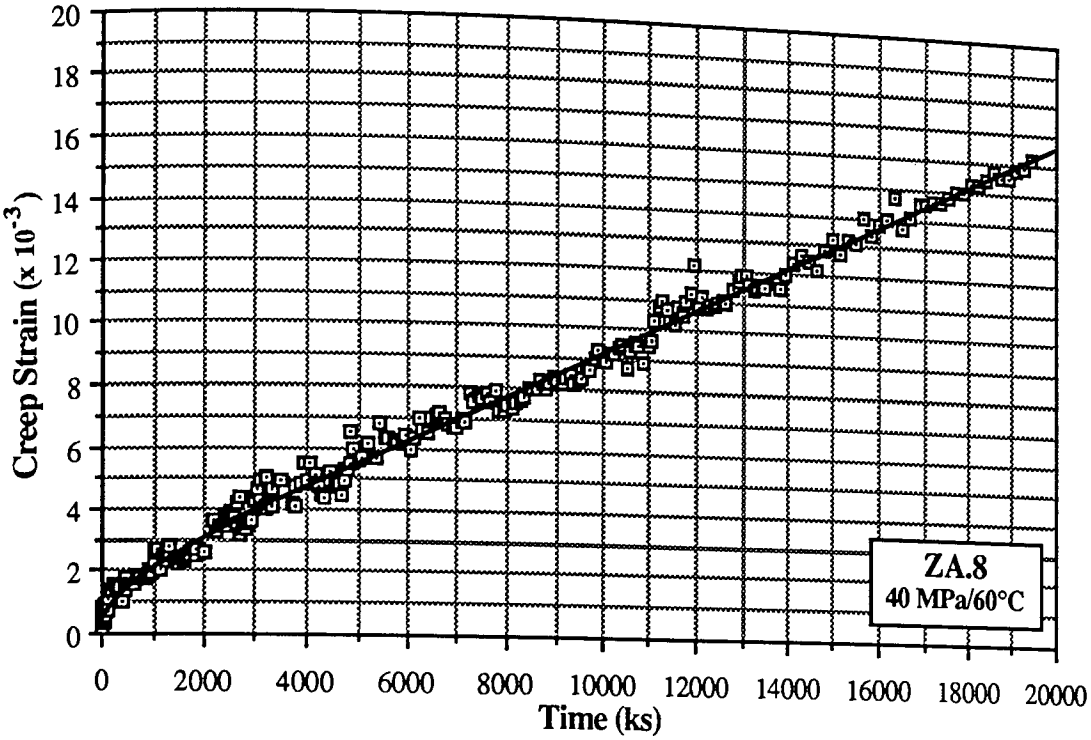

Figure 46. Creep curve of alloy ZA.8 at 40 MPa and 60 °C.

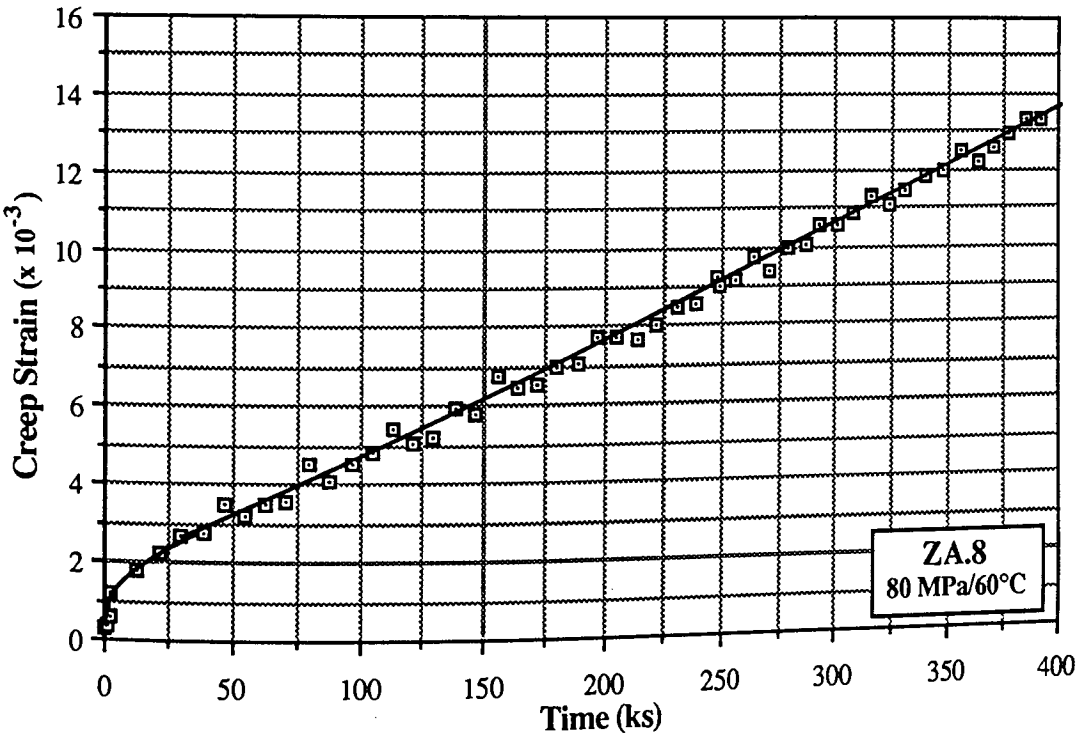

Figure 47. Creep curve of alloy ZA.8 at 80 MPa and 60 °C.

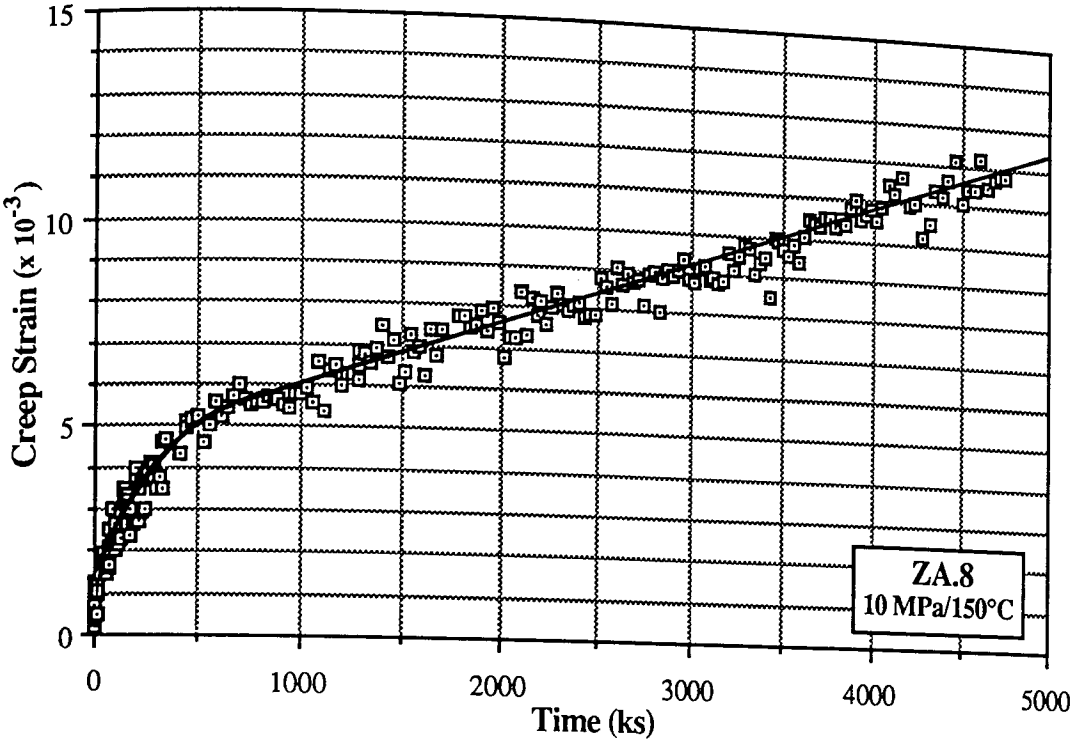

Figure 48. Creep curve of alloy ZA.8 at 10 MPa and 150°C.

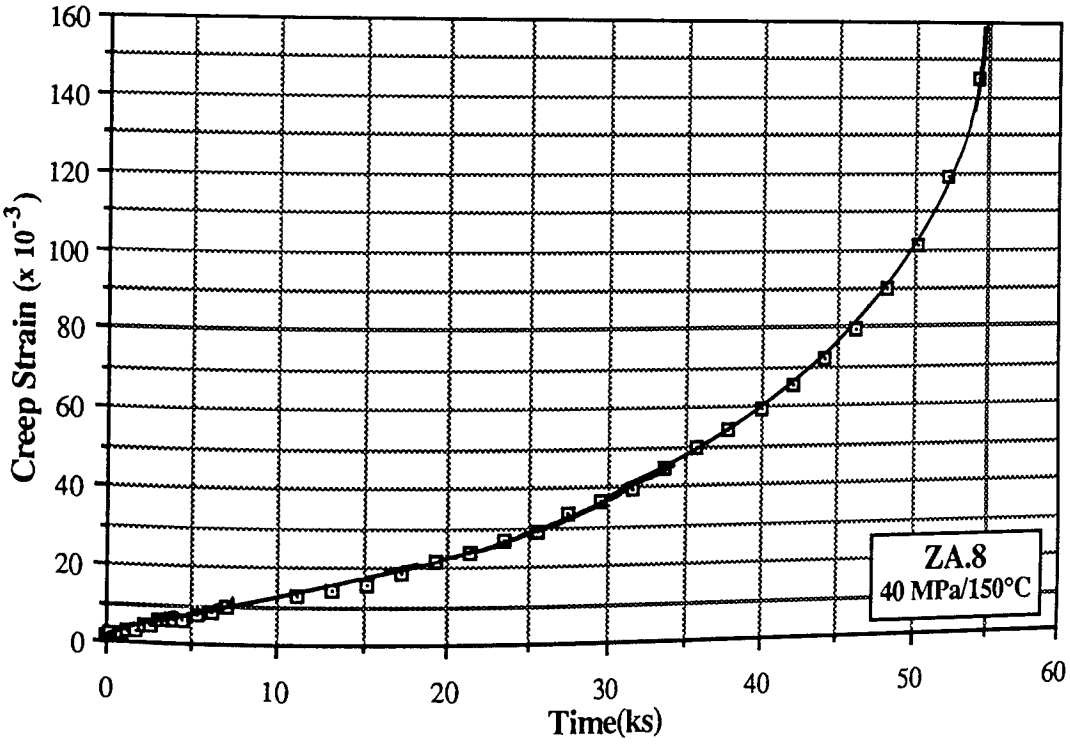

Figure 49. Creep curve of alloy ZA.8 at 40 MPa and 150°C.

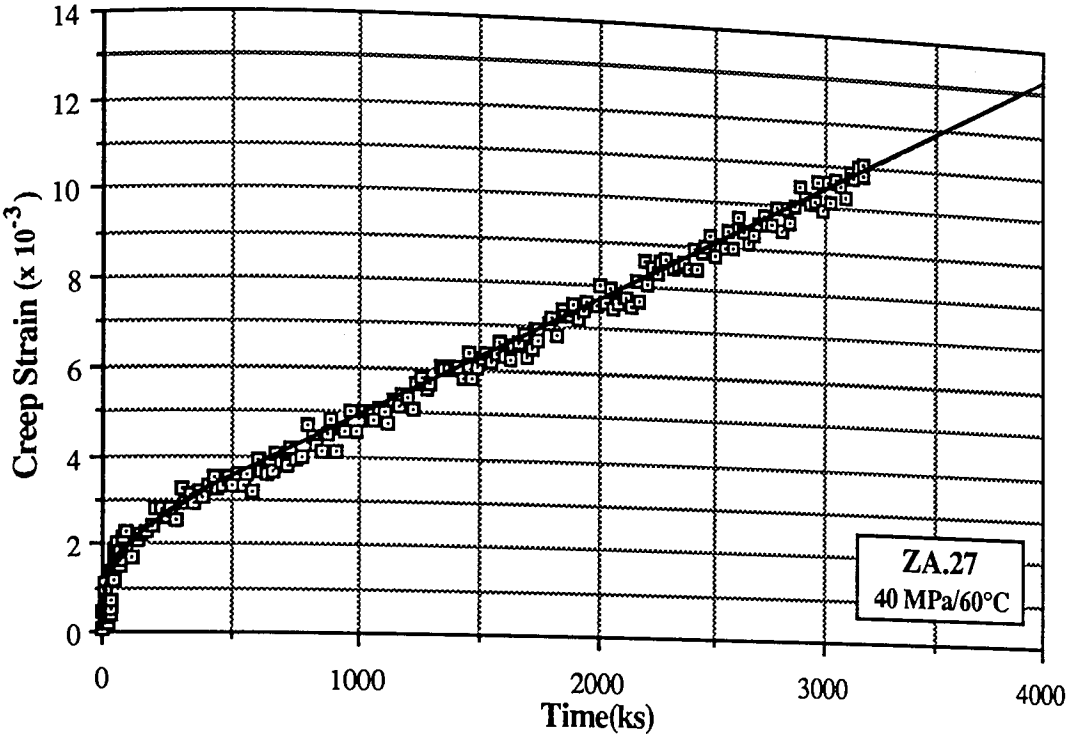

Figure 50. Creep curve of alloy ZA.27 at 40 MPa and 60°C.

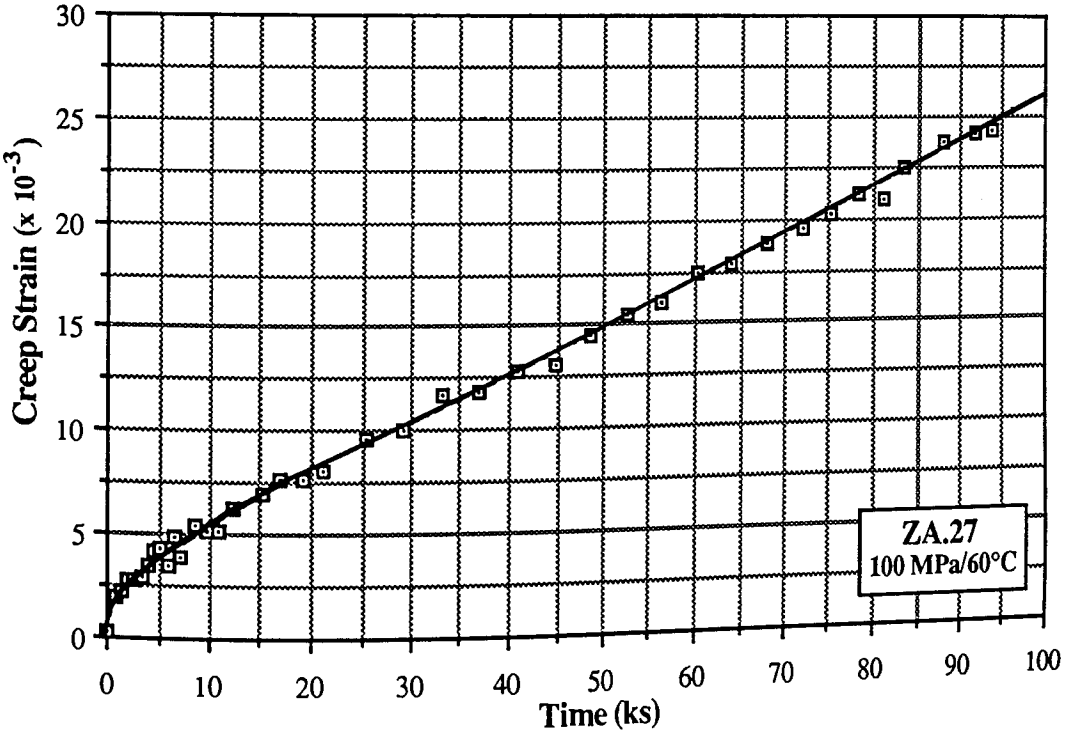

Figure 51. Creep curve of alloy ZA.27 at 100 MPa and 60°C.

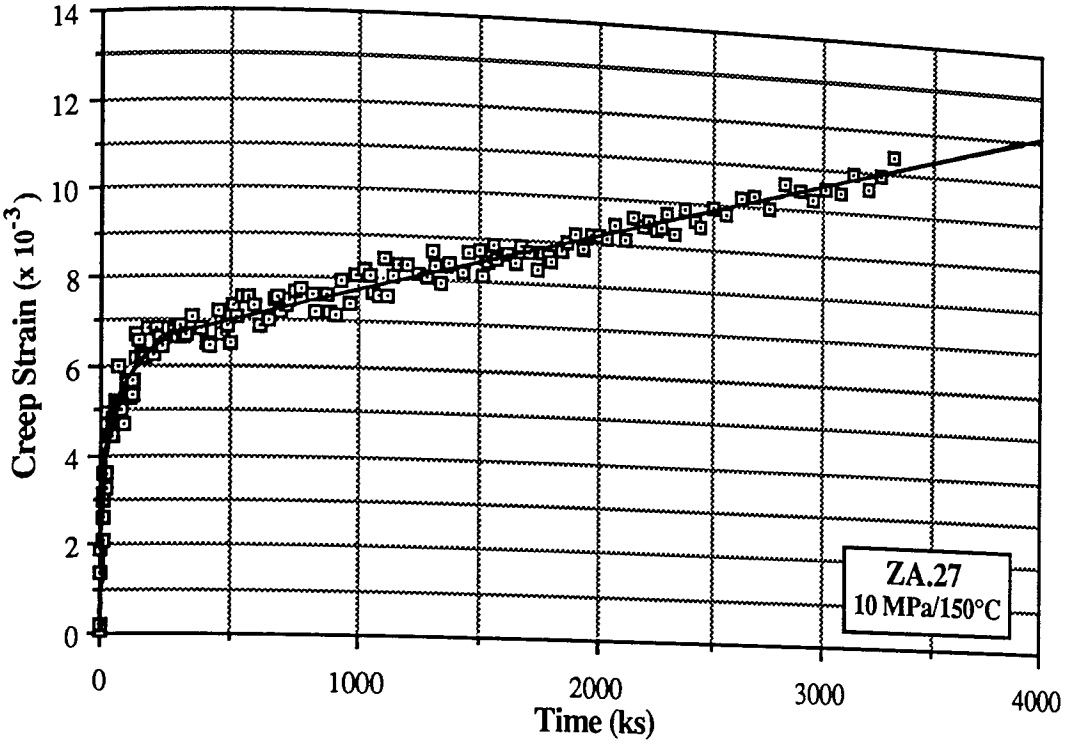

Figure 52. Creep curve of alloy ZA.27 at 10 MPa and 150°C.

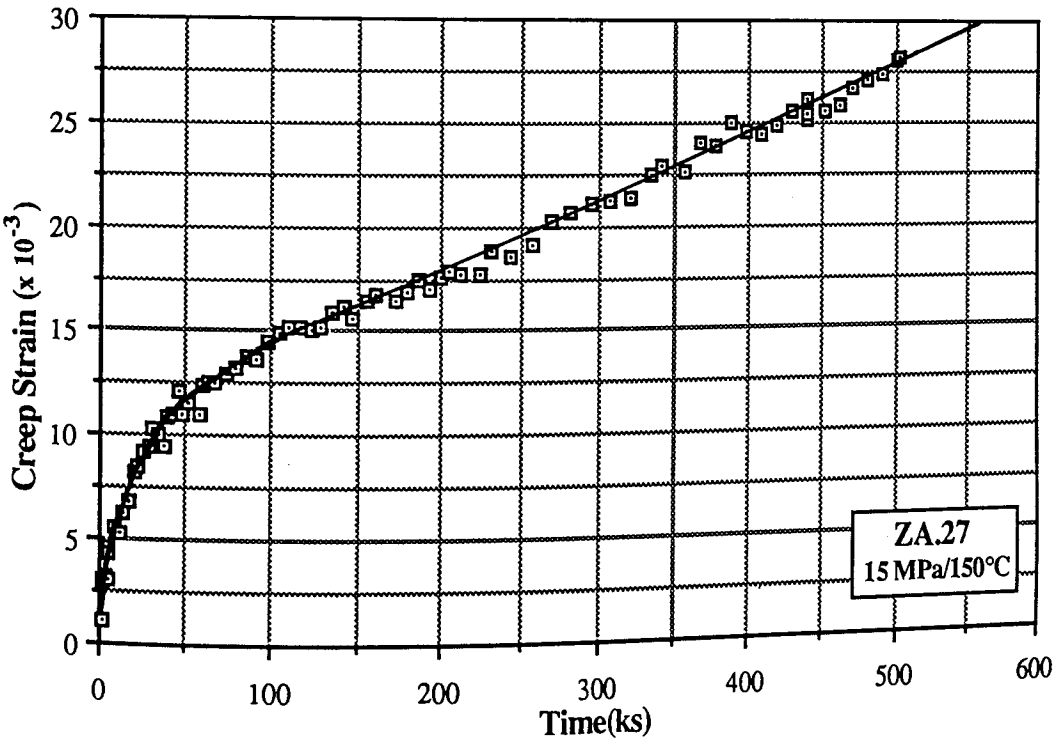

Figure 53. Creep curve of alloy ZA.27 at 15 MPa and 150°C.

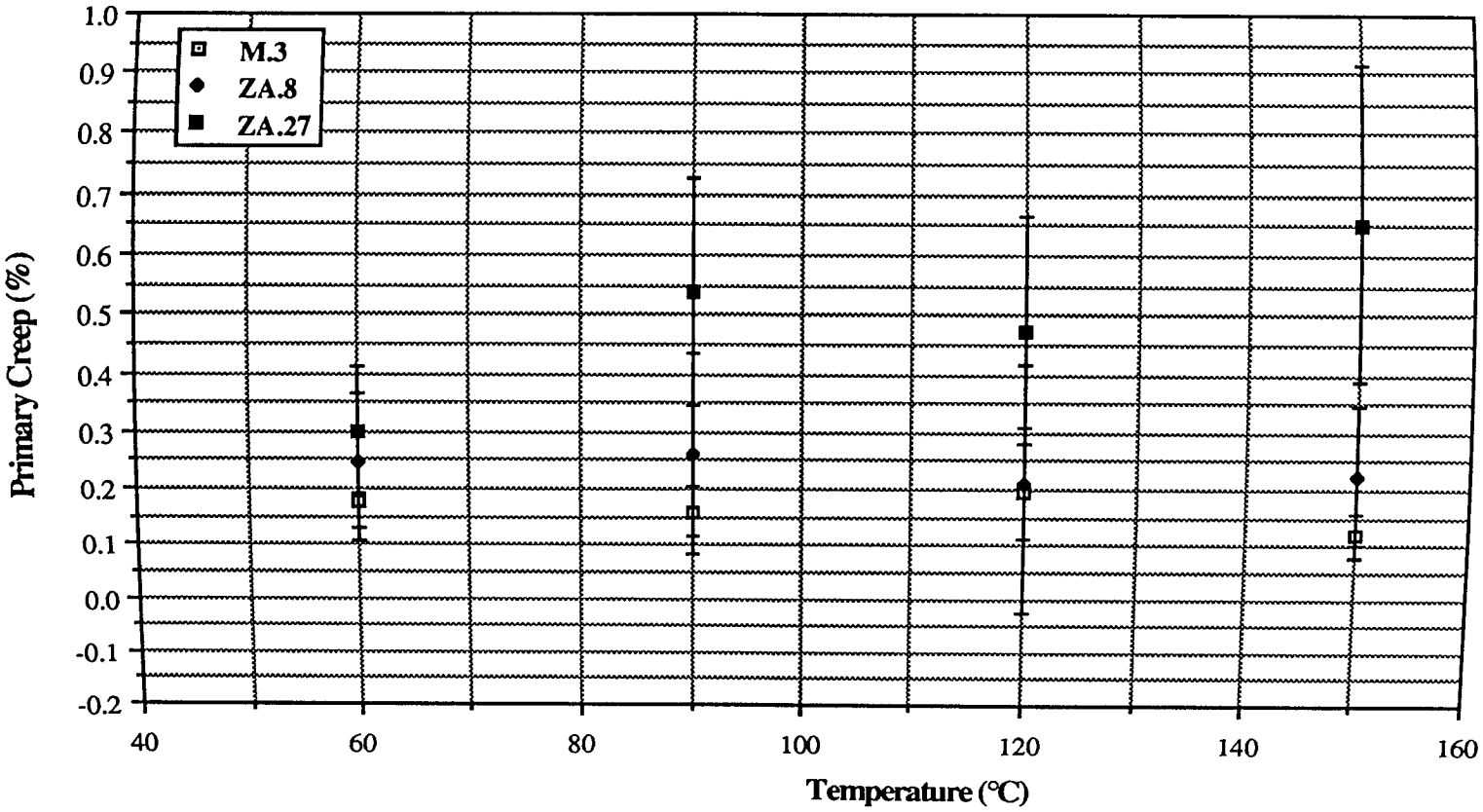

Figure 54. Variation of average primary creep extension of the alloys M.3, ZA.8 and ZA.27 with temperature.

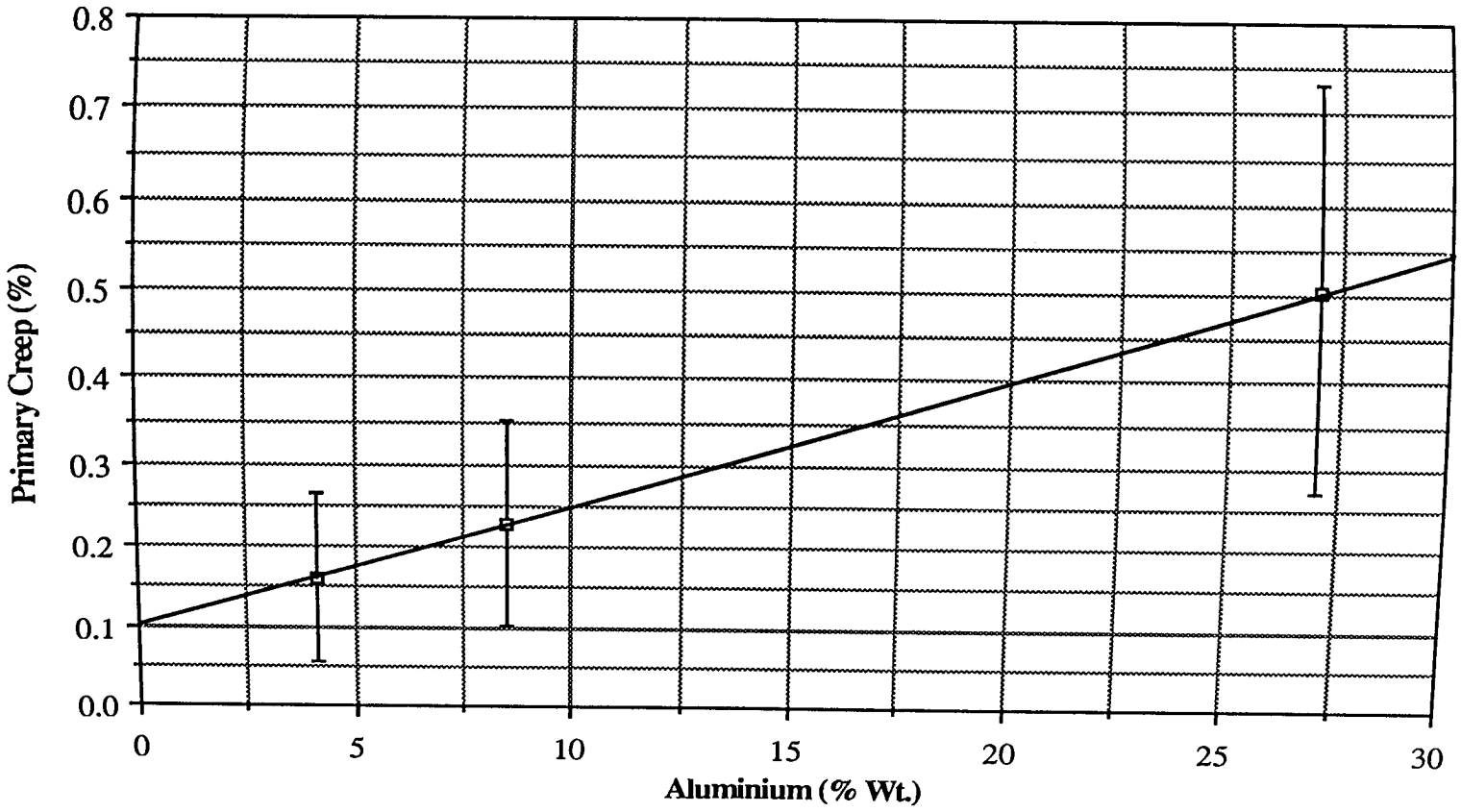

Figure 55. Variation of primary creep with aluminium content of the experimental alloys.

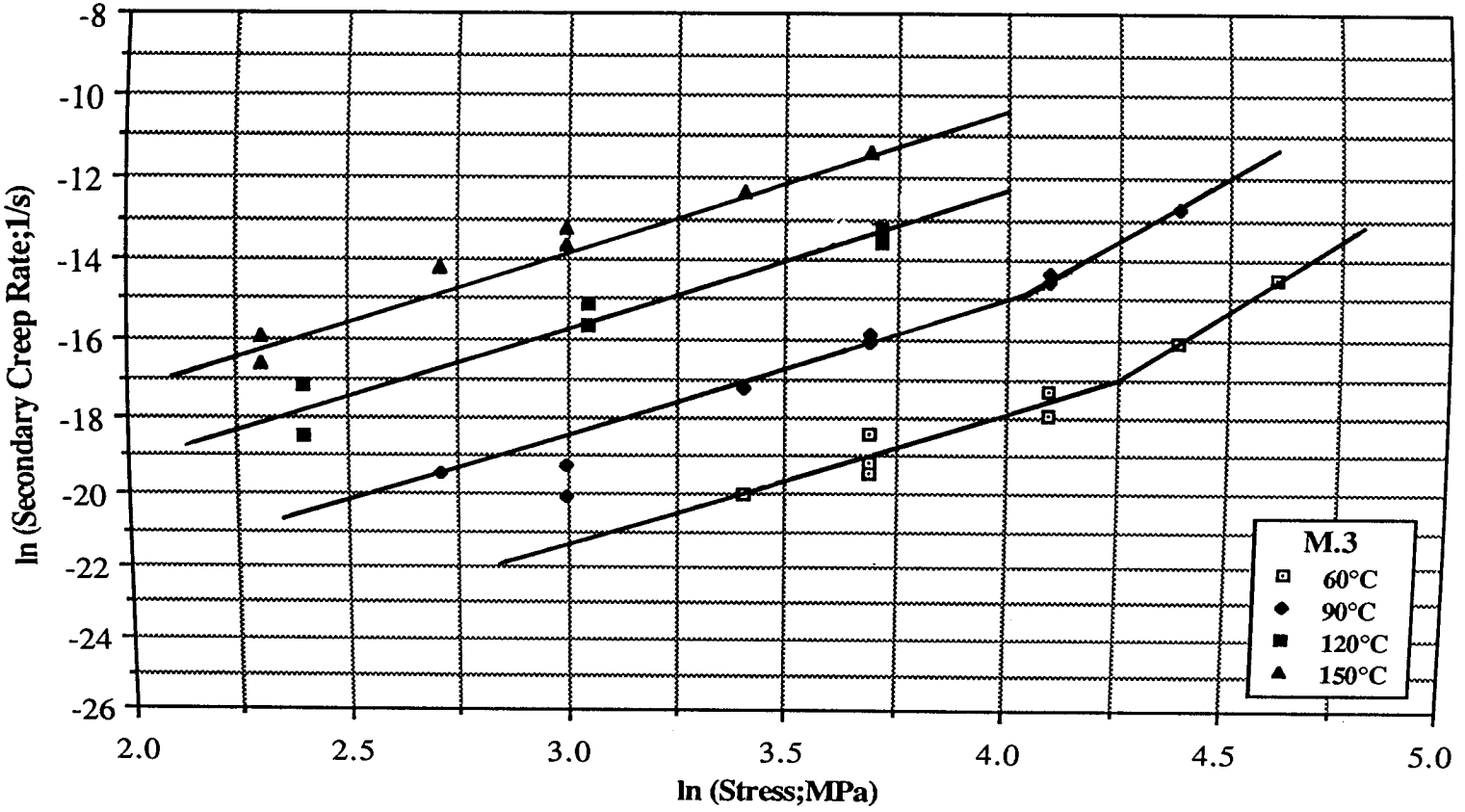

Figure 56. Variation of secondary creep rates of the alloy M.3 with applied stress at different temperatures.

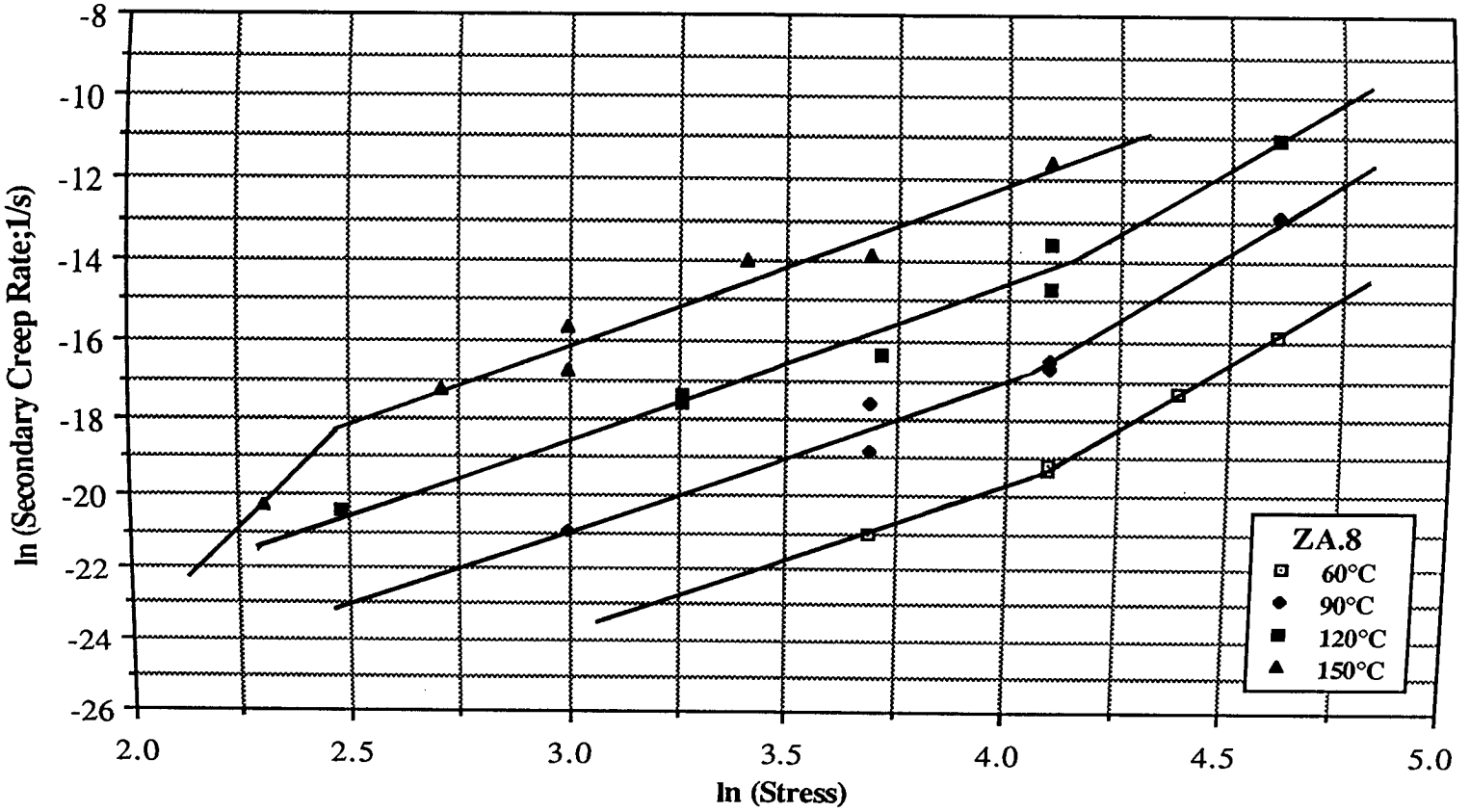

Figure 57. Variation of secondary creep rates of the alloy ZA.8 with applied stress at different temperatures.

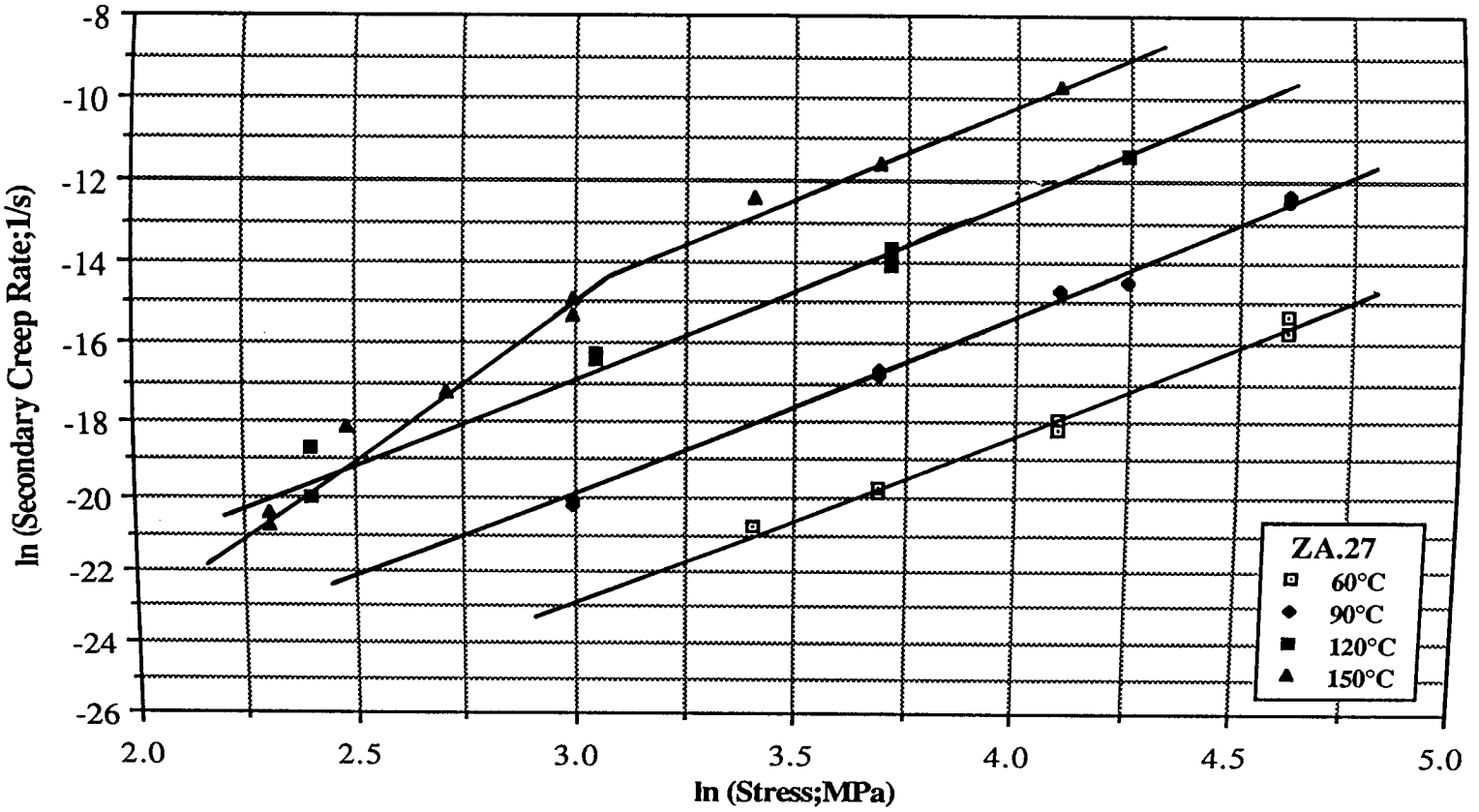

Figure 58. Variation of secondary creep rates of the alloy ZA.27 with applied stress at different temperatures.

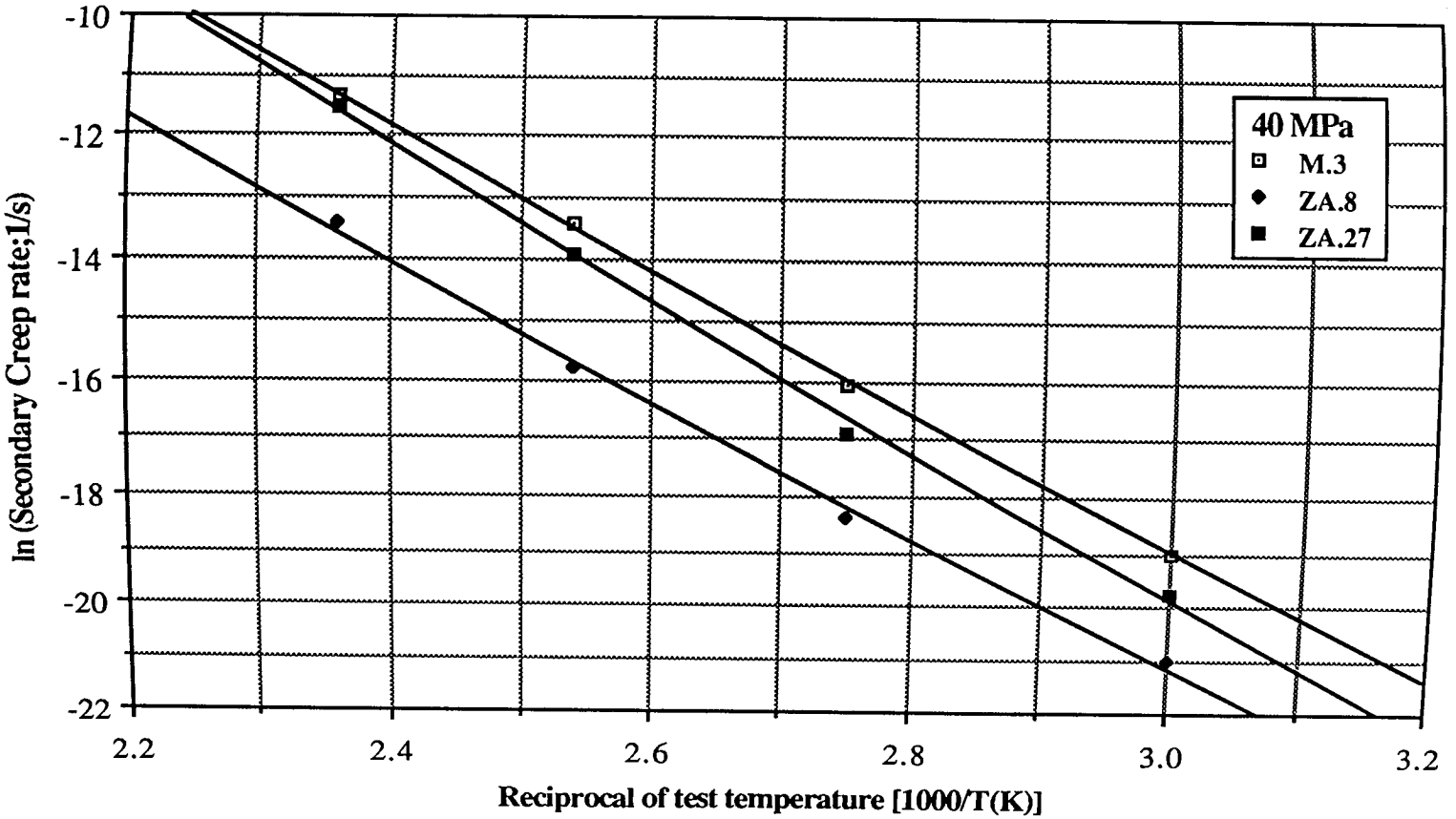

Figure 59. Variation of secondary creep rates of the alloys with the reciprocal test temperatures at 40 MPa.

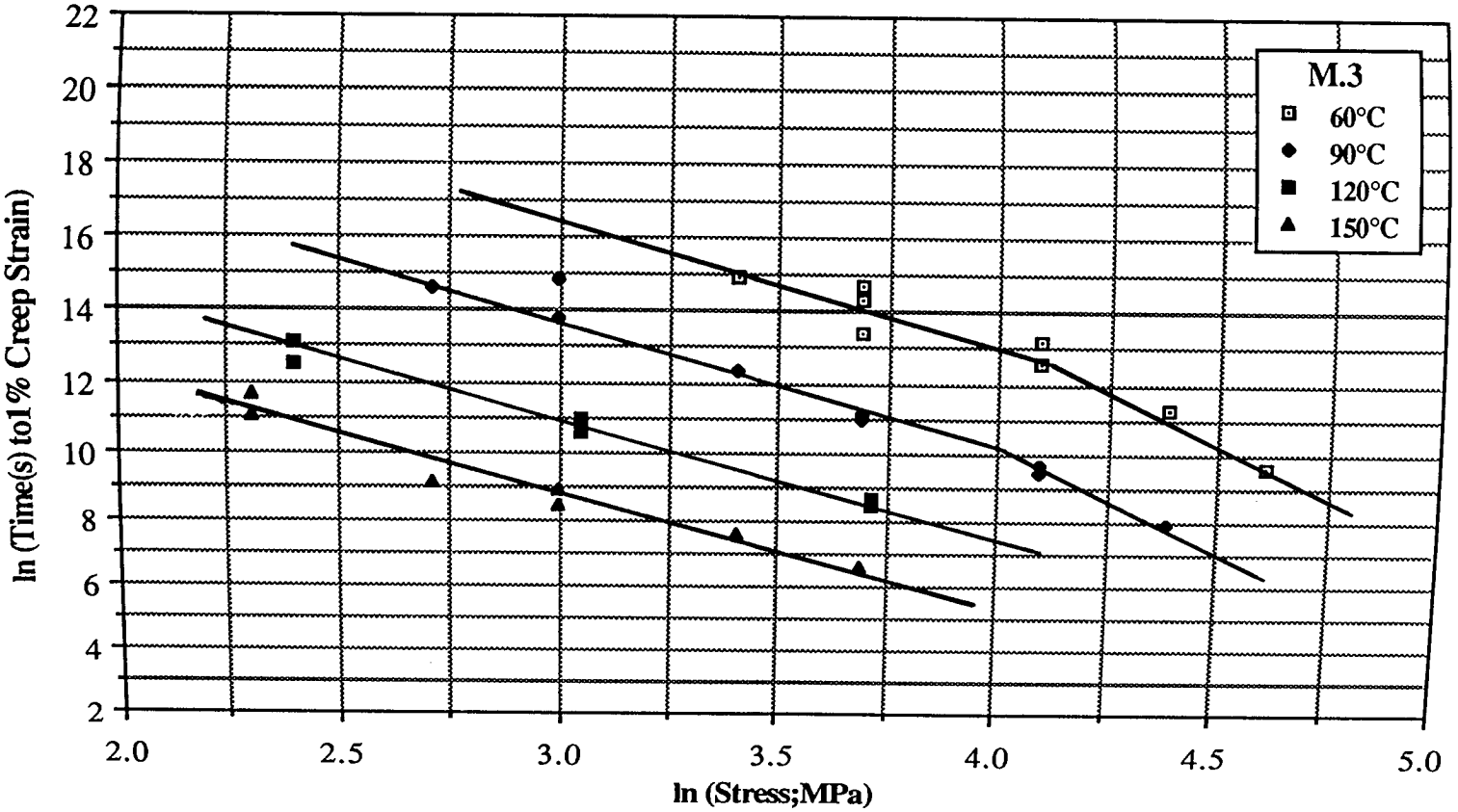

Figure 60. Variation of time to 1% creep strain with applied stress at different temperatures for alloy M.3.

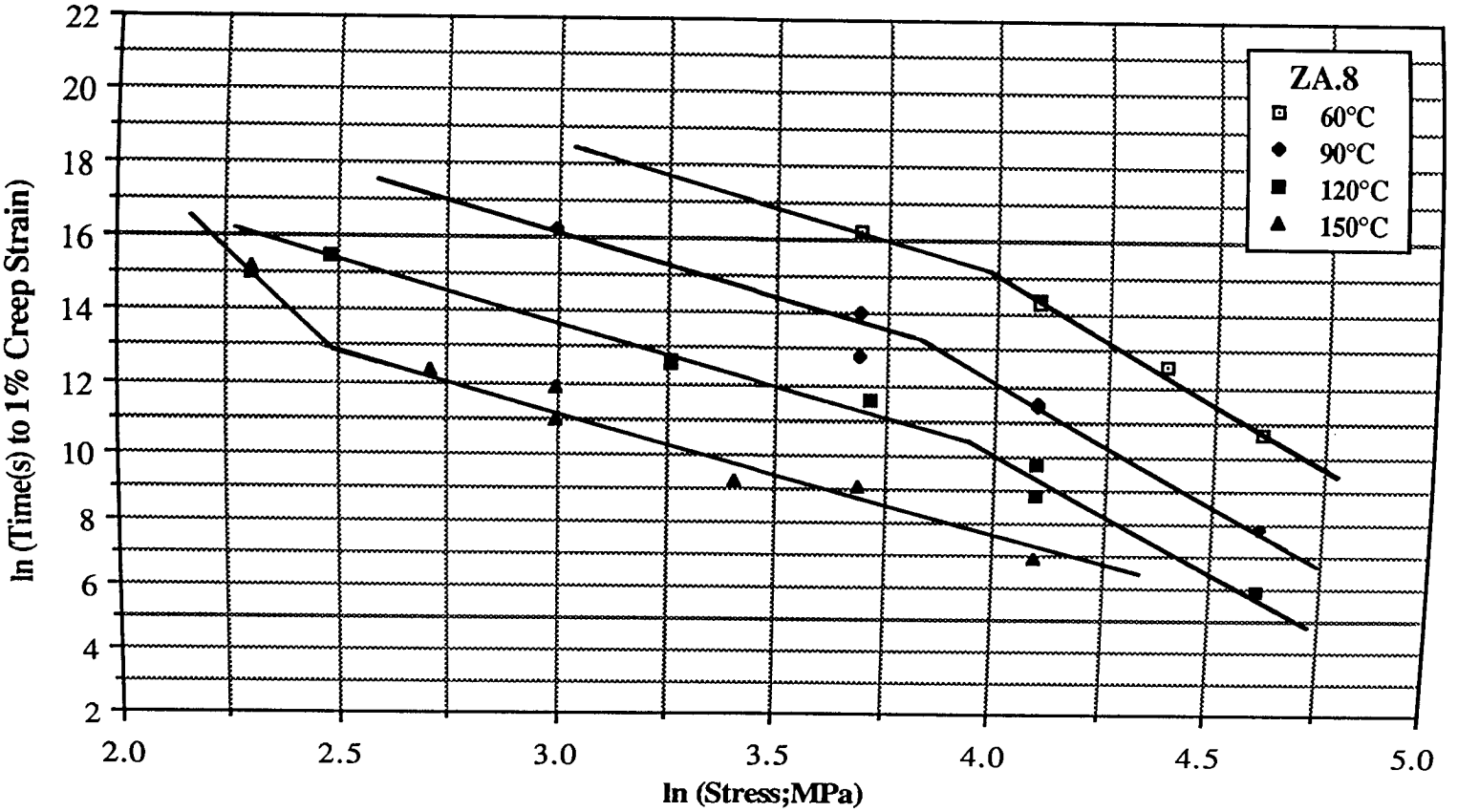

Figure 61. Variation of time to 1% creep strain with applied stress at different temperatures for alloy ZA.8.

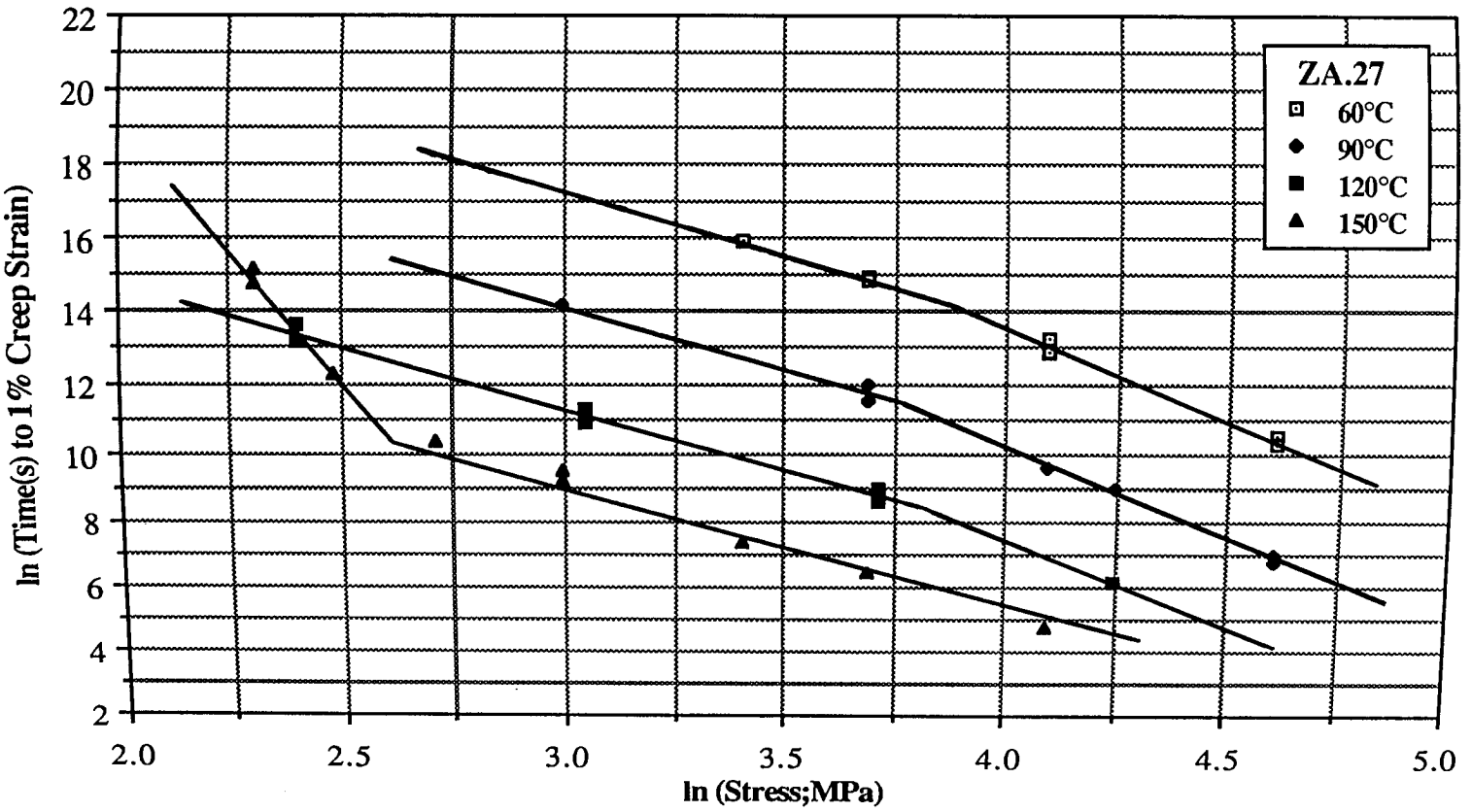

Figure 62. Variation of time to 1% creep strain with applied stress at different temperatures for alloy ZA.27.

4.3 Metallography of the commercial alloys Mazak.3, ZA.8 and ZA.27

The contrast in all the electron microscope images depends almost entirely on the average atomic number of the different phases present. Thus, in the following back-scattered SEM micrographs, zinc-rich phases appeared light and aluminium rich phases dark, since the zinc-rich phase with higher atomic number had more electron scattering power and gave rise to a greater number of back-scattered electrons than that of the aluminium-rich phase with lower atomic number, although the shade of contrast could be adjusted by electronically varying the sensitivity of the electron detector to the atomic number. However, in the following TEM micrographs, contrast is dominated by orientation and foil thickness variations, and atomic number effects are less important , The zinc-rich phases appeared dark and the Al-rich phases light in general due to the thickness differences resulting from the preferential thinning of phases when preparing foils. In the case of identification of small particles and precipitates, the other contrast mechanisms such as contrast due to the matrix being in diffracting orientation when the particles were not (or vice-versa), and local diffraction contrast changes due to coherency strain fields were also operative.

4.3.1 Alloy Mazak 3

The as-cast structure of alloy Mazak 3 is shown in *Figures 63, 64 and 65* at three different magnifications. The structure of the alloy was heterogeneous and consisted of a few large and numerous small primary Zn-rich (η) dendrites surrounded by a relatively small volume of lamellar eutectic matrix. Also associated with the hypo-eutectic η particles were many small, dark particles of the Al-rich former β phase. The whole structure was very fine, the average size of the primary particles was about 13 μm and the eutectic pools 20 μm. The development of the dark, Al-rich particles on the primary η shown at higher magnification in *Figure 64* indicates that this phase was eutectic β, nucleated on the primary η at high undercoolings. β is unstable below about 275°C and decomposes into Zn-rich η and Al-rich α phases. *Figure 65* shows

that the β in both the particles and the larger portion of the β constituent of the lamellar matrix were clearly decomposed.

TEM micrographs of small primary η particles set in the eutectic are shown at low magnifications in *Figure 66* and at high magnifications in detail in *Figures 67 and 68 (a)*. The solid solubility of aluminium in zinc is very little at room temperature and excess aluminium is removed by precipitation of the aluminium-rich phase (α) in zinc matrix. These three figures clearly show the precipitation of excess aluminium in primary η particles from different zones.

From the figures it appears that the precipitates have one habit in respect to the zinc matrix. Corresponding SADP's were taken to reveal the orientation relationship between the matrix and precipitates and one is shown in *Figure 68(b)* which was taken from the area shown in *Figure 68 (a)* and clearly showed the reflections of the zinc matrix with a beam direction of $[1\bar{2}10]$. However, as seen from the pattern, double diffraction effects were very prominent and it was not possible to identify the reflections from the precipitates in the course of this work.

In addition to the small dark Al-rich, former β particles associated with the primary η particles *(Figures 63 to 65)*, thin "haloes" of the eutectic Al-rich phase (α) can be seen in *Figures 66 and 67*. These were probably due to the process removing the excess aluminium from the supercooled liquid before normal eutectic solidification took place.

The morphology of the eutectic is shown in detail in *Figures 69 and 70*. Here, it appeared that the eutectic first grew asymmetrically to form irregular ribbon-like lamellae which acted as nuclei for further growth of irregular lamellae in a complex three-dimensional morphology. On cooling through the β-transformation the lamellae had broken up into strings of α particles, the zinc portion of the eutectoid adding on to the matrix phase.

STEM analyses which were carried out on different areas of the present phases are marked on TEM micrographs and the results are listed in *Table 10*. They show that all phases had decomposed into phases with the equilibrium compositions corresponding to the α and η phases of the binary Zn-Al system.

Table 10 shows an appreciable amount of copper equally distributed in zinc-rich phases, but a little lower in aluminium-rich phases. Although some small amount of copper was expected in impurity levels in this alloy, higher amounts quoted in the table were probably due to the error introduced by the background fitting process to the characteristic peaks of the elements. In the case of magnesium, the same problem was encountered during analyses, due to the small amount present. However, in all analyses carried out in this work, the magnesium content was consistent, with almost the same amount in primary and eutectic zinc-rich phases, but a much higher amount in aluminium-rich phase. Therefore, the majority of the magnesium present in the alloys must have been in solid solution in the aluminium rich phase.

Table 10. STEM microanalysis of the phases of alloy M.3.

Alloy : M.3	**Area marked in Figure ( )**	**Zn (%)**	**Al (%)**	**Cu (%)**	**Mg (%)**
Primary Particle (Matrix)	1 (67)	98.90	0.30	0.53	0.27
Eutectic (")	2 (70)	98.72	0.39	0.60	0.29
Eutectic α - lamellae	3 (70)	14.22	84.13	0.46	1.19

Figures 71 to 73 show the structure of the alloy Mazak 3 creep tested to failure at 40MPa and 120°C. Extensive plastic flow and cavities were observed in this alloy after the tests. Cavities of various sizes were found in primary particles as shown in *Figure 71* and failure eventually occurred by loss of external section particularly in necked regions where growth and coalescence of the cavities were greatest. However, as *Figures 72 and 73* show, cavities were not always present in all primary particles,

and if present were distributed randomly, indicating that cavities formed in certain primary particles with a particular orientation with respect to the tensile stressing direction.

The figures also reveal the effect of creep on the coarsening and elongation of primary particles, which occured to some extent in a relatively short time (~20 hrs) during the experiment. The most significant effect of creep, on the other hand, was the growth of precipitates in the primary particles, which can be noticed even in SEM micrographs in *Figure 72* at a low magnification.

The TEM micrographs shown in *Figures 74 and 75* clearly revealed that growth was in one direction and occurred by lengthening of the precipitates rather than thickening, indicating a low-mobility planar interface on the broad faces of the precipitates, but high-mobility incoherent edge advancing faster to produce high length-to-width shape.

Also evident in the figures was that the matrix dislocations had formed a dislocation substructure *(Figure 74)* and others were associated with the interphase grain boundaries *(Figure 75)*.

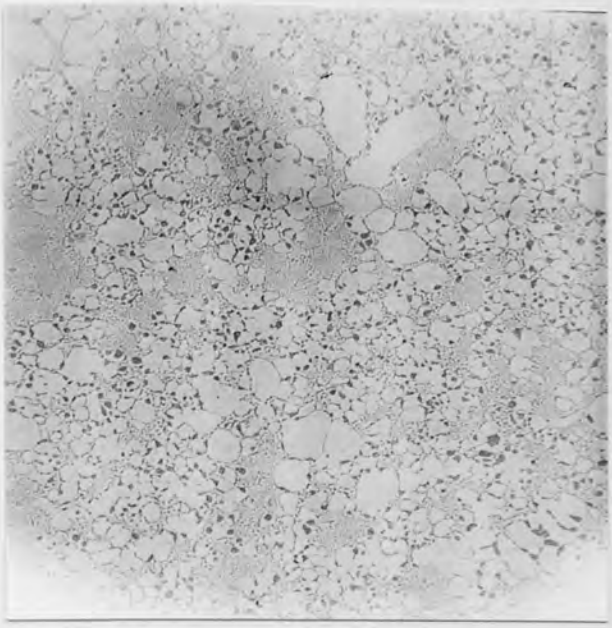

Figure 63. SEM. As-Cast structure of Alloy M.3 at low magnification, showing primary η particles and eutectic.

(365x)

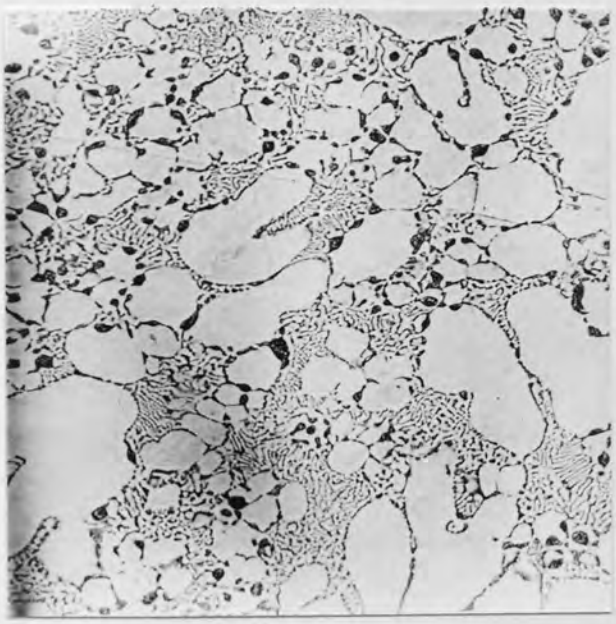

Figure 64. SEM. As-Cast structure of Alloy M.3 at medium magnification, showing eutectic β formed on primary η particles.

(730x)

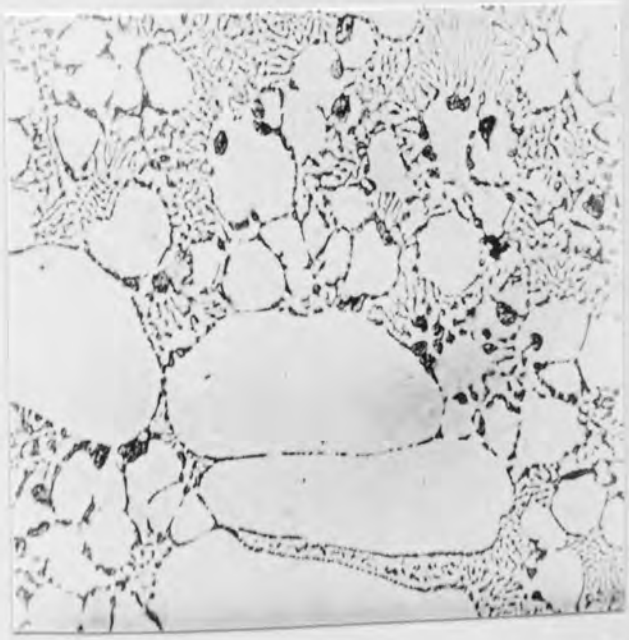

Figure 65. SEM. As-Cast structure of Alloy M.3 at high magnification.

(1460x)

Figure 66. TEM micrograph of small primary η particles set in the eutectic matrix.(11250x)

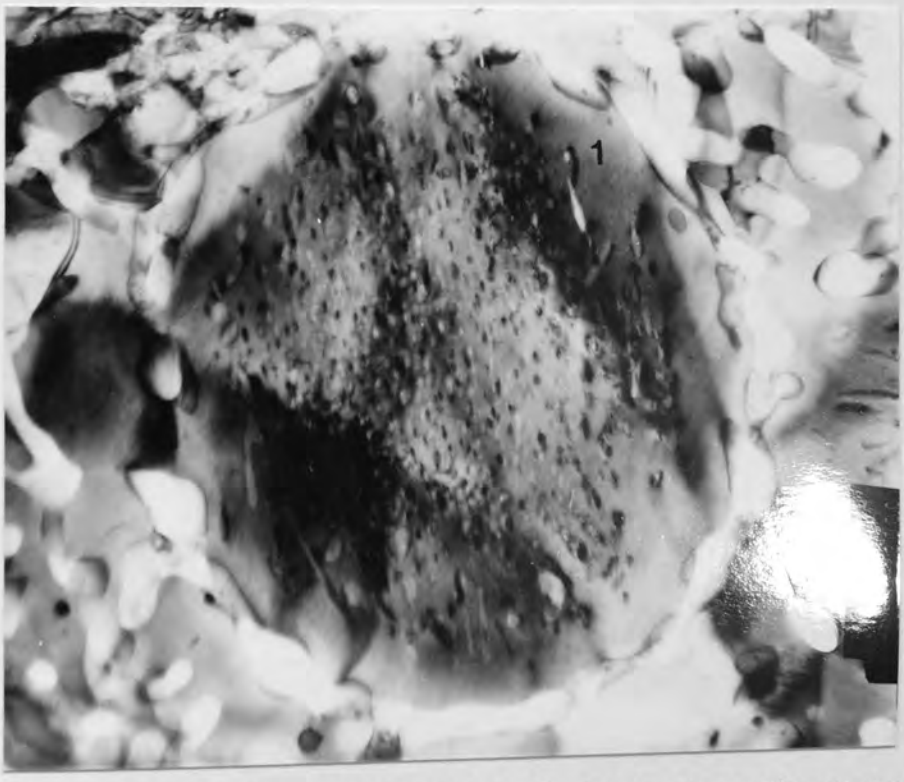

Figure 67.TEM. Precipitation of Al-rich phase a in a primary η particle surrounded by a thin aluminium rich eutectic "halo"(27250x)

(a)

(b)

Figure 68. (a) TEM micrograph of Al-rich precipitates in a primary η particle in detail.(51750x)
(b) SADP taken from area (a), consisting of the reflections $[1\bar{2}10]$ *zone of hcp zinc matrix.*

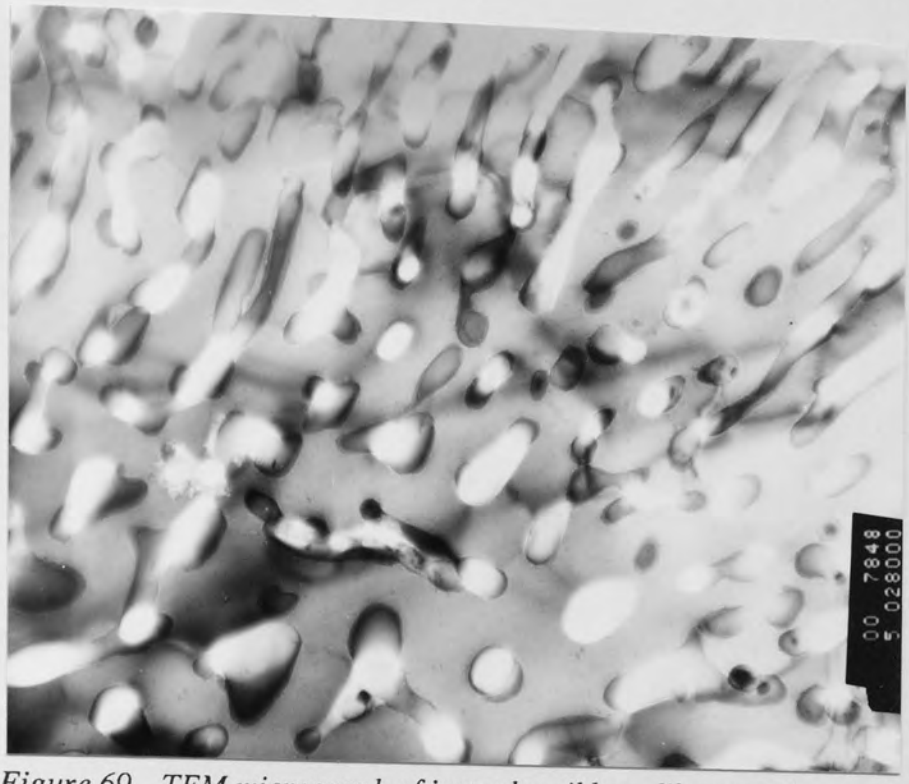

Figure 69. TEM micrograph of irregular ribbon -like eutectic morphology in the alloy M.3.(31500x)

Figure 70. TEM. Branching of eutectic in a complex three-dimensional morphology.(51750x)

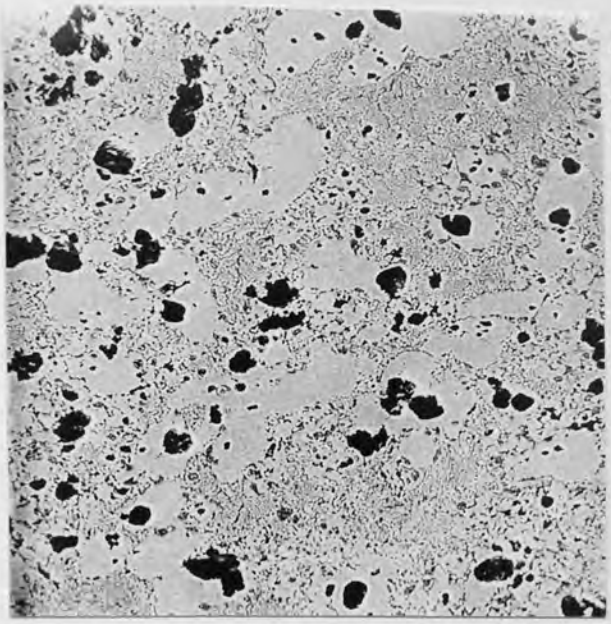

Figure 71. SEM micrograph of alloy M.3 tested at 40 MPa and 120°C, showing cavities formed randomly within the primary η - particles.

(400x)

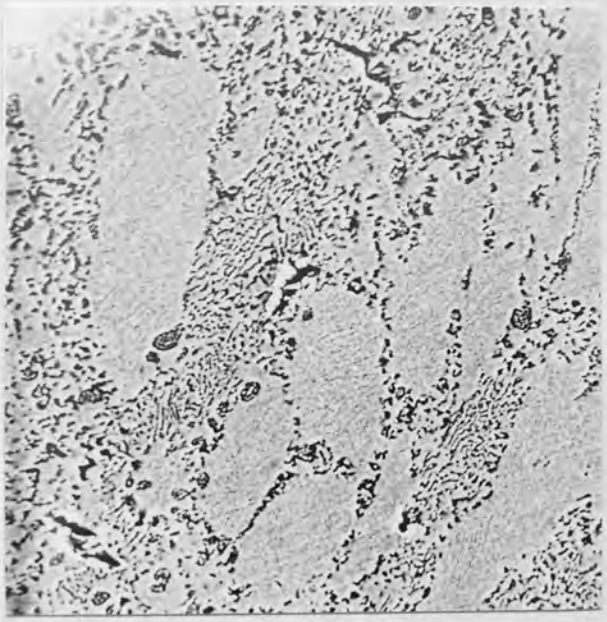

Figure 72. SEM. Alloy M.3 tested at 40MPa and 120°C, exhibiting deformation of η particles without cavitation.

(825x)

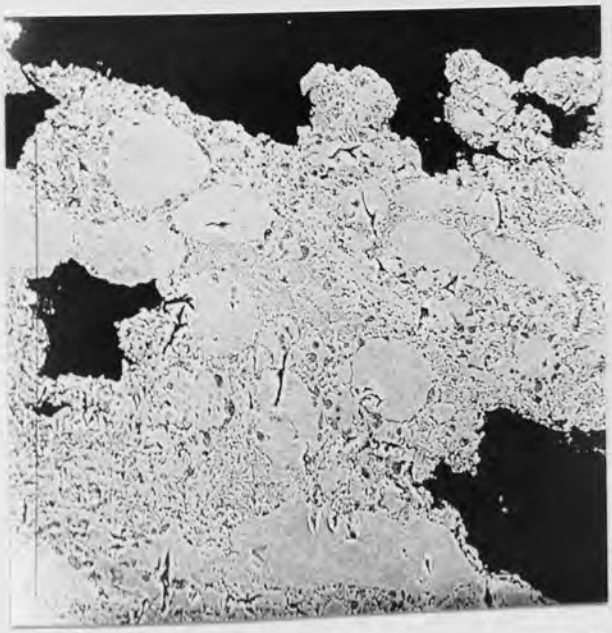

Figure 73. SEM. Creep fracture of alloy M.3 at 40 MPa and 120°C.

(410x)

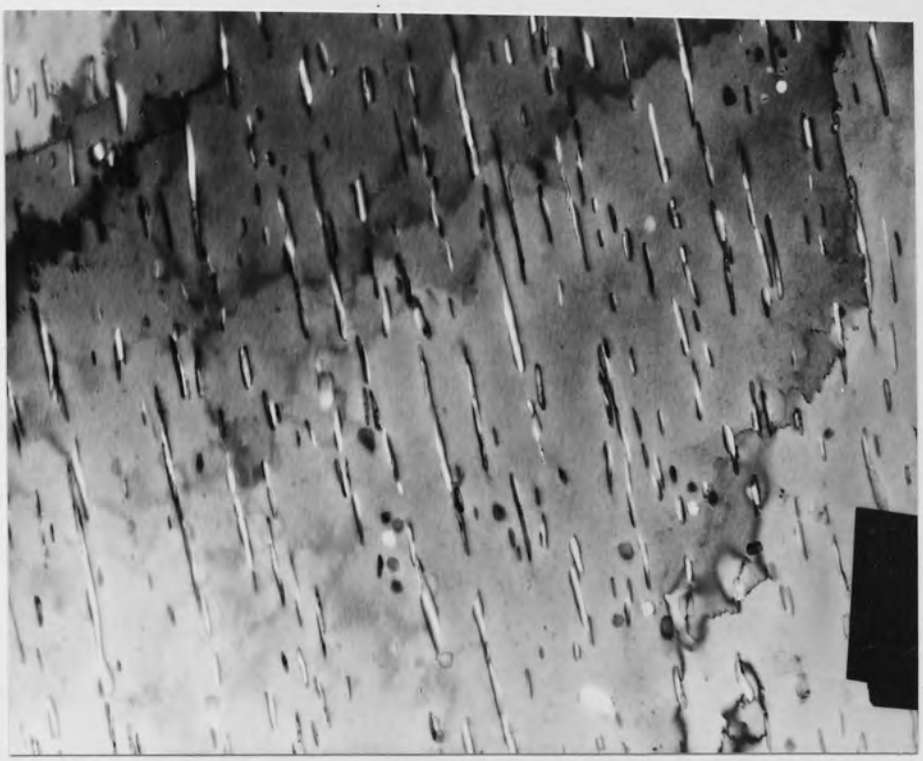

Figure 74. TEM micrograph of alloy M.3 tested at 40 MPa and 120°C, showing growth of aluminium-rich precipitates in high length-to-width shape in the primary η - dendrite.(14625x)

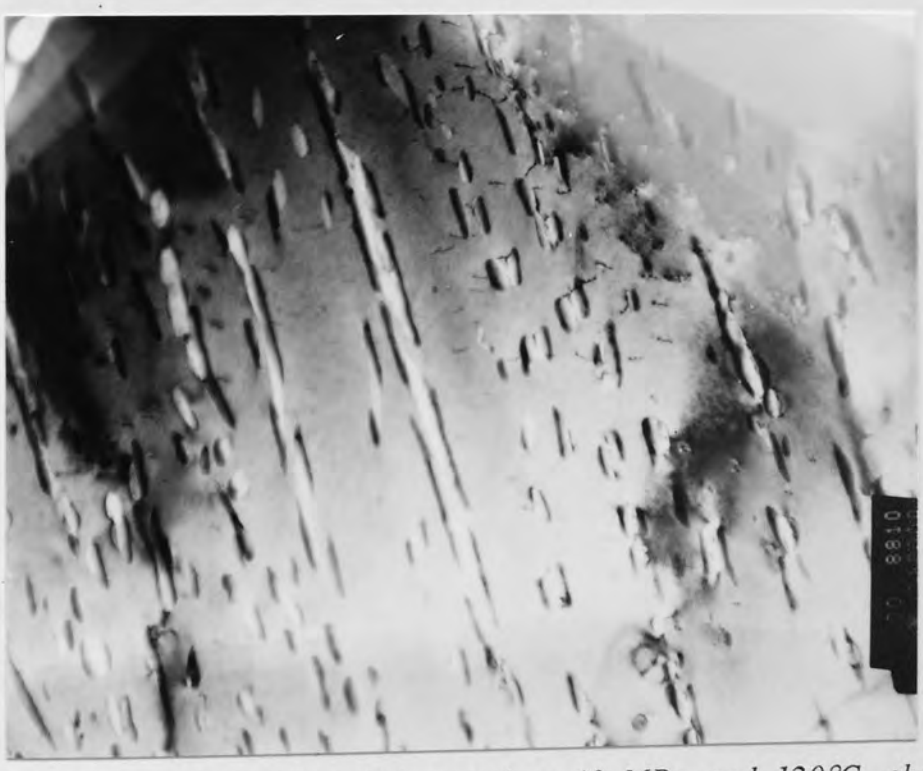

Figure 75. TEM. Alloy M.3 tested at 40 MPa and 120°C, showing dislocations in the zinc matrix attached to the phase boundaries in the primary η - particle.(19125x)

4.3.2 Alloy ZA.8

The as-cast structure of the alloy ZA.8 is shown in *Figures 76 to 78* at low to high magnifications, respectively. Here primary phase was β set in an eutectic matrix *(Figures 76 and 77)*. The scale of the structure was similar to that of alloy Mazak 3 with more uniformly distributed primary β particles. Decomposition of β particles showed two distinct morphologies *(Figures 77 and 78)*; well developed lamellar form usually in the central portion of the grains, surrounded by a rim of coarser mixture of the phases and, less frequently, only a coarse mixture of the phases. Also present in this alloy were a number of η particles of similar size to the primary β. These are thought to be eutectic η formed in highly-supersaturated zinc-rich liquid at temperatures below the eutectic temperature during rapid cooling. "Haloes" of η phase around β dendrites were also observed, as seen in *Figure 77*. In this case, they were much thicker than those of β around the primaries in the alloy Mazak 3. This was probably due to the higher undercooling applied to the alloy ZA.8 from the melt, since the casting temperature of this alloy is usually 15-30°C higher than that of alloy Mazak.3.

The as-cast structure of the alloy ZA.8 was also investigated in more detail by TEM. *Figure 79* shows the general structure of the alloy at low magnification in reverse contrast to that appearing in SEM micrographs.

Even at a very low magnification in this figure it clearly appeared that the lamellar morphology of the eutectic was somewhat different than that of the alloy Mazak 3. As seen more clearly in *Figure 80*, aluminium lamellar arms were more irregular and shorter and each ribbon of aluminium lamella enclosed a small dark particle of a different phase. These were of two types, usually as round particles with a diameter between 350 to 2000Å and less frequently as elongated shapes. STEM analysis, carried out on different phases present in this alloy and listed in *Table 11*, revealed that these small particles had a composition with 11% Al which did not correspond to

any equilibrium phases in the binary Zn-Al system.

Although the existence of transitional metastable phases of relatively short life duration had been reported in the binary Zn-Al system with high aluminium content (Section 2.6.1), observation of such a phase in this alloy which had been naturally aged at room temperature for a period of more than 5 years[1], revealed a strong metastable nature of the structure that was almost impossible to decompose at low temperatures.

It had been proposed[78,80] that, in the low temperature ($\alpha + \eta$) region of the zinc-aluminium binary system, two different metastable states could be formed in the areas bounded by extensions of the solubility limits of the regions ($\alpha + \alpha'$) and ($\alpha + \beta$) to the low temperature range. (See *Figure 19*).

Judging from the analyses obtained, the metastable phase observed in the alloy ZA.8 was in accordance with that bounded by the extension of the solubility limit of the ($\alpha + \beta$) boundary to room temperature at the zinc-rich side of the system. This also created a base for justification of the fact that the aluminium amount detected by STEM analysis *(Table 11)* in the aluminium-rich lamellae surrounding these metastable phases was higher (22%) than that expected from the equilibrium composition at room temperature, but in accordance with the extension of the solubility limit of the ($\alpha + \beta$) region to the aluminium-rich side of the system.

These facts indicated that the β in the eutectic had not decomposed into the equilibrium phases of the binary system. The reason for this at this stage is not known, but STEM analyses revealed that the metastable phase contained about 1.9% Cu. As shown previously, these metastable phases were absent from the eutectic of the alloy Mazak 3 with no copper, and, as will be shown later, were present in large quantities in the alloy ZA.27 with high copper, which suggests that copper has the primary effect of delaying the decomposition of these metastable phases at low temperatures.

[1]All alloy stocks used for preparation of thin foils were approximately 5 years old.

Figures 81 and 82 show the CBDP's of the aluminium-rich phase α in the eutectic, with the beam direction of [110], which yields a perfect symmetry of fcc structure of α-phase. The lattice parameter calculated by using an internal calibration method was found to be a little smaller than that of pure aluminium, as expected in the α region, since the lattice parameter of aluminium decreases in the α and β regions with increasing zinc content.

Figure 83 shows the CBDP of the small metastable phase with the same beam direction [110] to the α phase. Although the pattern seems to be yielding the reflections of the $\langle 110 \rangle$ zone of the reciprocal lattice of the fcc structure, a careful examination showed that fcc lattice was distorted along one of the closed packed atomic planes $\{111\}$, leading to a rhombohedral structure, and calculation of the interplanar spacing within the error of measurements confirmed that this was indeed a rhombohedral α''_m -phase with lattice parameters similar to those reported in earlier work[65] : a = 3.992Å; $\alpha = 91.36°$.

Further STEM analyses carried out in several different areas in the eutectic zinc matrix showed a high copper content with a mean value of about 3.4%. This observation led to one of the most exciting developments of this work. Tilting of the foil of such a eutectic area shown in *Figure 80* for example, showing unequal darkening of zinc matrix, clearly revealed heterogeneously nucleated precipitates in very large densities covering the entire matrix as shown in *Figures 84 and 85*.

The presence of the precipitation in such morphology in zinc-aluminium alloys had not been known previously. In order to identify these, considerable amounts of painstaking work in bright and dark fields with corresponding SADP's was carried out. *Figures 86 to 89* show the SADP's of the eutectic matrix taken from the major poles, $\langle 0001 \rangle$, $\langle 01\bar{1}2 \rangle$, $\langle \bar{2}4\bar{2}3 \rangle$ and $\langle 01\bar{1}1 \rangle$, respectively. All of these patterns

showed hcp symmetry corresponding to the zinc matrix, but failed to reveal any extra reflections of another phase. The extra spots which usually appeared around the main reflections of the zinc matrix were shown, by dark field image contrast, to be due to the double diffraction phenomenon. However, diffraction patterns obtained from $[0\bar{1}10]$ and $[1\bar{2}10]$ zones revealed streaked reflections around the zinc matrix spots. These are shown in *Figures 90 and 91* with their indexing, respectively. Both patterns showed two sets of streaked reflections with the same symmetry deviated by the same rotating angle of 4.5° and 5°, respectively, indicating two variant precipitate habits. For the sake of clarity, only one set of reflections was indexed in Figures 90 (b) and 91 (b). In both figures it was found that streaked reflections corresponded to the hcp ε-phase ($CuZn_4$) with beam directions parallel to $[0\bar{1}10]$ and $[1\bar{2}10]$ respectively.

As seen in *Figure 92*, a dark field image of the area shown in *Figure 92 (c)* obtained from (0002) streaks (circled in *Figure 92 (b)*) of the corresponding diffraction pattern from a $\langle 0\bar{1}10 \rangle$ zone highlights two sets of precipitates lying apparently parallel to two variants of matrix $(2\bar{1}\,\bar{1}\,\bar{2})$ planes.

So far, the orientation relationship between the zinc matrix and ε-precipitates was determined from two diffraction patterns in respect to the incident beam as :

$$[0\bar{1}10]_{Zn} \,//\, [0\bar{1}10]_{\varepsilon} \text{ and } [1\bar{2}10]_{Zn} \,//\, [1\bar{2}10]_{\varepsilon}$$

In order to establish a unique relationship and examine the proximity of the planes of the phases, a stereographic projection was drawn, as shown in *Figure 93*. Here, the projection of ε-phase on (0001) was rotated through an angle of 4.5° clockwise about $[0\bar{1}10]$ and superimposed on a (0001) standard projection for zinc matrix . As seen from the projection, superimposing of $(01\bar{1}0)_{\varepsilon}$ on one of $\{01\bar{1}0\}_{Zn}$ -type planes exhibits a similar proximity of planes observed in diffraction patterns in *Figures 90 and 91* and yields orientation relationship of several parallel planes of the phases. Two sets of these parallel planes were selected to define a unique orientation

relationship as :

$$\begin{bmatrix} (01\bar{1}0)_{Zn} & // & (01\bar{1}0)_{\varepsilon} \\ (\bar{2}112)_{Zn} & // & (\bar{2}112)_{\varepsilon} \end{bmatrix}$$

but with $[0001]_{\varepsilon}$ 4.5° from $[0001]_{Zn}$.

In addition to the crystallographic information obtained, further information in respect to the shape of the precipitates was also obtained by the aid of the established stereographic projection in conjunction with the dark field image of the precipitates with the corresponding diffraction pattern.

From the dark field image (*Figure 92(c)*) which provides information regarding true precipitate size and shape, it appeared that precipitates were either needles or plate-like, about 20-30Å thick and 800Å long, parallel to $(2\,\bar{1}\,\bar{1}\,\bar{2})$ and $(2\,\bar{1}\,\bar{1}\,2)$ planes of Zn-matrix. On the other hand, diffraction patterns consisting of $[0\bar{1}10]$ zone (*Figure 90*) showed that the streak run towards the $(2\,\bar{1}\,\bar{1}\,7)$ and $(\bar{2}\,1\,1\,7)$ plane normal of the Zn-matrix. In view of the formation of diffraction patterns in reciprocal space, if a crystal is thin in a direction normal to the beam, streaks are expected in the diffraction pattern parallel to this direction, due to lower scattering intensity along this direction[148]. Thus, streaks observed in the diffraction pattern (*Figure 90*) indicated that the precipitates were plate-like with $(2\,\bar{1}\,\bar{1}\,7)$ and $(\bar{2}\,1\,1\,7)$ - habits.

On the basis of this evidence, if it is presumed that precipitates were plate-like, it should be expected that ε-phase would form on a particular habit plane along which the atomic planes facing each other across the matrix-precipitate interface would have very similar arrangements (i.e. coherent interface with minimum misfit).

In view of this argument, examination of planes on the great circle shown in stereographic projection (*Figure 93*), consisting of $\langle 2\,\bar{1}\,\bar{1}\,3\rangle$ zone provided a fact that the planes of both phases in that zone were parallel to each other within the accuracy of 1°. These exact parallelism is achieved by a rotation of one crystal relative to the other, away from a symmetrical orientation relationship. Thus all other sets of planes are made non-parallel, including the {0001} close-packed planes.

Differences in the interplanar spacings of the planes of two phases in that zone were also calculated as follows:

$(hkl)_{Zn}$, ε	$\% \Delta \left[d(hkl)_{Zn} - d(hkl)_{\varepsilon} \right]$
$(01\bar{1}0)$, $(0\bar{1}10)$	2.8
$(\bar{1}3\bar{2}1)$, $(\bar{1}\bar{2}31)$	2.2
$(\bar{1}2\bar{1}\bar{1})$, $(\bar{1}\bar{1}21)$	1.4
$(\bar{1}101)$, $(\bar{1}011)$	0.68
$(\bar{2}112)$	1.44

The differences in decreasing order indicate decreasing misfit and, therefore, increasing coherency across the interface. Thus, it is very likely that the ε-phase would form and advance along the low energy coherent interface to produce thin plate-like shapes. Since the broad face of the plate known as the habit plane is defined by the matrix plane perpendicular to the planes across the interface, it can be seen from the stereographic projection that such an arrangement of the planes along the interface yields a habit plane of $(2\,\bar{1}\,\bar{1}\,7)_{Zn}$ which is in agreement with the direction of one set of the streaks of the precipitates parallel to the $(2\,\bar{1}\,\bar{1}\,\bar{2})_{Zn}$ plane normal. For the other set of precipitates parallel to $(2\,\bar{1}\,\bar{1}\,2)$ which produced streaks towards $(\bar{2}\,1\,1\,7)$ planes of the zinc matrix (*Figure 90*), another habit plane of $(\bar{2}\,1\,1\,7)$ can also be realised as one of the possible variants of the same type planes.

Decomposition of the primary β particles into final products with different morphologies is shown in *Figures 94 to 97*. *Figure 94* shows a small primary β particle decomposed into irregular lamellae. Well developed regular lamellar morphology was observed usually in the central portion of the β dendrites as shown in *Figures 95 and 96*. Here the average interlamellar spacing was 0.15 μm. A change in the morphology from a lamellar to a granular mixture of the phases towards the surfaces of the β particles was a peculiar feature of the decomposition. Besides, the occurrence of this granular product was often observed throughout the entire volume

of the β particles. *Figure 97* shows a mixture of the phases of this type in which granular η particles with average diameters of 0.2μm appeared to be embedded in the aluminium -rich α matrix. STEM analysis (*Table 11*) showed that both α and η lamellae from the decomposed β, in general, were in equilibrium, although some dark metastable particles as seen in *Figures 94 to 96*, similar to metastable α' observed within the eutectic α, were found within the α-lamellae. But, comparing 1 with 6 in *Table 11*, the aluminium content of these was found to be much higher with about 22.7% Al and the copper content was lower by about 0.5% at 1.4% This was also in accordance with the metastable extensions of the binary Zn-Al system, but in this case, bounded by the extension of the (α+α') region to low temperatures. Thus the metastable phase here was an analogue, not of the β phase but of the α' phase, due to the more aluminium-enriched nature of the primary particles than the eutectic β. This may also explain the lower copper content of the later phase since the β phase dissolves more copper than the α at high temperatures [59].

Table 11. Mean STEM microanalysis of the phases in the alloy ZA.8.

Area marked in Figure ( )	Zn (%)	Al (%)	Cu (%)	Mg (%)
1 (80)	86.8±0.7	11.0±0.7	1.9±0.6	0.3±0.2
2 (80)	22.1±2.9	75.2±3.2	2.0±0.2	0.7±0.1
3 (80)	95.8±1.2	0.5±0.3	3.4±1.2	0.4±0.1
4 (96)	16.2±5.7	82.3±5.8	0.8±0.1	0.6±0.0
5 (96)	95.0±1.1	1.1±0.9	3.3±0.1	0.4±0.1
6 (96)	75.7±4.9	22.8±5.1	1.4±0.2	0.1±0.1

In view of these evidences, it is believed that decomposition of β in this alloy involves two different transformation schemes, depending on the ratio of zinc-aluminium content it contains. Upon rapid cooling, first solidification would occur, with considerable undercooling, followed by retention of the high temperature β phase to

low temperatures, at which decomposition would then occur.

The β phase under equilibrium conditions would decompose into η and α at about 275°C. However if the decomposition were to occur at low temperatures where diffusion rates were small, it is probable that the cellular decomposition products would not be the same.

In the case of the aluminium-rich cores of the primary β, it is suggested that a lamellar or sub-lamellar product of η and transitional metastable α'_T was formed, due to the difficulty of reducing the zinc content of the aluminium-rich plates to that of α in one step. α'_T and α are crystallographically identical and differ only in chemical composition and thus lattice parameter, and α'_T is known to persist for a substantial time on low temperature ageing [65-67]. Since α'_T contains much more zinc than α, the η plates of the eutectoid mixture would be very thin.

Later, as a closer approach to equilibrium was made, the α'_T in contact with the η would have changed discontinuously into α since they are separated by a large miscibility gap at low temperatures. The obvious mechanism for this would be diffusion of zinc from the α'_T into the η plate, which would thus grow sideways, and the formation of an α layer adjoining it. The structures shown in *Figures 94-96* are considered to show a late stage in this process where the α'_T had been almost consumed and remained only as strings of elongated particles in the middle of the aluminium-rich lamellae.

For the case of the β lamellae or particles forming part of the eutectic, the process is essentially the same, but due to the higher zinc content of the β, the metastable phase formed in the cellular decomposition reaction would be the lower aluminium metastable phase indicated by extension of the (α+β) phase field to lower temperatures. Effectively this means the decomposition of β into η plus another, higher-aluminium version of β metastable phase at the transformation temperature.

It is important to realise that this mechanism depends on subtle alterations in the chemical composition of the alloys as a whole, and the phases formed in them on cooling. The Mazak 3 alloy, for example, containing no copper, did not show the presence of any metastable α'_T in the eutectic, and it is possible that some combination of copper and magnesium may be necessary to stabilise the α'_T phases sufficiently for the proposed mechanism to be possible. Thus an alternative to the proposed (α+β) products as the first stage in the eutectic β decomposition in ZA.8 is simply another (η + α'_T) where the composition of the α'_T is different from that formed from primary β due to the lower aluminium and increased copper content of the eutectic β phase.

Further evidence will also be presented in the case of alloy ZA.27 with higher copper content, in the next section.

SEM micrographs shown in *Figures 98 to 100* show the structure of the alloy after creep testing to the failure at 40 MPa and 120°C. As evidenced from the micrographs there was no significant cavity formation during the creep of the alloy, although a very little amount was observed rarely in interdendritic η areas. Nor was there a significant plastic flow. Brittle creep fracture usually occurred by loss of internal strength in the areas where a localised necking without significant elongation was induced. As seen from the figures, primary β particles did not change their shape much, although coarsening of fine decomposed products was observed to some extent, so that all the fine granular particles were converted into coarse concentric rims around the primary β with coarse (α+η) in the central portions. The fine lamellae were little altered. However, as seen from the TEM micrographs in *Figures 101 and 102*, which show the structure of the shoulder unstressed part of a sample creep tested at 10 MPa and 150°C, coarsening at 150°C for experiments of long duration resulted in significant growth of the precipitates in the eutectic, and it can be noticed that metastable phases in the α-lamellae in both eutectic and primary dendrites had decomposed completely

into the equilibrium phases.

Figure 103 shows the SADP with its indexing taken from the eutectic area shown in *Figure 102*, consisting of $[0\bar{1}10]_{Zn,\,\varepsilon}$ zone. Here, additional spots appeared in addition to those of zinc and ε-precipitates. The intensity of the latter was highly reduced. The additional reflections were found to correspond to rhombohedral T'-phase, which can be indexed according to the simpler structure in this case. Thus the zone axis of T' is shown as the $\langle 011 \rangle$, signifying that a four-phase reaction had occurred as a result of the long duration of the experiment (~40 days), according to the reaction sequence[59];

$$\alpha + \varepsilon \Leftrightarrow \eta + T'$$

with an orientation relationship consist with the approximation:

$$[0\bar{1}10]_{Zn} \,//\, [0\bar{1}10]_{\varepsilon} \,//\, [011]_{T'}$$

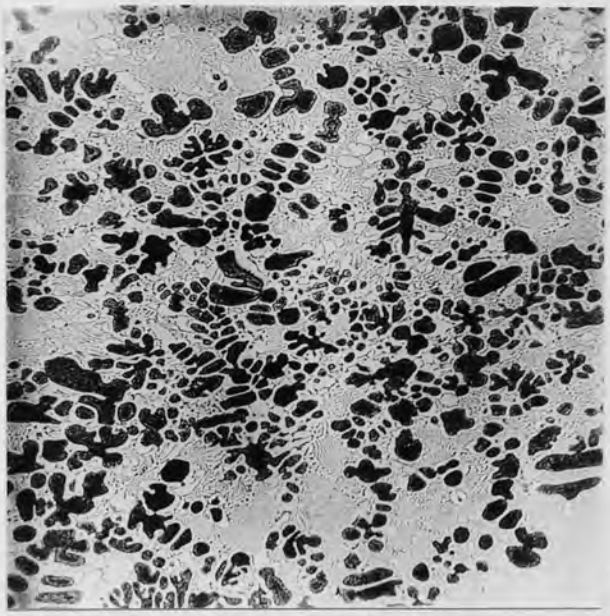

Figure 76. SEM. As-Cast structure of Alloy ZA.8 at low magnification, showing primary β particles in the eutectic matrix.

(365x)

Figure 77. SEM. As-Cast structure of Alloy ZA.8 at medium magnification, showing decomposed β particles surrounded by lamellar eutectic.

(1460x)

Figure 78. SEM. As-Cast structure of Alloy ZA.8 at high magnification, showing decomposition of β dendrites into fine lamellar and coarse granular mixture of the phases.

(3650x)

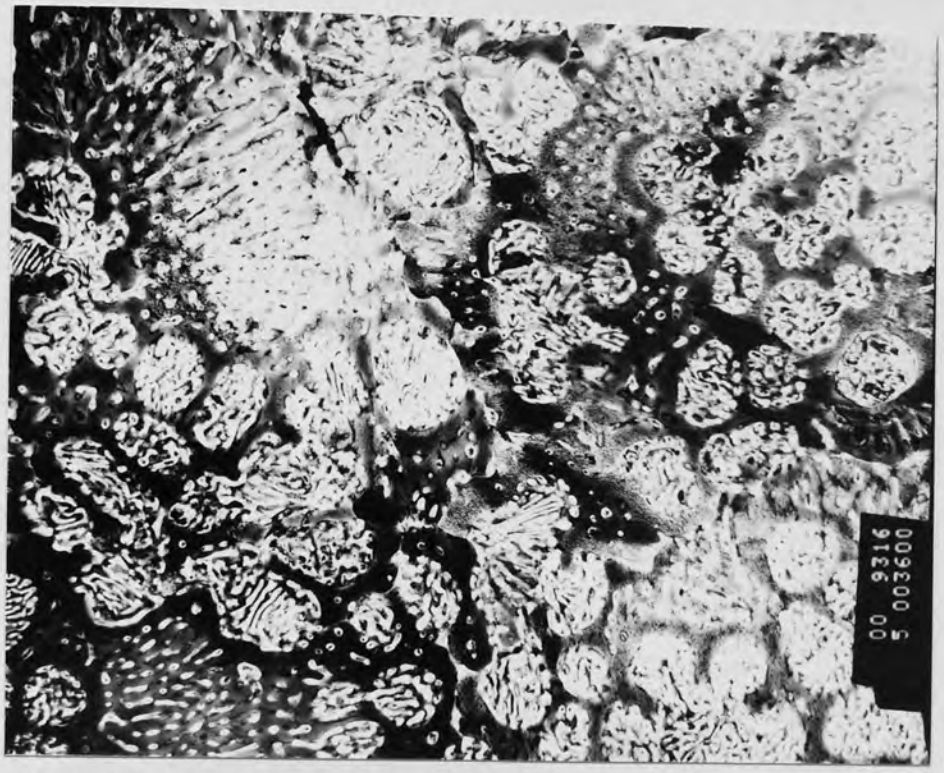

Figure 79. TEM micrograph of general structure of alloy ZA.8 (4050x)

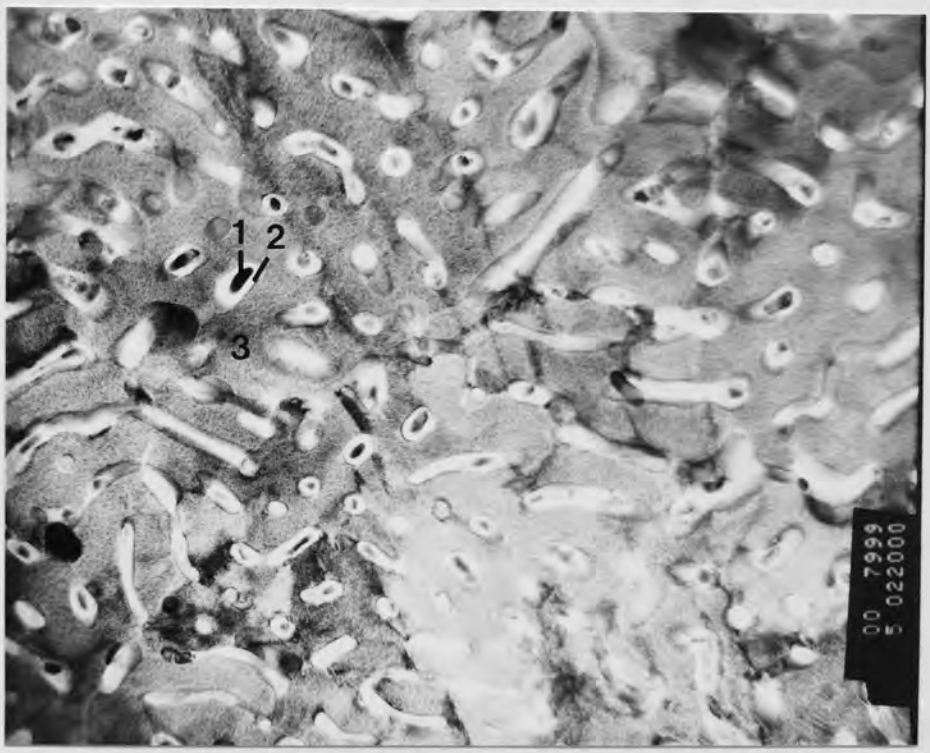

Figure 80. TEM. Eutectic in the alloy ZA.8 with irregular ribbon-like α- lamellae, enclosing a metastable phase.(24750x)

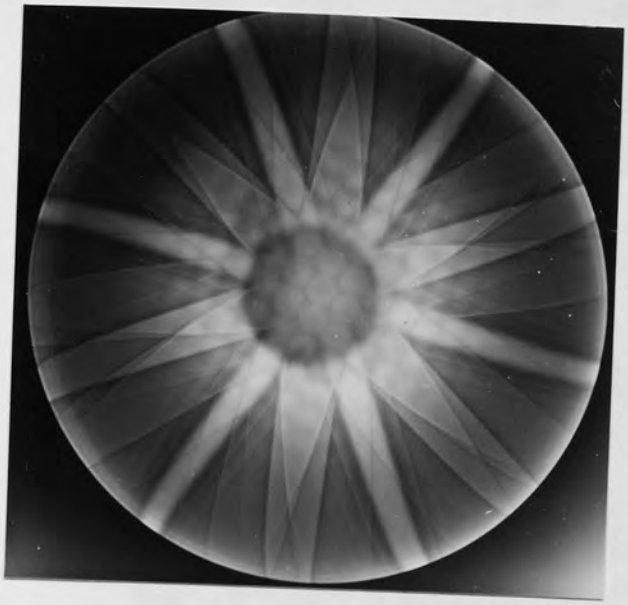

Figure 81. CBDP from eutectic Al-rich lamellar of alloy ZA.8. Beam direction is [110].

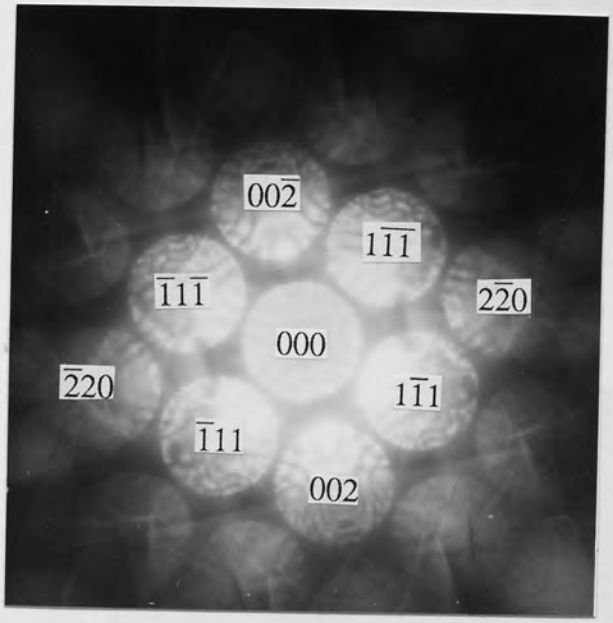

Figure 82. Same CBDP as above at high camera length, showing perfect fcc symmetry of α- phase.

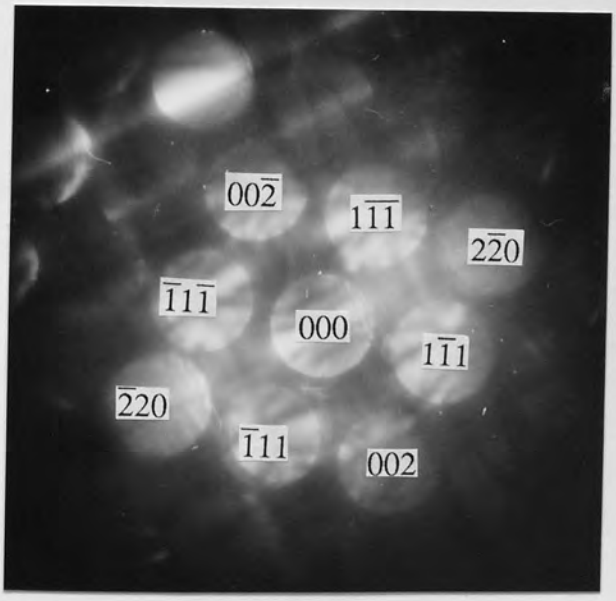

Figure 83. CBDP from the metastable phase, exhibiting a rhombohedral distortion of the fcc lattice, corresponding to the rhombohedral α''_m phase with beam direction [110].

Figure 84 TEM micrograph of eutectic in the alloy ZA.8, showing heterogenously nucleated precipitation of ε -phase in large densities covering the entire zinc matrix.(24750x)

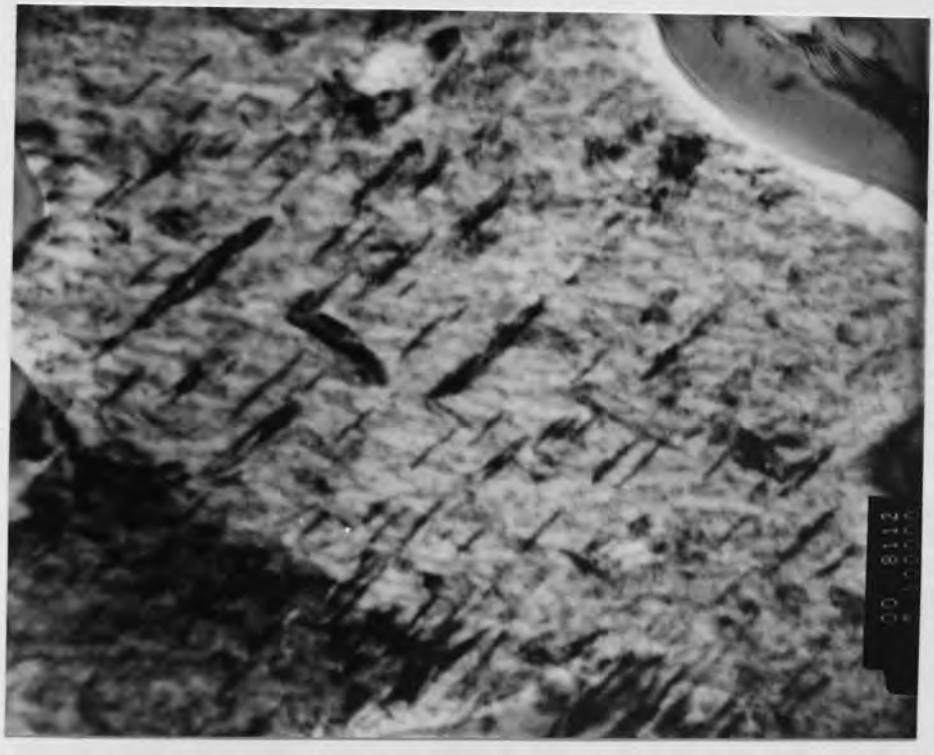

Figure 85. TEM. Precipitation of ε -phase in the eutectic at high magnification.(112500x)

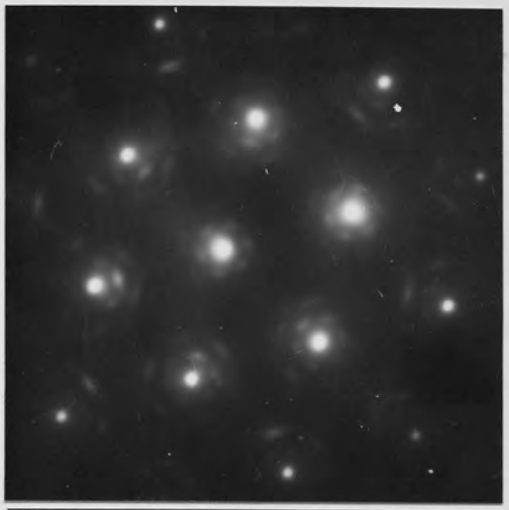

Figure 86. SADP from the eutectic in alloy ZA.8, consisting of [0001] *zone.*

Figure 87. SADP from the eutectic in alloy ZA.8, consisting of $[01\bar{1}2]$ *zone of hcp zinc matrix.*

Figure 88. SADP from the eutectic in alloy ZA.8, consisting of $[\bar{2}4\bar{2}3]$ *zone of hcp zinc matrix.*

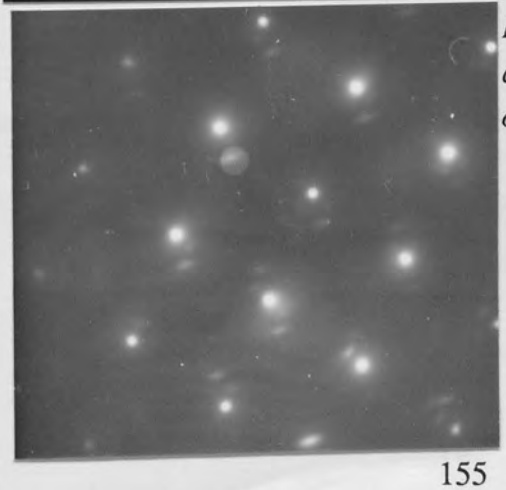

Figure 89. SADP from the eutectic in alloy ZA.8, consisting of $[01\bar{1}1]$ *zone of hcp zinc matrix.*

(a)

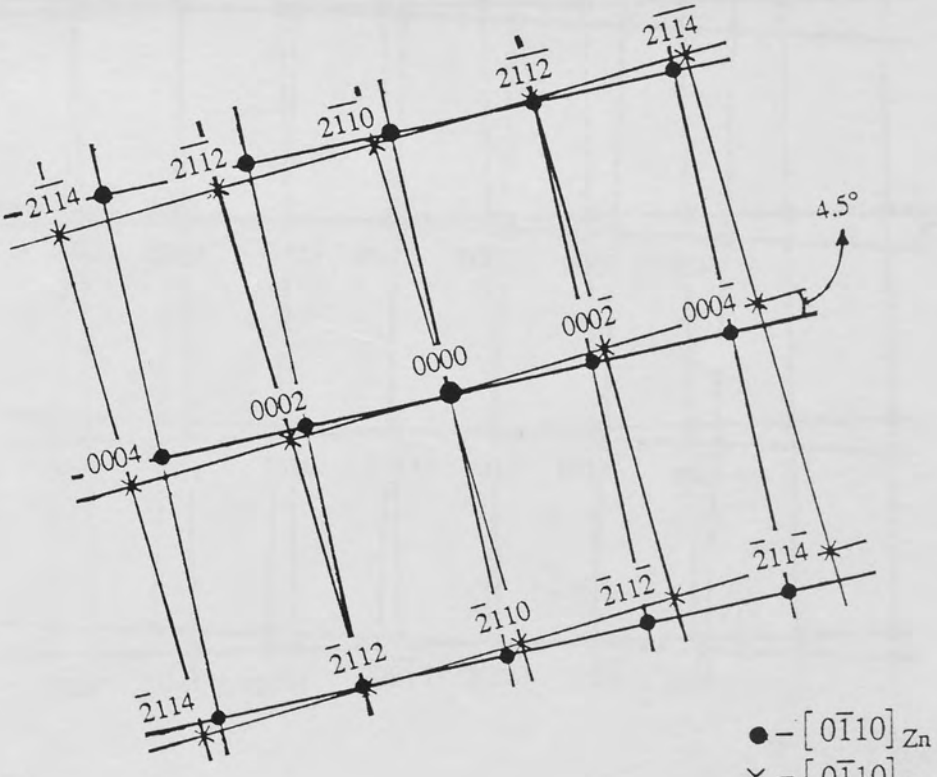

(b)

Figure 90. (a) SADP from the eutectic in alloy ZA.8, consisting of $[0\bar{1}10]$ *zone of hcp zinc matrix, showing streaked reflections of* ε *precipitates.*

b) Indexing of the above pattern.

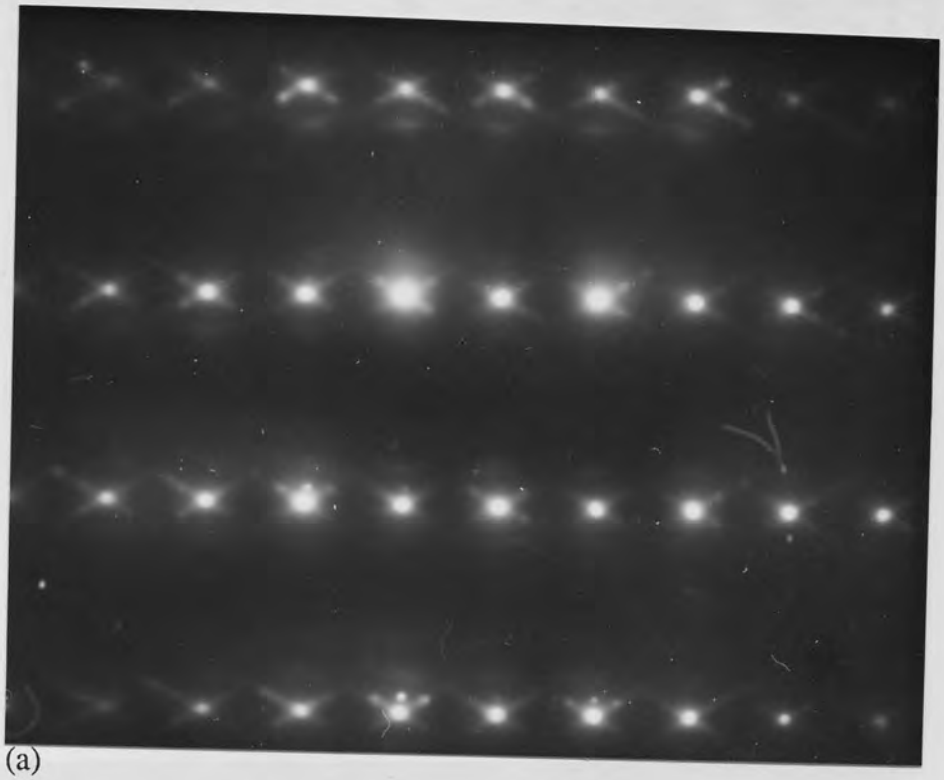

(a)

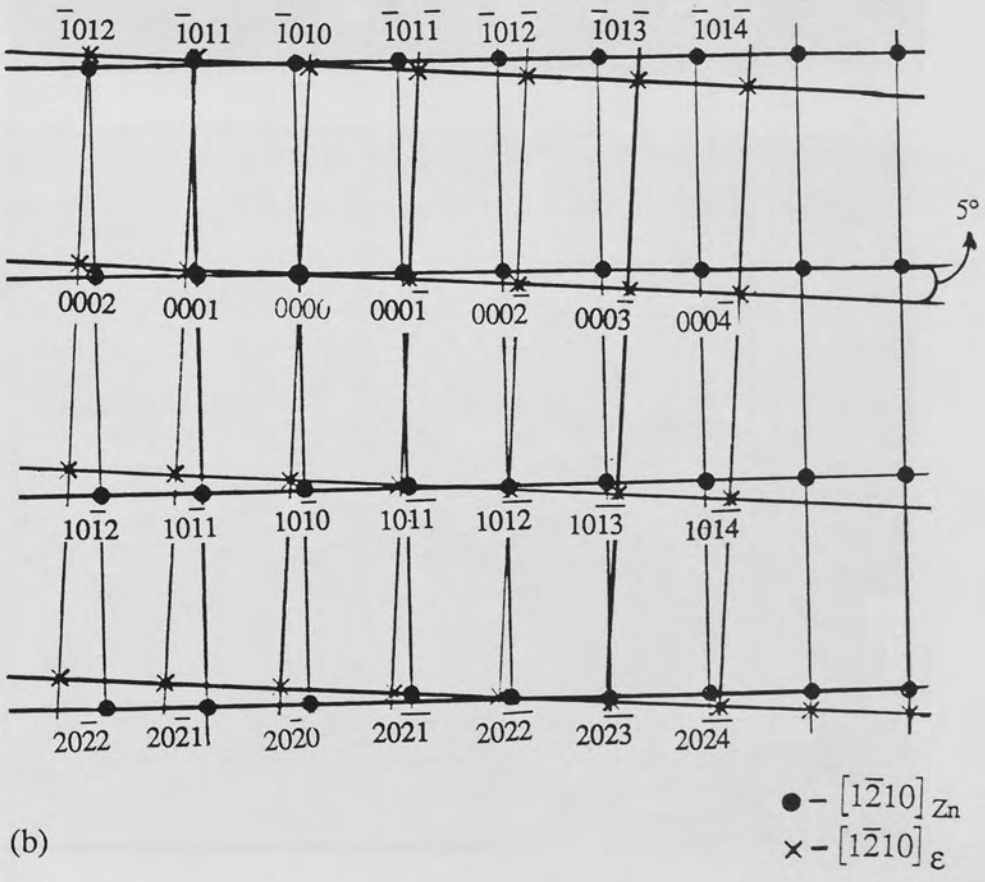

(b)

Figure 91. (a) SADP from the eutectic in alloy ZA.8, consisting of $[1\bar{2}10]$ *zone of hcp zinc matrix, showing streaked reflections of* ε *precipitates.*

b) Indexing of the above pattern.

(a)

(b)

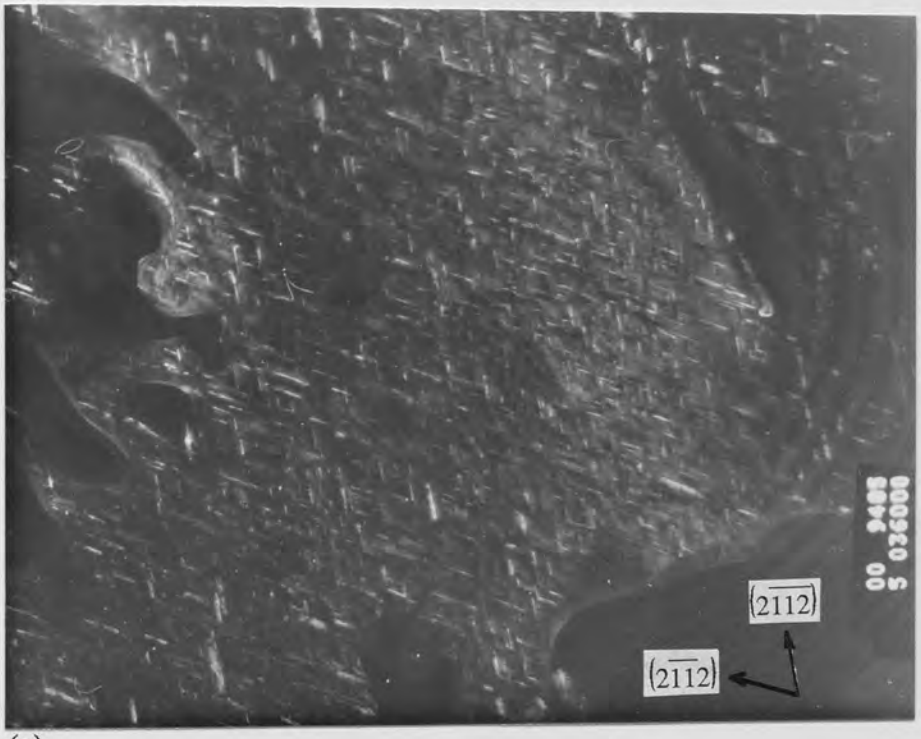

(c)

Figure 92. (a) Bright field image of the eutectic with ε -precipitates.(40500x)
(b) SADP of the area from the beam direction closely parallel to $[0\bar{1}10]$.
(c) Dark field image of the above area obtained from (0002) streaks (circled)

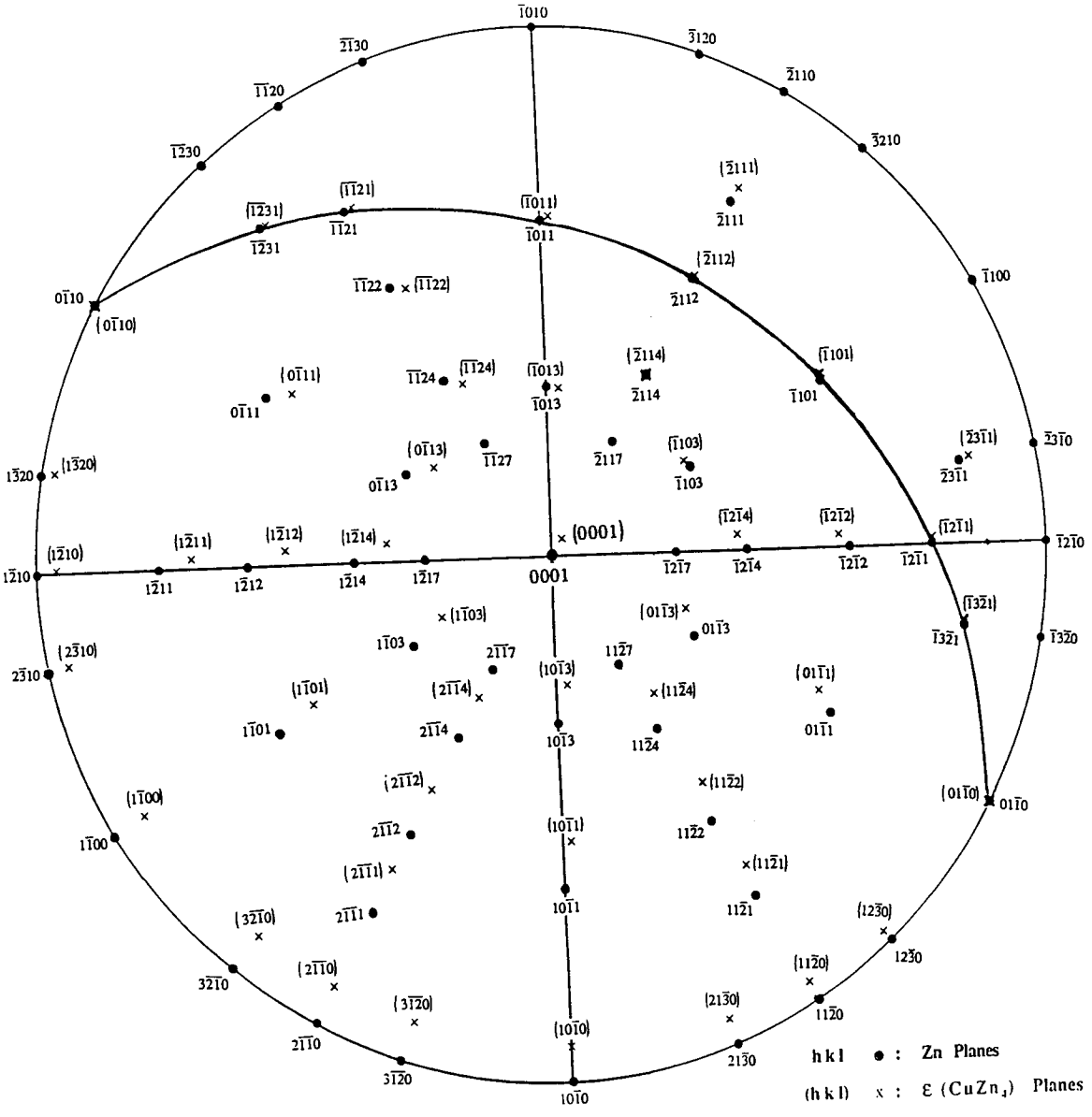

Figure 93. Stereographic projection of Zn and ε phases representing the orientation relationship between the two phases.

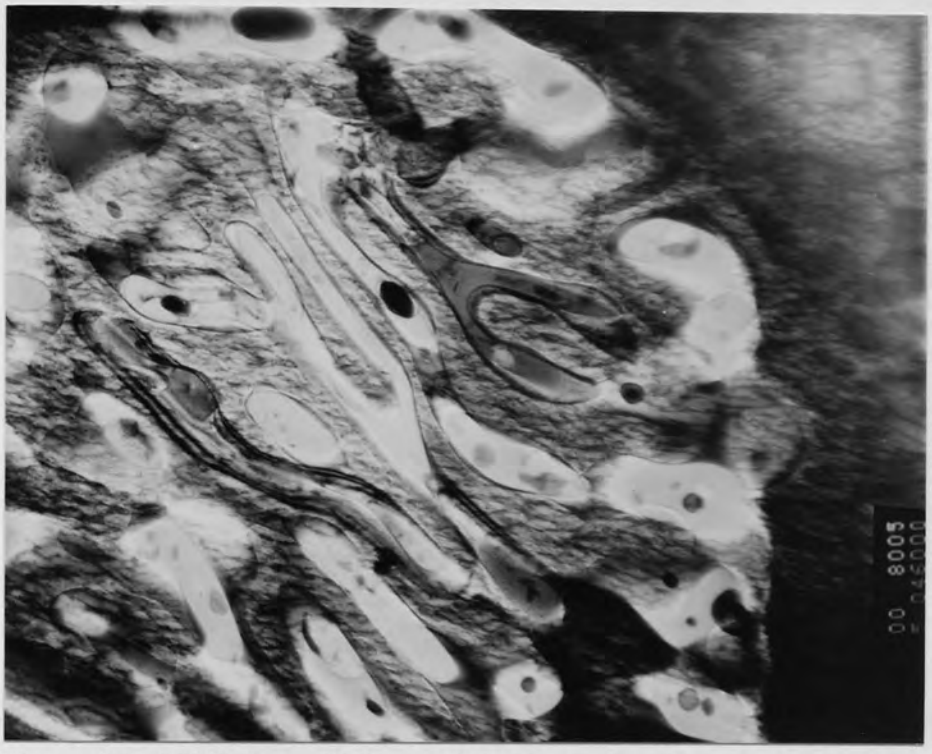

Figure 94. TEM. A small β - particle decomposed into irregular ribbon-like lamellae.(51750x)

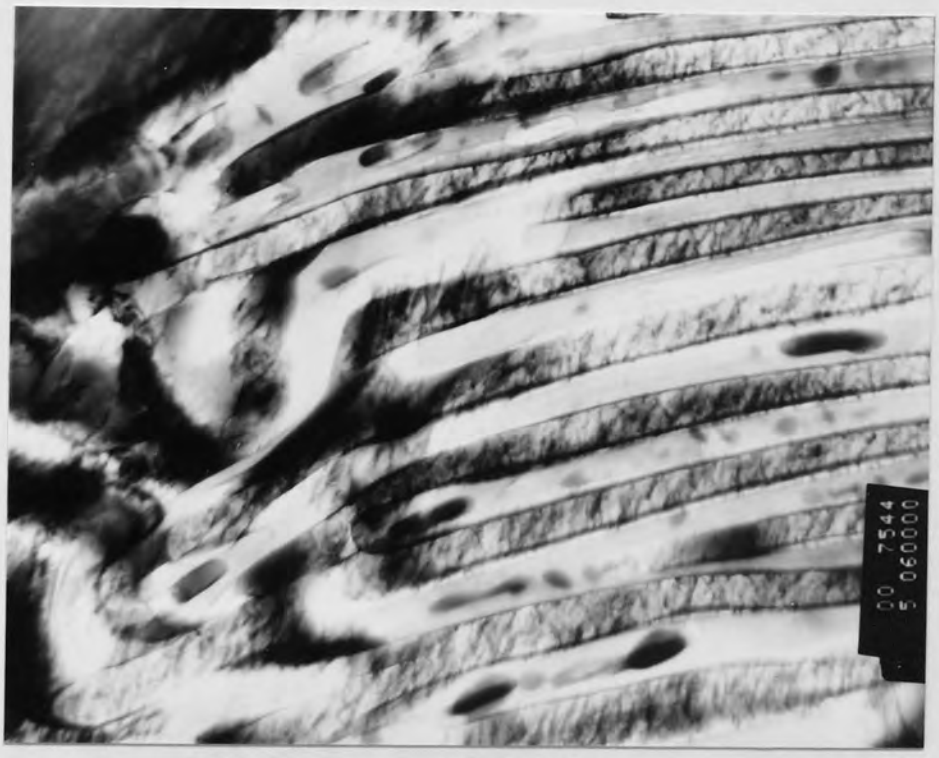

Figure 95. TEM. Decomposition of β into regular lamellae.(67500x)

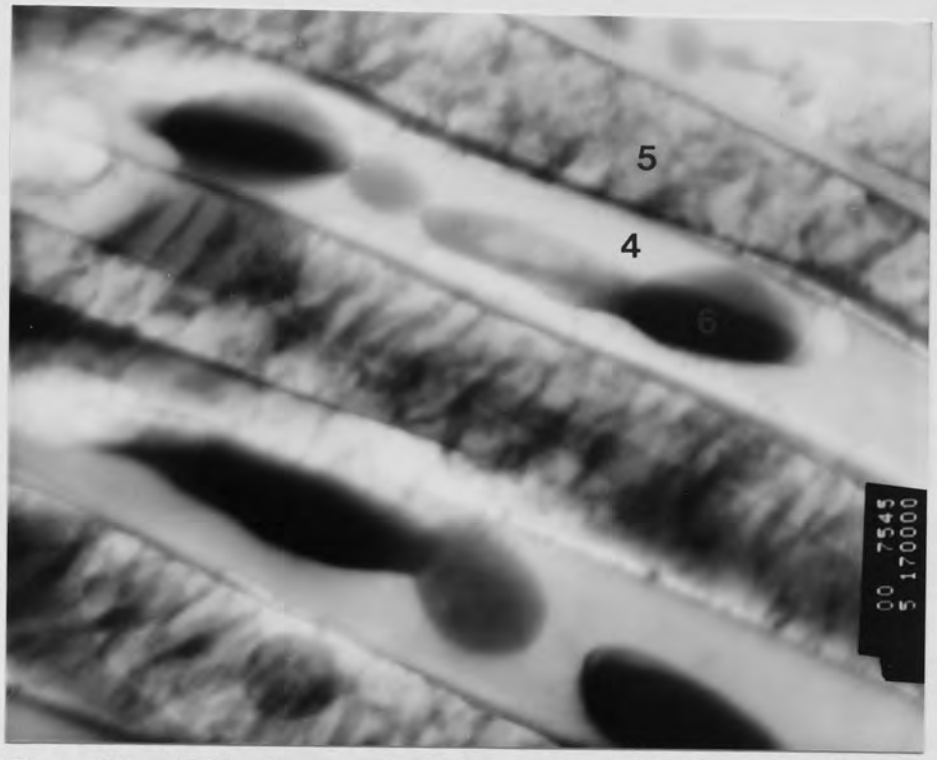

Figure 96. TEM micrograph of decomposed β - phase into lamellae with metastable phases accommodated within the Al-rich lamellae. (191250x)

Figure 97. TEM. Decomposition of β into a coarse mixture of phases.(51750x)

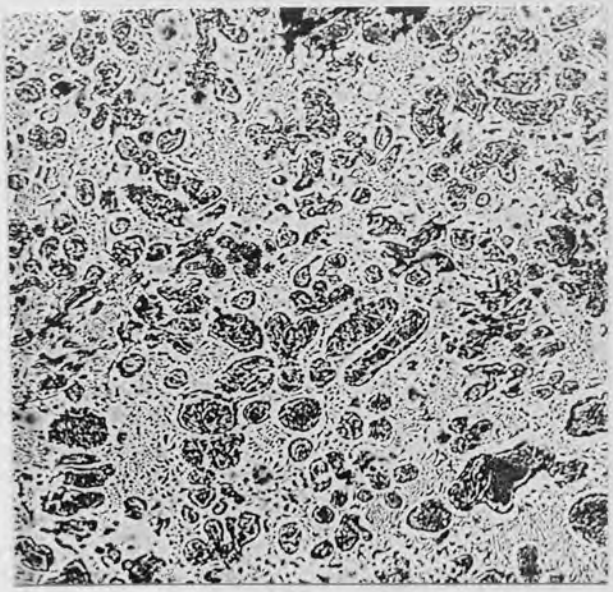

Figure 98. SEM micrograph of alloy ZA.8 tested at 40 MPa and 120℃.

(760x)

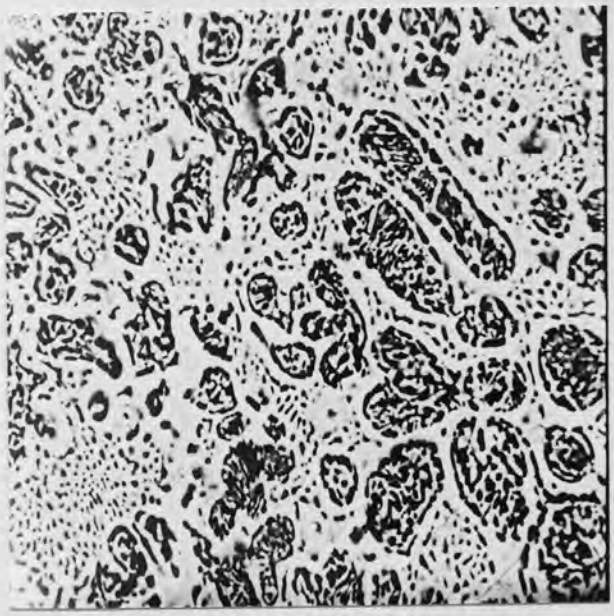

Figure 99. SEM. Alloy ZA.8 tested at 40MPa and 120℃, exhibiting nil deformation of β particles, and very little cavitation.

(1520x)

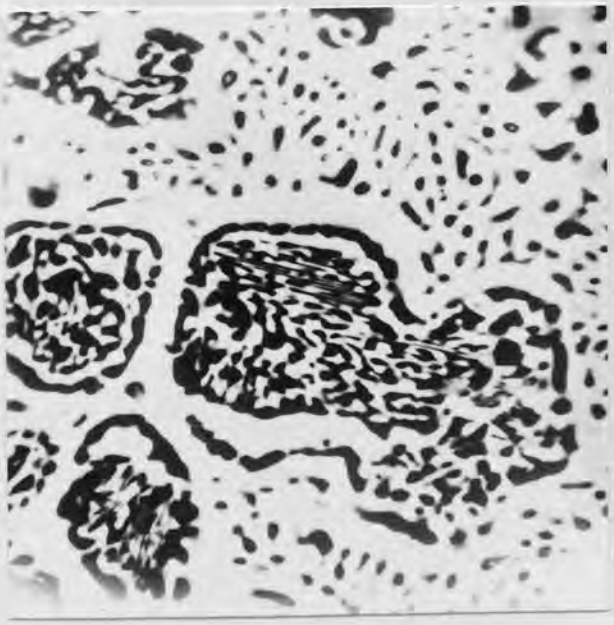

Figure 100. SEM. Alloy ZA.8 tested at 40MPa and 120℃, showing coarsening of coarsening of fine (a+η) particulates at the edge of the former β primaries into continuous rims of α and η.

(3500x)

Figure 101. TEM micrograph of shoulder part of the alloy ZA.8 tested at 10 MPa and 150°C, exhibiting a considerable amount of coarsening of primary particle and eutectic, and decomposition of metastable phases into the equilibrium phases.(11250x)

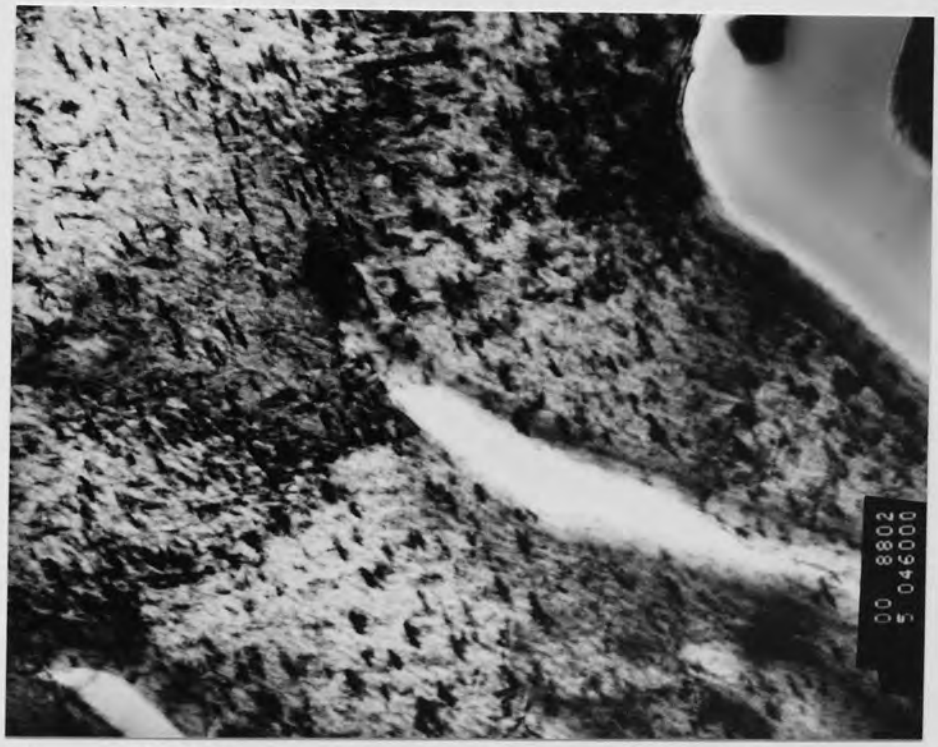

Figure 102. TEM. Eutectic area from shoulder part of the sample tested at 10 MPa and 150°C.(51750x)

(a)

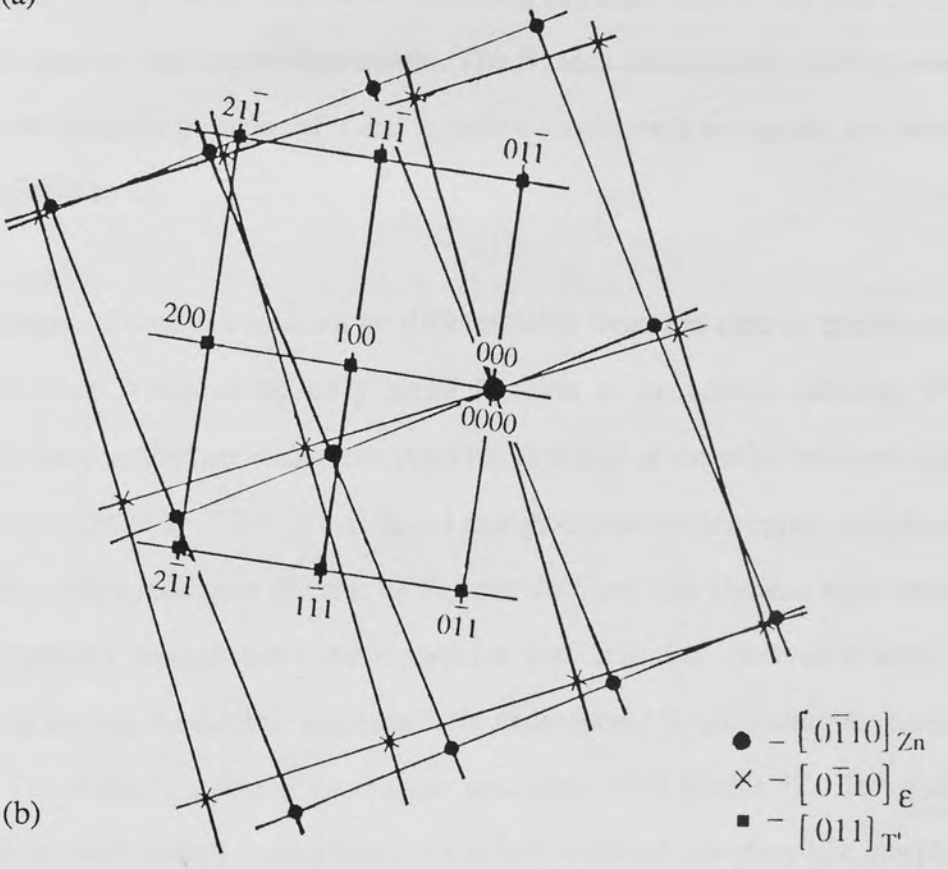

(b)

Figure 103. (a) SADP from the eutectic area in Figure 102, consisting of $[0\bar{1}10]$ *zones of hcp zinc matrix and* ε *- precipitates, shows transformation of* ε*- precipitates into T' phase with an orientation relationship;* $[0\bar{1}10]_{Zn}$ // $[0\bar{1}10]_{\varepsilon}$ // $[011]_{T'}$ *, (using cubic indexing for T').*
(b) Indexing of the above pattern.

4.3.3 Alloy ZA.27

Compared with the two other alloys (Mazak 3 and ZA.8), alloy ZA.27, with higher aluminium and copper content, had a more complex multi-phase microstructure distinctly different from the previous alloys. *Figure 104* shows a fine structure of dendrites in a mass of much smaller aluminium-rich particles and some pools of eutectic zinc. As appeared in *Figures 105 and 106* at higher magnifications, solidification of this alloy had begun with the formation of aluminium-rich (α–α') dendrites, and proceeded by precipitation of much more zinc-rich β phase. The latter formed around the primary dendrites through a peritectic reaction between the first-formed α-phase and residual liquid. The cores decomposed in some parts into coarse, lamellar cellular products, and more frequently in others into a very fine mixture of zinc-rich phases in an aluminium matrix. The β areas subsequently decomposed into lamellar or irregular particles of α and η, with eutectic pools occupying the remaining interdendritic areas.

Precipitation of copper could not be differentiated from the zinc by atomic number contrast since it differs by only small fraction of an atomic number. But its precipitation morphology within the complex structure of the alloy was revealed and examined in detail by TEM. It was found that precipitation of copper as ε-phase had two distinct morphologies. Firstly, as *Figures 107 and 108* show, a high density of heterogeneously precipitated ε-phase particles, similar to that observed in alloy ZA.8, was found in both the eutectic and lamellarly-decomposed β, decorating the entire zinc matrix. The copper content of these areas was about 6.3% (*Table 12*). This indicates that ε-phase preferentially precipitates in a strictly oriented thin plate-like morphology in the available η in both the eutectic matrix and in decomposed β.

Secondly, discrete ε-particles of irregular sizes (dark acicular particles in *Figures 107 and 108*) were also found, distributed irregularly in the interdendritic channels.

Figure 109 shows the CBDP of a particle shown in *Figure 108*, corresponding to the hexagonal lattice of ε-phase, consisting of $[0\bar{1}11]$ zone. STEM analysis carried out on different particles also confirmed that they were in accordance with the known equilibrium composition within the standard deviation limit of the analysis *(Table 12)*. These discrete ε-particles probably formed in the copper-enriched liquid when the eutectic reaction took place.

Figure 110 illustrates a typical complex structure of the decomposed α dendrites, in which the cellular precipitates, the continuously decomposed matrix and large precipitates of a metastable phase were co-existent, decorating the whole grain. Here, the lamellar structure appeared to develop from the interface of the large precipitates of the metastable phase if the matrix had not already undergone any continuous reaction. The continuously decomposed matrix was however most frequently observed, as shown in *Figures 111 and 112* at low and high magnifications respectively. Here the equiaxed mixture of the phases was extremely fine with an average particle diameter of about 900Å. Around the spinodal matrix was a coarse lamellar structure. Analyses of the overall compositions of the spinodal matrix showed that it contained ~ 30.7% Zn with ~3.5% Cu in the aluminium matrix. This indicates that the spinodal matrix was from the first formed α-dendrites, richer in aluminium, and that the development of these two completely different morphologies must be due to the real differences in composition of the cores of the α dendrites compared with the β surfaces.

Compared with the low copper alloy ZA.8, the metastable phases were in much larger quantities in this alloy. As in the previously shown *Figure 108*, the eutectic α-lamellae were found to contain a metastable phase similar to α'_T in the eutectic of the ZA.8, with higher zinc (~14.8%) and copper (~4%) content, (*Table 12*) but in ZA.27 they were much also bigger in size.

The decomposition of β-phase was also very similar to that of the alloy ZA.8.

Figures 113 to 115 show the decomposed products of the β in lamellar and particulate products, respectively. The former was very much like that of the alloy ZA.8 and STEM analysis carried out on the central portions of the aluminium lamellae showed a non-unequilibrium composition of α phase with about 27.2% Zn, which is very much in accordance with the previous argument for the two-stage development of the lamellar structure.

The particulate structure shown in *Figures 114 and 115* was also similar to that observed in ZA.8, but with a much higher amount of metastable phases which clearly appeared to enjoy their presence with higher copper content of the alloy, and the obvious suppression of the cellular decomposition shown in the figures was also probably due to the same reason discussed in the previous section in the case of the alloy ZA.8.

Table 12. Mean STEM microanalysis of the phases in the alloy ZA.27.

Area marked in Figure ( )	Zn (%)	Al (%)	Cu (%)	Mg (%)
1 (107)	92.6±1.1	0.9±0.3	6.3±0.7	0.1±0.1
2 (108)	84.2±1.0	0.7±0.4	14.8±1.2	0.2±0.1
3 (111)	30.7	64.8	3.5	0.9
4 (108)	80.7±1.0	14.8±3.0	4.1±2.0	0.4±0.0
5 (113)	27.2±0.8	70.0±0.8	1.8±0.2	1.0±0.1

The wide freezing range of this alloy makes it prone to microshrinkage and, as illustrated in *Figure 116*, it was the only alloy which contained an appreciable amount of interdendritic porosity on casting. Creep failure of the alloy occurred as a result of coalescence of these cavities (*Figures 117*), after exhibiting a great amount of plastic flow.

Figures 118 and 119 show the extensive changes observed in the α-cored dendrites of a sample tested at 40 MPa and 120°C. The changes in the α-dendrites, as shown in

these figures were rather characteristic features of the deformation of this alloy in such a way that zinc-rich stringers normal to the tensile direction crossed the dendrites, dividing them into the smaller ones. The figures also show that the stringers were blocked at the coarsened aluminium rich rims of the grains.

This phenomenon was more prominent at test temperature of 150°C, as shown in *Figures 120 and 121* of a sample tested under a stress of 30 MPa. Here, the stringers divided the α-dendrites into large numbers of small particles with curved interphase boundaries, consisting of cusps and protuberances.These stringers are considered to be cross sections of irregular plates of η phase, the development of which is a failure mode in the creep process. These plates originated in suitably orientated zinc-rich regions such as where coarse lamellar or particulate parts of the dendrites were in contact with the α' core or the interdendritic η. Under a tensile stress, zinc-rich regions lying normal to the stress direction have broadened by stress-induced diffusion of zinc atoms to the faces under tension.

In experiments of long duration at 150°C, a considerable degree of coarsening of the phases was observed. *Figures 122 and 123* show the areas taken from the shoulder of the specimen tested at 10 MPa and 150°C, i.e. a long-term test. Here, smaller particles of decomposed β tended to shrink and eventually disappeared, while the bigger ones were flourishing (Ostwald ripening-type coarsening). In the primary α-dendrites, a discontinuous coarsening of the fine lamellar products also occurred, but the fine-grained, equiaxed products remained essentially unchanged.

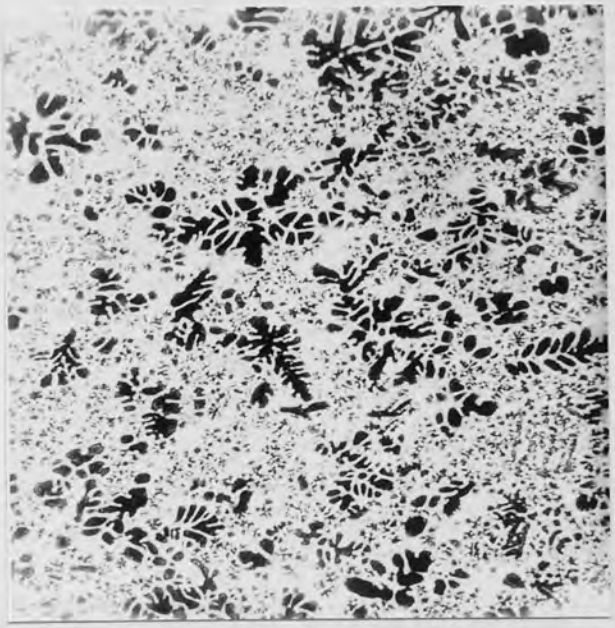

Figure 104. SEM. As-Cast structure of Alloy ZA.27 at low magnification, showing α- cored dendrites in β and η - matrix.

(165x)

Figure 105. SEM. As-Cast structure of Alloy ZA.27 at medium magnification, showing decomposition morphology of α-dendrites, surrounded by decomposed β and eutectic.

(1650x)

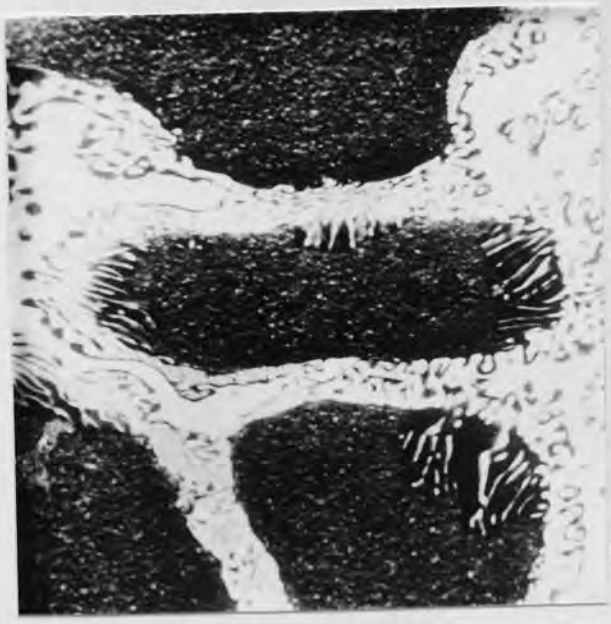

Figure 106. SEM. As-Cast structure of Alloy ZA.27 at high magnification, showing fine equiaxed structure of α-dendrites surrounded by decomposed β and eutectic.

(4150x)

Figure 107. TEM micrograph of alloy ZA.27 illustrating precipitation of ε -phase in both zinc lamellae and eutectic in high densities, together with discrete ε - particles.(40500x)

Figure 108. TEM. Interdendritic area with ε -precipitates and particles and eutectic containing an appreciable amount of metastable phases.(31500x)

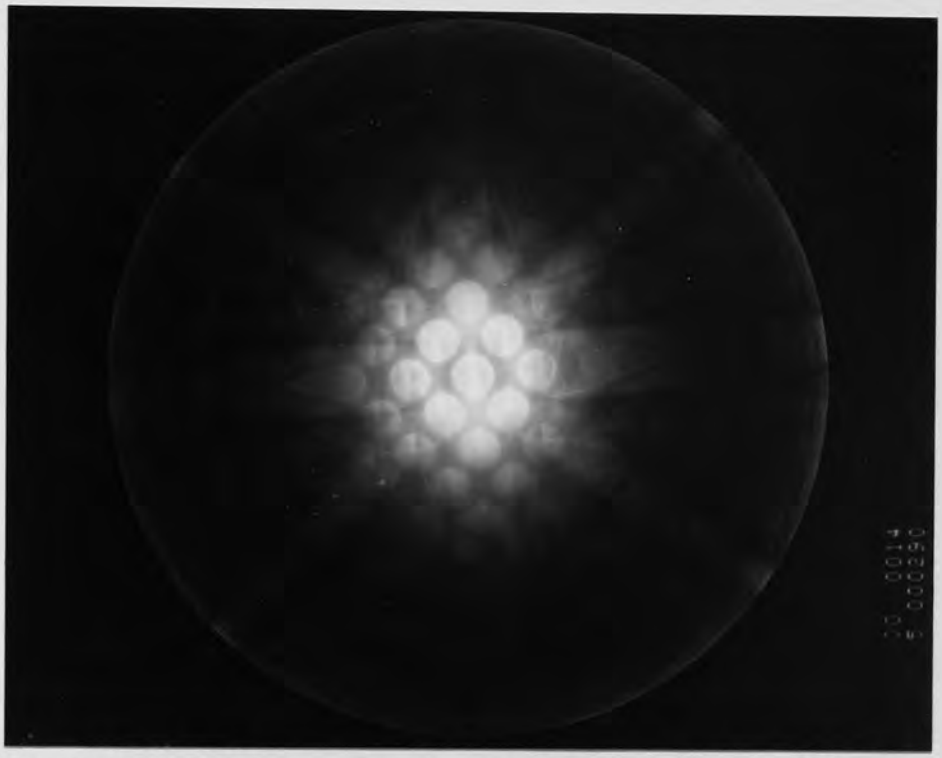

Figure 109. CBDP from the ε -particle seen in Figure 108, showing the hcp symmetry of $[0\bar{1}11]$ *zone.*

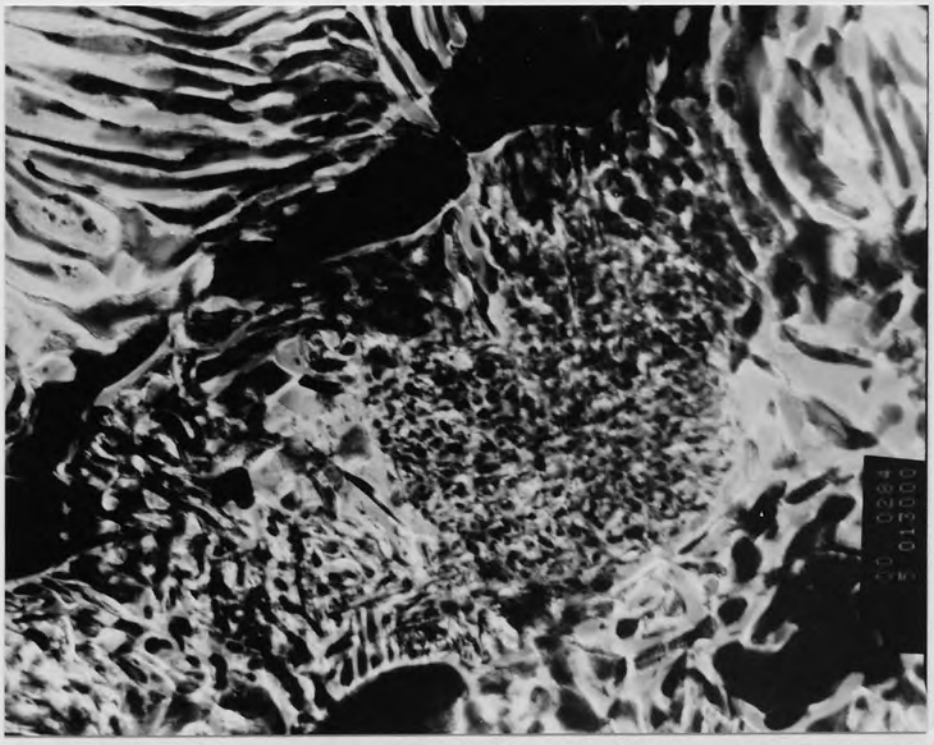

Figure 110. TEM micrograph of alloy ZA.27, illustrating the complex decomposition of an α' -dendrite and coexistence of the cellular colonies, the continuously decomposed matrix and the metastable phases decorating the dendrite.(14600x)

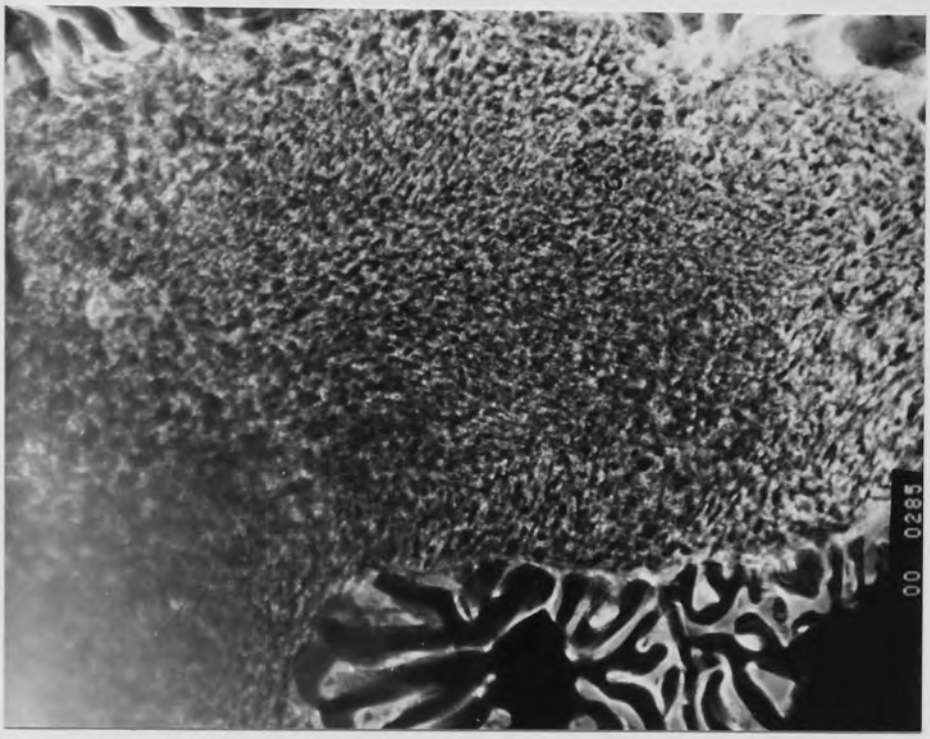

Figure 111. TEM. Spinodally decomposed α -matrix with a very fine mixture of the phases, surrounded by coarse lamellae.(14600)

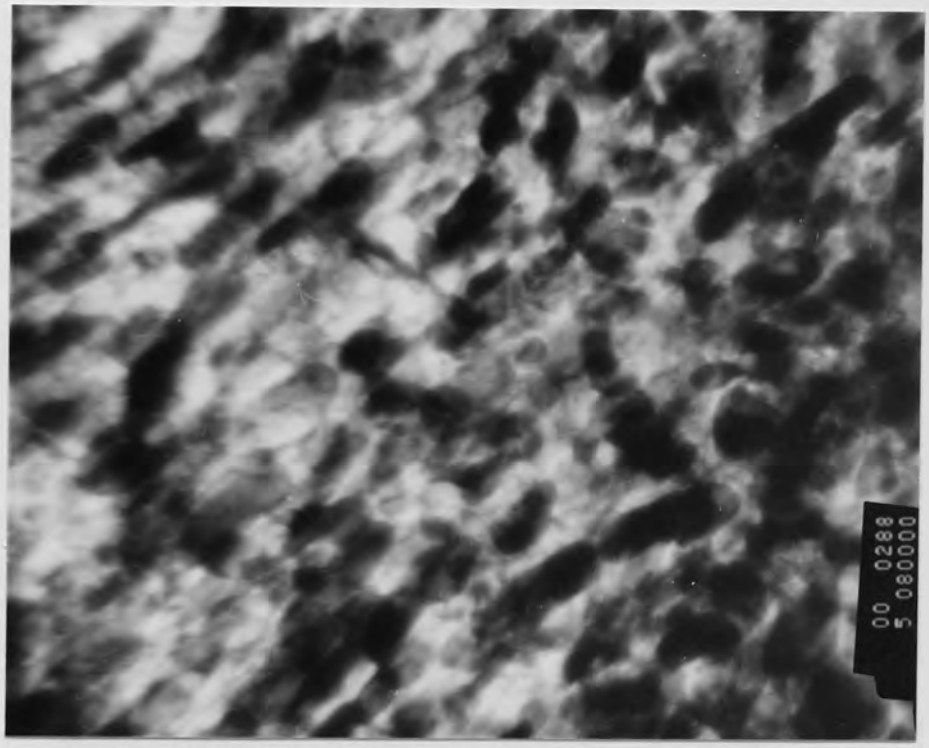

Figure 112. TEM. Spinodally decomposed α -matrix at high magnification, showing fine, irregular mixture of the phases.(90000x)

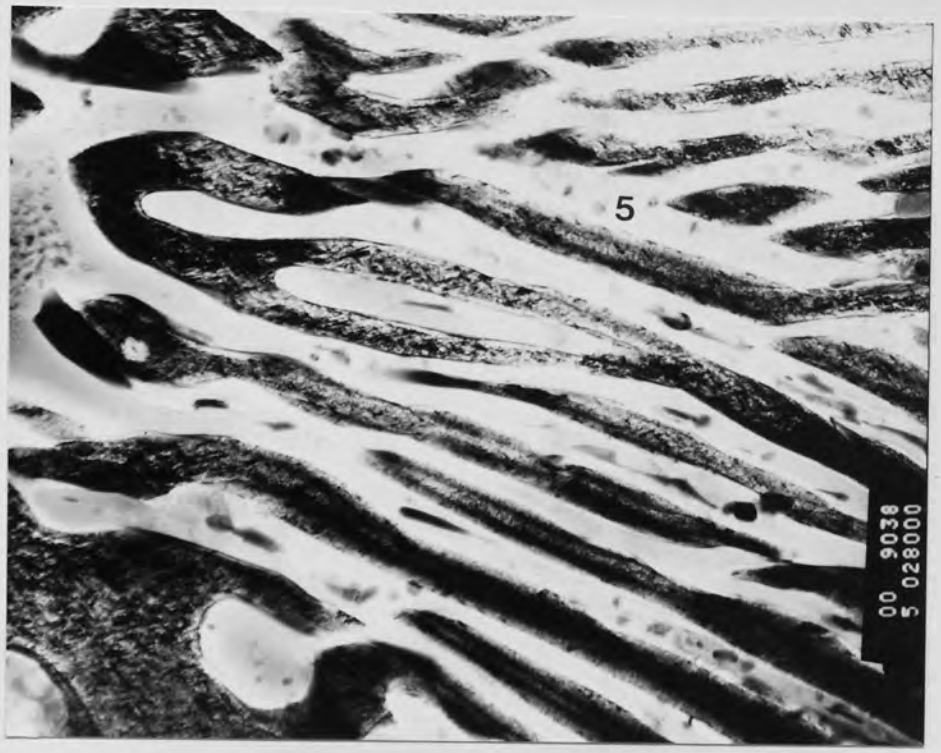

Figure 113. TEM. Decomposition of β in the alloy ZA.27, showing the regular structure and branching of the lamellae.(31500x)

Figure 114. TEM. Occurrence of different modes of decomposition of β in particulate and lamellar products with a considerable amount of metastable phases.(24800x)

Figure 115. TEM. Same area shown in figure 114 in detail, illustrating the evidence for the lamellar growth suppressed by particulate phases and also for two stage decomposition.(40500x)

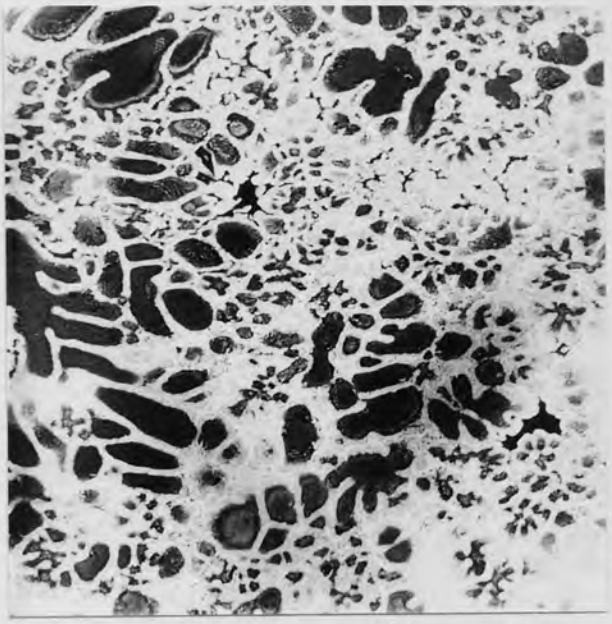

Figure 116. SEM. As-Cast structure of Alloy ZA.27, showing microshrinkage porosity in the interdendritic area.

(415x)

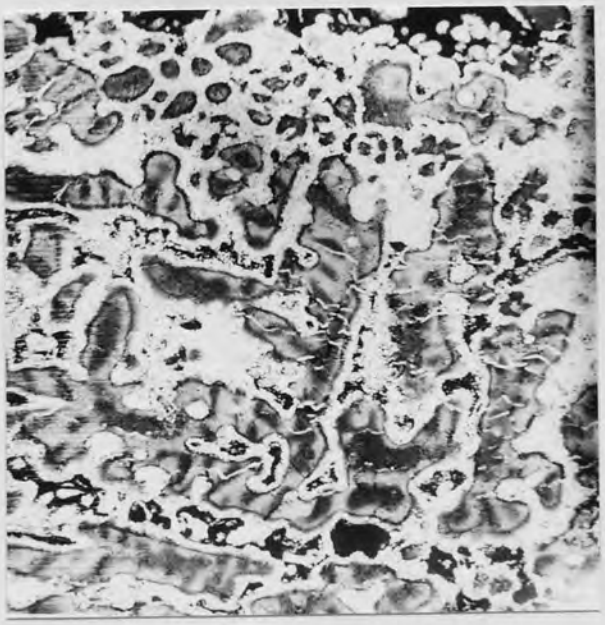

Figure 117. Alloy ZA.27 tested at 40MPa and 120°C, showing the coalescence of the cavities.

(340x)

Figure 118. Alloy ZA.27 tested at 40MPa and 120°C, showing zinc-rich stringers crossing the α- dendrites, normal to the stress direction.

(1340x)

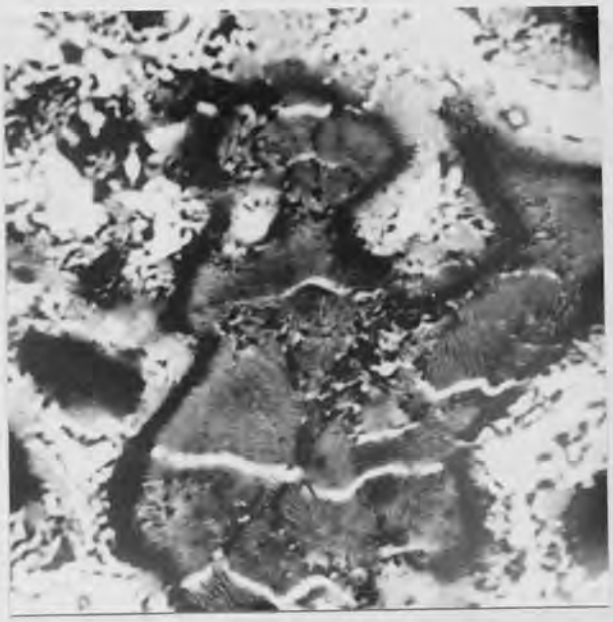

Figure 119. SEM. Alloy ZA.27, tested at 40MPa and 120°C, showing zinc-rich stringers crossing a dendrite, terminated by a coarsened Al-rich rim around the dendrite.

(3350x)

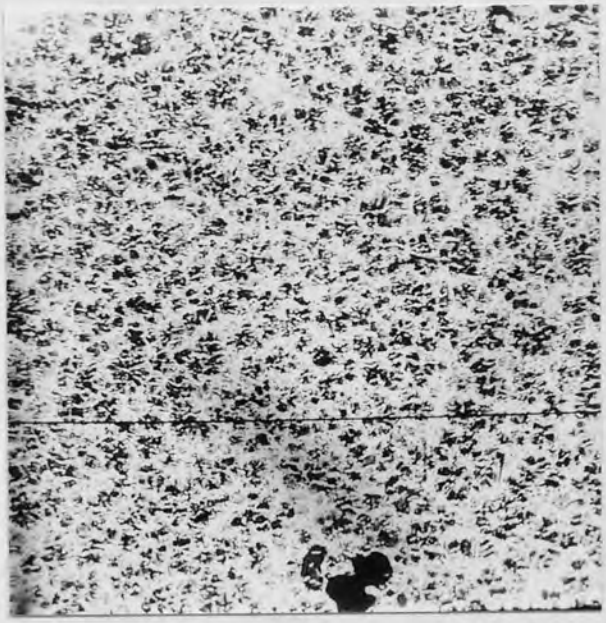

Figure 120. Alloy ZA.27 tested at 30MPa and 150°C, showing extensive break-up of the α- particles.

(375x)

Figure 121. Above area in detail, showing the curved interphase boundaries with cusps.

(1500x)

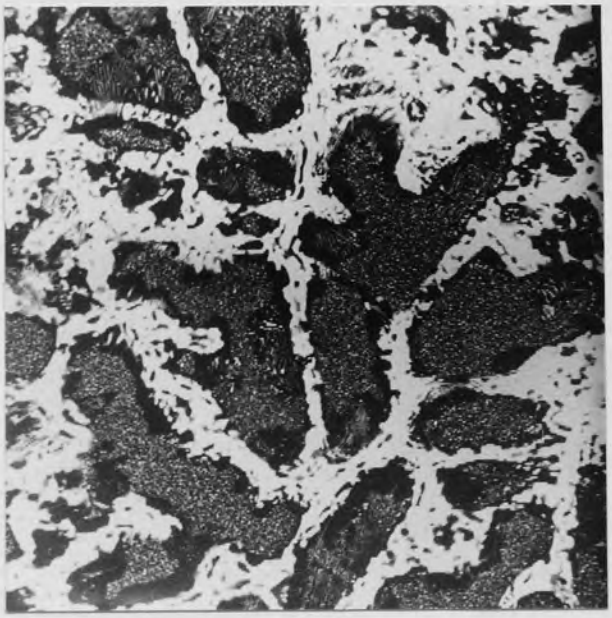

Figure 122. SEM. Alloy ZA.27, tested at 10MPa and 150°C, showing coarsening of fine decomposed β particles.

(1400x)

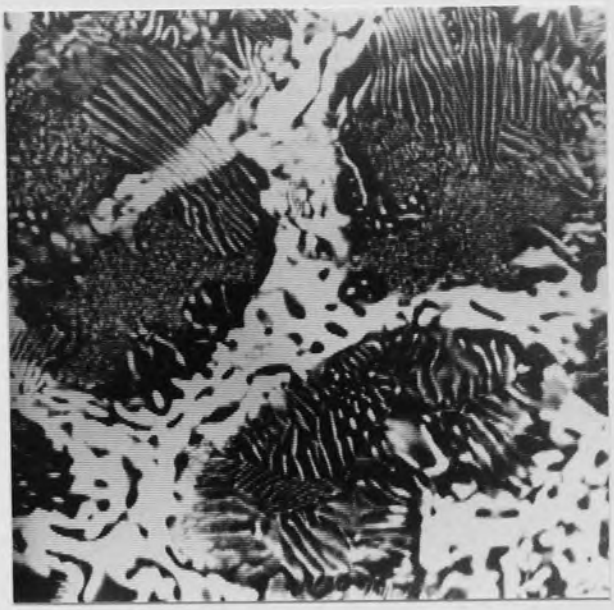

Figure 123. Alloy ZA.27 tested at 10MPa and 150°C at high magnification, showing coarsening of α-lamellae.

(3650x)

4.4 Creep Results of the Die-Cast Alloys

Creep tests of the alloys 1 to 10, produced in our own foundry, and including commercial alloys, Mazak 3, ZA.8, ZA.12 and ZA.27 were carried out only at 40 MPa and 120°C to the point of fracture, in duplicate. The creep curves of these tests, one from each alloy, are shown in *Figure 124*. Creep data obtained from the curves were primary creep extensions, times to produce a creep elongation of 1%, and secondary creep rates, which are all listed in *Table 13*.

Comparing the commercial alloys in this series with those used in the main creep work, the former ones showed much lower primary creep and times to produce a total elongation, and much higher creep rates in the secondary creep regions. Differences in the times to produce 1% total creep elongation were lower by a magnitude of 3, 6 and 2 and in the secondary creep rates was similarly higher for the alloys Mazak 3, ZA.8 and ZA.27, respectively. The reason for these appreciable differences in the creep performance of the alloys, especially in the case of the alloy 5(ZA.8), has not been fully understood yet. In the case of alloy 2(M.3) as it can be seen from the *Figure 128* (next section) that the average grain size of the primary particles in this alloy was much smaller (about three times), compared with the previous alloy (*Figure 64*). From an earlier work[149], it is known that the grain size of the alloy M.3 is strongly dependant on gate velocity as increasing gate velocity was reported to cause a sharp decrease in the grain size of the alloy. Besides, in a very recent work[150] which was carried out on alloy Mazak.5, it was shown that the gate velocity had also an important effect on the creep performance of the alloy and secondary creep rate was shown to increase by up to 300% as the gate velocity increasd from 30 to 70 m/s. In the present work, the gate velocity used was about 53 m/s and this was later found to be higher than that used in the existing casting practice[151] and partially explains the lower creep strengths of the alloy.2(M.3). However in the cases of hyper-eutectic alloys, especially for the alloy.5(ZA.8), the reason for the dramatic reduction in the

creep strength appeared not to be so simple, since the difference in the grain size, as will be shown in the next section, was not so significant. In these cases however, it appeared from the structure of the alloys that the creep performances of the alloys were dependant on the different decomposition morphologies of the β phase. In the case of alloy.5(ZA.8) which exhibited the most dramatic decrease in the creep strength, for example, the lamellar structure, which usually appeared in the cores of the β-dendrites in the previous alloy ZA.8, was not developed and β phase in these regions seemed to be still undecomposed (*Figure 132*).

The lack of lamellar structure appears to be the obvious reason for the most dramatic reduction in the creep strength observed in the case of alloy.5(ZA.8) and this may also explain the reason for the alloy 9(ZA.27) with the less amount of β phase showing the least decrease in the creep strength, compared with the previous ZA.27 alloy.

Average primary creep extensions of the alloys are shown in *Figure 125*, which clearly reveals the tendency of increasing primary creep with increasing aluminium content, as found earlier in the main creep work. As seen from the figure, primary creep was very small in the hypo-eutectic and eutectic alloys, but steadily increased with increasing amounts of β, followed by α-phase.

Alloys 3 and 4 in this series were cast for the intention of producing a good lamellar morphology of the eutectic. But, because of the fast cooling rate of the casting process, as will be shown later, the mixture of both β and η primary-type phases set in a small eutectic was obtained in both alloys instead of eutectic morphology. That is why they do not represent a true eutectic-structured alloy.

Average secondary creep rates $(\dot{\varepsilon}_s)$ of the alloys is shown in *Figure 126*. $\dot{\varepsilon}_s$ increased dramatically with increasing aluminium content in the hypo-eutectic area, and reached a maximum in the eutectic alloy without copper (alloy 3). Addition of the copper (~1%) reduced the $\dot{\varepsilon}_s$ of the alloy by a factor of 2. It then reached a minimum

value in the alloy 5 (ZA.8), followed by a steady increase until the second maxima in the composition of ZA.27 was reached. At that point, it can be seen by comparing the alloy 8 with 1% Cu with alloy 9 (ZA.27) with similar composition but with higher Cu content, addition of extra copper above 1% was not very beneficial in improving the creep resistance of these alloys. Increasing the aluminium content above that of the alloy ZA.27 appeared to lower the $\dot{\varepsilon}_s$ again in the alloy 10.

Relative total creep performances of the alloys as mean values of times (ks) to produce 1% creep strain can be compared in *Figure 127*. They were well in accordance with the creep performances of the alloys implied by the secondary creep rates above, for this instance, time to produce 1% creep strain was a minimum for the alloy 2 (Mazak 3) and the alloy 3 with a very small amount of difference, and maximum for the alloy 5 (ZA.8), followed by a sharp decrease until the alloy ZA.27. No additional benefit was achieved by increasing the copper above 1% at this composition, but increasing aluminium appeared to improve the total creep resistance of the alloy ZA.27.

4.5 Metallography of the Die-Cast. Alloys

The structure of the alloy 2 (Mazak 3) die-cast in our foundry is shown in *Figure 128*. The structure was similar to that of the same alloy used in the main creep work, as discussed previously. But, primary η dendrites were much smaller by about a factor of 4, compared with those of the previous alloy.

The similar structure of the eutectic alloys 3 and 4 is shown in *Figures 129 and 130* at low and high magnification, respectively. As mentioned earlier, although the production of a good lamellar structure had been aimed for, because of the fast cooling rate of the casting process, the structure obtained was a fine mixture of the phases with a few primary particles of both η and β phases, set in an eutectic matrix as seen from the figures. β particles also decomposed into a fine mixture of phases *(Figure 130)*.

As-cast structure of alloy 5 (ZA.8) is shown in *Figures 131 to 133*. Here, the size of the β dendrites was similar to that of the previous ZA.8 alloy. However, development of the cellular reaction leading to a lamellar structure which had usually appeared in the central portions of the dendrites in the previous alloy, was not observed (*Figure 132 and 133*). As discussed previously, it appeared from these figures that decomposition in these regions were still not completed although the particulate structure of the rims of the cores and smaller β particles was well developed. This may be the reason that the creep strength of this alloy was lowered most significantly, compared with the other two alloys. In addition, if it is remembered that the reduction in creep strength (time to 1% creep strain) of the alloy ZA.27, which contained less of β phase, was by only a factor of 2

The as-cast structure of the alloy 6 (ZA.12) shown in *Figure 134* is similar to that of the alloy 5 (ZA.8), but with a higher amount of primary particles set in less amount of the eutectic.

The structure of alloy 7 is shown in *Figures 135 and 136* at low and high magnifications, respectively. Here, the first formed α-dendrites surrounded by β phase, (which formed through the peritectic reaction), and primary β particles were coexistent and set in a comparatively less amount of the eutectic.

Figures 137 and 138 show the structure of the alloy 8 which had very similar structure to alloy 9 (ZA.27) (*Figures 139 and 140*). In both alloys, on the other hand, the size of the α-dendrites was much smaller, compared with that of the previous diecast plates of alloy ZA.27. It also appeared from these figures that decomposition of β was not completed.

Alloy 10 had also a similar structure to those above, but with more cored structure of the α-phase, due to its higher aluminium content (*Figures 141 and 142*).

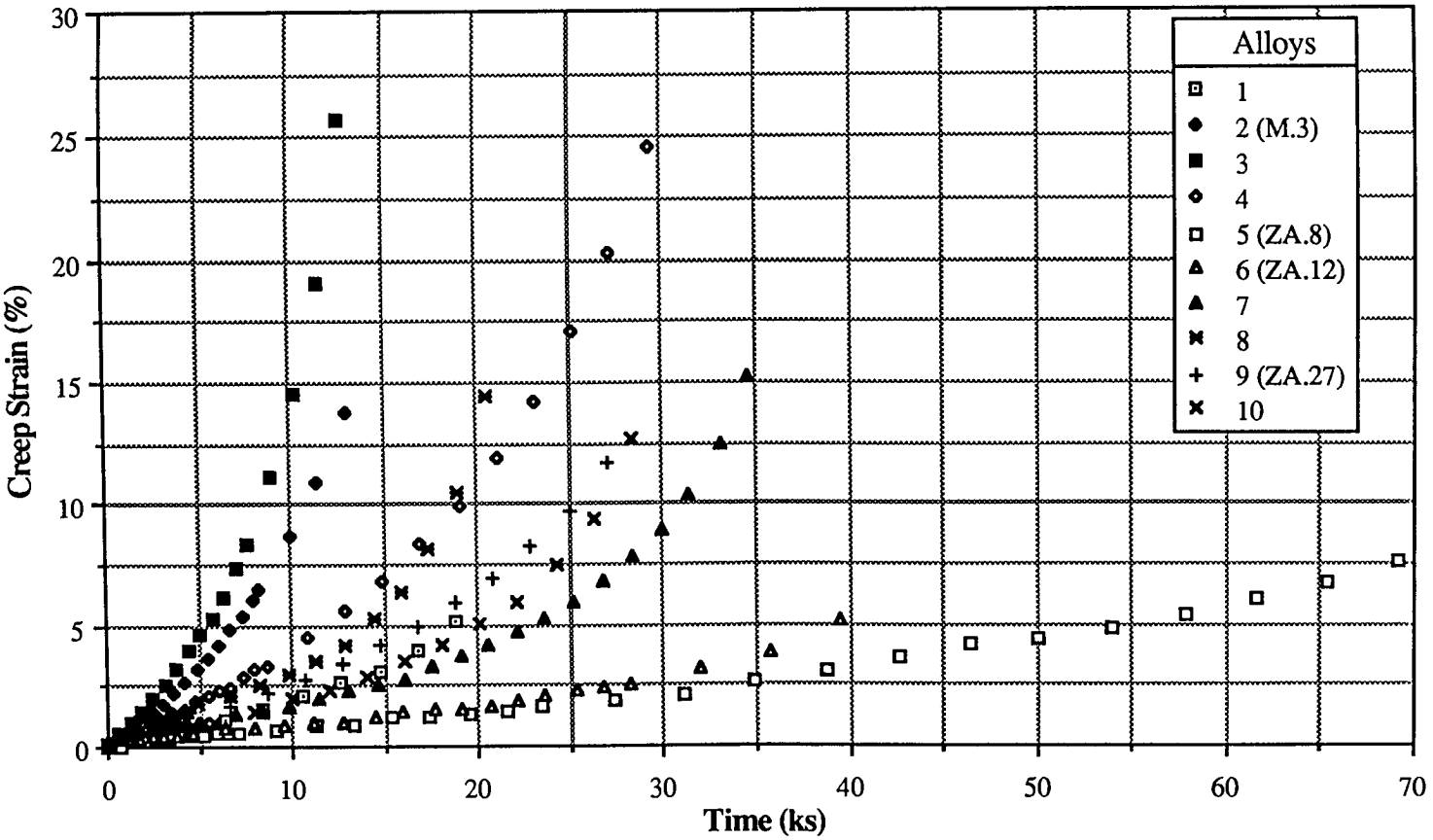

Figure 124. Creep curves of the alloys (1 to 10) die-cast, tested at 120 ℃ under the stress of 40 MPa

Table 13. Creep Data of the alloys 1 to 10 die-cast.

Alloy	Primary Creep (%)	Time to 1% CreepStrain (s)	Secondary Creep Rate ($x10^6$;1/s)
Alloy.1	0.04	4400	2.08
"	0.00	5700	1.75
Alloy.2(M.3)	0.05	1750	5.03
"	0.07	1550	6.02
Alloy.3	0.02	1230	7.91
"	0.02	1290	7.55
Alloy.4	0.02	2450	3.99
"	0.15	2420	3.50
Alloy.5(ZA.8)	0.09	12570	0.72
"	0.12	13670	0.65
Alloy.6(ZA.12)	0.11	9630	0.93
"	0.26	11390	0.65
Alloy.7	0.12	7830	1.12
"	0.28	4800	1.49
Alloy.8	0.18	3440	2.39
"	0.20	2740	2.92
Alloy.9(ZA.27)	0.12	4100	2.16
"	0.31	3140	2.20
Alloy.10	0.27	5320	1.38
"	0.47	3600	1.47

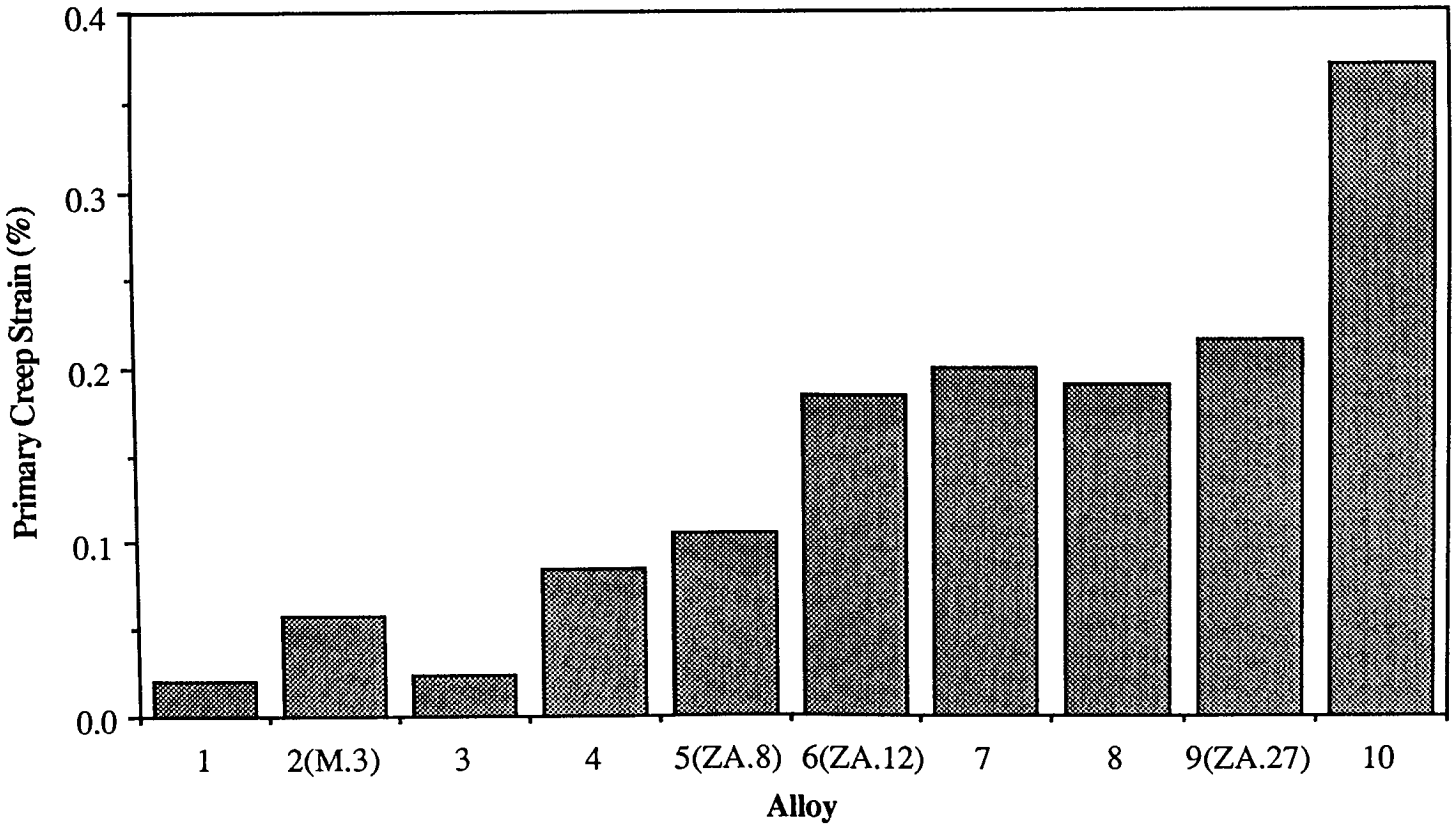

Figure 125. Variation of the average primary creep elongations of the alloys (1 to 10) with increasing Al content.

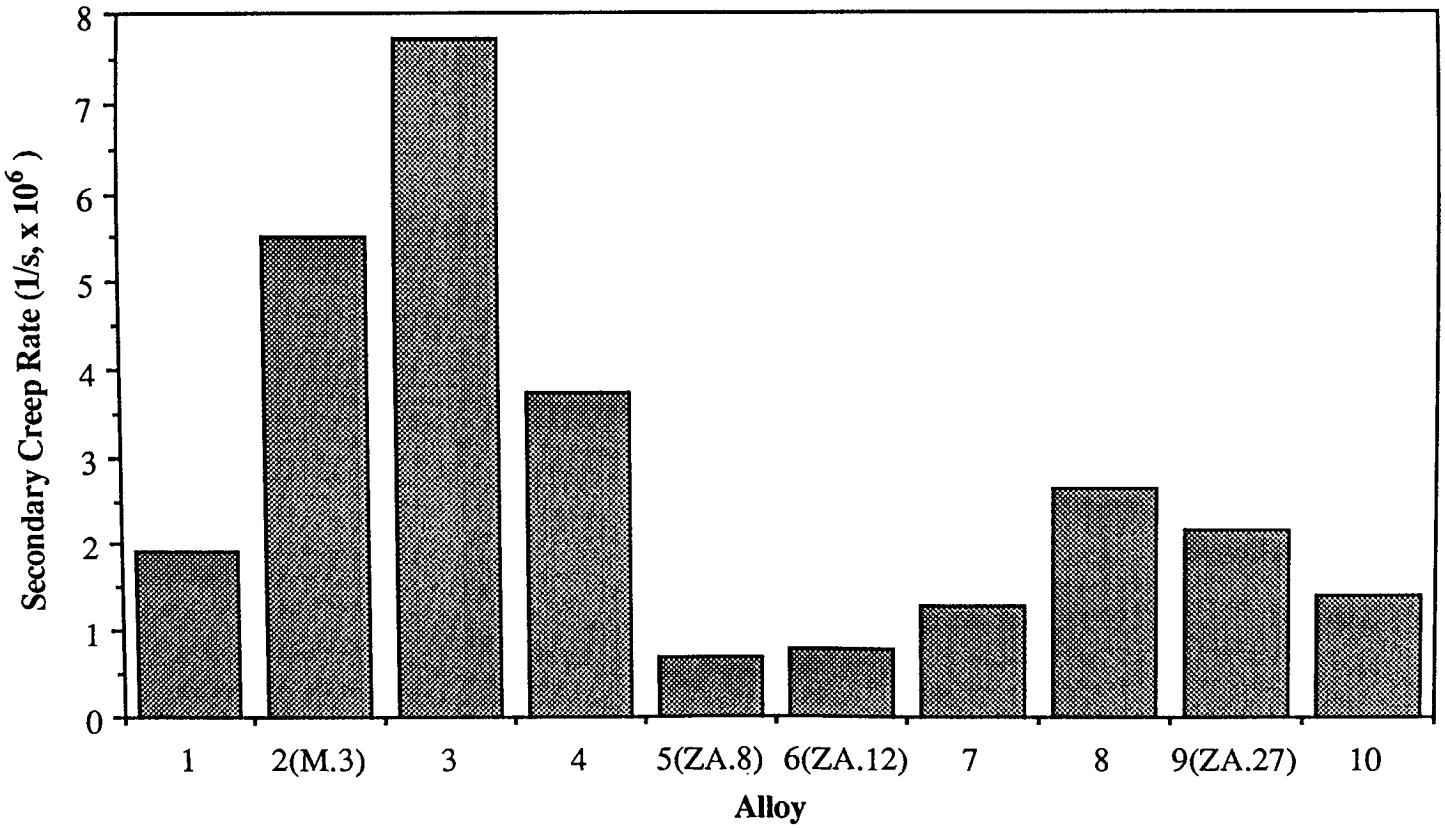

Figure 126. Variation of the average secondary creep rates of the alloys (1 to 10) with increasing Al content.

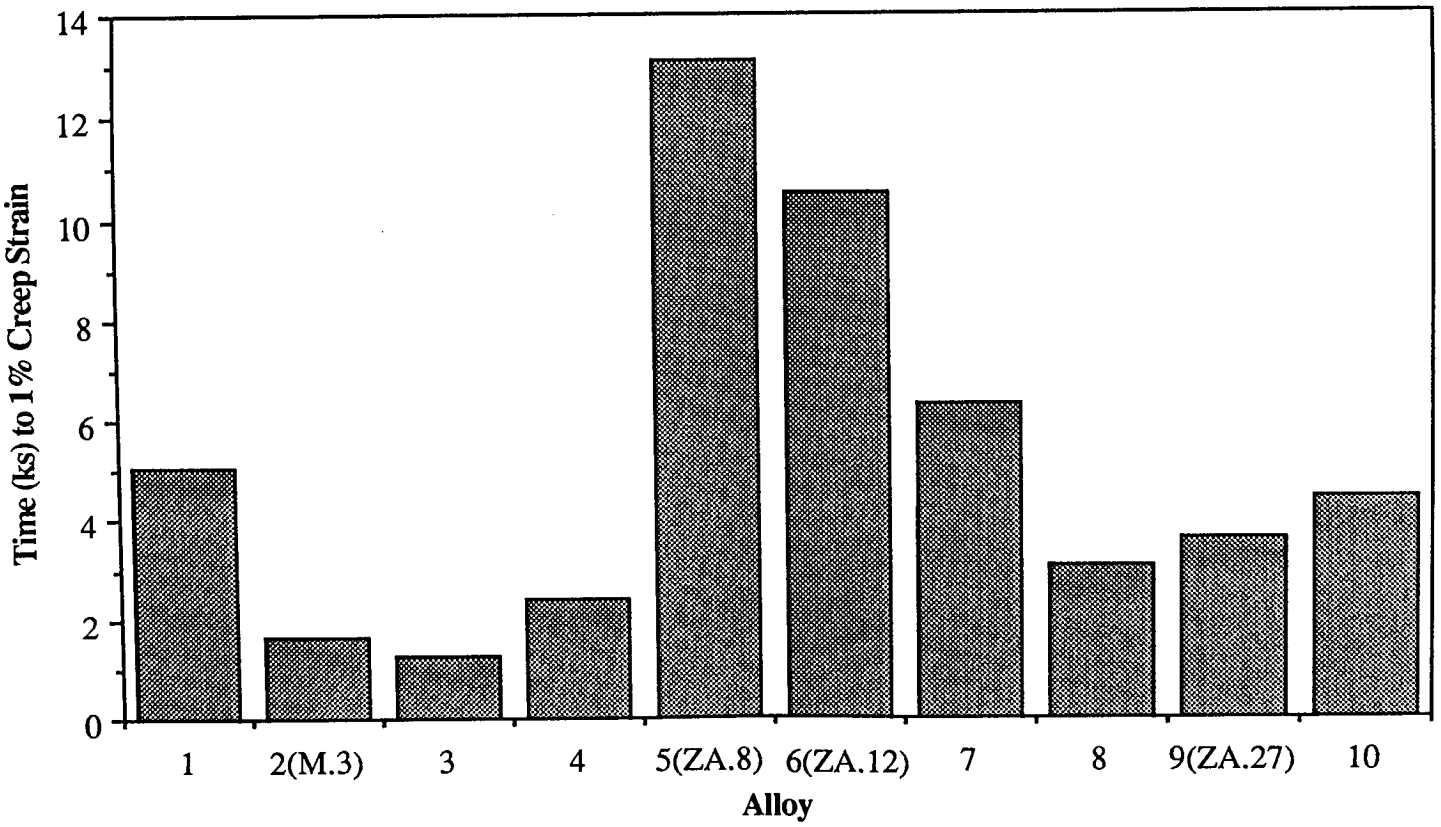

Figure 127. Variation of the average times to produce 1% creep strain of the alloys (1 to 10) with increasing Al content.

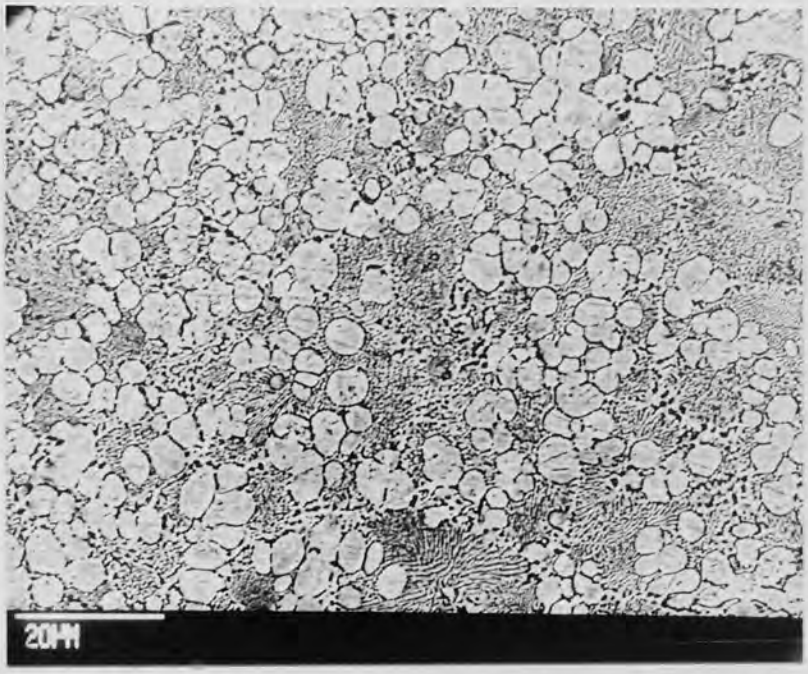

Figure 128. SEM. As-cast structure of die-cast alloy.2(M.3)

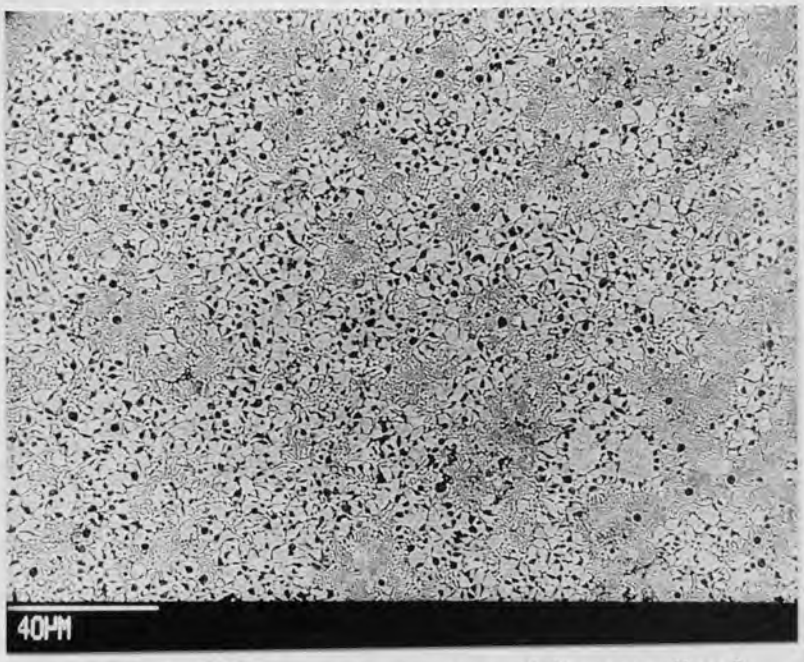

Figure 129. SEM. As-cast structure of die-cast alloy.3.

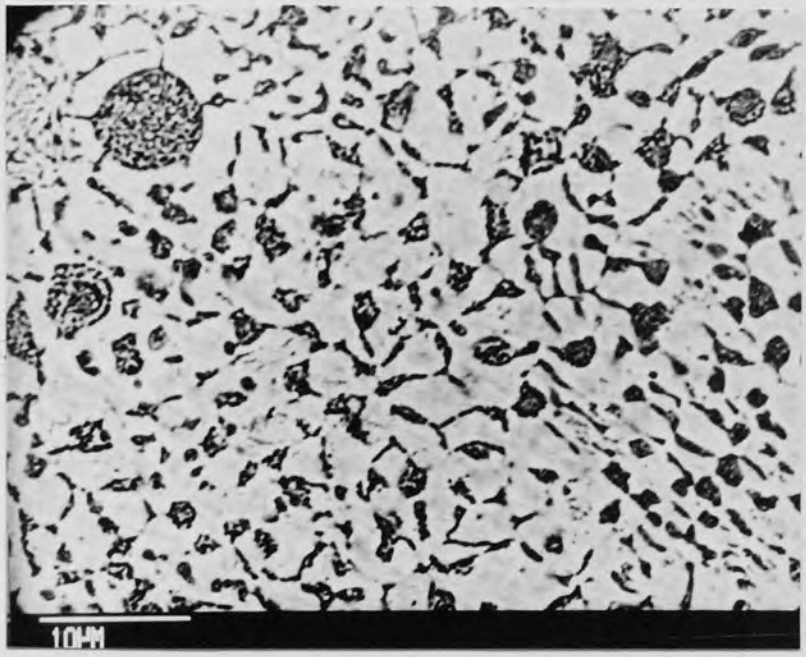

Figure 130. SEM. As-cast structure of die-cast alloy.4.

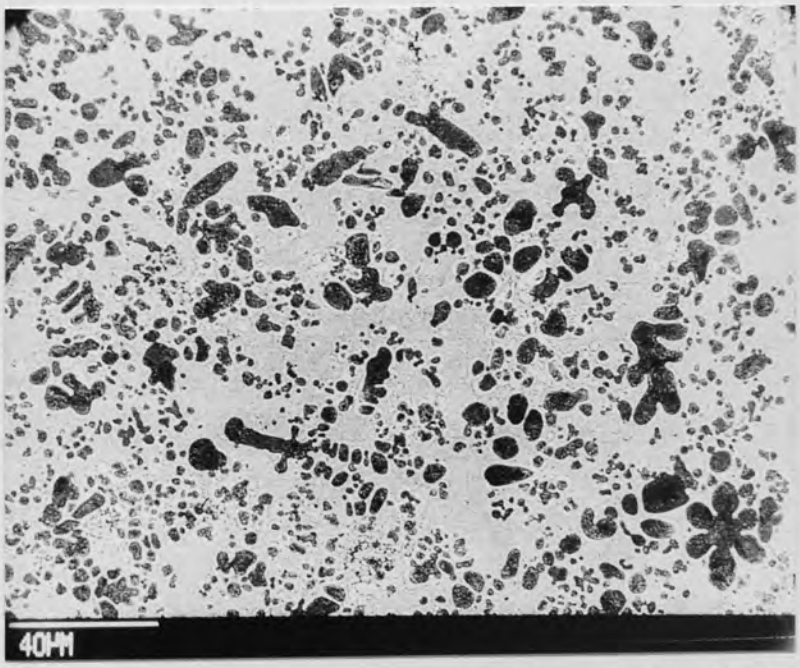

Figure 131. SEM. As-cast structure of die-cast alloy.5(ZA.8)

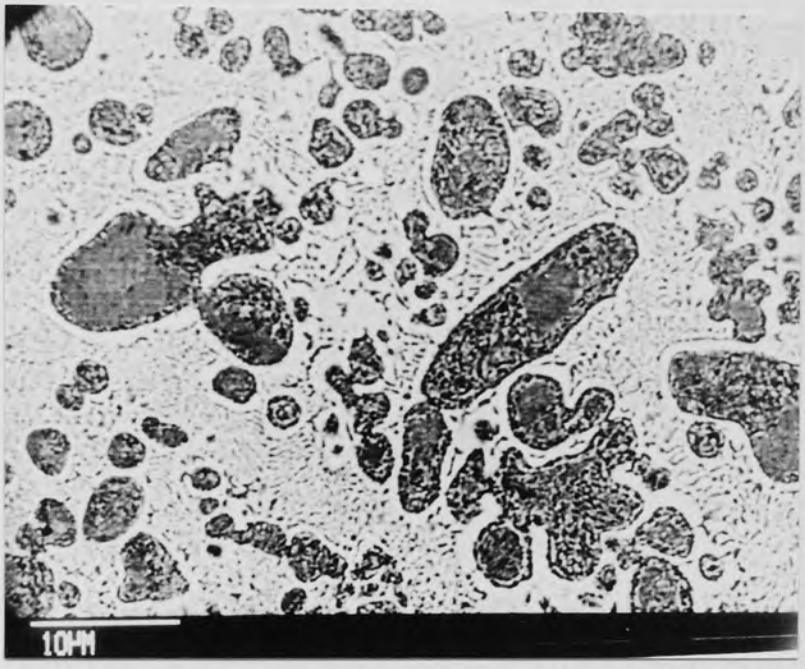

Figure 132. SEM. As-cast structure of die-cast alloy.5(ZA.8), showing the cores of the dendrites still undecomposed.

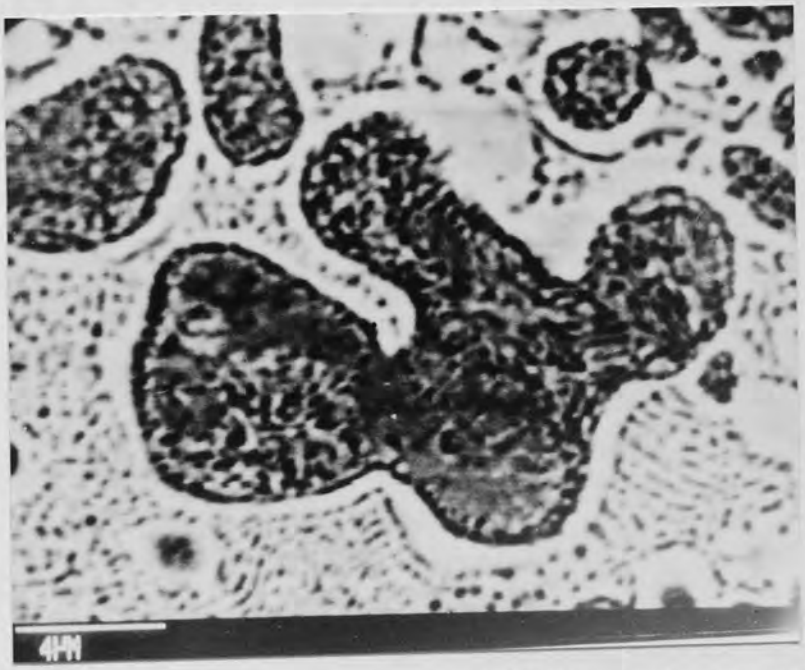

Figure 133. The structure of alloy.5(ZA.8) at high magnification, showing the absence of lamellar structure.

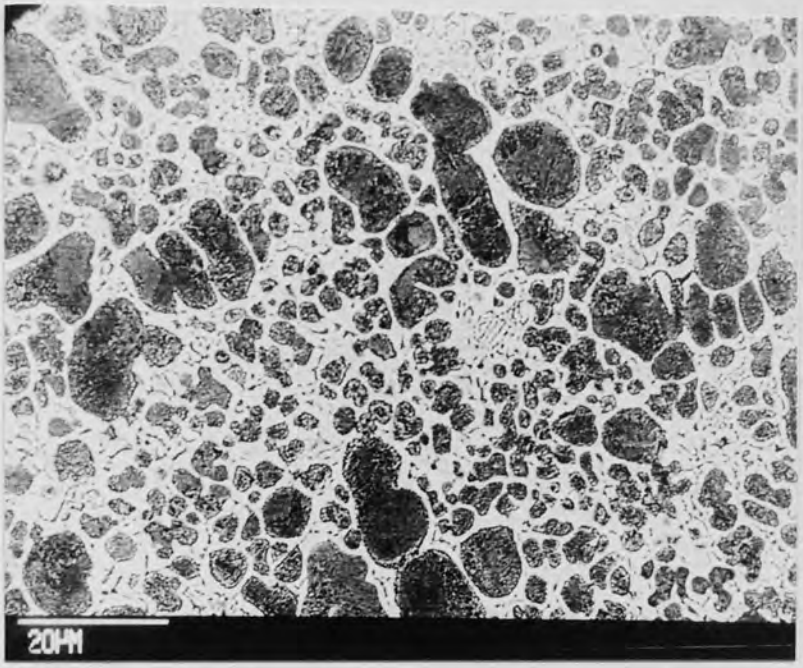

Figure 134. SEM. As-cast structure of die-cast alloy.6(ZA.12).

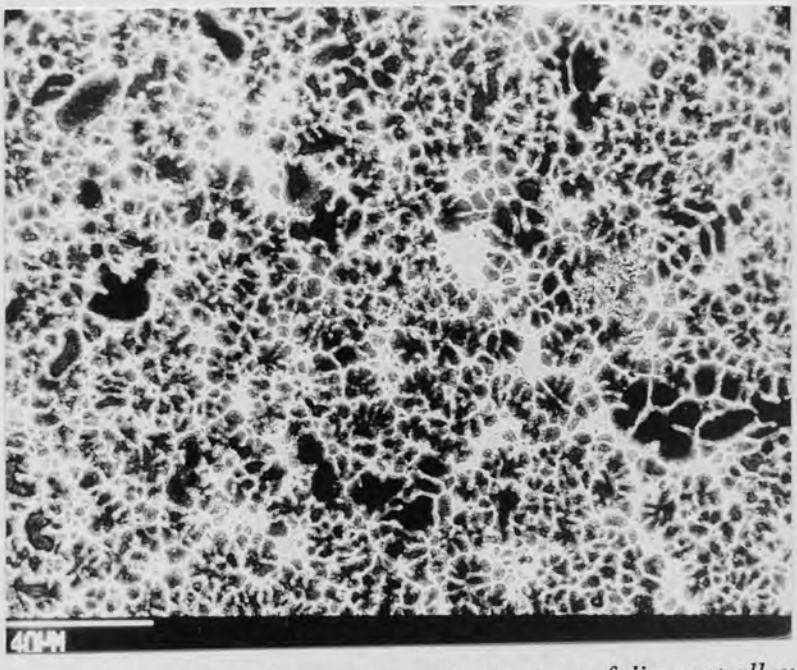

Figure 135. SEM. General as-cast structure of die-cast alloy.7.

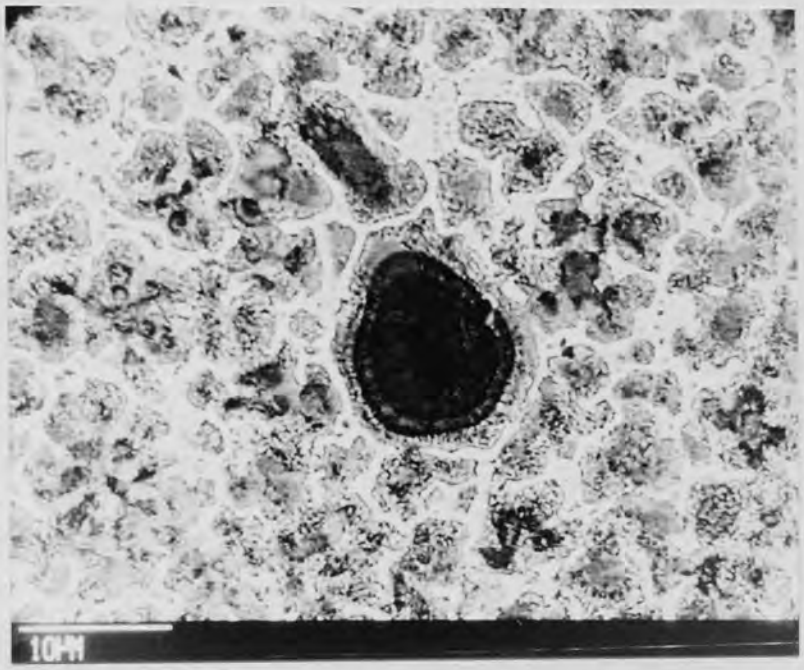

Figure 136. SEM. As-cast structure of die-cast alloy.7 at higher magnification, showing undecomposed β phase around cores.

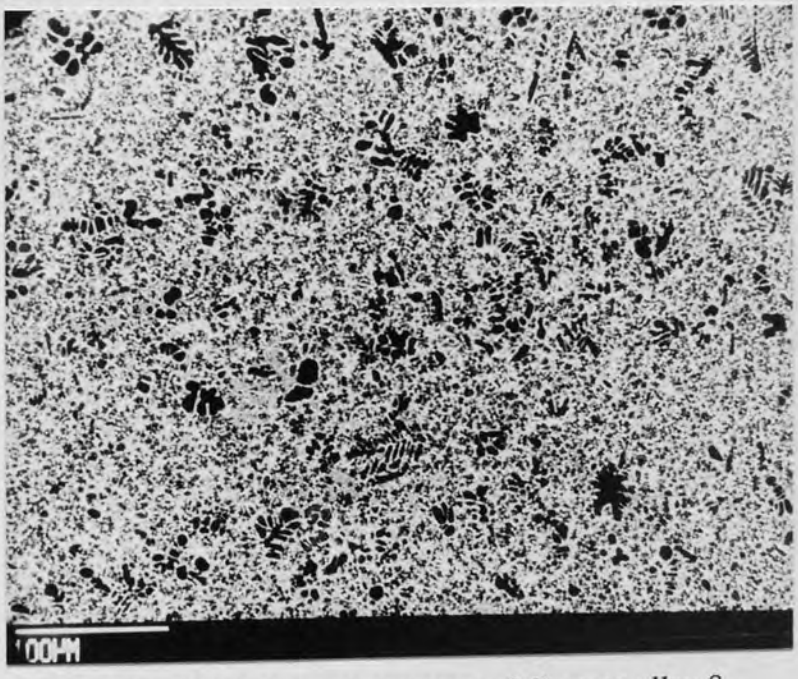

Figure 137. SEM. As-cast structure of die-cast alloy.8.

Figure 138. SEM. As-cast structure of die-cast alloy.8 at higher magnification.

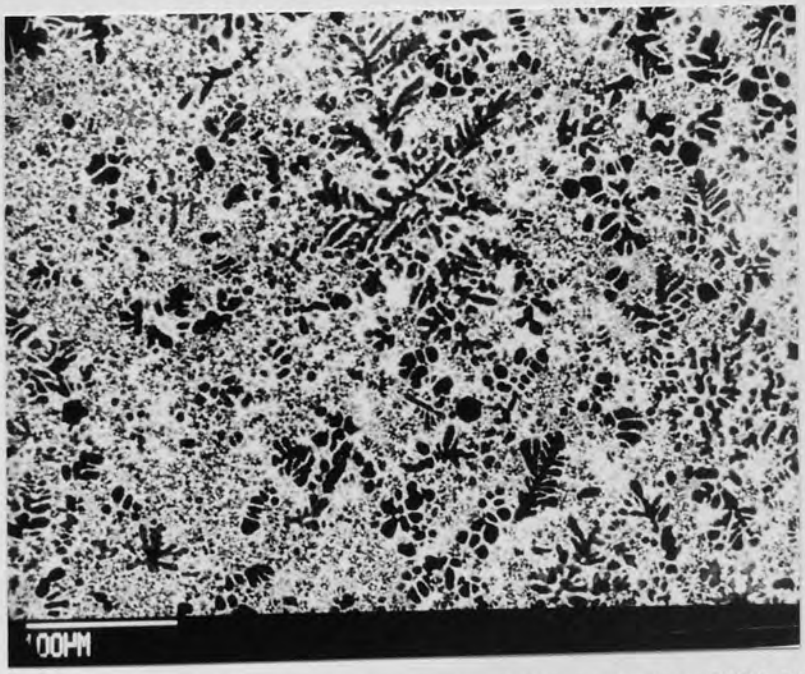

Figure 139. SEM. As-cast structure of die-cast alloy.9(ZA.27).

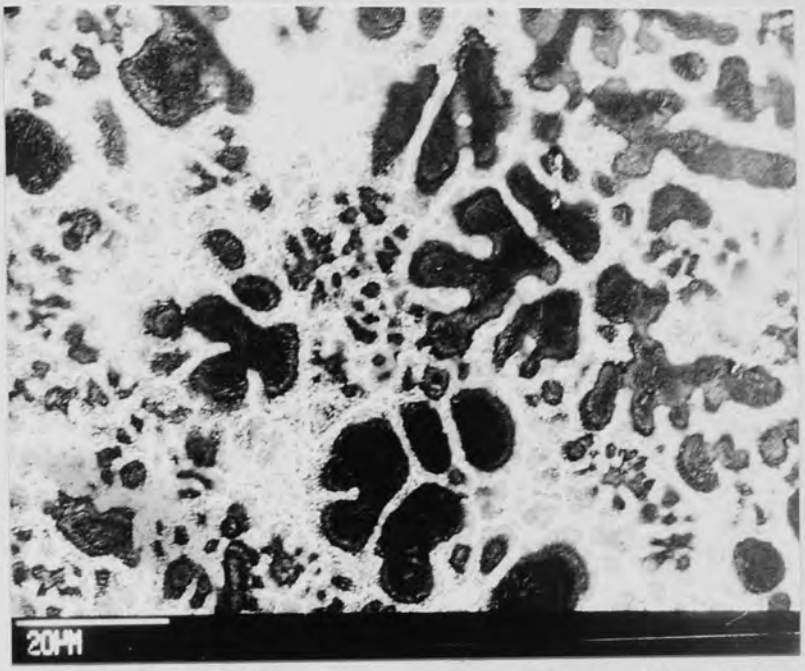

Figure 140. SEM. As-cast structure of die-cast alloy.9(ZA.27).

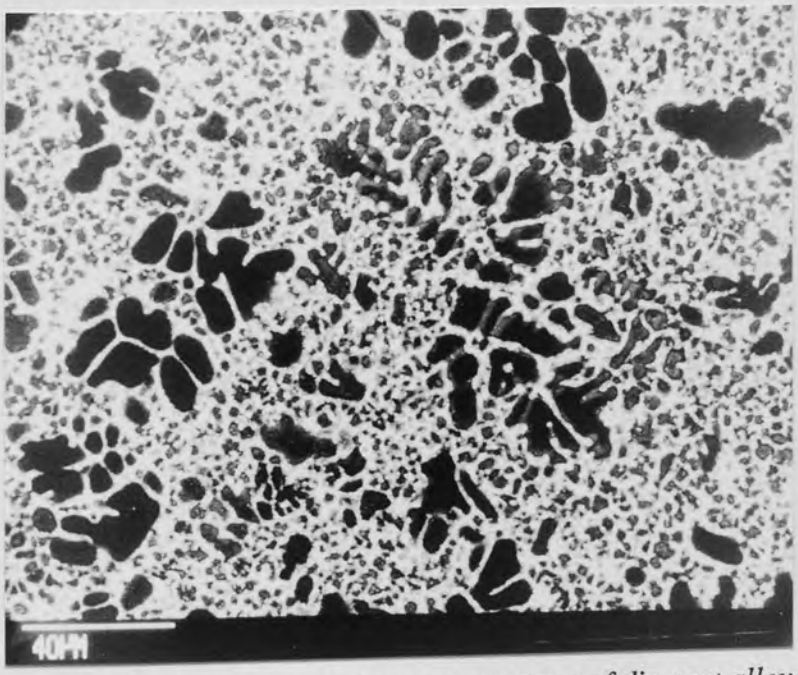

Figure 141. SEM. General as-cast structure of die-cast alloy.10.

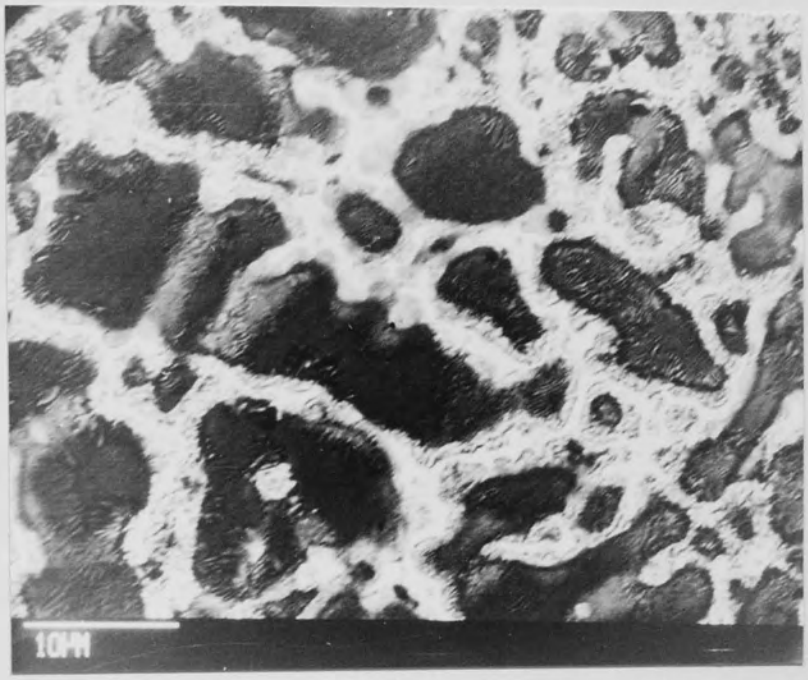

Figure 142. SEM. Cored structure of die-cast alloy.10 at higher magnification, with less β-phase around the cores

4.6 Gravity Cast Alloys

It appeared from the creep tests and metallography of the alloys that copper which preferentially precipitated as ε-phase in the eutectic zinc matrix had the most significant effect on the creep strength of the alloys and was the primary responsible element for the much high creep resistance of the alloy ZA.8 compared with Mazak.3. If so, an eutectic alloy with the same amount of copper should be expected to produce a better creep resistance than the alloy ZA.8. Unfortunately the aim of producing a true eutectic alloy by the pressure die-casting process failed due to the fast cooling rate of the process. In order to verify the above argument, two eutectic alloys 3 and 4 were gravity cast to obtain a better equilibrium freezing and, therefore, a true eutectic structure of the alloys. Alloy 5 (ZA.8) was also gravity cast in order to be able to compare the creep results of the alloys under the same casting conditions.

The structure of the eutectic alloys 3 and 4 was very similar. *Figure 143* shows the structure of the alloy 4 with well developed, regular lamellar cells of various sizes. Only at the points of impingement of the cells was the regularity of the lamellar structure disturbed.

The structure of the alloy 5 (ZA.8) is shown in *Figures 144 and 145* at low and high magnification, respectively. In *Figure 144* dendrites set in the eutectic were more well developed due to the slow cooling rate of the casting. *Figure 145* shows the dendrites in detail. As seen from this figure, the large central portion of a bigger dendrite decomposed into a perfect lamellar form, whereas the rim and other smaller particles formed into a particulate structure, which also appear to be in good agreement with the previous argument for the two different decomposition modes of the β phase.

Creep tests of these three alloys were carried out at 40MPa and 120°C in duplicate and

creep curves of the tests are shown in *Figure 146*. Creep data obtained from the curves were primary creep extensions, time to produce 1% creep strain and secondary creep rates, which are listed in *Table 14*.

As seen from the figure and table, total creep performance of the eutectic alloy.4 (with copper) was substantially better (by 235%) than alloy.5(ZA.8) which was, in turn, much better (by 220%) than the eutectic alloy 3 (with no copper).
Improvement obtained by copper addition in the eutectic alloy was 520%.
Decrease in the secondary creep rates obtained was also substantial and similar in the same order stated above (*Table 14*).

Table 14. Creep data of gravity-cast alloys tested at 40 MPa and 120°C.

Alloy	**Primary Creep (%)**	**Time to 1% CreepStrain (ks)**	**Secondary Creep Rate ($x10^{8}$;1/s)**
Alloy.3	0.25	47	8.78
"	0.18	63	9.52
Alloy.4	0.14	265	3.25
"	0.00	305	3.38
Alloy.5(ZA.8)	0.09	107	7.79
"	0.12	135	5.15

Examination of the creep curves in *Figure 146* clearly reveals that the improvements obtained in overall creep resistance were due to the increased period of the secondary creep regions with increasing eutectic zinc matrix in which ε-phase precipitated. This, in turn, clearly reveals that the creep strength of the eutectic derives from the precipitation-hardening due to the presence of small ε-precipitates in the zinc matrix.

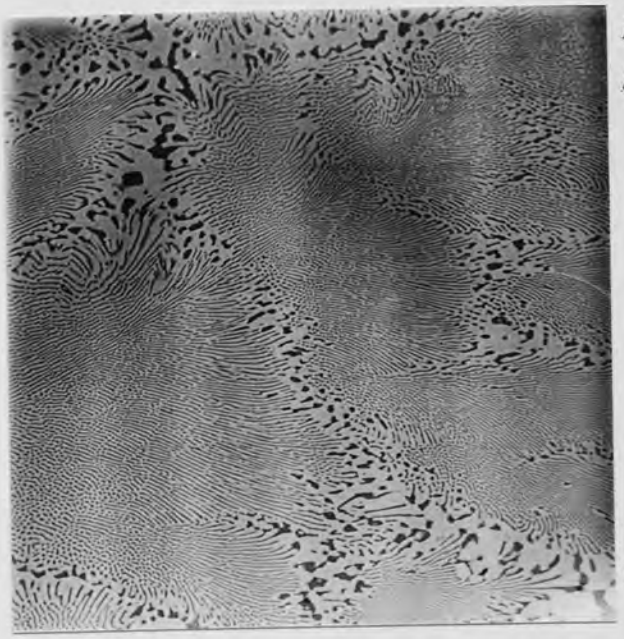

Figure 143. SEM. As-Cast structure of gravity-cast Alloy 4.

(400x)

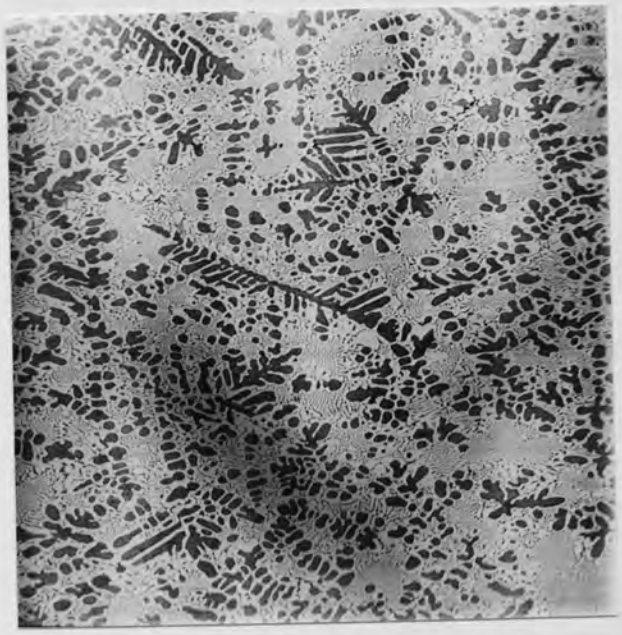

Figure 144. SEM. As-Cast structure of gravity-cast Alloy 5(ZA.8).

(160x)

Figure 145. SEM. As-Cast structure of gravity-cast Alloy 5(ZA.8).

(1560x)

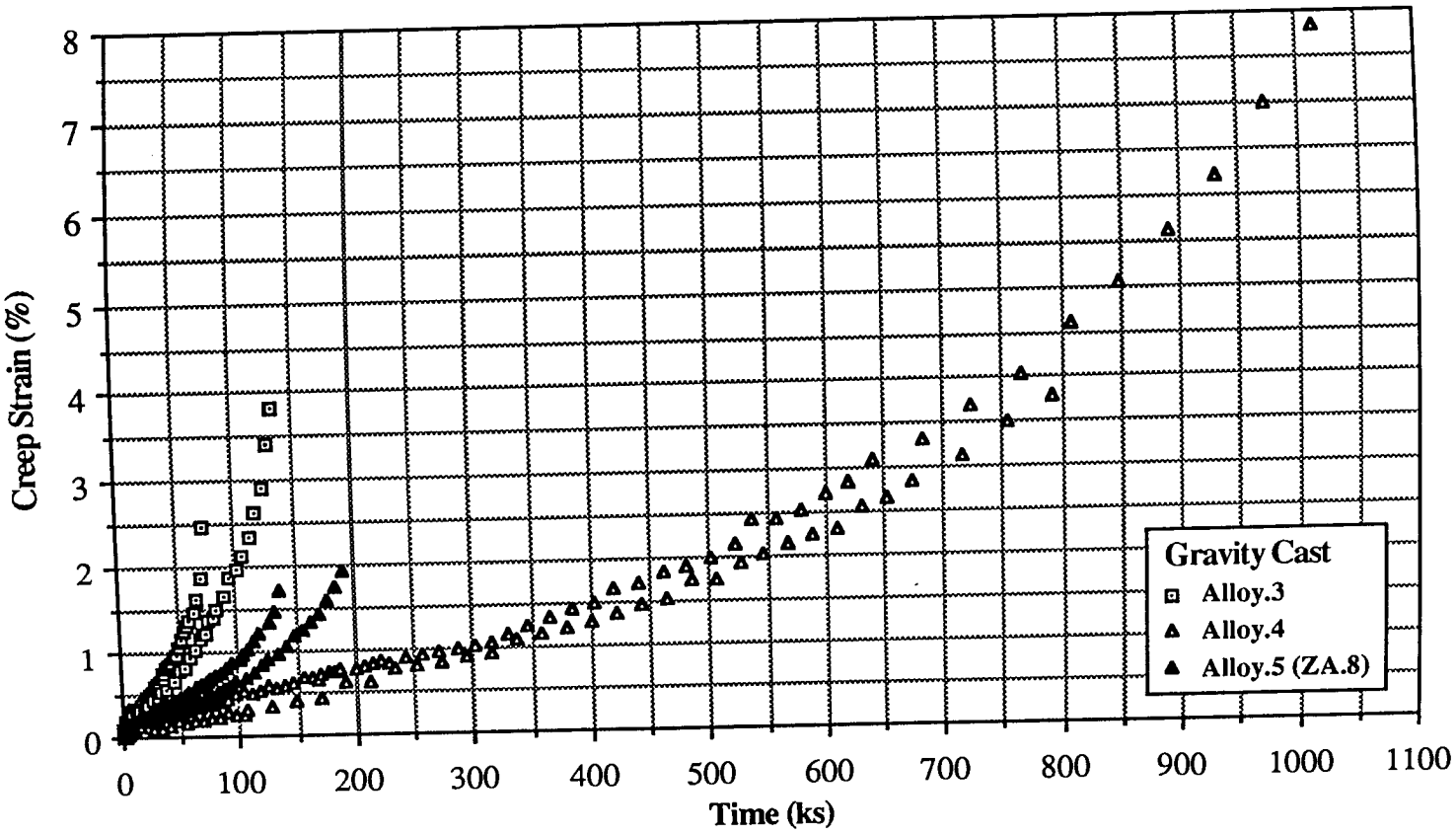

Figure 146. Creep curves of the gravity cast alloys 3,4 and 5(ZA.8), tested at 40MPa and 120 °C.

CHAPTER 5

5.0 DISCUSSION OF EXPERIMENTAL RESULTS

5.1 Correlation of Creep Data of the Commercial Alloys Mazak 3, ZA.8 and ZA.27

For any material, simple graphical representations of the creep curves under certain stress and temperatures are adequate to establish creep design data such as the time to attain a prescribed creep strain. However, the costs and duration of the experiments required to obtain long term design data are great. It is therefore, for many practical and theoretical purposes, necessary to seek mathematical relationships which would satisfactorily correlate the creep data obtained from a limited number of tests of relatively short duration and allow a quantitative assessment of the creep behaviour of a material under different conditions.

For that reason, numerous empirical or semi-empirical mathematical relationships suggested in the literature are exclusively based on secondary creep rate data as steady-state behaviour is considered as the most definitive characterisation of creep behaviour of materials, offering numerous advantages.

However, the relative importance of the primary, secondary and tertiary creep regions may vary significantly with variations in stress, temperature and/or metallurgical structure.

As far as the metallurgical structure is concerned, the present study showed that the primary creep extension of the experimental alloys increased dramatically with increasing aluminium content *(Figures 55 and 125)*. Especially in the case of alloys ZA.8 and ZA.27 the primary creep elongation was increasingly higher with significant average values of 0.23 and 0.50% respectively, and these considerable amounts of creep strains were reached in a very early stage of the creep life of these alloys. The

primary creep extension of the latter alloy (ZA.27) was also found to be strongly dependent on temperature and increased rapidly with increasing temperature *(Figure 54)* and in some experiments, as shown in *Figure 53* for example, 1% creep strain was reached in the primary creep region.

On the other hand, for the alloy Mazak 3, which showed the least amount of primary creep extension of all, duration of the secondary creep regions of the tests were comparatively short, and in the majority of the tests a creep strain of 1% was reached in tertiary creep region *(Figures 42 to 45)*.

If it is considered that the time to attain a specified creep strain, say 1% or so, is an essential requirement for many engineering design procedures, any approach which is to be based on the secondary creep rate data of the experimental alloys would obviously lead to an inaccurate over-estimation of such strains.

On the other hand, the observation of linear relationship between applied stress and the time to attain 1% creep strain in *Figures 60, 61 and 62* for alloys Mazak 3, ZA.8 and ZA.27 respectively had indicated that the times to a given elongation were a simple power law function of the applied stress, and implied that the total creep elongation of the alloys could be correlated by *equation 21* which had been originally used by Murphy and Savaskan[117] to correlate experimental data of gravity cast alloys of near-eutectoid composition. Later it was indeed shown by two co-operative works of the author [141,152] (see Appendix B) that *equation 21* was able to correlate the total creep elongation (up to 1%) of the alloys with the testing conditions where n = 3.5 and Q = 106 KJ/mole for all alloys tested. Here *equation 21* was:

$$f(\varepsilon) = A\, t\, \sigma^n \exp(-Q/RT)$$

where A is a constant which takes into account the effects of composition and

metallurgical structure, σ the nominal stress, n the stress exponent, t the creep time, Q an effective activation energy for creep, R the universal gas constant, T the absolute temperature of the tests, and $f(\varepsilon)$ an undefined function of the creep strain ε, and when A, σ, n, Q and T are constant, $f(\varepsilon)$ represents the shape of the creep strain versus time curve.

Based on the above derived equation, the parametric plots for the alloys have shown that the total creep extension (up to 1%) can be related to the applied stress, temperature and the time of the tests. However, deviations from the constant slopes, as seen in *Figures 60 to 62*, predicted by the power law function of *the equation 21* were found at high stresses above 40 MPa in all alloys, and at very low stresses at 150°C in alloys ZA.8 and ZA.27, indicating that the general applicability of the equation holds only up to 40 MPa and 120°C. A metallographic study in the present study showed that the latter effects were primarily due to phase coarsening *(Figures 99 to 101 and 122,123)* and partial transformation of small ε precipitates into T' phase *(Figures 102,103).*

The reason for the increased slopes at high stresses is not clear, but based on the existing knowledge of secondary creep rates, similar behaviour, known as power law break-down, is frequently observed and is attributed to a change in the mechanism of creep at high stresses. In these regions, the stress dependence of the creep rate is better expressed by an exponential form of the stress *(Equation 15).*

In order to see the correlation of the creep data of the experimental alloys by a similar equation, which will also yield a new constant (β) to be used in the final equation later, a similar equation to *equation 21*, incorporating an exponential form of stress-dependence, can be written as:

$$f(\varepsilon) = B\, t \exp(\beta\sigma) \exp(-Q/RT) \qquad (22)$$

where B, β and R are constants. Similarly, taking logarithms and rearranging:

$$\ln t = \ln f(\varepsilon) - \ln B - \beta\sigma + Q/RT$$

but at constant strain:

$$\ln t = B' - \beta\sigma + Q/RT$$

where B' is a new constant which incorporates B and ε. If this relation is obeyed, a plot of ln time to any fixed creep strain against stress at constant temperature should be linear with a slope of $-\beta$. Such plots as ln time to 1% creep strain against stress were plotted and shown in *Figures 147, 148 and 149* for alloys Mazak 3, ZA.8 and ZA.27, respectively. As seen from these figures, the plots were in fact all linear at high stress levels (above about 30 MPa) with a constant slope of $-\beta$ for each alloy. The value of β was calculated by a linear regression analysis in high stress regions and found to be *0.085* for the alloys Mazak 3 and ZA.27 and *0.093* for alloy ZA.8. Quite severe deviations from the constant slopes however, occurred at low stresses below about 30 MPa for all alloys tested.

Alternatively, putting together these observations and taking inspiration from the original relation of Garofalo,*(Equation 16)* which has been shown to correlate secondary creep rate data of many metals and alloys satisfactorily[26], a new single relation can be written to inter-relate the creep data of the experimental alloys for all ranges of stresses as:

$$f(\varepsilon) = C \cdot t \cdot (\text{Sinh } \alpha\sigma)^n \exp(-Q/RT) \qquad (23)$$

where, in addition to previously defined terms, C and α are constants.

For low stress levels where $\alpha\sigma < 0.8$ the above equation can be approximated by[1]:

$$f(\varepsilon) = C\, t\, \alpha^n\, \sigma^n \exp(-Q/RT)$$

Thus, *relation 23* reduces to *relation 21* for low stress levels, where $C\,\alpha^n = A$, which has been shown to correlate the creep data of the alloys at low stresses *(Figures 60 to 62)*.

For high stress levels where $\alpha\sigma > 1.2$, *the equation 23* can also be well approximated by[2]:

$$f(\varepsilon) = \frac{C}{2^n}\, t\, \exp(n\,\alpha\,\sigma)\, \exp(-Q/RT)$$

This equation is also the same equation as *relation 22*, where $C / 2^n = B$ and $\alpha = \beta / n$, which has also been shown to correlate the creep data of the experimental alloys *(Figures 147, 148 and 149)*.

So, the constant α in the single *equation 23* was calculated from the previously established values of n and β and found to be 2.43×10^{-2} for the alloys Mazak 3 and ZA.27, and 2.66×10^{-2} for the alloy ZA.8.

Knowing the α value for each alloy in the single *equation 23* and taking logarithms and rearranging gives:

---

[1] For $\alpha\sigma = 0.8$, the difference between $\sinh \alpha\sigma$ and $\alpha\sigma$ is less than 10% and for smaller values of $\alpha\sigma$ this difference diminishes very rapidly.

[2] For $\alpha\sigma = 1.2$, the difference between $\sinh \alpha\sigma$ and $(e^{\alpha\sigma} / 2)$ is less than 10% and for greater values of $\alpha\sigma$ the difference diminishes again very rapidly.

$$\ln t = \ln f(\varepsilon) - \ln C - n \ln [\text{Sinh}(\alpha\sigma)] + Q/RT$$

but for a fixed creep strain:

$$\ln t = C' - n \ln \text{Sinh}(\alpha\sigma) + Q/RT$$

where C' is a new constant which incorporates C and ε.

If this final equation is obeyed for the experimental alloys studied here, a plot of ln time to any fixed creep strain against ln [Sinh(ασ)] at constant temperature should yield straight lines of slope (-n) with an intercept of (C' + Q/RT), or a plot of the ln time to any fixed creep strain versus 1/T at constant stress should be linear with a slope of Q/R, and an intercept of [C' - n ln (Sinh (ασ))].

Such plots, as shown in *Figures 150 to 152*, plotted as ln time to 1% strain versus ln [Sinh (ασ)] were in fact all linear with a very good correlation of the experimental data, cover all stress and temperature ranges for all alloys studied, indicating a new stress exponent (n) of *3* for the alloys Mazak 3 and ZA.27 *(Figures 150 and 152)* and *3.2* for the alloy ZA.8 *(Figure 151)*. Deviations from these constant slopes occurred only for the alloy ZA.8 and ZA.27 at 150°C at very low stress levels (below 15 MPa) where the phase coarsening was shown to take place to a significant degree in these high temperature, long-term tests.

The plot of ln time to 1% creep strain versus 1/T at 20 MPa shown in *Figure 153* for all three alloys was also linear with a very good correlation of the data, indicating an activation energy for creep (Q) of *106 kJ/mole* for the alloys Mazak 3 and ZA.27, and *99 kJ/mole* for the alloy ZA.8. These activation energies are the same as those reported in previous work[141,152] for the alloys Mazak 3 and ZA.27. In the case of the alloy ZA.8, however, it is lower, due to additional tests carried out at 60°C for this

alloy in the later course of the work.

So far, it has been shown that all of the above linear plots were in accordance with the form of the single equation used and thus the creep behaviour of the alloys could be related to the testing conditions by this single equation over all stress and temperature ranges, with exception of where phase coarsening occurred. Once the values of α, n and Q are known, the constant C', which is characteristic for each alloy and the chosen % strain, can be calculated from the intercepts (C' + Q/RT) or [C' - n ln (Sinh ($\alpha\sigma$))]. Such a parametric plot, therefore, should allow the total creep strain to be calculated for any combination of temperature, applied stress and time.

However, a considerable degree of extrapolation is required to obtain C' in this way. Instead, C' is obtained and correlation of the data is shown more clearly by a parametric plot of {Q/RT - n ln [Sinh ($\alpha\sigma$)]} against ln time to a given % elongation, which should give linear plots of 'unit slope' and intercept a characteristic constant for the alloy and the chosen % strain, and the differences in creep behaviour between the alloys are derived solely from differences in the values of this constant.

Figures 154, 155 and 156 show plots of ln time to creep elongations of 0.2, 0.5, 0.7 and 1% creep elongation versus the above parameter for the alloys Mazak 3, ZA.8 and ZA.27, respectively, using the unsmoothed original data from individual creep curves *(Appendice A)* and excluding the data at stress levels below 15 MPa at 150°C for the alloys ZA.8 and ZA.27, where phase coarsening occurred.

Linear regression analysis carried out to check the correlation of the data and the results, slope, intercepts and coefficient of correlation (R) of the regressions are listed in *Table 15* with intercepts (C') obtained from the unit slopes of the plots. As seen from the table, although there is a good deal of scatter in the 0.2% plots, where differences between individual tests are most marked, a very good correlation of the

data is obtained in general by the parametric plots, showing that the parameter may be used to estimate the creep behaviour of the alloys with high confidence.

In order to compare the relative creep performances of the alloys for the same amount of creep elongation, the parametric plots for creep elongations of 1.0, 0.7, 0.5 and 0.2% are plotted in *Figures 157 to 160*, respectively. These figures clearly show that alloy ZA.8 has a substantially better creep performance than the alloy ZA.27 for all strain levels, and the alloy ZA.27 in turn is marginally better than the alloy Mazak 3 for creep elongations higher than 0.5%, but inferior for smaller strains due to its higher primary creep contribution to the total creep strains.

For general use of the *equation 23*, values of the constant C' listed in *Table 15* are plotted against % elongations as C' versus ln (% creep elongation) in *Figure 161* for all three alloys. Such a plot yielded a linear relationship, with a good correlation of the data, so that the value of C' can be calculated from the plot easily for any given % elongation and using the *equation 23*, such data can be used to calculate the permissible combinations of stress, temperature and creep life for any creep strain within the range of 0.2 to 1.0%.

For practical purposes, the maximum continuous design stresses which will produce 0.2%, 0.5%. 0.7% or 1.0% creep strains in 100,000 hrs (11.4 years) at various temperatures were calculated. These are listed in *Table 16* and the results of the calculations are also plotted as a family of curves in *Figures 162, 163 and 164* for the alloys Mazak 3, ZA.8 and ZA.27, respectively, which enable the creep strain within the range of 0.2 to 1.0% to be determined from any combination of stress and temperature for service lives of 100,000 hrs (11.4 years).

Although the general applicability of the parametric plot is not valid for stress levels below 15 MPa at 150°C for the alloys ZA.8 and ZA.27, maximum design stresses

predicted by the equation and included in the *Table 16* and *Figures 163, 164* are not true stresses reflected by the equation, but they can be used with extra higher safety since the actual creep resistance of the these alloys in this range will be much higher due to the phase coarsening phenomenon noted earlier.

Design stresses shown in the above figures are in good agreement with those of the previously reported works [141,152] for the alloys Mazak.3 and ZA.27 within the applicability range of the equation used. For the case of the alloy ZA.8, however they were considerably lower and this was mainly due to the lower activation energy for creep for this alloy found as a result of additional experiments carried out at 60°C.

The Equation 23 has been found to estimate allowable design stress for a given temperature and elongation under different conditions in a very close agreement with all known data of the alloy Mazak.3 which is the only experimental alloy for which long-term actual creep data are available in the literature (*Figure 27*). For example, *Figure 27* which presents the experimental data of this alloy at at 25°C indicates an allowable design stress of 30 and 25.8 MPa to produce 0.5% total creep strain in 5 and 10 years respectively. The allowable design stresses for the same amount strain in the same periods at 25°C is estimated by the empirical equation as 31.9 and 26.16 respectively, which are in extremely close agreement with the actual data of the alloy, proving the reliability of the equation that can be used with high confidence even for long-term design lives.

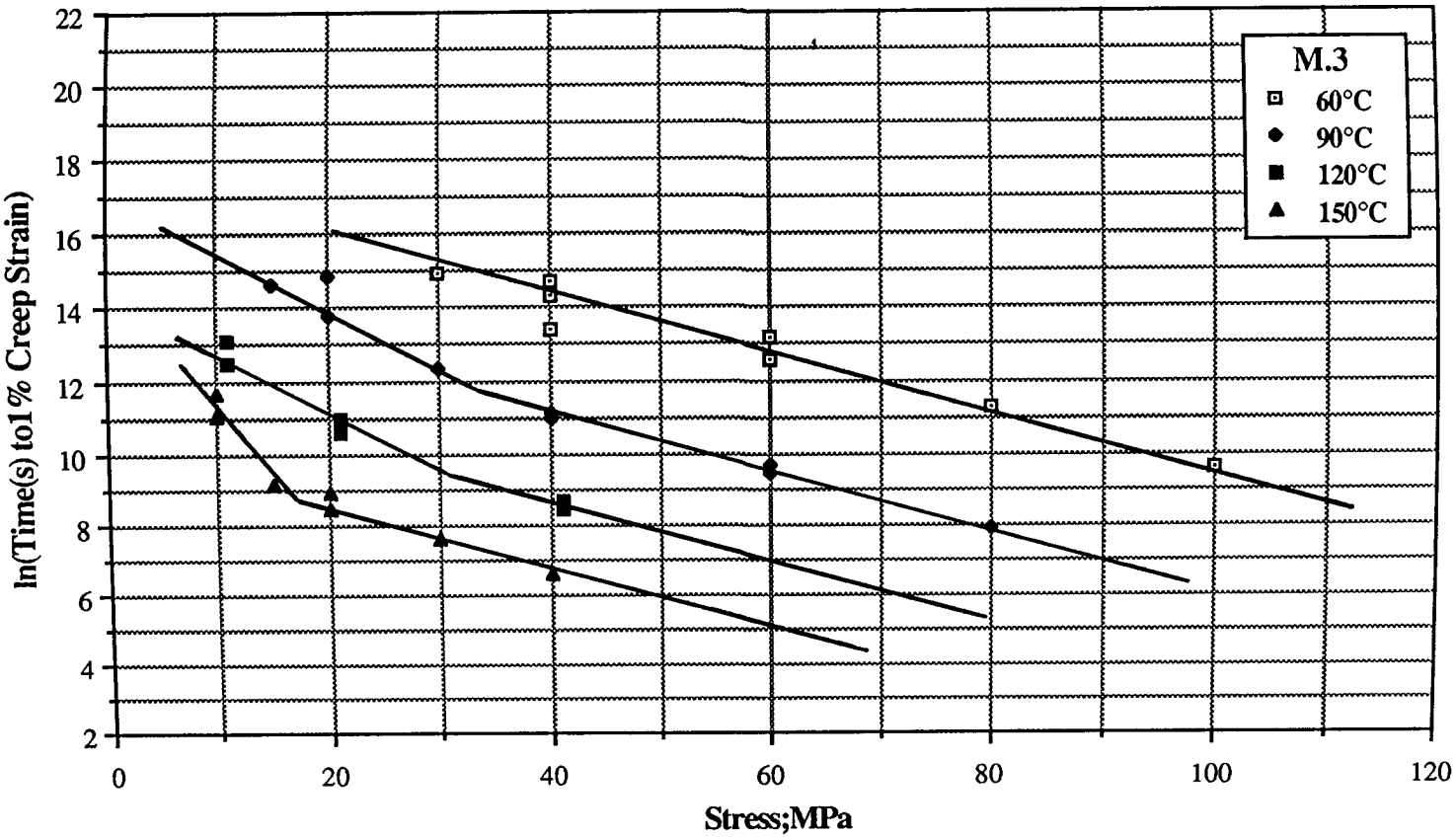

Figure 147. Variation of ln(times(s) to 1% creep strain with stress for alloy Mazak.3 at different temperatures.

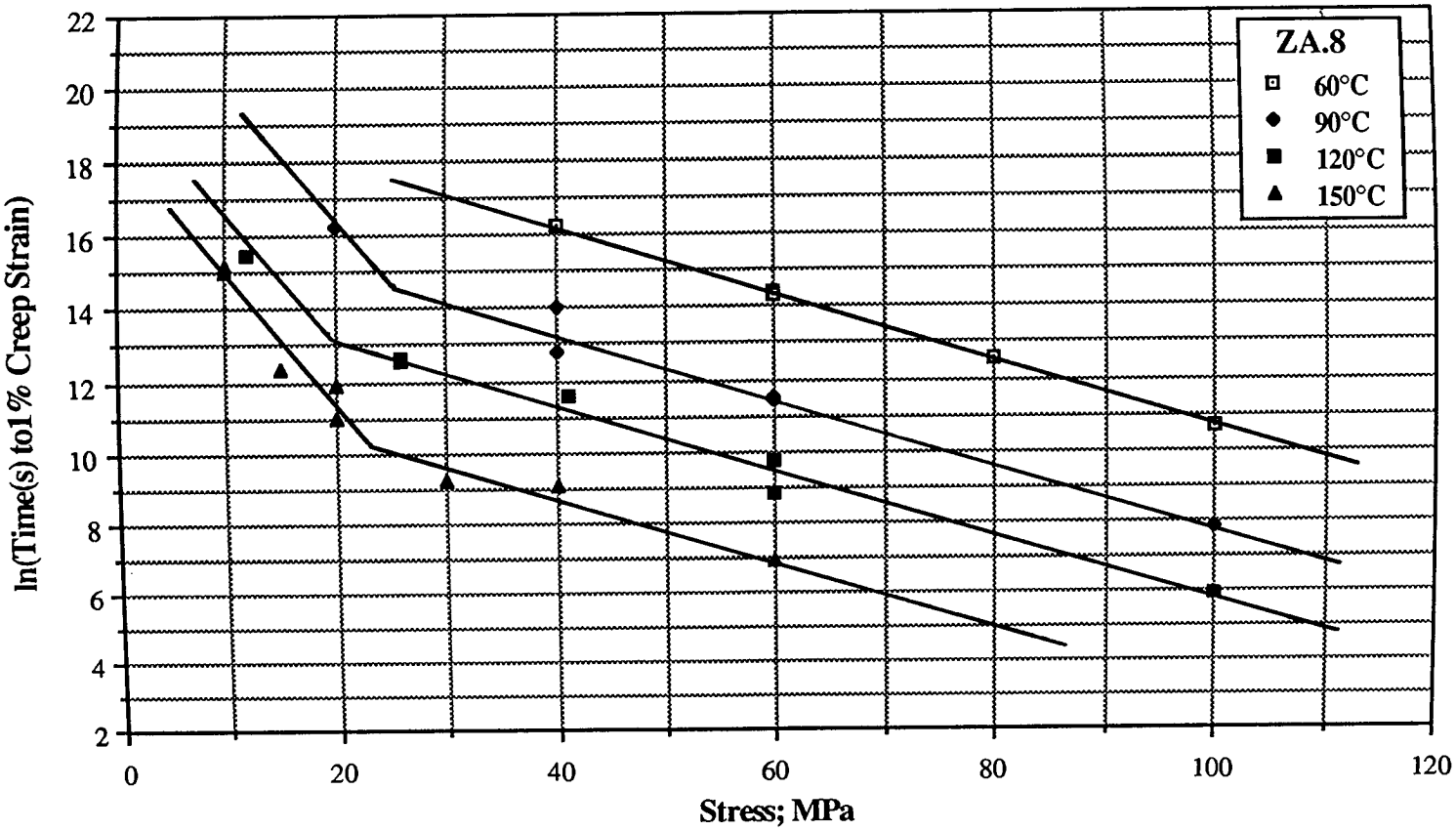

Figure 148. Variation of ln(times(s) to 1% creep strain with stress for alloy ZA.8 at different temperatures.

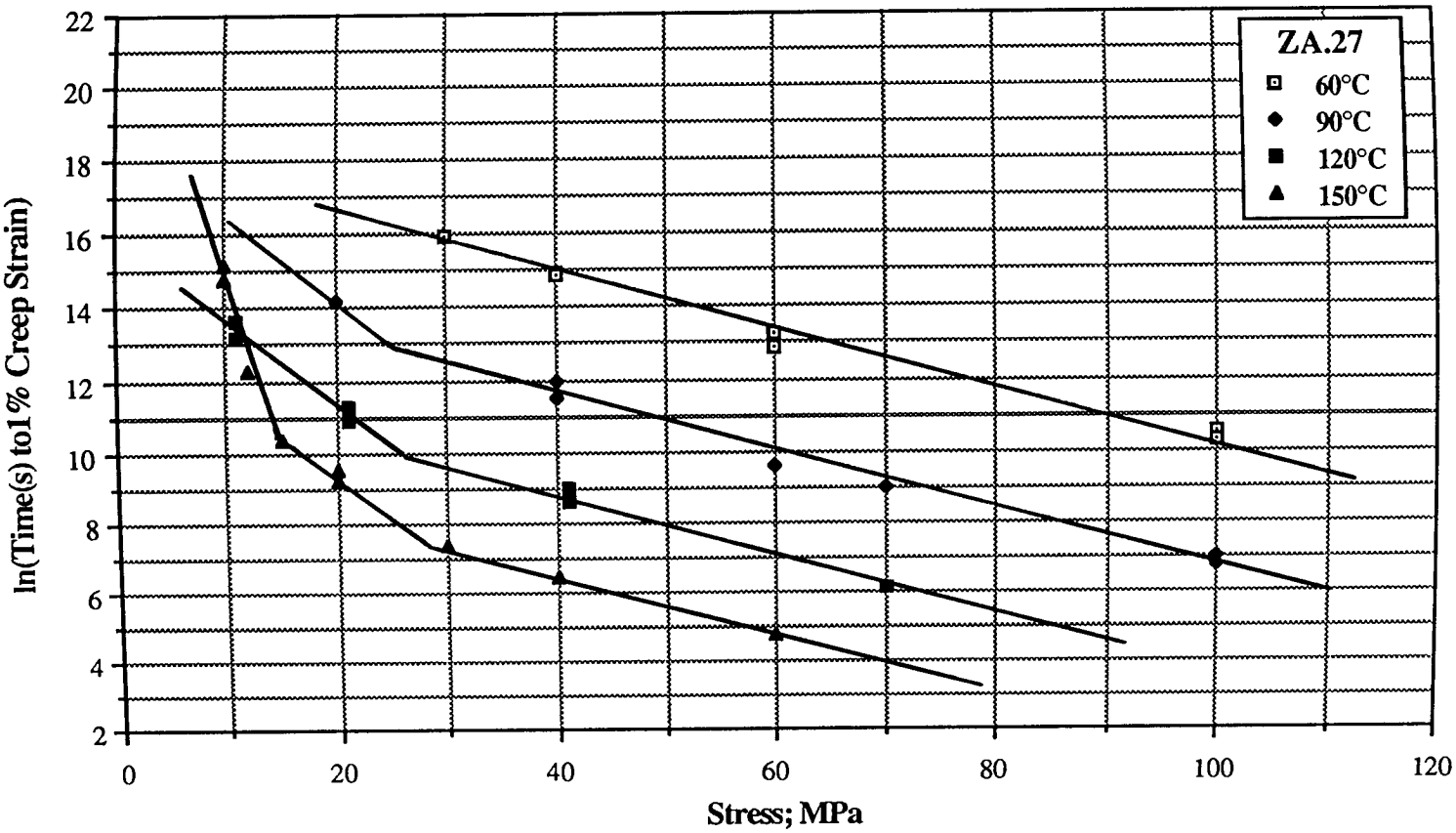

Figure 149. Variation of ln(times(s) to 1% creep strain with stress for alloy ZA.27 at different temperatures.

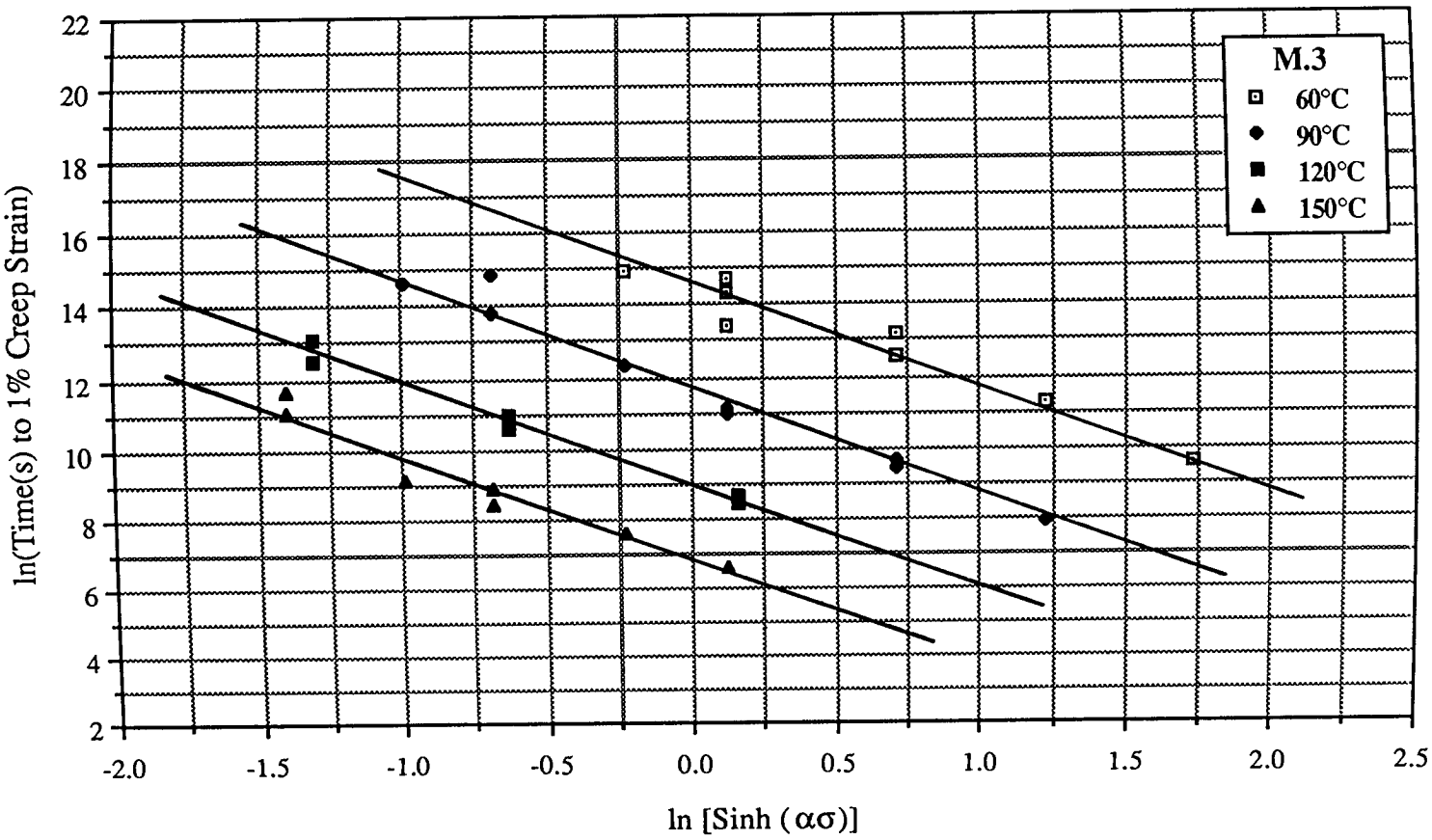

Figure 150. Variation of ln(times(s) to 1% creep strain with ln[Sinh(ασ)] for alloy Mazak.3 at different temperatures.

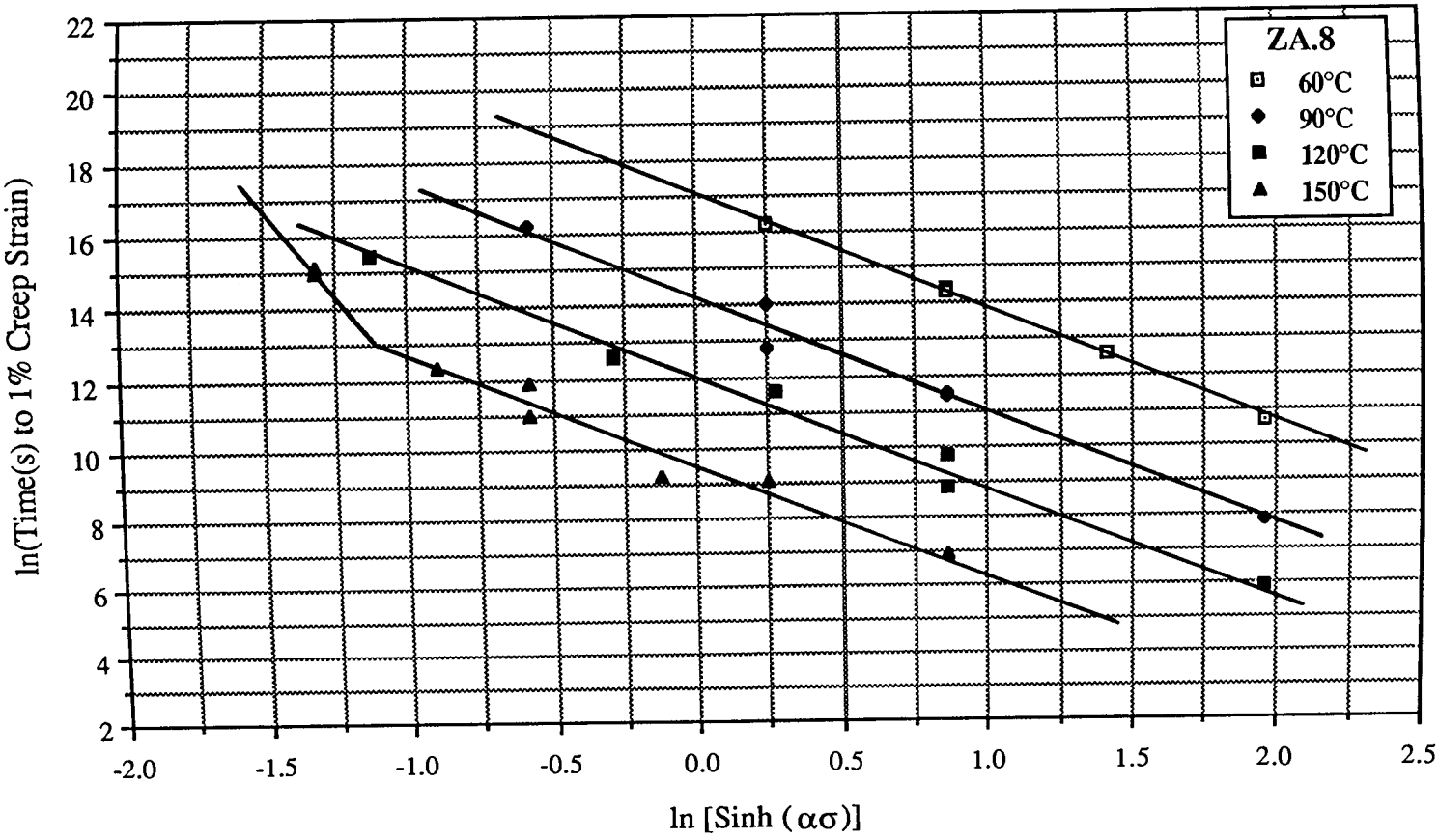

Figure 151. Variation of ln(times(s) to 1% creep strain with ln[Sinh(ασ)] for alloy ZA.8 at different temperatures.

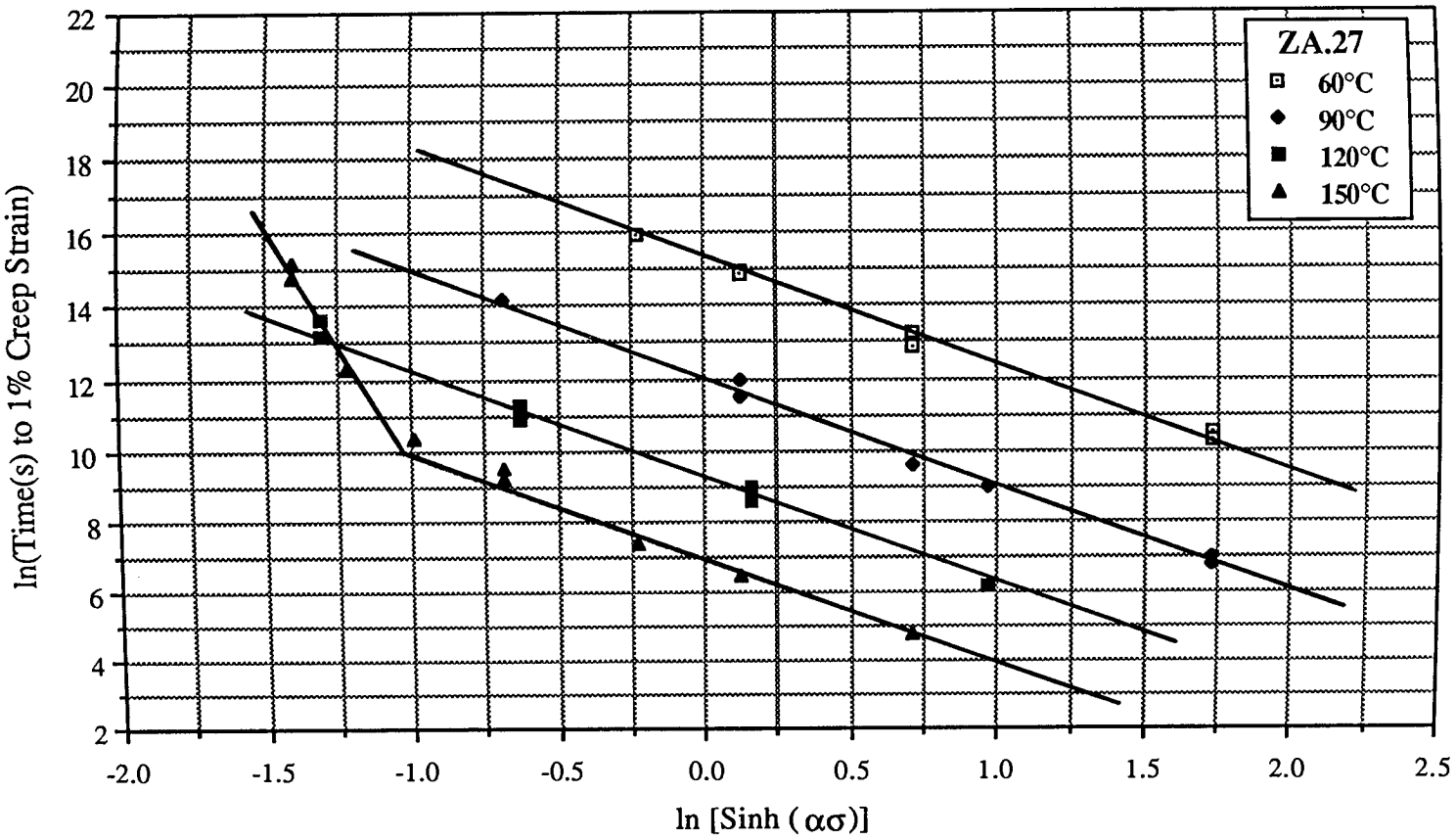

Figure 152. Variation of ln(times(s) to 1% creep strain with ln[Sinh(ασ)] for alloy ZA.27 at different temperatures.

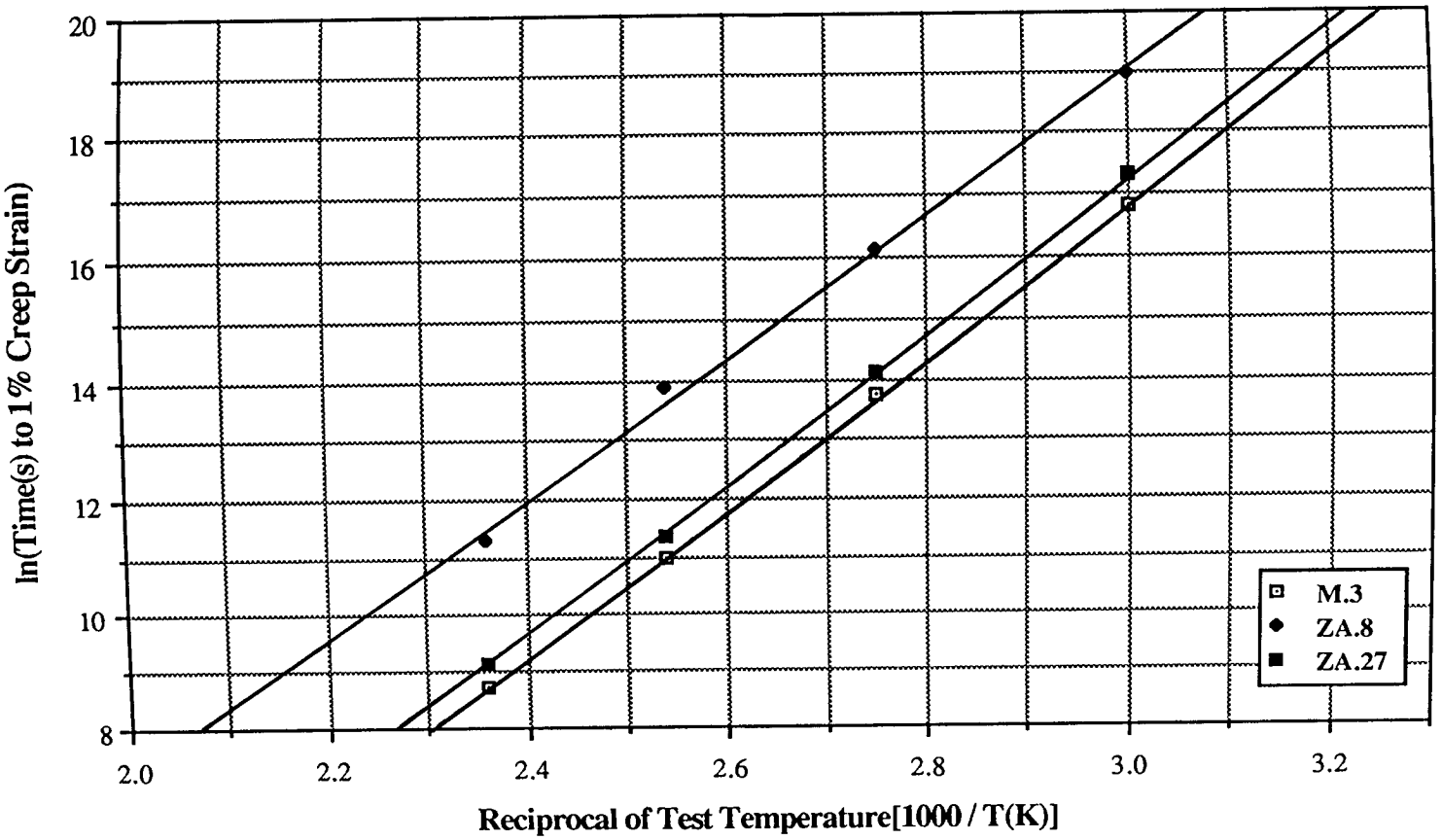

Figure 153. Ln times(s) to 1% creep strain versus reciprocal of test temperature for all 3 alloys at 20 MPa.

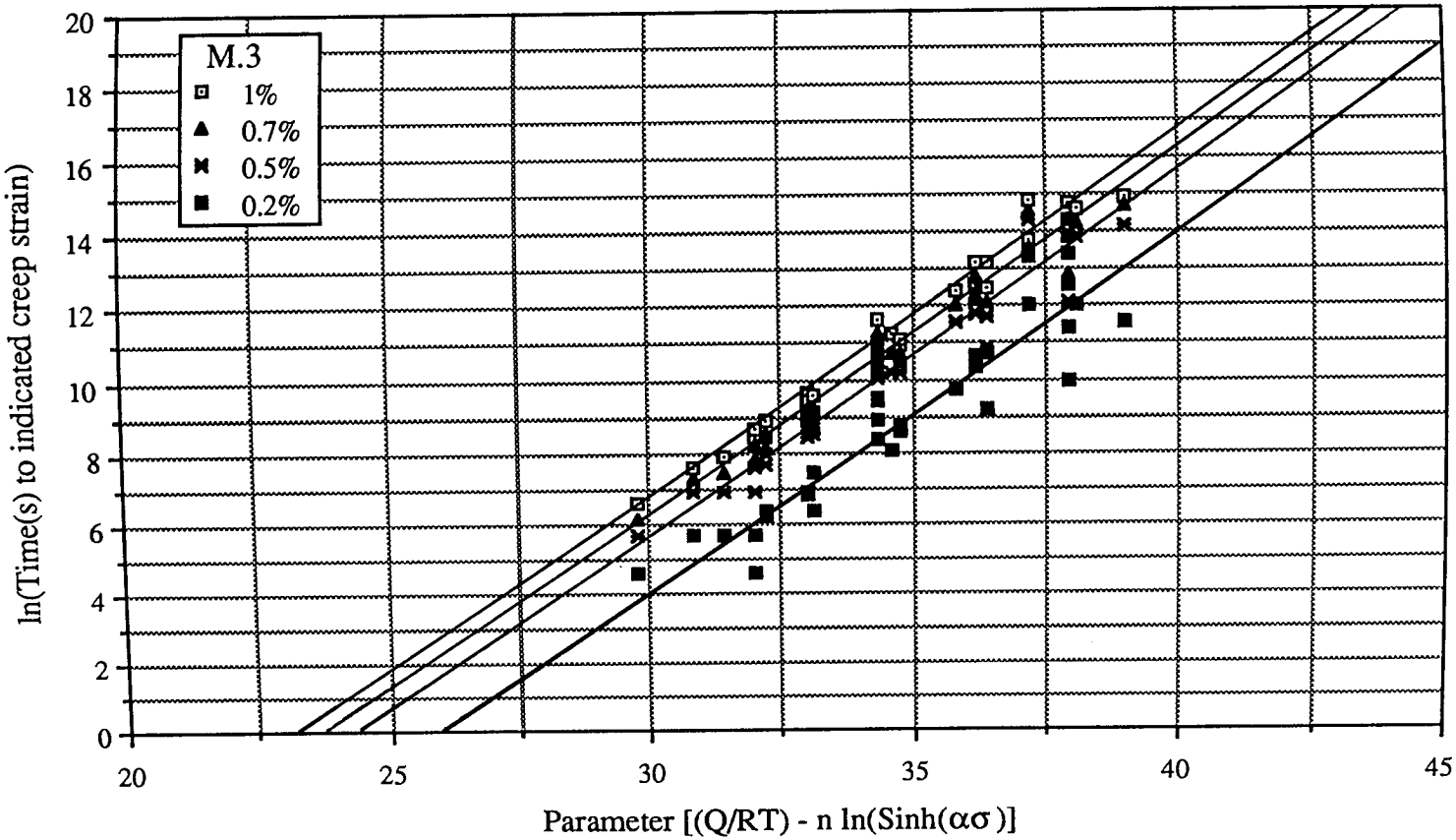

Figure 154. Ln(times(s) to various creep strains versus creep parameter for alloy Mazak.3.

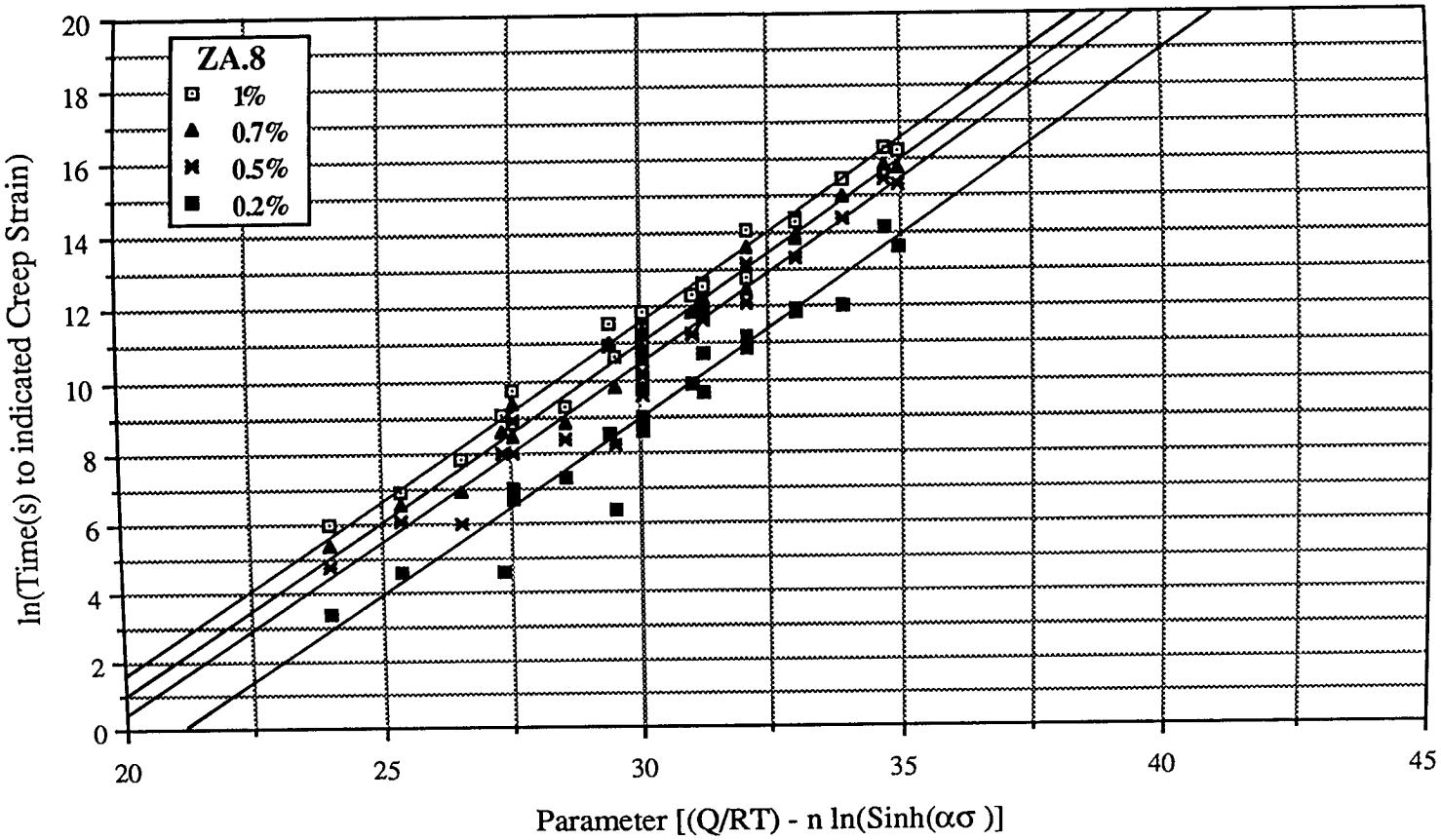

Figure 155. Ln(times(s) to various creep strains versus creep parameter for alloy ZA.8.

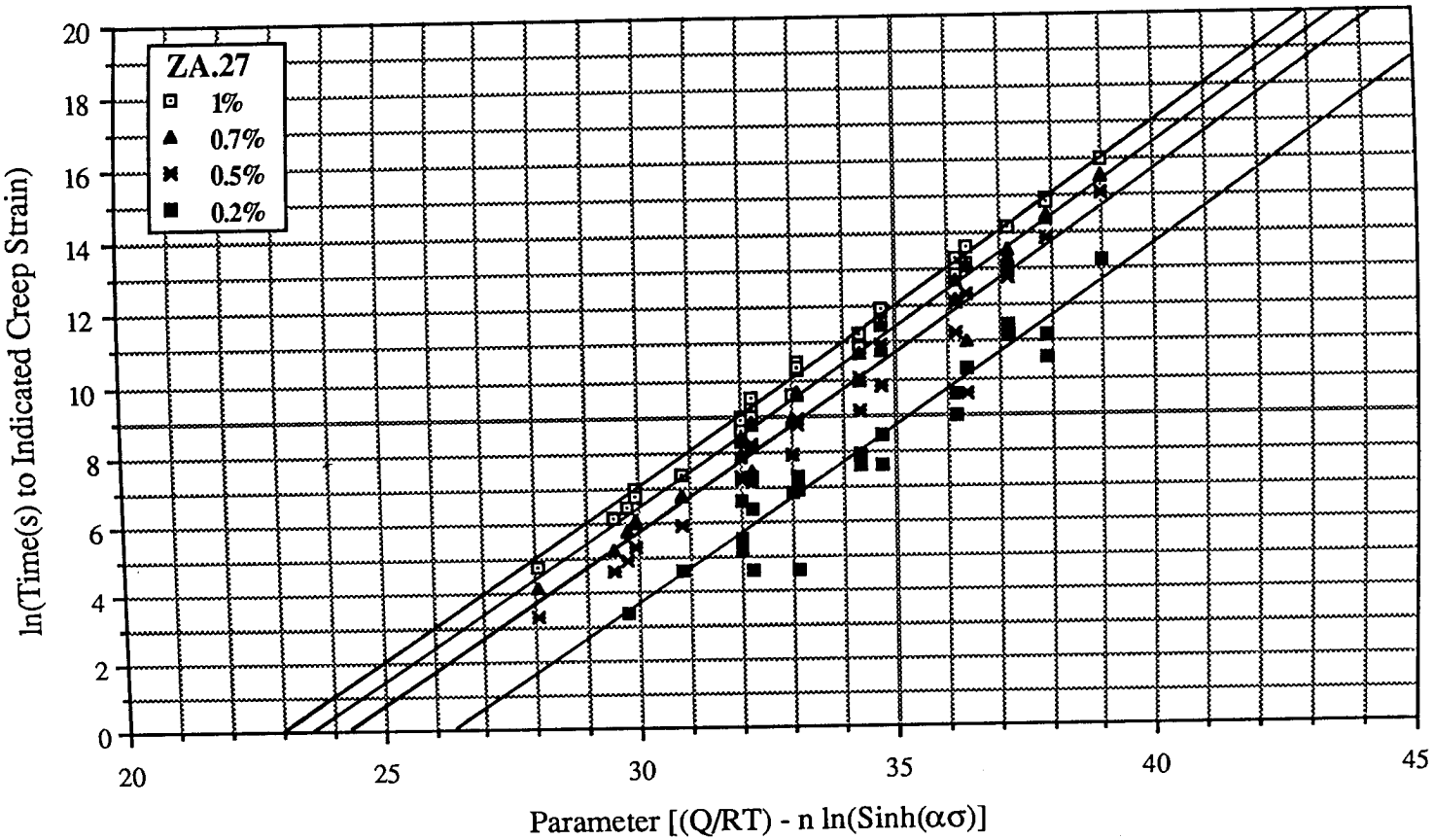

Figure 156. Ln(times(s) to various creep strains versus creep parameter for alloy ZA.27.

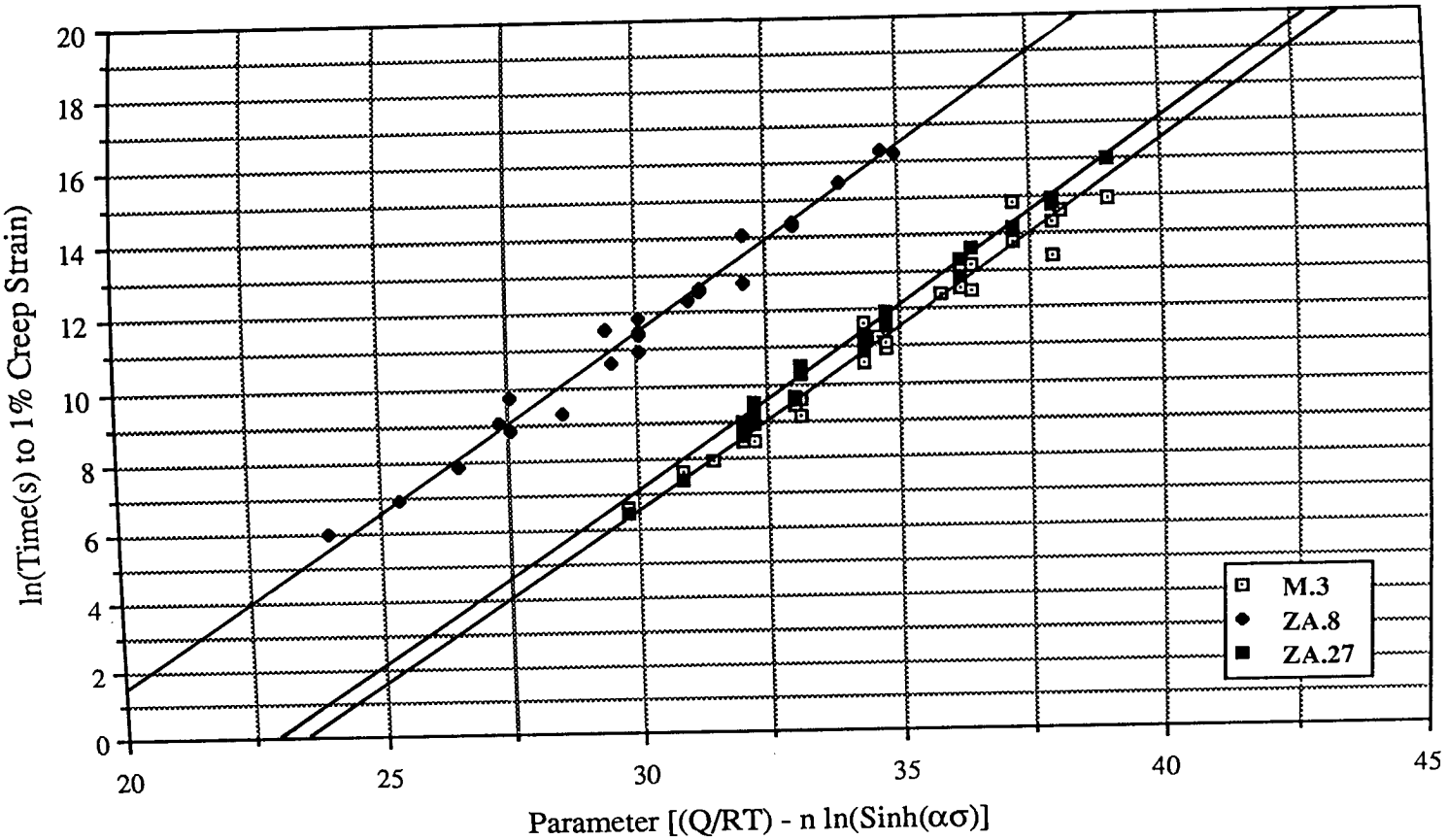

Figure 157. Ln times(s) to 1% creep strain versus creep parameter for alloys Mazak.3, ZA.8 and ZA.27.

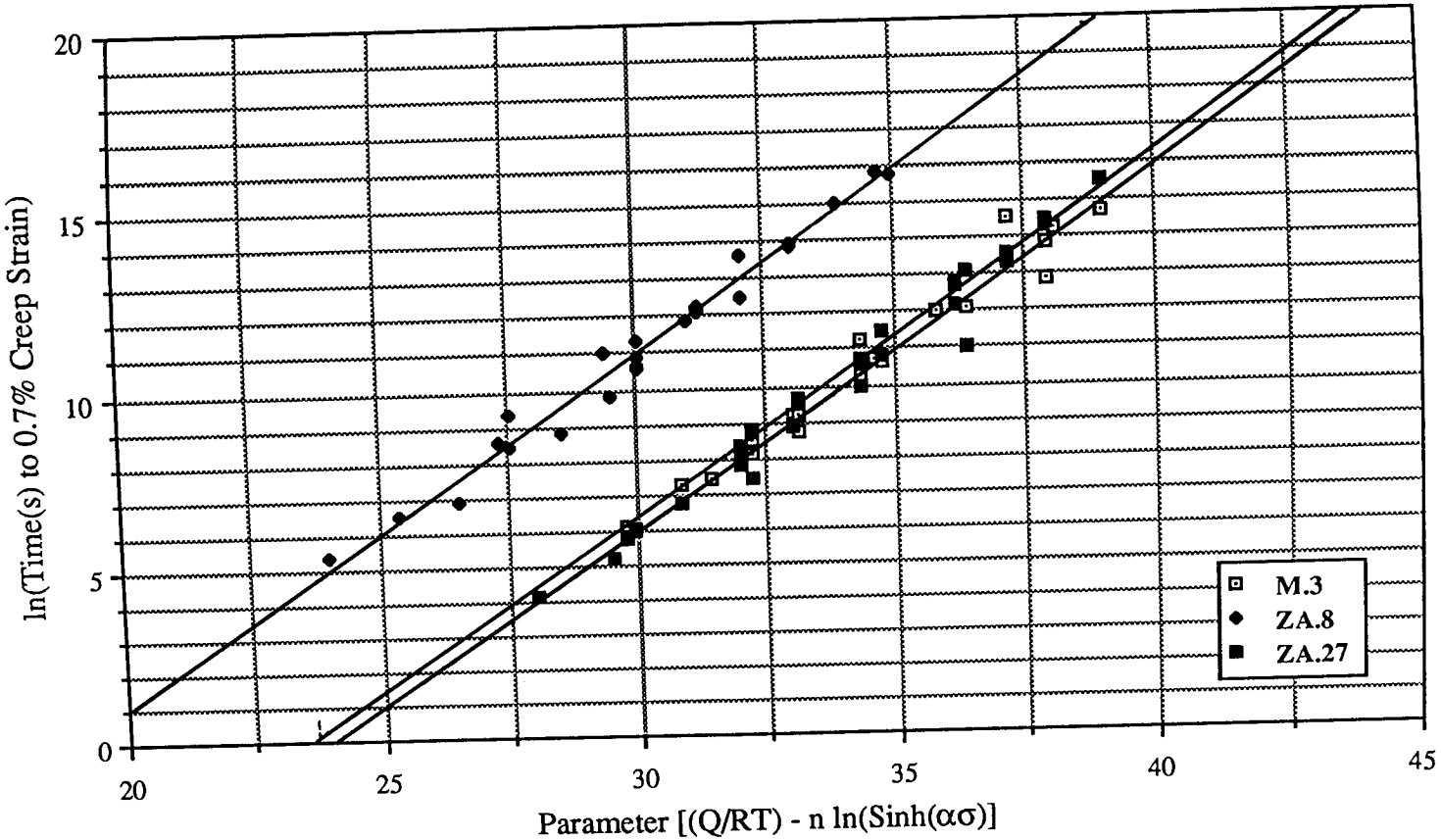

Figure 158. Ln times(s) to 0.7% creep strain versus creep parameter for alloys Mazak.3, ZA.8 and ZA.27.

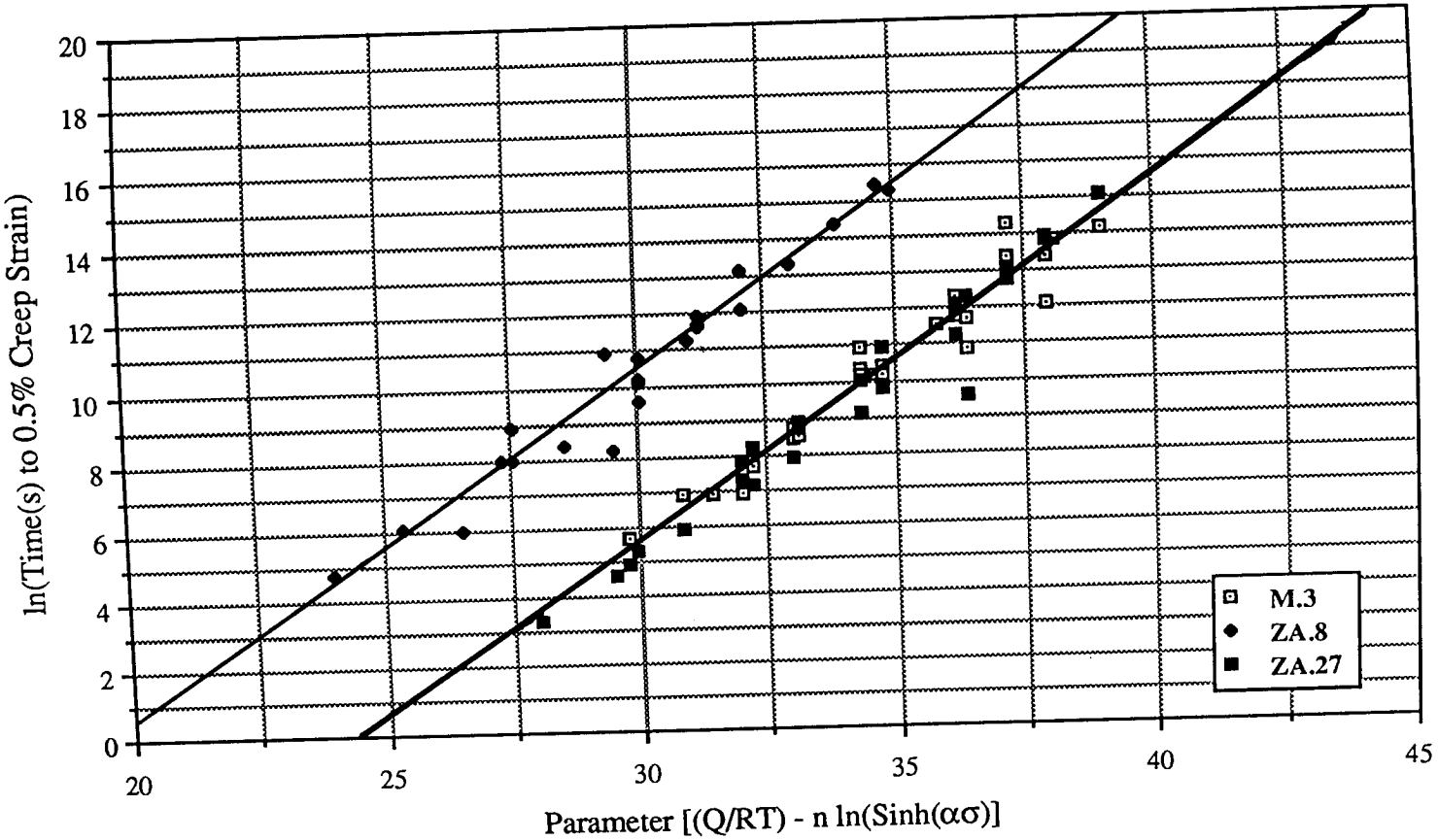

Figure 159. Ln times(s) to 0.5% creep strain versus creep parameter for alloys Mazak.3, ZA.8 and ZA.27.

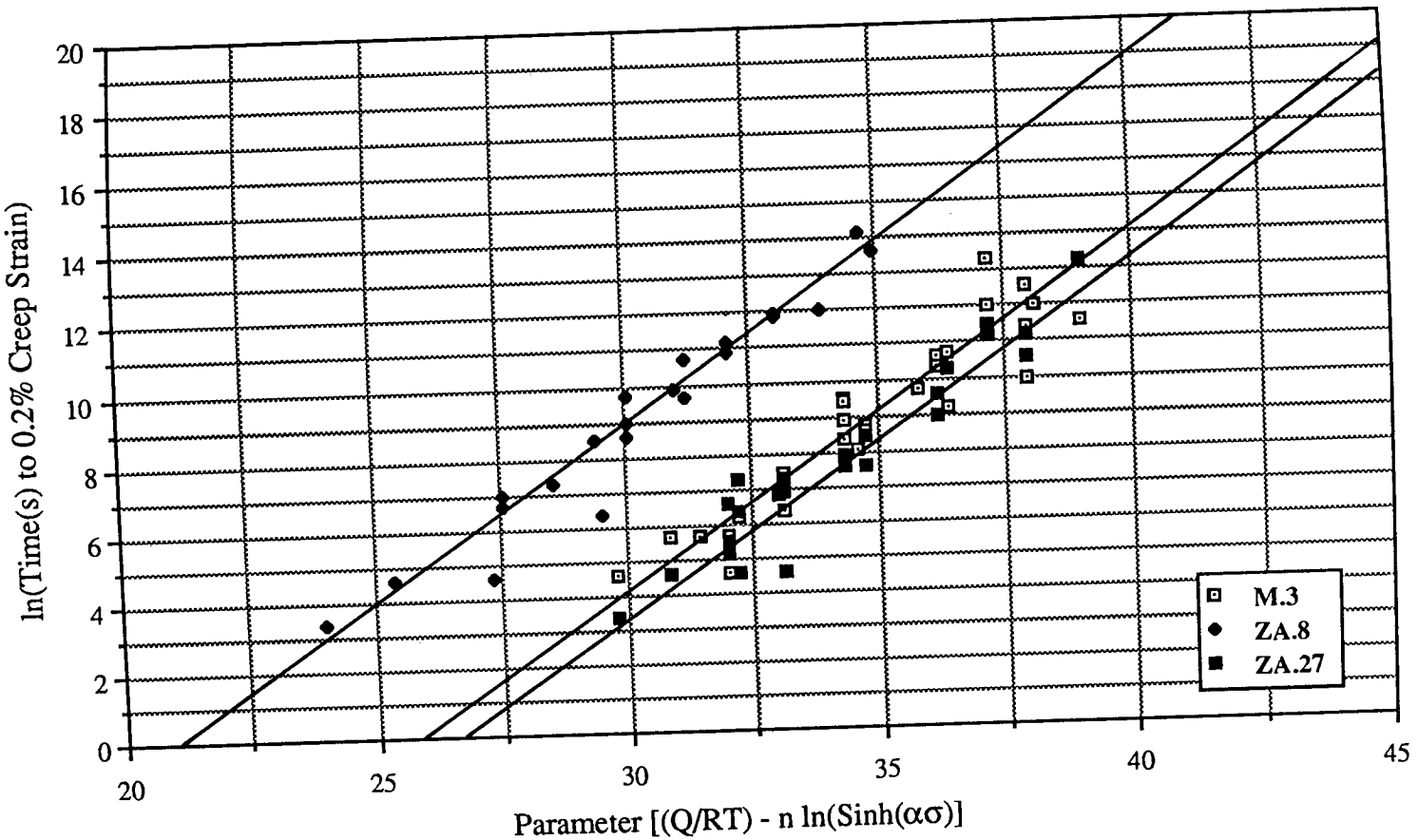

Figure 160. Ln times(s) to 0.2% creep strain versus creep parameter for alloys Mazak.3, ZA.8 and ZA.27.

Table 15. Results of the Regression analyses for parametric plots and values of the creep constant C' for the alloys Mazak.3, ZA.8 and ZA.27.

Alloy	Strain (%)	Slope of Regression	Intercept of Regression	Coefficient of Correlation	Intercept of unit slope (C')
Mazak.3	0.2	0.95	-24.07	0.94	-25.83
"	0.5	0.99	-23.95	0.98	-24.36
"	0.7	0.99	-23.39	0.99	-23.85
"	1.0	0.98	-22.85	0.99	-23.46
ZA.8	0.2	0.99	-20.96	0.97	-21.23
"	0.5	1.00	-19.76	0.98	-19.62
"	0.7	0.99	-18.77	0.99	-19.00
"	1.0	0.98	-17.84	0.99	-18.65
ZA.27	0.2	0.98	-25.87	0.95	-26.37
"	0.5	1.04	-26.06	0.98	-24.35
"	0.7	1.03	-24.98	0.99	-23.63
"	1.0	1.03	-24.00	1.00	-23.00

Table 16. Maximum continuous design stresses (MPa) to produce % strain in 100,000 hours (11.4 years).

Temperature(°C)		20	40	60	80	100	120	150
M.3	0.2 %	20.19	8.26	3.67	1.78	0.94	0.52	0.24
	0.5 %	31.22	13.34	5.98	2.90	1.53	0.86	0.40
	0.7 %	35.92	15.71	7.08	3.45	1.81	1.01	0.47
	1.0 %	39.80	17.77	8.06	3.93	2.06	1.16	0.54
ZA.8	0.2 %	30.80	14.87	7.42	3.96	2.25	1.36	0.69
	0.5 %	45.17	23.65	12.15	6.53	3.72	2.24	1.15
	0.7 %	51.42	27.98	14.63	7.91	4.52	2.72	1.39
	1.0 %	55.07	30.67	16.23	8.81	5.03	3.04	1.55
ZA.27	0.2 %	17.03	6.90	3.07	1.49	0.78	0.44	0.20
	0.5 %	31.31	13.38	6.00	2.92	1.53	0.86	0.40
	0.7 %	38.13	16.87	7.63	3.72	1.95	1.09	0.51
	1.0 %	44.67	20.50	9.37	4.58	2.40	1.35	0.63

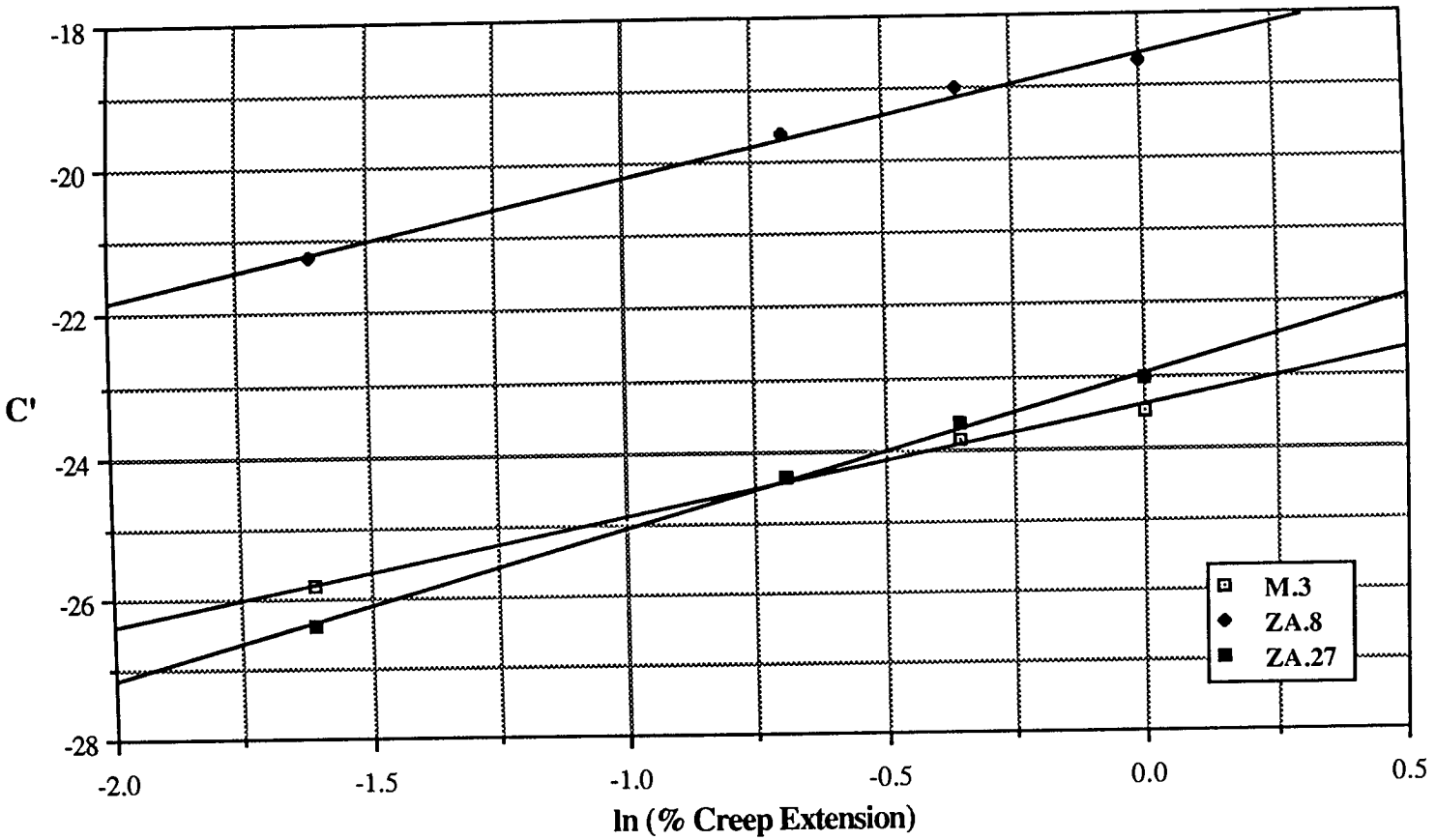

Figure 161. Variation of constant C' with creep elongations for alloys Mazak.3, ZA.8 and ZA.27.

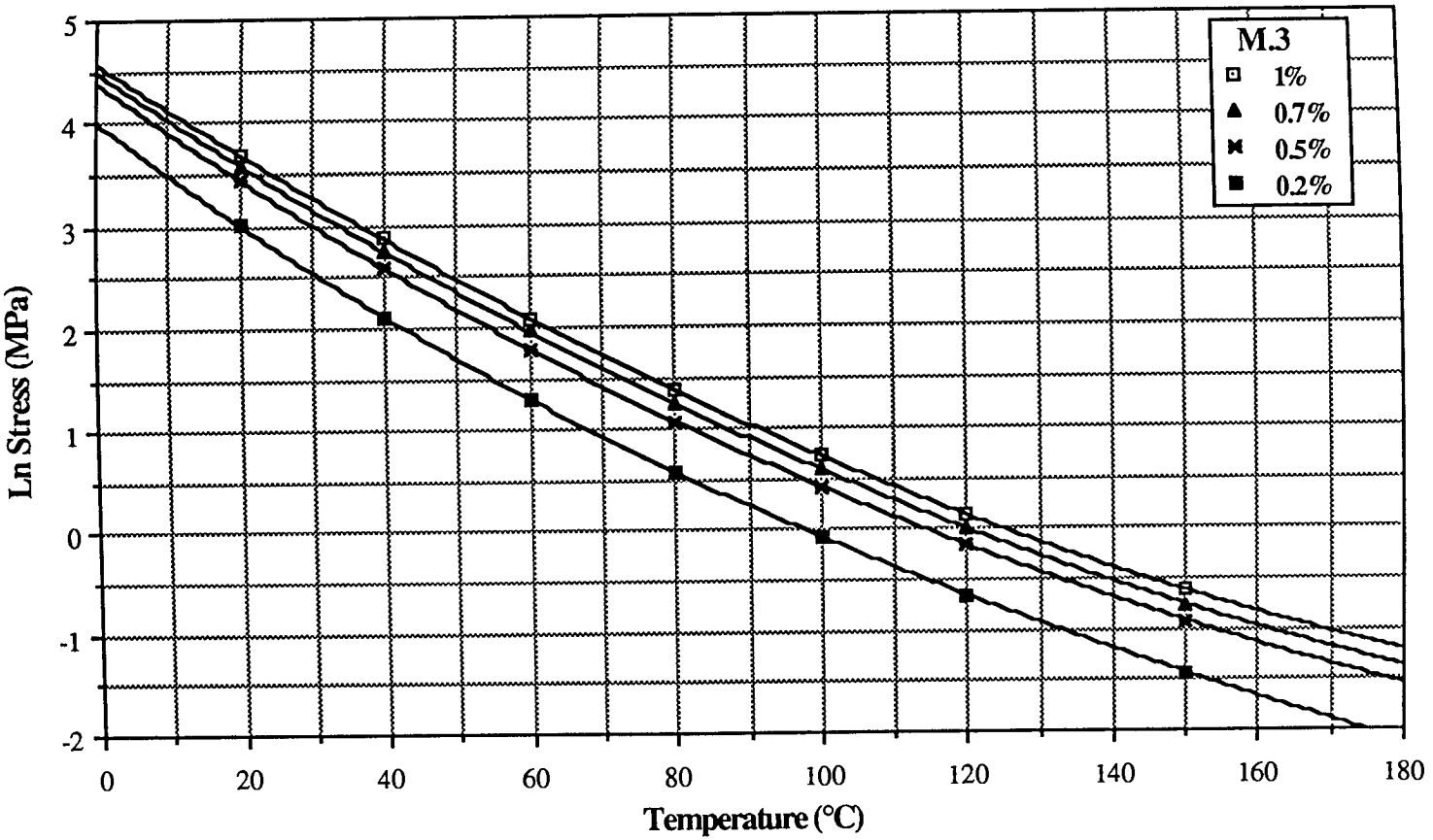

Figure 162. Maximum continous design stresses for various allowable creep strains in 100000 hours (11.4 years) design life for alloy Mazak.3.

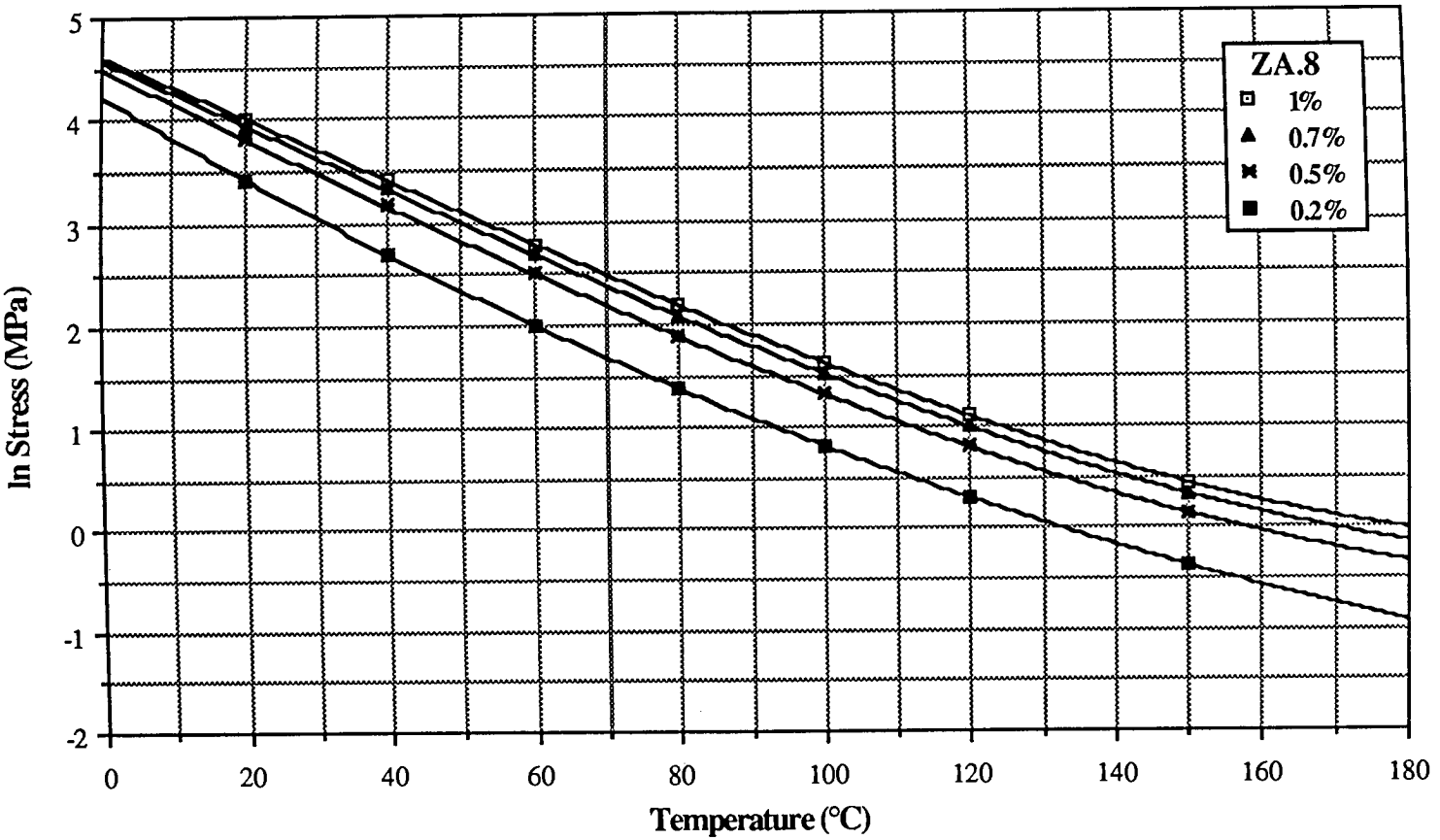

Figure 163. Maximum continous design stresses for various allowable creep strains in 100000 hours (11.4 years) design life for alloy ZA.8.

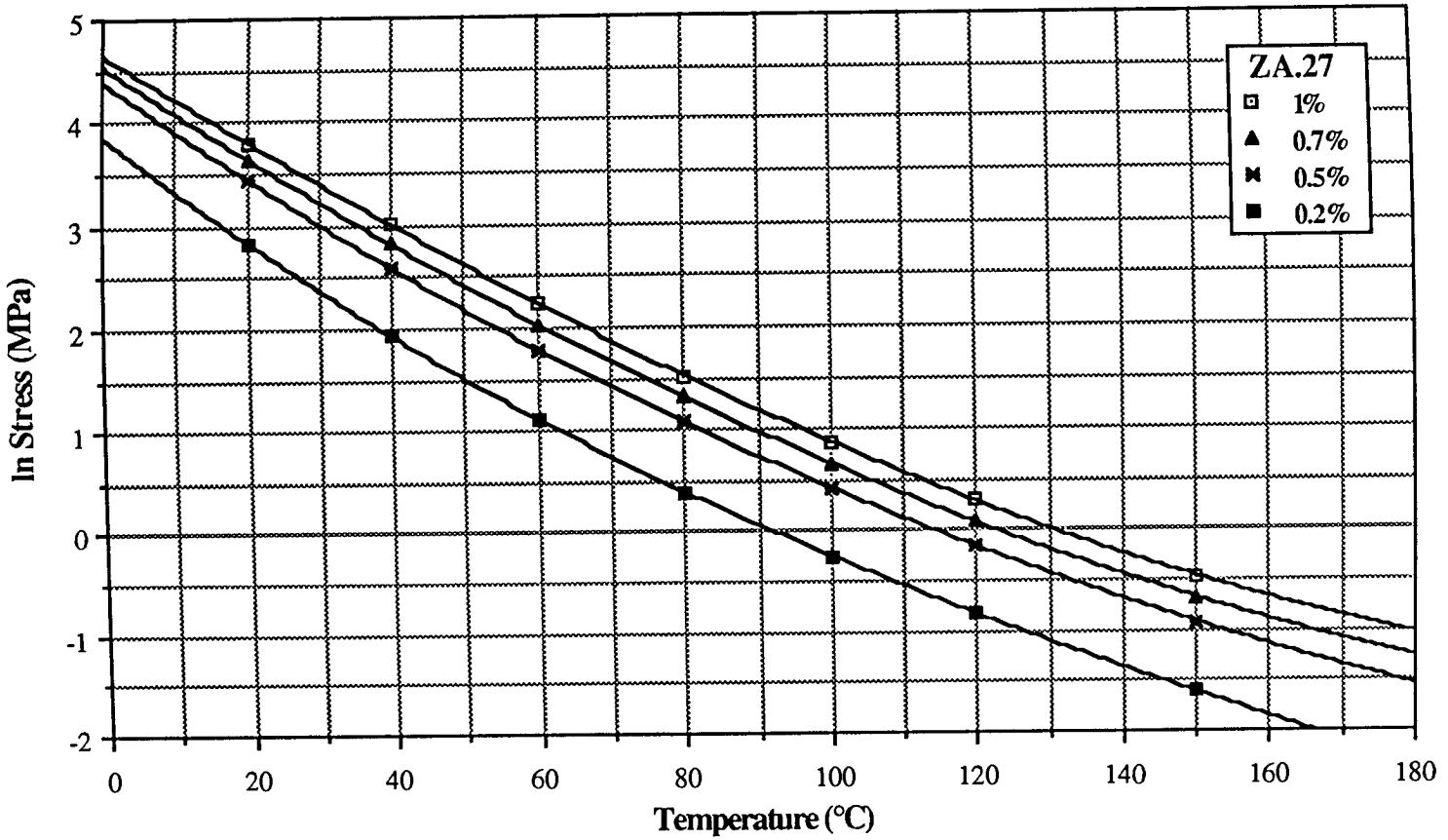

Figure 164. Maximum continous design stresses for various allowable creep strains in 100000 hours (11.4 years) design life for alloy ZA.27.

5.2 Theoretical and Metallographic Consideration

Secondary creep rate is recognised as the most definitive characterisation of creep behaviour, it is therefore widely used as a measure of relative creep resistance and is a basis for theoretical interpretation of the ways in which creep varies with temperature, stress and material parameters.

On this basis, a comparison of the secondary creep data obtained from the *Figures 56 to 58* at 40 MPa (*Table 9*), showed that alloy ZA.8 had a substantially lower secondary creep rate than those of the other two alloys at any given testing temperature and stress. Alloy ZA.27 was in turn better than the alloy Mazak 3.

However, overall creep extensions of the alloys were very much affected by the primary creep contribution. Alloy ZA.8 had much smaller primary creep strain than alloy ZA.27 and thus also showed a considerably better overall creep resistance. Alloy ZA.27, in turn, had much smaller secondary creep rate but much higher primary creep elongation, compared with the alloy Mazak 3 and thus is superior to the alloy Mazak 3 for the total creep strains above 0.5% (*Figures 157 to 159*). For smaller strains this behaviour is reversed, and Mazak.3 is superior to ZA.27.

Based on the secondary creep rates, the activation energies for creep were found to be 99.5 ± 0.5 kJ/mole for alloys Mazak 3 and ZA.8, and 108 kJ/mole for ZA.27, which values are similar to those obtained from the empirical equation (*Equation 23*).

These values are also in excellent agreement with those for self diffusion in polycrystalline zinc (91 - 110 kJ/mole) reported by various workers[153-155] and much higher than that for grain boundary self-diffusion in pure zinc, about 61 kJ/mole[156].

On the other hand, the activation energies for creep in polycrystalline zinc, published

in the literature, are discrete and vary from 87 to 152 kJ/mole [155,157,158]. However, within the small temperature and stress ranges studied here, the activation energies reported by the above workers were between 87 and 109 kJ/mole. Calculated activation energies for creep in the experimental alloys, being in the same range as those found for creep and self-diffusion in zinc, suggest that creep rate in the experimental alloys is controlled by diffusion in the zinc-rich phase and the rate controlling process for creep might also be the rate controlling process for lattice diffusion in zinc.

Such a correlation between the activation energy for creep and that for self-diffusion is consistent with the observations manifested for almost all pure metals and solid solutions in high temperature creep regions[25] and strongly supports the suggestion first made by Weertman [2,3] that the most likely mechanism in such cases is that of dislocation climb.

Based on the climb of edge dislocations, Weertman proposed two slightly different models [2,3], predicting stress exponents of 3 and 4.5 (*Equation 2, 3*), respectively. These values are indeed in excellent agreement with the stress exponents 3.5, 4.0 and 4.5 obtained for the alloys Mazak 3, ZA.8 and ZA.27, respectively. However, the first model predicting a stress exponent of 3 was later shown to be limited only to fcc metals.

On the other hand, based on the assumption that climb and glide are sequential processes and,.therefore, that the rate-controlling process would be associated with the slowest of the two, a viscous glide model in which one of the microcreep mechanisms (most probably solute atmosphere) formulated also by Weertman [4] gives a stress exponent of 3. In practice, this was found to be between 3 and 3.5 for any solid solution alloys, forming Class I-type solid solutions [25]. Another important characteristic of the alloys in this class is that they exhibit none, or very little, primary

creep, whereas the alloys which form Class II-type solid solutions obey a dislocation climb law with a stress exponent of 4.5 and exhibit a large primary creep[25].

Taking together these very similar characteristic features observed in the experimental alloys, it is believed that creep in the alloy Mazak 3 is controlled by a viscous glide process, whereas in alloys ZA.8 and ZA.27 with stress exponents of 4 and 4.5, respectively, it is controlled by a dislocation climb process. In the case of the alloy ZA.8, although the stress exponent is lower that that predicted by Weertman's dislocation climb model, as will be discussed in detail later, another model which is based on the climb over second-phase particles predicts the exact value of the stress exponent for this alloy.

5.2.1 Alloy Mazak.3

The creep behaviour of the experimental alloys must be directly related to their metallographic structures. Compared with two other alloys, Mazak 3, as discussed in detail earlier, had the least complex microstructure, consisting mainly of primary η particles set in an eutectic matrix.

As far as the creep in this alloy is concerned, comparison of the creep results of alloy 2 (Mazak 3), alloy 1 and the eutectic alloy 3, cast in the university, reveal an important fact that the overall creep resistance of the alloy 2 (Mazak 3) was much lower (by a factor of about 2.5-3) than alloy 1 and similar to alloy 3. However, as explained earlier, the pressure die-cast eutectic alloys 3 and 4 did not have a regular structure in the eutectic. The structure of these alloys, as shown in *Figure 129 and 130* was a fine mixture of η and β phases set in a comparatively small amount of regular eutectic, and the former morphology should be expected to give a higher creep rate due to low strength and high mobility of increased volume of grain boundaries at high temperatures. Thus, it is believed that the creep strength of the eutectic in the alloy Mazak 3 is higher than that of the primary η particles, and the lower overall resistance

of this alloy is mostly contributed by these primary particles.

The equilibrium solid solubility of aluminium in zinc is 1.1% at the eutectic temperature and decreases to a very small value at room temperature [28]. Upon solidification excess aluminium is removed by precipitation of aluminium as a phase in the zinc-rich matrix. The morphology of these precipitates in primary η particles is shown in the TEM micrographs of *Figures 67 and 68*.

Since the creep resistance of alloy 1 with no aluminium is higher than that of alloy 2 (Mazak 3), it is reasonably safe to conclude that the creep resistance of zinc is further reduced by precipitation of aluminium in the zinc matrix. This view was also in accordance with the observations reported for the superplastic behaviour of zinc with small amounts of aluminium (0.2 and 0.4%)[95,96]. These alloys were reported to have better superplasticity than a series of binary zinc-aluminium alloys, including the well known eutectoid alloy, at low temperatures, but they were not superplastic at 250°C. This must have been due to the fact that in low-aluminium alloys all the aluminium dissolved in the zinc solid solution at this temperature, since the solubility of aluminium in zinc is 0.42% at 227°C [28].

Precipitation morphology, after the creep tests shown in *Figures 74 and 75*, suggests that a significant growth of aluminium-rich precipitates in high length-to-width shapes takes place during creep. For the precipitates to grow in this morphology, it is highly probable that the broad faces of the precipitates have a very good atomic fit. Unfortunately, a brief attempt in the course of this work failed to determine the orientation relationship between the precipitates and η-matrix, but it is likely that closed-packed {0001} planes of zinc were set parallel to close-packed {111} planes of the f.c.c. aluminium-rich precipitates, as this was the case for the precipitation of zinc from aluminium-rich solid solutions reported by various workers [65-67]. If this is assumed to be the case, the migration of broad faces of such precipitates having

good atomic fit and low mobile-interface with zinc matrix, is only possible by lateral movement of ledges at the interface [159]. But if there are problems in maintaining a constant supply of ledges, the incoherent highly mobile interface, on the other hand, is expected to advance faster than the less mobile interface to produce such high length-to-width shapes.

The effect of such high length-to-width shape precipitates in creep is obviously to increase the area of smooth interface between two phases, and therefore the contribution of grain boundary sliding (GBS) to total creep strain is expected to be important, and this appears to be the reason for low creep resistance of η phase.

Theoretical models for GBS in literature fall into two general groups, those involving a pure-diffusion mechanism and those involving a dislocation mechanism. Although any speculation about the mechanism of sliding between the η-matrix and α-precipitates is difficult because of the lack of knowledge of the structure of two interphase boundaries, the possibility of any pure diffusional model is remote due to the low-mobility interface. On the other hand, it appears from the geometry of the precipitation that a dislocation mechanism is more likely as such dislocations along the interface of a particular orientation, with respect to the stress, may be expected to be mobile.

MacLean [102] proposed a theoretical dislocation model in which it is assumed that an edge dislocation generated in the bulk of the grain travels along its slip plane until it meets a grain boundary, at which point it is resolved into two component dislocations, one being parallel to the grain boundary and the other being normal to the grain boundary. The further movement of the former then proceeds by glide along the boundary by the shear stress resolved parallel to the grain boundary, and that of the latter by vacancy emission or absorption (climb) by the direct stress resolved normal to the grain boundary. If the component dislocations are assumed to move together,

the whole dislocation motion along the boundary is governed partly by direct and partly by shear stress, resulting in sliding of one grain with respect to the other and emission or absorption of vacacncies.

It is obvious in this model, that sliding is caused in amounts depending on the orientation of the dislocation's Burgers vector, which in turn depends on grain orientation. Consequently, emission or absorption of vacancies by grain boundaries, and also sliding, depend on the orientation with respect to the applied stress of the grains as well as of the grain boundaries.

Matrix dislocations associated with precipitate-matrix interface in primary η particles, shown in *Figures 74 and 75*, may well be considered to exhibit the evidence for dislocations in the early stage of the above mechanism. In addition, if this mechanism is to be operative, a wide variation in cavitation is expected depending on grain orientation with respect to the applied stress, and if vacancies play a more important role than sliding, cavitation on transverse grain boundaries is expected to be more than those of 45° grain boundaries. Indeed, such a wide variation in cavities of various sizes which were randomly distributed within some primary η particles were quite distinctly evident in this alloy after the creep tests (*Figures 71 to 73*). However, the information obtained in this study is probably insufficient to allow a certain conclusion on this issue.

5.2.2 Alloy ZA.8

The microstructure of the alloy ZA.8 was revealed by SEM and TEM studies and discussed in a previous chapter in great detail. As a result, the information obtained particularly from TEM study, was extremely precious in order to evaluate the creep behaviour of this alloy. It has now been well established by the present work that superior creep resistance of this alloy is principally derived from precipitation hardening, due to the existence of heterogeneously nucleated small precipitates of ε ($Cu\ Zn_4$) phase in the zinc matrix of both eutectic and lamellarly decomposed β-

phase.

This view is experimentally supported by testing gravity-cast eutectic alloys 3, 4 and 5 (ZA.8). Comparison of the results of these tests clearly showed that the wholly eutectic alloy 4 with copper, was substantially better than the alloy 5 (ZA.8) and the eutectic alloy 3 without copper.

The present study has established that ε phase forms as coherent plate-like precipitates on a variant of $\{2\bar{1}\bar{1}7\}$-type habit planes and advances along a low-energy coherent interface consisting of $[2\bar{1}\bar{1}3]_{Zn,\varepsilon}$-zone with the following orientation relationship to the zinc-rich matrix;

$$(01\bar{1}0)_{Zn} \parallel (01\bar{1}0)_{\varepsilon}$$

$$(\bar{2}112)_{Zn} \parallel (\bar{2}112)_{\varepsilon}$$

but with $[0001]_{\varepsilon}$ 4.5° from $[0001]_{Zn}$. (*See Section 4.3.2*)

Although the misfit across the above interface was found to be as low as 2.8% or below, final precipitates of about 20-30 Å thick and 800 Å long are probably semi-coherent with some periodic dislocations to take up the misfit induced by increased strain coherency along the matrix-precipitate interface.

A full exploration of the established orientation relationship and morphology of these precipitates is yet to be made with respect to the creep and other mechanical properties for which they are responsible. However, as far as the creep is concerned the straight forward idea of the role of the precipitates is that they act as obstacles to dislocation movement. On encountering particles on the glide plane, a moving dislocation attempts to cut through or bow between the particles, or to by-pass them by climb and cross slip [23].

High temperature creep theories in materials hardened by second-phase particles, on the other hand, fall into two general categories, those assuming a rate controlling mechanism such as climb over the second-phase particles, and those assuming that it is recovery-creep. Based on the climb model, the first major attempt to develop a theory for high temperature creep of alloys hardened by a second phase was made by Ansell and Weertman [160]. In their theory, they considered two different processes depending on the stress level. At low stresses (below Orowan stresses), they suggested that dislocations climb over the particles with no pile-up or bowing of dislocations at the particles, and for this case, they arrived at an expression obeying a first power law:

$$\dot{\varepsilon} = \frac{\pi \sigma b^3 D}{2kT h^2}$$

where σ is the applied stress, b the Burgers vector, D the self diffusion coefficient, h the particle size, k the Boltzmann's constant and T is the absolute temperature.

At high stress levels (higher than $\mu b/\lambda$, where μ is the shear modulus and λ the interparticle spacing) on the other hand, they considered dislocations to be forced past particles by bowing out and pinching off loops around the particles until further bowing was prevented by back the stress induced by the loops around the particles. The rate controlling process is then climb of the first pinched off loop around the particles, by diffusion of vacancies away from or towards the dislocation line. On climbing to the top of the particle, the pinched off loop then meets the dislocations of opposite sign and is annihilated. The steady-state creep rate in this process is given as:

$$\dot{\varepsilon} = \frac{2\pi \sigma^4 \lambda^2 D}{h \mu^3 kT}$$

As seen from this expression, the secondary creep rate / stress relation obeys a fourth power law which is the same stress exponent value obtained from the $\ln \dot{\varepsilon} / \ln \sigma$ plot for the alloy ZA.8.

Theories based on recovery creep in materials hardened by a second phase are essentially the same as those proposed for pure metals and solid solutions (*Chapter 2*), except that second phase particles reduce the recovery rate and this, in turn, reduces the creep rate. It was shown that this model could account for the very large stress-dependence of creep rate, the exponent varying from 5 to 11 [161]. Taking these together with the activation energy for creep, which was found to be equal to that for lattice diffusion in zinc, it seems reasonable to conclude that the rate-controlling mechanism for creep in the alloy ZA.8 over a large stress and temperature range is the climb of dislocations over ε-precipitates by the latter process proposed by Ansell and Weertman.

ε-phase is however not a stable phase at low temperatures, and according to the established ternary aluminium-zinc-copper diagrams, it undergoes a four phase reaction below 273°C with α phase to form stable copper and zinc-rich T' and η phases, respectively [59]. Due to the low diffusivity of zinc in aluminium matrix at low temperatures, time to complete the final four phase reaction may however require a period of a month or year [59,83-86]. This four-phase reaction was observed in experiments of long duration at 150°C, where only partial transformation of ε-precipitates to T' phase occurred, with an orientation relationship:

$$[0\bar{1}10]_{Zn} \parallel [0\bar{1}10]_{\varepsilon} \parallel [011]_{T'}$$

This structural instability may cause some deviation from the creep kinetics of the alloy in long term service lives of some components. However, the ε-phase precipitated in the zinc eutectic matrix requires a large volume of α-phase to transform to T' phase and practically it may therefore be considered that transformation of a large portion of ε-phase would not be possible due to the low solubility of aluminium in zinc.

In the temperature and stress range in which the above phase reaction was observed, there was also a significant phase coarsening of primary β particles and eutectic, which all caused a significant increase in creep resistance of the alloy, and it was therefore not possible to distinguish the effect of the ε transformation on the creep kinetics of the alloy.

It is obvious from the above argument that if the eutectic matrix is responsible for the higher creep resistance of the alloy ZA.8, the creep resistance should be expected to decrease with decreasing volume of the eutectic (or increasing value of primary particles) in hypo-eutectic alloys. Comparison of the results of alloys 5 (ZA.8) to 7 clearly shows this gradual decrease in the creep resistance of these alloys (*Figures 126 and 127*).

On the other hand, the morphology of the final products of decomposition of primary β particles themselves was found to have a substantial effect on creep of the alloys. As discussed earlier in detail, two distinct final products, one being lamellae which usually formed the central portions of the primary particles and the other being a coarse mixture of the zinc and aluminium-rich phases were peculiar features of the decomposition. The decomposition kinetics of these products were discussed in *Section 4.3.2* and it is proposed that the cellular decomposition of β phase into the final stable phases does not follow the traditional scheme indicated by the binary zinc-aluminium system. Instead, it occurs through a metastable transitional phase (α'_T) in the following sequence:

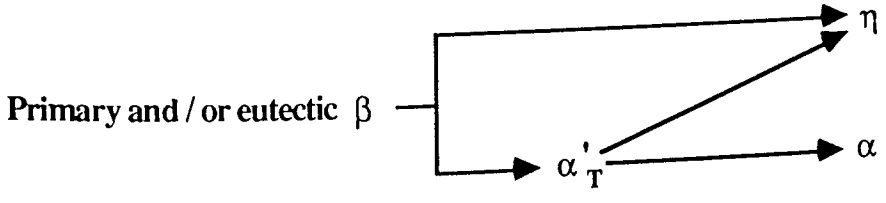

But in the case of the β lamellae around the surface of the primary particles and

eutectic β, α'_T phase is lower in aluminium content compared with that formed from the cores of the primary β particles.

It is important to remember that the above proposed decomposition sequence entirely depends on a significant copper content in the β phase which, possibly together with magnesium, stabilizes the α'_T sufficiently for the proposed mechanism to be possible, and two different distinct morphologies of the final products depends on subtle alterations in the composition of the β phase as a whole.

The importance of these two different morphologies of final products of lamellar and particulate form, from the creep point of view, is that the former is expected to give a lower creep rate compared to the latter, due to its geometrical factor. In addition, the former was found to accommodate small ε-precipitates in its zinc matrix. Thus, it is expected to give a creep rate similar to (or perhaps better than) eutectic. Indeed, in the absence of the lamellar product in alloy 5 (ZA.8) cast in the university, (*Figures 126,127*), a drastic reduction in creep strength of this alloy was measured, compared with the commercially cast alloy ZA.8, and this reduced to a minimum in alloy 9 (ZA.27) compared with the commercial cast alloy ZA.27, possibly due to comparatively low volumes of β-phase in the alloy ZA.27.

5.2.3 Alloy ZA.27

Compared with the two other previous alloys, the assessment of creep behaviour of the alloy ZA.27, with respect to its metallography, is more complex due to its multi-phase structure.

The microstructure of this alloy as revealed by SEM and TEM investigations and discussed in detail in Section 4.3.3, consists of mainly primary α and/or α' dendrites of various sizes surrounded by decomposed β together with eutectic pools occupying the interdendritic areas.

Copper as ε-phase precipitated in interdendritic channels in two different morphologies; preferentially in the zinc matrix of both the eutectic and lamellarly decomposed β in a strictly-oriented, thin plate-like morphology similar to that found in the alloy ZA.8, but in much higher densities due to the high copper content of the alloy and less amount of available volume of eutectic zinc and β-phase in the alloy (*Figures 107 and 108*).

Compared with the other parts of the structure, the creep resistance of these phases should, therefore, be expected to be much higher due to the precipitation hardening of the zinc matrix, as discussed earlier in the case of the alloy ZA.8.

Secondly, the excess copper was also shown to precipitate in interdendritic channels, as discrete particles formed in the copper-enriched liquid when the eutectic solidification took place. From the creep point of view, it is believed that these discrete particles are not beneficial in improving the creep resistance of the alloy since no additional benefit in creep performance was obtained by increasing the copper content of alloy 8 to that of alloy 9 (ZA.27) cast in our foundry (*Figures 126 and 127*).

Decomposition of β phase was similar to that of the alloy ZA.8 with lamellar and particulate mixture of the η and α phases *(Figure 113-115)*, but particulate products were much more frequently observed, probably due to the higher copper of the alloy suppressing the development of regular lamellar morphology.

α dendrites decomposed into the final products shown in *Figures 110 to 112*, which were mainly two types: fine equiaxed mixtures of η and α phases, and lamellar mixture of the same products. This change in the morphology of transformed products is attributed to the change in the decomposition mechanism from spinoidal decomposition to conventional cellular reaction. Both reactions had been previously

shown by various workers [68-70,74-80] to take place in concentrated zinc-aluminium alloys, depending entirely on cooling rate and ageing temperature. Of these two types of products, the occurrence of the extremely fine equiaxed mixture of α and η grains was however much more frequent in as-cast structures of the alloy ZA.27, probably due to the rapid cooling on casting.

The effect of such a morphology in creep is that the two-phase mixture of equiaxed grains restricts grain growth at elevated temperatures and becomes prone to superplastic flow, and it has been reported by several workers [91-95] that this morphology was mainly responsible for the excellent structural superplasticity of zinc-aluminium alloys. Thus, it is believed that the low creep strength of this alloy principally results from the particulate products of decomposed β phase and the continuously decomposed products of α-dendrites.

Under various conditions of stress and temperature, various deformation mechanisms could be rate-controlling for superplastic deformation. In general, at low stresses, diffusion creep should be expected to be rate-controlling [93]. Development of η-stringers within the α dendrites, shown in *Figures 117 to 119*, shows some evidence for the occurrence of this type of creep. An activation energy for creep found to be in the range of self diffusion in zinc suggests that volume diffusion may be the dominant diffusion path for the above process, rather than grain boundary diffusion.

At intermediate stress levels, GBS is usually observed as the major deformation mode, accommodated by either diffusional and/or dislocation mechanisms. Qualitative evidence for internal GBS in the α grains was also observed, as shown in *Figures 120 and121*. In these figures, it is believed that extensive internal GBS is the most probable mechanism for the development of the broken-up stringers.

On the other hand, the stress exponent value η obtained from the plots of $\ln \dot{\varepsilon}_s / \ln \sigma$

as 4.5 is in good agreement with the strain rate sensitivity m (1/n) observed in the deformation of superplastic alloys at high stress levels. (i.e. region III in *Figure 21*), where it is generally accepted that the rate controlling mechanism is due to the climb of edge dislocations.

It appears from these evidences that several inseparable mechanisms are operative during deformation of α-dendrites and, based on the data of activation energy and stress exponent value, η, it is not possible to distinguish the most dominant one due to the complex multi-structure of the alloy itself as a whole.

CHAPTER 6

6.0 CONCLUSIONS

1. The total creep elongation of commercial pressure-diecasting alloys was shown to be correlated by a creep equation of the form:

$$f(\varepsilon) = C\ (\text{Sinh}\ \alpha\sigma)^n\ \exp(-Q/RT)$$

where $n = 3$, $\alpha = 2.43 \times 10^{-2}$ and $Q = 106$ kJ/mole for alloys Mazak 3 and ZA.27 and $n = 3.2$, $\alpha = 2.66 \times 10^{-2}$ and $Q = 99$ kJ/mole for alloy ZA.8.

Based on this equation, a parametric relationship was derived which allows the total creep extension to be related to the applied stress, the temperature and the time of the test, allowing a quantitative assessment of creep kinetics of the alloys under different conditions to be made.

2. Deviation from the creep kinetics occurred in alloys ZA.8 and ZA.27 at 150°C when tested at very low stresses, due to structural coarsening of phases. Partial transformation of ε-phase into T' phase was also found under these conditions.

3. The primary creep extension was found to increase with increasing aluminium content.

4. Based on the above empirical equation, design stresses were calculated which showed that the alloy ZA.8 had a substantially better total creep resistance than the alloy ZA.27, which in turn was marginally better than the alloy Mazak 3, for allowable creep strains higher than 0.5%, but inferior for smaller strains, due to its higher primary creep contribution to total creep strain.

5. The secondary creep rates of the alloy ZA.8 were found to be substantially lower than those of the alloy ZA.27, which was in turn also much better than those of the alloy Mazak 3.

6. The superior creep resistance of the alloy ZA.8 was shown to result solely from precipitation hardening due to the presence of strictly-orientated thin plate-like precipitates of ε phase ($CuZn_4$) in the zinc matrix of the eutectic and the lamellarly decomposed β phase. Its precipitation morphology and the unique orientation relationship to the zinc matrix with the common habit-plane were determined.

7. Activation energies (Q) for creep of the alloys were found to be in the range of activation energies for lattice diffusion in pure zinc, indicating that the creep rate was being controlled by diffusion in the zinc-rich phase.

8. Stress exponent values calculated from the plots of $\ln \dot{\varepsilon}_s / \ln \sigma$ were found to be 3.5, 4 and 4.5 for alloys Mazak 3, ZA.8 and ZA.27, respectively, which are in accordance with those of well established proposed rate-controlling mechanisms; viscous glide for alloy Mazak 3, dislocation climb over second phase particles for alloy ZA.8, and dislocation climb for alloy ZA.27.

Deviations from the otherwise constant slopes were observed at high stresses for alloy Mazak 3, at high and low stresses for alloy ZA.8, and at low stresses for alloy ZA.27, indicating possible changes in the mechanism of creep.

9. The precipitation of aluminium from solid solution of zinc as α-phase has been shown to further increase the creep rate of inherently low-creep-resistant, pure zinc. Primary η-phase particles in alloy Mazak 3 possessed a lower resistance to creep compared with the eutectic. The eutectic also accommodates α-precipitates, but

because of the constraints imposed by a lamellar network, its creep rate is lower than the former, and the overall low creep strength of the alloy is, therefore, mostly due to the primary η particles.

10. The regular morphology of the eutectic in the presence of copper was shown to give the highest creep strength, due to its large volume of zinc matrix strengthened by precipiation of copper from solid solution in the zinc.
The creep resistance of the hyper-eutectic alloys with the same amounts of copper gradually decreased inversely proportional to the amount of the eutectic which they contained.

11. Decomposition of β-phase into the final equilibrium phases has been shown not to follow the scheme of the binary system in copper containing alloys. A new mechanism was proposed, in which β-phase decomposes through a transitional metastable phase α'_T, which is strongly stabilised by copper.

12. The final products of primary β decomposition were found to have a profound effect on the creep kinetics of the alloys. Two different types of decomposition products ; lamellae and a particulate mixture of multi-phases, were found to persist after decomposition, possibly due to real differences in composition, and the latter produced a substantially higher creep rate than the former.

13. In the alloy ZA.27 with a high copper content, the thin plate-like precipitates of ε-phase were also present in high densities, decorating the entire zinc matrix of the eutectic and the lamellarly decomposed β-phase in the interdendritic channels, forming small, highly creep resistant regions within the whole structure.

In addition, due to the high copper content and comparatively small amount of available eutectic zinc and β-phase in the structure, excess copper was shown to form

discrete acicular particles of ε-phase in the copper-enriched liquid when the eutectic solidification took place. These particles were not beneficial in improving the creep resistance of the alloy. Increasing the copper content of the alloy above 1% was, therefore, not effective in retarding overall creep rate.

14. The overall low creep resistance of the alloy ZA.27 derives from the superplastic behaviour of particulate products of decomposed β-phase and a large volume of fine equiaxed phases from spinodally decomposed α-dendrites.

15. Increasing the aluminium content above that of the alloy ZA.27 appears to reduce the overall creep rate in the hyper-eutectoid areas of the phase diagram.

CHAPTER 7

7.0 SUGGESTIONS FOR FURTHER WORK

1. The present work has shown that the precipitation of aluminium from a solid solution of zinc had an important effect on the creep of the alloy Mazak 3, significantly increasing the creep rate. Although its precipitation morphology has been shown to some extent, its orientation relationship to zinc matrix and the structure of phase boundaries are still not known. Further TEM work would be essential on that aspect to understand the mechanism involved more clearly.

2. It has been shown that the decomposition of the β phase with its different decomposition products has had a significant effect on the creep kinetics of the alloys in the hyper-eutectic area, which was also directly related to the pressure diecasting parameters (particularly gate velocity and die temperature). It is therefore important to further study its decomposition, with respect to diecasting parameters, in more detail, to better understand its decomposition kinetics and optimise its effect on creep.

3. The electron microscopy study in this work has mainly concentrated on understanding creep involved in experimental alloys in terms of their metallographic structure. The metallographic study was therefore, mainly carried out on as-cast structures of the alloys. Further TEM and SEM work on creep-tested samples would be very useful to understand the creep mechanisms involved in the alloys more clearly.

4. The superior creep behaviour of alloy ZA.8, with the complete characterisation established by this work, will now increase its popularity and promote its structural and stressed applications for service at elevated temperatures.

Its creep behaviour is now also well established in terms of its structure. In particular the effects of the kinetics of decomposition of the β-phase and of the precipitation of the ε-phase are vitally important, and responsible for its superior creep behaviour. It is, therefore, believed that further development of this alloy is possible on the above parameters by further detailed research.

REFERENCES

1. **Weertman J. and Weertman J.R.** Physical Metallurgy. *3rd Edition, Vol. 2, Editors : Cahn R.W. and Haasen P. North Holland Physics Publishing, 1983, Netherlands.*

2. **Weertman J.** Theory of Steady State Creep Based on Dislocation Climb. *J. Applied Physics, Vol. 26, 1213-1217, 1955.*

3. **Weertman J.** Steady State Creep Through Dislocation Climb. *J. Applied Physics, Vol. 28, 362-364, 1957.*

4. **Weertman J.** Creep of Indium, Lead and Some Other Alloys with Various Metals,. *Trans. Metall. Soc., AIME, Vol. 218, 207-218, 1960.*

5. **Farghhalli A.M. and Langdon T.G.,** The Transition from Dislocation Climb to Viscous Glide in Creep of Solid Solution Alloys. *Acta Metall., Vol. 22, 779-788, 1974.*

6. **Cottrell A.H. and Jawson M.A.,** Distribution of solute atoms round a slow dislocation. *Proc. Roy. Soc., A.199, Vol.104, 104-114, 1949.*

7. **Sellars C.M. and Quarrell A.G.** The High Temperature Creep of Gold-Nickel Alloys. *J. Inst. Met., Vol. 90, 329-336, 1961-62.*

8. **Smallman R.E.** Modern Physical Metallurgy, *3rd Edition, Butterworth & Co. (Publishers) Ltd., 1970, Scotland.*

9. **Lagneborg R.** Dislocation Mechanisms in Creep. *Int. Metall. Rev., Vol.17, 130-146, 1972.*

10. **Barrett C.R. and Nix W.D.** A Model for Steady State Creep Based on the Motion of Jogged Screw Dislocations. *Acta Metall., Vol. 13, 1247-1258, 1965.*

11. **Mukherjee A.K, Bird J.E. and Dorn J.E.** Experimental Correlations for High Temperature Creep. *Trans. ASM, Vol. 62, 155-178, 1969.*

12. **McLean D.** The Physics of High Temperature Creep in Metals. *Reports on Progress in Physics, Vol. 29, 1-33, 1969.*

13. **Lagneborg R.** Development and Refinement of the Recovery Creep Theory. *Met. Sci. Journal, Vol. 3, 161-168, 1969.*

14. **Nabarro F.R.N.** Deformation of Crystals by the Motion of Single Ions. *Report of a Conference on the Strength of Solids, Phy. Soc., 75-90, 1948.*

15. **Herring C.** Diffusional Viscosity of a Polycrystalline Solid. *J. Appl. Phy., Vol. 21, 437-445, 1950.*

16. **Coble R.L.** A Model for Boundary Diffusion Controlled Creep in Polycrystalline Materials. *J. Appl. Phy., Vol. 34, 1679-1682, 1963.*

17. **Garofalo F.** Fundamentals of Creep and Creep Rupture in Metals. *The MacMillan Company, 1965, New York.*

18. **Garofalo F., Richmond C, Domis W.F. and Gemmingen F.** Strain-Time, Rate-Stress and Rate-Temperature Relations During Range Deformation in Creep. *Joint Int. Conf. on Creep, London. The Inst. Mech. Eng., Paper 30, 1-31-39, 1963.*

19. **Evans W.J. and Wilshire B.** Transient and Steady-State Creep Behaviour of Nickel, Zinc and Iron. *Trans. Metall. Soc. AIME, Vol. 242, 1303-1307, 1968.*

20. **Evans W.J. and Wilshire B.** The High Temperature Creep and Fracture Behaviour of 70-30 Alpha-Brass. *Metall. Trans., Vol. 1, 2133-2139, 1970.*

21. **Evans R.W., Parker J.D. and Wilshire B.** Recent Advances in Creep and Fracture of Engineering Materials and Structures. *Editors : Wilshire B. and Owen D.R.T., Pineridge Press, Swansea, 1982.*

22. **Evans R.W., Beden I. and Wilshire B.** Proc. 2nd Int. Conf. on Creep and Fracture of Engineering Materials and Structures. *Editors :Wilshire B. and Owen D.R.T., Pineridge Press, Swansea, 1984.*

23. **Evans R.W. and Wilshire B.** Creep of Metals and Alloys. *The Inst. of Metals, London, 1985.*

24. **Evans R.W. and Wilshire B.** Proc 3rd Int. Conf. on Creep and Fracture of Engineering Materials and Structures. *Editors : Wilshire B. and Evans R.W., The Inst. of Metals, Swansea, 1987.*

25. **Sherby O.D. and Burke P.M.** Mechanical Behaviour of Crystalline Solids at Elevated Temperatures. *Prog. Mat. Sci., Vol. 13, 325-390, 1966-67.*

26. **Garofalo F.** An Empirical Relation Defining the Stress Dependence of Minimum Creep Rate in Metals. *Trans. Metall. Soc. AIME, Vol. 227, 351-355, 1963*

27. **Murray J.L.** The Al-Zn System. *Bulletin of Alloy Phase Diagrams, Vol. 4, No. 1, 55-73, 1983.*

28. **Mondolfo L.F.** Aluminium Alloys - Structure and Properties, *Butterworth, London, 1976.*

29. **Hanson D. and Gayler M.L.V.** Further Study of the Alloys of Aluminium and Zinc. *J. Inst. Met., Vol. 27, 267-306, 1922.*

30. **Tanabe T.** Studies in the Aluminium-Zinc System. *J. Inst. Met., Vol. 32, 415-453, 1924.*

31. **Isihara T.** On the Equilibrium Diagram of the Aluminium-Zinc System. *J. Inst. Met., Vol. 33, 73-90, 1925.*

32. **Owen E.A. and Pickup L.** X-ray Study of Aluminium-Zinc Alloys at Elevated Temperatures. *Phil. Mag., Vol. 20, 761-777, 1935.*

33. **Ellwood E.C.** An X-ray Study of the Constitution of Aluminium-Zinc Alloys of High Purity Above 275°C, with a Description of a New High Temperature X-ray Camera. *J. Inst. Met., Vol. 66, 87-96, 1940.*

34. **Ellwood E.C.** The Solid Solutions of Zinc in Aluminium. *J. Inst. Met., Vol. 80, 217-224, 1951-1952.*

35. **Fink W.L. and Willey L.A.** Equilibrium Relations in Aluminium-Zinc Alloys of High Purity, II. *Trans. Amer. Inst. Min. Met. Eng., Vol. 122, 244-265, 1936.*

36. **Grayler M.L.V.and Sutherland E.G.** The Constitution of Aluminium-Zinc Alloys of High Purity, the Nature of the Thermal Change at 443°C. *J. Inst. Met., Vol. 63, 123-147, 1938.*

37. **Hansen M. and Anderko K.** Constitution of Binary Alloys. *2nd Ed., McGraw Hill Book Company Inc., USA, 1958.*

38. **Presnyakov A.A., Gorban Yu A. and Chervyakova V.V.** The Aluminium-Zinc Phase Diagram. *Russian Journal of Physical Chemistry, Vol. 35, No. 6, 632-633, 1961.*

39. **Goldak G.R. and Parr J.G.** A High Temperature X-ray Diffractometer Study of the Zinc-Aluminium System in the Region 40-75 wt % Zinc. *J. Inst. Met., Vol. 92, 230-233, 1963-64.*

40. **Pearson W.B.** A Handbook of the Lattice Spacings and Structures of Metals and Alloys. Vol. 2, *Pergamon Press, London, 1967.*

41. **Lohberg K.** Rontgenographische bestimmung des losurgsvermogens des zink fur aluminium und kupfer. *Z.Metallkunde, Vol.32, 86-90, 1940.*

42. **Metal's Handbook.** Phase Diagrams of Binary Alloy Systems. *8th Ed., Vol. 8, American Society for Metals, Ohio, 1973.*

43. **Massalski T.B. and King H.W.** The Lattice Spacing Relationship in h.c.p. ε and η Phases in the Systems Cu-Zn, Ag-Zn, Au-Zn and Ag-Cd. *Acta Met., Vol. 10, 1171-1181, 1962.*

44. **Koster W. and Moeller K.** Uber den Aufbau und die Volumenanderungen der Zinc-Kupfer-Aluminium-Legierungen; I. Die Aufteilung der Konzentrationsebene bei 350°C. *Z. Metallkunde, Vol. 33, 278-283, 1941.*

45. **Koster W and Moeller K.** Uber den Aufbau und die Volumenanderungen der Zinc-Kupfer-Aluminium-Legierungen; II. Der Zusammenhang von CuAl

mit der ternaren kristallart. *Z. Metallkunde, Vol. 33, 284-288, 1941.*

46. **Koster W and Moeller K.** Uber den Aufbau und die Volumenanderungen der Zinc-Kupfer-Aluminium-Legierungen; V. Die aufspaltung der ternaren kristallart bei tiefen temperaturen, *Z. Metallkunde, Vol. 34, 206-207, 1947.*

47. **Gebhardt E.** Uber den Aufban und die volumenanderungen der zinc-kupfer-aluminium-legierungen; IV. Die ursachen der volumenanderungen und ein verfahren zur erzielung der maβhaltigkeit. *Z. Metallkunde, Vol. 33, 297-305, 1941.*

48. **Gebhardt E.** Uber den Aufban und die volumenanderungen der zinc-kupfer-aluminium-legierungen; VI. Ubersicht uber den gleichgewichtsverlauf auf der zinc-aluminium-seite unterhalb 350°C. *Z. Metallkunde, Vol. 34, 208-215, 1942.*

49 **Gebhardt E.** Gleichgewichtsuntersuchungen in den systemen zinc-aluminium und zinc-aluminium-kupfer. *Z. Metalkunde, Vol. 40, 136-140, 1949.*

50. **Bauer O. and Hansen M.** Der einfluβ von dritten matellen auf die konstitution der messinglegieningen. *Z. Metallkunde, Vol. 24, 1-6, 1932.*

51. **Bauer O. and Hansen M.** Der einfluβ von dritten matellen auf die konstitution der messinglegieningen. *Z. Metallkunde, Vol. 24, 73-78, 1932.*

52. **Fletcher A.J. and Thomas D.L.** Solid State Transformations in Certain Copper-Aluminium-Zinc Alloys. *J. Inst. Met., Vol. 98, 188-192, 1970.*

53. **Koster W.** Uber den aufbau und die volumenanderungen der zinc-kupfer-aluminium-legrerungen. *Z. Metallkunde, Vol. 33, 289-296, 1941.*

54. **Willey L.A.** Aluminium-Copper-Zinc. Metals Handbook, *8th Edition, Vol. 8, 390-391, American Society for Metals, Ohio, 1973.*

55. **Arndt H.H. and Moeller K.** Die ternare phase im system kupfer-aluminium-zink; I. Der Zerfall der T-phase zwischen 200 und 300°. *Z. Metallkunde, Vol. 51, 596-600, 1960.*

56. **Arndt H.H. and Moeller K.** Die ternare phase im system kupfer-aluminium-zink; II. Das Zustandsgebiet der T-phase oborhalb 500°. *Z. Metallkunde, Vol. 51, 656-662, 1960.*

57. **Strawbridge D.J., Hulme-Rothery W. and Little A.T.** The Constitution of Aluminium-Copper-Magnesium-Zinc Alloys at 460°C. *J. Inst. Met., Vol. 74, 191-225, 1947-48.*

58. **Burkhardt A.** Zinklegierungen als Austauschuekstoff. *Z. Metallkunde, Vol. 28, 299-308, 1936.*

59. **Murphy S.** Solid-Phase Reactions in the Low-Copper Part of the Al-Cu-Zn System. *Z. Metallkunde, Vol. 71, 96-102, 1980.*

60. **Murphy S.** The Structure of the T' Phase in the System Al-Cu-Zn. *Met. Sci., Vol. 9, 163-168, 1975.*

61. **Garwood R.D., Davies A.L. and Richards G.L.** A Transition Phase in the Ageing of Aluminium-Zinc Alloys. *J. Inst. Met., Vol. 88, 375-378, 1959-60.*

62. **Richards G.L. and Garwood R.D.** An Electron-Microscope Study of the Isothermal Decomposition of an Aluminium-25% Zinc Alloy. J. *Inst. Met., Vol. 93, 393-397, 1964-65.*

63. **Merz W. and Gerold V.** Strukturelle Untersuchungen der ausscheidung in aluminium-zinc-legierungen. *Z. Metallkunde, Vol. 57, 607-615, 1966.*

64. **Carpenter G.T.C. and Garwood R.D.** Hardness Reversion and the Metastable Phase Boundary for G.P. Zones in Aluminium-Zinc Alloys. *J. Inst. Met., Vol. 94, 301-303, 1966.*

65. **Simerska M. and Synecek V.** The Mechanism of Structure Transformations in Supersaturated Al-Zn Alloys. *Acta. Metall., Vol. 15, 223-230, 1967.*

66. **Carpenter G.J.C. and Garwood R.D.** The Ageing of a Quenched Aluminium - 22.5% Zinc Alloy. *Met. Sci. J., Vol. 1, 202-211, 1967.*

67. **Jacobs M.H.** The Morphology of Crystal Structure of a New Precipitate in Rapidly Quenched Aluminium-Zinc Alloys. *Met. Sci. J., Vol. 6, 143-148, 1972.*

68. **Ramaswamy V., Butler E.D. and Swann P.R.** Direct Observation of Discontinuous Precipitation in Al-28 at % Zn. *J. Microscopy, Vol. 97, 259-26, 1973*

69. **Vijayalakshmi M., Seetharaman V. and Raghunathan V.S.** Cellular Decomposition in Al-Zn Alloys. *Acta Metall., Vol. 30, 1147-1155, 1982.*

70. **Vijayalakshmi M., Seetharaman V. and Raghunathan V.S.** Morphological Features of Discontinuous Reactions in Al-Zn Alloys. *Mat. Sci. Eng., Vol. 52, 249-256, 1982.*

71. **Fournelle R.A. and Clark J.B.** The Genesis of the Cellular Precipitation Reaction. *Metall. Trans., Vol. 3, 2757-2767, 1972.*

72. **Boswell P.G. and Chadwick G.A.** Eutectoid Decomposition of Zn-Al Splat-Quenched and Bulk Specimens. *Acta Metall., Vol. 25, 779-792, 1977.*

73. **Cheetham D. and Ridley N.** Isothermal-Transformation and Directional-Growth Studies on a Zn-Al Eutectoid Alloy, *J. Inst. Met., Vol. 99, 371-376, 1971.*

74. **Nuttall K. and Nicholson R.B.** Microstructure of Superplastic Alloys. *Phil. Mag., Vol. 17, 1087-1091, 1968.*

75. **Ardell A.J., Nuttall K. and Nicholson, R.B.** The Decomposition of Concentrated Al-Zn Alloys. The Mechanism of Phase Transformations in Crystalline Solids. *Inst. of Met., Monograph No. 33, 22-26, London, 1969.*

76. **Rundman K.B. and Hilliard J.E.** Early Stages of Spinodal Decomposition in an Al-Zn Alloy. *Acta Metall., Vol. 15, 1025-1033, 1967.*

77. **Toldin V.A., Kleshchev G.V., Shumilov D.V. and Sheynkman A.J.** A Generalised Scheme of the Sequence of Metastable Phases in Al-Zn Alloys. *Fiz. Metal. Metalloved., Vol. 40, No. 6, 1223-1226, 1975.*

78. **Toldin V.A., Burykin A.A. and Kleshchev G.V.** Natural Ageing of Aluminium-Zinc Alloys with a High Zinc Concentration. *Phys. Met. Metall., Vol. 45, No. 2, 97-100, 1978.*

79. **Toldin V.A., Burykin A.A. and Kleshchev G.V.** Influence of Magnesium Additions on the Phase Sequence During Ageing of Al-Zn Alloys with a High Zinc Content. *Phys. Met. Metall., Vol. 51, No. 1, 116-124, 1981.*

80. **Krupkowski A, Ciach R. and Krol J.** Decomposition of the α'-phase in the Al-Zn alloys with 60-78 per cent zinc. *Bulletin De L'Academie Polonaise des Sciences, Vol.15, No.11,975-979,1967.*

81. **Smith A.E.W. and Hare G.A.** Controlling the Zinc-Aluminium Eutectoid Reaction. *J. Inst. Met., Vol. 101, 320-328, 1973.*

82. **Youdelis W.V. and Dallin G.W.** Effect of Magnesium and Copper on the Decomposition Kinetics and Mechanical Properties of Zinc-Aluminium Alloys. *Conference of Metallurgists, The Canadian Inst. Mining Metall., Paper 40, University of Toronto, August 28-31, 1966.*

83. **Zhu Y.H.** Phase Relationships in Zn-Al Based Alloys. *Ph.D. Thesis, The University of Aston in Birmingham, 1983.*

84. **Murphy S., Mykura N. and Zhu Y.H.** Solid-State Reactions in Zn-Al Based Alloys. *24th. Ann. Conf. of Metallurgist, CIM, Vancouver-Canada,1985.*

85. **Mykura N., Murphy S. and Zhu Y.H.** Volume Change in Ternary Zn-Al-Cu Alloys. *Mat. Res. Soc. Proc., Vol. 21, 841-846, 1984.*

86. **Mykura N., Zhu Y.H. and Murphy S.** Solid-State Reactions in Zn-Al Based Alloys. *Canadian Metall. Quarterly, Vol. 25, No. 2, 151-159, 1986.*

87. **Edington J.W., Melton K.N. and Cutler C.P.** Superplasticity. *Prog. Mat. Sci., Vol. 21, 61-170, 1976.*

88. **Mukherjee A.K.** Deformation Mechanisms in Superplasticity. *Ann. Rev. Mat. Sci., Vol. 9, 191-217, 1979.*

89. **Edington J.W.** Microstructural aspects of superplasticity. *Metall. Trans.* , *Vol.13A, 703-715, 1982.*

90. **Langdon T.G.** The Mechanical Properties of Superplastic Materials. *Metall. Trans., Vol. 13A, 689-701, 1982.*

91. **Chaudhari P.** Deformation Behaviour of Superplastic Zn-Al Alloys. *Acta. Metall., Vol. 15, 1777-1786, 1967.*

92. **Farghalli A.M., Mohamed M.I.A. and Langdon T.G.** Factors Influencing Ductility in the Superplastic Zn - 22% Al Eutectoid. *Metall. Trans., Vol. 8A, 933-938, 1977.*

93. **Arieli A., Yu A.K.S. and Mukherjee A.K.** Low Stress and Superplastic Creep Behaviour of Zn - 22% Al Eutectoid Alloy. *Metall. Trans., Vol. 11A, 181-191, 1980.*

94. **Livesey D.W. and Ridley N.** Investigation of the Stress-Strain Rate Curve at Low Strain Rates for Superplastic Zn - 22% Al Alloy. *Scripta Metall., Vol. 16, 165-168, 1982.*

95. **Kaybyshev O.A., Kazachkov I.V. and Rodionov B.V.** Influence of Structure and Composition on the Superplasticity of Zinc-Aluminium Alloys. *Fiz. Metal. Metalloved., Vol. 39, No. 2, 338-346, 1975.*

96. **Cook R.C. and Risebrough N.R.** Superplasticity in a Dilute Zinc-Aluminium Alloy. *Scripta Metall., Vol. 2, 487-490, 1968.*

97. **Suery M. and Mukherjee A.K.** Superplasticity Correlation Between Structure and Properties, Creep Behaviour of Crystalline Solids. *Editors : Wilshire B. and Evans R.W., Vol. 3 in the Series Progress in Creep and Fracture, 137-200, Pineridge Press, Swansea, 1985.*

98. **Chen I.W.** Migration Assisted Diffusional Creep by Grain-Boundary Diffusion. *Acta Metall., Vol. 30, 1317-1323, 1982.*

99. **Ashby M.F. and Verrall R.A.** Diffusion Accommodated Flow and Superplasticity. *Acta Metall., Vol. 21, 149-163, 1973.*

100. **Novikov I.I., Portnoy V.K. and Levchenko V.J.** Investigation of Structural Changes During Superplastic Deformation of Zn - 22% Al Alloy by Replica Locating Technique. *Acta Metall., Vol. 29, 1077-1090, 1981.*

101. **Shariat D., Vastava R.B. and Langelo T.G.** An Evaluation of the Roles of Intercrystalline and Interphase Boundary Sliding in Two-Phase Superplastic Alloys. *Acta Metall., Vol. 30, 285-296, 1982.*

102. **McLean D.** Grain Boundary Dislocations : Their Effect on Vacancies and Sliding. *Phil. Mag., Vol. 23, 467-472, 1971.*

103. **Raj R. and Ashby M.F.** On Grain Boundary Sliding and Diffusional Creep. *Metall. Trans., Vol. 2, 1113-1127, 1971.*

104. **Naziri H., Pearce R.P., Brown M.H. and Hale K.F.** In Situ Superplasticity Experiments in the 1 Million Volt Electron Microscope. *J. of Microscopy, Vol. 97, No. 1/2, 229-238, 1973.*

105. **Hazzledine P.M. and Newbury D.E.** A Model for Micrograin Superplastic Flow. *3rd I.C.S.M.A., 202-206, Inst. of Metals, London, 1973.*

106. **Ball A. and Hutchinson M.M.** Superplasticity in the Aluminium-Zinc Eutectoid. *Met. Sci. J., Vol. 3, 1-7, 1969.*

107. **Mukherjee A.K.** The Rate Controlling Mechanism in Superplasticity. *Mater. Sci. Eng., Vol. 8, 83-89, 1971.*

108. **Gifkins R.C.** Grain Boundary Sliding and its Accommodation During Creep and Superplasticity. *Metall. Trans., Vol. 7A, 1225-1232, 1976.*

109. **Gifkins R.C.** Grain Rearrangement During Superplastic Deformation. J. *Mat. Sci., Vol. 13, 1927-1935, 1978.*

110. **Gittus J.H.** Theory of Superplastic Flow in Two-Phase Materials : Roles of Interphase-Boundary Dislocations, Ledges and Diffusion. T*rans. ASME, J. Eng. Mat. Tech., Vol. 7, 244-251, 1977.*

111. **Spingarn J.R. and Nix W.D.** A Model for Creep Based on the Climb of Dislocations at Grain Boundaries. *Acta Metall., Vol. 27, 171-177, 1979.*

112. **Naziri H and Pearce R.** The Influence of Copper Additions on the Superplastic Forming Behaviour of the Zn-Al Eutectoid. *Inst. J. Mech. Sci., Vol. 12, 513-521, 1970.*

113. **Nuttall K.** Effect of Some Ternary Additions on the Mechanical Properties of the Zn-Al Eutectoid Alloy. *J. Inst. Met., Vol. 101, 329-333, 1973.*

114. **Mulvania L.E., Weltzin R.D. and Talcott P.A.** A Superplastic Zn-Al Alloy with Creep Resistance. *Met. Eng. Quarterly, Vol. 14, 55-60, 1974.*

115. **Savaskan T.** The Structure and Properties of Zinc-Aluminium Based Bearing Alloys. *Ph.D. Thesis, The University of Aston In Birmingham, 1980.*

116. **Savaskan T. and Murphy S.** Creep Behaviour of Zn-Al-Cu Bearing Alloys. *Z. Metallkunde, Vol. 74, 76-82, 1983.*

117. **Murphy S., Savaskan T. and Hill J.** The Creep Kinetics of Zinc-Aluminium Based Alloys. *Presented at 24th Ann. Conf. of Metallurgists, CIM, Vancouver, Canada, 1985.*

118. **Apelian D., Palival M. and Herrschart D.C.** Casting with Zinc Alloys. *J. Metals, Vol. 33, 12-20, Nov. 1981.*

119. **Morgan S.W.K.** Zinc and its Alloys. *Industrial Metal Series, MacDonald and Evans Ltd., 1977.*

120. **Calayag T. and Ferres D.** High Performance High Aluminium Zinc Alloys for Low Speed Bearings and Bushings. *SAE Technical Paper Series, Earthmoving Industry Conf., Peoria, Illinois, April 19-21, 1982.*

121. Engineering Properties of Zinc Alloys. *Published by Int. Lead Zinc Research Organisation Inc., 2nd Ed., N.Y. 1981.*

122. Mazak Zinc Alloys for Pressure Die-Castings. *A Booklet for Designers, Mazak Ltd., Bristol, U.K., 1972.*

123. A Technical Data Sheet for Mazak 3 Pressure Die-Cast Zinc Alloy Ingot, *Mazak Ltd., Bristol, U.K.*

124. A Technical Data Sheet for Mazak 5 Pressure Die-Cast Zinc Alloy Ingot, *Mazak Ltd., Bristol, U.K.*

125. **Balliett R.W.** Mechanical Properties of Creep Resistant Zinc Die-Casting Alloys. *Paper No. G575-OB, 8th SDCH Int. Die-Casting Exposition and Congress, Detroit, Michigan, March 17-20, 1975.*

126. **Sosa G.D., Greday T. and Coutsouradis D.** Les alliages de zinc moules leur resistance au fluage a chaud et leur agressivite vis-a-vis de l'acier. *ATB Metallurgie XXIV, No. 3, 253-273, 1984.*

127. **Rennhack E.H. and Conard G.P.** Creep Deformation of Rolled Zn-Ti Alloys. *Trans Metall. Soc. AIME, Vol. 236, 1441-1444, 1966.*

128. **Rennhack E.H. and Conard G.P.** Structural Aspects of Fibering in Rolled Zn-Ti Alloys and their Relation to Creep. *Trans. Metall. Soc. AIME, Vol. 236, 694-698, 1966.*

129. **Battiston L., Lockhead T.F. and Adams G.R.** Hot Chamber Casting of ILZRO 16 Alloy. *ILZRO Project ZM-216, Report No. 5, 1977-78.*

130. **Anderson E.A. and Werkey G.L.** A New Zinc Alloy for Gravity Casting. *ILZRO Research Summary, Project ZM-5, July 1962.*

131. **Gervais E., Levert H. and Bess M.** Development of a Family of Zinc Based Foundry Alloys. *Presented at the 84th Casting Congress and Exposition, and published in the Transactions of the American Foundrymen's Society, St. Louis, Missouri, U.S.A., April 21-25, 1980.*

132. **Barber M.J. and Jones P.E.** A New Family of Foundry Alloys. Foundry *Trade J., 114-120, Jan. 17, 1980.*

133. **Lyon R.** The Properties and Applications of ZA Alloys. *The British Foundrymen, 344-349, August/Sept., 1986.*

134. **Lynch R.F.** Zinc Castings for Hazardous Location Electrical Equipment. *Proc. 25th CIM Conf., Toronto, Canada, 277-288, 1986.*

135. **Calayag T.S.** The Practicality of Using Zinc-Aluminium Alloys for Friction-Type Bearings. *Proc. 25th CIM Conf., Toronto, Canada, 305-314, 1986.*

136. **Rollez D., Meens M. and Groothaert L.** Excellent Wear Resistance of ZA.27 Alloy Opens Broad Market Prospects. *Proc. 25th CIM Conf., Toronto, Canada, 315-326, 1986.*

137. **Snodgrass E.M. and Rutherford J.D.** ZA Applications in the Transportation Industry. *Proc. 25th CIM Conf., Toronto, Canada, 327-337, 1986.*

138. **Loong C.A., Gervais E. and Lefebvre M.** Properties and Die-Casting ZA Alloys. *Trans. 13th SDCE Int. Die-Casting Congress and Exposition, Paper No. G-T85-055, June 3-6, Milwaukee, USA, 1985.*

139. **Bess M., Loong C.A. and Olven J.** A Long Term Evaluation of Machine and Tooling Performance During ZA.8 Hot-Chamber Die-Casting. *Trans. 13th SDCE Int. Die-Casting Congress and Exposition, June 3-6, Milwaukee, USA, 1985.*

140. **Rutherford J.** ZA.8 Hot-Chamber Die-Casting Alloys and Process Development. *Trans. 13th SDCE Int. Die-Casting Congress and Exposition, June 3-6, Milwaukee, USA, 1985.*

141. **Murphy S., Hill J. and Durman M.** Creep Behaviour of Commercial Pressure Die Cast Zinc Alloys. *Presented at 12th Int. Pressure Diecaster Conf., Florence, Italy, 1987.*

142. **Loong C.A.** Temperature and Aging and Thickness Effects on Die-Casting Alloys. *Proc. 25th CIM Conf., 157-170, Toronto, Canada, 1986.*

143. BNF Guide to Better Aluminium Diecasting. *The British Non-Ferrous Metals Research Association, Grove Laboratories, Wantage, Berkshire, Nov. 1973.*

144. **Upton B.** Pressure Diecasting, Part 1, Metal, Machines, Furnaces, *1st Ed., Pergamon Press Ltd., 1982.*

145. **Allsop D.F. and Kennedy D.** Pressure Diecasting, Part 2, The Technology of the Diecasting and the Die., *1st Ed., Pergamon Press Ltd., 1982.*

146. **Gervais E., Kandeil A.Y. and Levert H.** Properties and Die Casting of the Zn - 27% Al - 2% Cu - 0.01% Mg Alloy. *11th SDCE Int. Die Casting Congress, Paper No. G-T81-086, Cleveland, Ohio, June 1-4, 1981.*

147. Method for Tensile Testing of Metals, Part 1, Non-Ferrous Metals. *British Standards Inst., BS18 : Part 1, 1970.*

148. **Hirsch P.B., Howie, A., Nicholson R.B., Pashley D.W. and Whelan M.J.** Electron Microscopy of Thin Crystals, *4th Ed., Butterworths, London, 1971.*

149. Die Cast Zinc. *ILZRO Project Report, 1982.*

150. **Klein F.** Creep Behaviour of Zinc Die Casting Alloys. *SDCF 14th Int. Die Casting Congress and Exposition, Paper No. G-787-028, Toronto, Ontario, Canada, May 11-14, 1987.*

151. **Private Communication**, *Mazak Ltd., Bristol, U.K.*

152. **Murphy S., Durman M. and Hill. J** Kinetics of Creep in Pressure Diecast Commercial Zinc-Aluminium Alloys. *Z. Metallkunde, Vol. 79, 243-247, 1988.*

153. **Shirn G.A., Wajda E.S. and Huntington N.B.** Self-Diffusion in Zinc. *Acta Metall., Vol. 1, 515-518, 1953.*

154. **Hilliard J.E., Averbach B.L. and Cohen M.** Self and Inter Diffusion in Aluminium-Zinc Alloys. *Acta Metall., Vol. 7, 86-92, 1959.*

155. **Tegart W.J.M. and Sherby O.D.** Activation Energies for High Temperature Creep of Polycrystalline Zinc. *Phil Mag., Vol. 5, 1287-1296, 1958.*

156. **Wajda E.S.** Grain Boundary Self-Diffusion in Zinc. *Acta Metall., Vol. 2, 184-187, 1954.*

157. **Sherby O.D., Orr R.L. and Dorn J.E.** Creep Correlations of Metals at Elevated Temperatures. *Trans. AIME, J. Metals, Vol. 200, 71-80, 1954.*

158. **Flinn J.E. and Munson D.E.** Stress-Dependence of the Transition Behaviour in Multi-Mechanism Creep Reactions : with Special Reference to Zinc. *Phil. Mag., Vol. 11, 861-870, 1967.*

159. **Weatherby G.C.** The Structure of Ledges at Plate-Shaped Precipitates. *Acta Metall., Vol. 19, 181-192, 1971.*

160. **Ansell G.S. and Weertman J.** Creep of a Dispersion-Hardened Aluminium Alloy. *Trans Metall. Soc. AIME, Vol. 215, 838-843, 1959.*

161. **Lagneborg R.** Recovery Creep in Materials Hardened by a Second Phase. *J. Mat. Sci., Vol. 3, 596-602, 1968.*

APPENDICES

APPENDIX A

CREEP TEST DATA OF THE ALLOYS M.3, ZA.8 AND ZA.27

Creep Test Data of Alloy Mazak.3 at 60°C.

M.3 - Temperature : 60°C						
Stress (MPa)	Primary Creep (%)	Secondary Creep Rate (1/s)	Time to 1% Creep Strain (ks)	Time to 0.7% Creep Strain (ks)	Time to 0.5% Creep Strain (ks)	Time to 0.2% Creep Strain (ks)
30	0.192	2.100×10^{-9}	3125.00	2384.00	1468.00	106.00
40	0.175	4.800×10^{-9}	1718.00	1093.00	676.00	90.00
40	0.101	3.500×10^{-9}	2567.00	1710.00	1138.40	281.30
40	0.313	1.010×10^{-8}	680.43	383.40	185.40	21.00
60	0.106	3.060×10^{-8}	292.00	194.20	128.80	30.70
60	0.131	1.600×10^{-8}	542.90	355.40	230.40	42.90
80	0.224	1.016×10^{-7}	76.00	46.86	27.00	3.03
100	0.163	4.997×10^{-7}	15.00	10.00	6.74	0.59

Creep Test Data of Alloy Mazak.3 at 90℃.

M.3 - Temperature : 90°C						
Stress (MPa)	**Primary Creep (%)**	**Secondary Creep Rate (1/s)**	**Time to 1% Creep Strain (ks)**	**Time to 0.7% Creep Strain (ks)**	**Time to 0.5% Creep Strain (ks)**	**Time to 0.2% Creep Strain (ks)**
15	0.141	3.500×10^{-9}	2308.00	1598.00	1026.80	169.70
20	0.124	4.400×10^{-9}	990.00	806.50	667.60	172.30
20	0.083	1.900×10^{-9}	2801.00	2086.00	1674.00	616.00
30	0.173	3.150×10^{-8}	238.00	167.25	103.80	16.25
40	0.135	1.085×10^{-7}	59.50	44.80	33.00	6.00
40	0.143	1.308×10^{-7}	65.50	42.56	27.30	5.30
60	0.202	4.949×10^{-7}	16.13	10.00	6.02	1.00
60	0.230	6.076×10^{-7}	12.60	7.74	4.45	0.90
80	0.197	2.956×10^{-6}	2.71	1.70	1.02	0.30

Creep Test Data of Alloy Mazak.3 at 120°C.

M.3 - Temperature : 120°C						
Stress (MPa)	Primary Creep (%)	Secondary Creep Rate (1/s)	Time to 1% Creep Strain (ks)	Time to 0.7% Creep Strain (ks)	Time to 0.5% Creep Strain (ks)	Time to 0.2% Creep Strain (ks)
11	0.53	9.300×10^{-9}	510.00	187.50	55.00	10.00
11	0.04	3.570×10^{-8}	269.50	184.00	128.00	44.00
21	0	1.560×10^{-7}	59.70	45.00	32.00	13.00
21	0	2.750×10^{-7}	40.30	29.50	22.50	7.50
41	0.36	1.770×10^{-6}	4.50	2.40	1.00	0.10
41	0.25	1.300×10^{-6}	5.95	3.60	1.90	0.30

Data at this temperature is from the work of Murphy et al.(ref. 117)

Creep Test Data of Alloy Mazak.3 at 150℃.

M.3 - Temperature : 150°C						
Stress (MPa)	**Primary Creep (%)**	**Secondary Creep Rate (1/s)**	**Time to 1% Creep Strain (ks)**	**Time to 0.7% Creep Strain (ks)**	**Time to 0.5% Creep Strain (ks)**	**Time to 0.2% Creep Strain (ks)**
10	0.172	1.206×10^{-7}	63.400	43.750	27.165	4.327
10	0.121	6.140×10^{-8}	111.500	79.500	56.000	12.860
15	0.093	6.550×10^{-7}	9.220	6.400	5.000	1.680
20	0.113	1.768×10^{-6}	4.500	3.300	2.180	0.500
20	0.121	1.183×10^{-6}	7.290	4.890	3.000	0.600
30	0.047	4.487×10^{-6}	2.000	1.450	1.000	0.300
40	0.157	1.151×10^{-5}	0.732	0.470	0.298	0.100

Creep Test Data of Alloy ZA.8 at 60°C.

ZA.8 - Temperature : 60°C						
Stress (MPa)	**Primary Creep (%)**	**Secondary Creep Rate (1/s)**	**Time to 1% Creep Strain (ks)**	**Time to 0.7% Creep Strain (ks)**	**Time to 0.5% Creep Strain (ks)**	**Time to 0.2% Creep Strain (ks)**
40	0.171	7.483×10^{-10}	11076.000	7067.000	4394.000	850.000
60	0.241	4.100×10^{-9}	1852.000	1120.000	632.000	140.000
60	0.206	4.800×10^{-9}	1654.000	1029.000	612.400	150.000
80	0.167	2.970×10^{-8}	280.600	179.600	112.250	16.000
100	0.454	1.304×10^{-7}	41.860	18.850	3.510	0.600

Creep Test Data of Alloy ZA.8 at 90°C.

ZA.8 - Temperature : 90°C						
Stress (MPa)	Primary Creep (%)	Secondary Creep Rate (1/s)	Time to 1% Creep Strain (ks)	Time to 0.7% Creep Strain (ks)	Time to 0.5% Creep Strain (ks)	Time to 0.2% Creep Strain (ks)
20	0.093	7.657×10^{-10}	11848.000	7930.000	5318.000	1400.000
40	0.151	6.600×10^{-9}	1287.000	832.000	529.000	74.000
40	0.072	2.380×10^{-8}	363.000	258.300	179.700	53.700
60	0.454	5.660×10^{-8}	96.460	43.460	14.580	0.000
60	0.326	6.950×10^{-8}	92.000	53.750	25.000	5.400
100	0.459	2.489×10^{-6}	2.500	0.970	0.400	0.000

Creep Test Data of Alloy ZA.8 at 120°C.

ZA.8 - Temperature : 120°C						
Stress (MPa)	**Primary Creep (%)**	**Secondary Creep Rate (1/s)**	**Time to 1% Creep Strain (ks)**	**Time to 0.7% Creep Strain (ks)**	**Time to 0.5% Creep Strain (ks)**	**Time to 0.2% Creep Strain (ks)**
12	0.24	1.394×10^{-9}	5350.000	3299.000	1850.000	170.000
26	0.07	2.875×10^{-8}	321.000	196.000	150.000	47.000
26	0.21	2.300×10^{-8}	290.000	212.000	126.000	16.000
41	0.20	8.230×10^{-8}	104.700	61.000	57.000	5.000
60	0.19	4.125×10^{-7}	17.300	11.500	7.400	1.100
60	0.16	1.230×10^{-6}	6.850	4.500	2.900	0.800
100	0.40	1.580×10^{-5}	0.380	0.220	0.120	0.030

Data at this temperature is from the work of Murphy et al.(ref. 117)

Creep Test Data of Alloy ZA.8 at 150°C.

ZA.8 - Temperature : 150°C						
Stress (MPa)	Primary Creep (%)	Secondary Creep Rate (1/s)	Time to 1% Creep Strain (ks)	Time to 0.7% Creep Strain (ks)	Time to 0.5% Creep Strain (ks)	Time to 0.2% Creep Strain (ks)
10	0.352	1.600×10^{-9}	4050.000	2175.000	925.400	146.000
10	0.441	1.600×10^{-9}	3490.000	1615.000	500.000	53.000
15	0.230	3.360×10^{-8}	229.000	139.800	80.300	20.000
20	0.241	5.290×10^{-8}	143.400	86.700	48.800	16.500
20	0.076	1.572×10^{-7}	58.770	39.680	26.960	7.800
30	0.154	8.198×10^{-7}	10.300	6.650	4.200	1.500
40	0.196	9.690×10^{-7}	8.290	5.200	3.000	0.100
60	0.108	9.094×10^{-6}	0.980	0.650	0.430	0.100

Creep Test Data of Alloy ZA.27 at 60 °C.

ZA.27 - Temperature : 60°C						
Stress (MPa)	Primary Creep (%)	Secondary Creep Rate (1/s)	Time to 1% Creep Strain (ks)	Time to 0.7% Creep Strain (ks)	Time to 0.5% Creep Strain (ks)	Time to 0.2% Creep Strain (ks)
30	0.162	9.610×10^{-10}	8717.000	5595.000	3514.000	580.000
40	0.244	2.400×10^{-9}	3149.000	1898.800	1065.500	38.500
40	0.200	2.800×10^{-9}	2857.000	1785.000	1071.000	74.500
60	0.373	1.610×10^{-8}	389.600	203.240	79.000	15.000
60	0.284	1.200×10^{-8}	597.000	347.000	180.300	7.700
100	0.478	1.450×10^{-7}	36.000	15.310	6.000	0.100
100	0.369	2.221×10^{-7}	28.400	14.890	7.500	1.000

Creep Test Data of Alloy ZA.27 at 90°C.

ZA.27 - Temperature : 90°C						
Stress (MPa)	**Primary Creep (%)**	**Secondary Creep Rate (1/s)**	**Time to 1% Creep Strain (ks)**	**Time to 0.7% Creep Strain (ks)**	**Time to 0.5% Creep Strain (ks)**	**Time to 0.2% Creep Strain (ks)**
20	0.725	1.900×10^{-9}	1448.000	750.000	468.000	101.000
20	0.755	1.700×10^{-9}	1442.000	625.000	348.000	72.000
40	0.206	4.980×10^{-8}	159.500	99.300	59.100	4.700
40	0.419	5.660×10^{-8}	102.600	49.580	18.500	2.000
60	0.383	4.302×10^{-7}	14.400	7.370	2.700	0.950
70	0.617	5.032×10^{-7}	7.610	1.650	1.250	0.100
100	0.519	4.483×10^{-6}	1.070	0.400	0.200	0.000
100	0.671	3.829×10^{-6}	0.860	0.420	0.200	0.000

Creep Test Data of Alloy ZA.27 at 120°C.

ZA.27 - Temperature : 120°C						
Stress (MPa)	**Primary Creep (%)**	**Secondary Creep Rate (1/s)**	**Time to 1% Creep Strain (ks)**	**Time to 0.7% Creep Strain (ks)**	**Time to 0.5% Creep Strain (ks)**	**Time to 0.2% Creep Strain (ks)**
11	0.890	2.070×10^{-9}	535.000	60.000	15.000	—
11	0.325	7.890×10^{-9}	858.000	474.000	222.000	28.000
21	0.310	8.570×10^{-8}	80.200	45.500	22.500	2.750
21	0.600	7.270×10^{-8}	53.700	21.000	9.000	2.000
41	0.400	7.767×10^{-7}	7.700	3.850	1.500	0.170
41	0.375	8.570×10^{-7}	7.500	4.250	2.500	0.750
41	0.400	1.140×10^{-6}	5.300	2.700	1.300	0.250
70	0.480	1.158×10^{-5}	0.450	0.190	0.100	0.000

Data at this temperature is from the work of Murphy et al.(ref. 117)

Creep Test Data of Alloy ZA.27 at 150°C.

ZA.27 - Temperature : 150°C						
Stress (MPa)	**Primary Creep (%)**	**Secondary Creep Rate (1/s)**	**Time to 1% Creep Strain (ks)**	**Time to 0.7% Creep Strain (ks)**	**Time to 0.5% Creep Strain (ks)**	**Time to 0.2% Creep Strain (ks)**
10	0.622	9.550×10^{-10}	3962.000	820.000	156.000	8.000
10	0.631	1.400×10^{-9}	2635.000	492.000	62.500	6.000
12	0.721	1.320×10^{-8}	211.100	40.600	15.600	3.100
15	1.106	3.330×10^{-8}	31.250	15.600	6.250	1.500
20	0.972	3.508×10^{-7}	10.000	6.000	3.500	1.500
20	0.703	2.321×10^{-7}	13.750	6.670	3.330	0.600
30	0.363	3.960×10^{-6}	1.610	0.850	0.360	0.100
40	0.415	9.120×10^{-6}	0.641	0.312	0.140	0.030
60	0.339	5.822×10^{-5}	0.114	0.062	0.026	0.000

APPENDIX B

PAPER PUBLISHED IN ZEITSCHRIFT FUR METALLKUNDE

Volume: 79, 1988

Kinetics of Creep in Pressure Diecast Commercial Zinc-Aluminium Alloys

Samuel Murphy*, Mehmet Durman*, and Jonathon Hill**

(*Aston University, Aston Triangle, Birmingham, B4.7ET, and **Mazak (a Division of AM&S Europe Ltd.), Bristol, U.K.)

Aston University

Content has been removed for copyright reasons